Centrifugal Dredge Pumps

A study on particle trajectories near impeller blades

T. van den Boogaard

Delft University of Technology
Faculty Mechanical, Maritime and Materials Engineering
Section of Dredging Engineering

TU Delft

Centrifugal Dredge Pumps

A study on particle trajectories near impeller blades

by

T. van den Boogaard

to obtain the degree of Master of Science
at the Delft University of Technology, to be defended publicly on Monday November 2, 2020 at 01:00 PM.

Student number:	4617762	
Project duration:	December 1, 2019 – November 2, 2020	
Thesis committee:	Ir. X. Chen,	TU Delft, daily supervisor
	Dr. Ir. S.A. Miedema,	TU Delft, supervisor and chairman of committee
	Dr. Ir. D.L. Schott,	TU Delft

TU Delft

Preface

In front of you lays a master thesis that has followed an extraordinary path to become what it is today. Originally, this master thesis would be a result of an international collaboration between two research institutions. However, due to the outbreak of COVID-19, this collaboration/exchange had to be cancelled last minute. This resulted in a certain delay of some extent regarding literature research and experimental data gathering. As of already invested time and a strong motivation of continuing, Prof. Dr. Ir. C. van Rhee made a special (emergency) TU Delft budget available for funding the needed experimental setup. The funding has only been used for building material and parts.

I want to use this section to show my gratitude towards my supervisors and others who helped me successfully completing this thesis. As to start with, Ir. Xiuhan Chen for his constantly support and availability. Especially, during writing and setting up the guidelines for the literature research and this final document. I also want to say thanks to him regarding the time spend on setting up an exchange that sadly did not happen. Further, Dr. Ir. Sape Miedema for his time and expertise in reviewing drafts and guiding me through the "Master's Thesis Project". Also, "de Koning BV Vijfhuizen" should not be forgotten for offering their facilities to build the experimental setup during the outbreak of COVID-19. Without these facilities, the experimental setup could not have been fabricated and assembled with an eye on budget and time management.

At last, I want to say thanks to my family and friends for supporting me with my studies along the way.

T. van den Boogaard
Delft, November 2020

Abstract

Transportation of slurries over a distance has always been one of the main objectives for the dredging industry. To accomplish a transport, centrifugal dredge pumps and mixture pipelines need to be perfectly intertwined. On the slurry transport side, an extensive amount of research has already been conducted towards flow assurance and plugging. For the centrifugal dredge pump on the other hand, available information is relatively scattered or confidential. The performance of a centrifugal pump is mainly determined by conducting experiments with actual slurries or estimated on the performance characteristics obtained from water.

Besides empirical research in laboratories and field studies, numerical Computational Fluid Dynamics (CFD) simulations have become an interesting asset in creating models for multiphase situations. This mainly due to increasing computational power that is currently available. At the 22^{nd} World Dredging Congress, Cao et al. (2019) was awarded with an IADC Young Author Award for her outstanding paper on "Numerical investigation of the head and unsteady flow characteristics of a dredge pump loading high-concentration sands". By chance, a similar unfinished empirical research on particle trajectories near impeller blades had been conducted by Hofstra et al. (2008) at the Technical University of Delft (TU Delft). The similarity between these research, arose the interest to conduct an experimental study, within the facilities of the dredging laboratory, to validate (visually) the numerical outcomes of Cao et al. (2019) for unsteady head and particle trajectories near impeller blades.

The goal of this research is to gather and analyse information on particle trajectories near impeller blades and its unsteady head characteristics in a centrifugal dredge pump for visual validation of Cao et al. (2019) CFD model outcomes. In the literature research part, information was gathered on empirical models, CFD simulations, an analytical description of particle behaviours along impeller blades, (dimensionless) pump characteristics and impeller/shell designs. On the experimental side, the executed experiments consist out of head and discharge recordings by throttling the exit valve for pump characteristics in single phase water conditions and mixture conditions at 564, 846, 1128 and 1410 RPM. The used impeller has a diameter of 155 mm and is a so called "open impeller". At mixture conditions, delivered volumetric concentration (C_{vd}) of 5%, 8%, 12%, 15% and 20% are reached with glass bead particles of 1.5 mm and 3.0 mm with a density of 2500 kg/m^3. High speed image recording are made of the impeller blades at above mentioned situations but with a steady exit valve set to 50% open.

The experimental study gives an interesting inside on the behaviour of particles internally. On the particle trajectory side, where PIVlab image analysis are conducted, the result can be used partially on the streamline verification from the CFD model of Cao et al. (2019). This especially applies for the single phase situations and partially less for the mixture situation due to problems with particle distinguishing. Summarized, this means that the conducted experimental study is not able to fully verify the CFD model outcomes of Cao et al. (2019) for the instantaneous streamlines and concentration distribution between the impeller blades. Though, it supplies a steady base for further research.

For the unsteady head characteristics, that are enhanced during mixture loading, at high-concentrations on the other hand, interesting data is collected. The unsteady head characteristics shows an enhancement in noise at the lower side of the frequency spectra with an increase of concentration and engine speed. At low engine speed, the unsteady head amplitude has a wider spread that results in a lot of short quick amplitude changes. With an increase in speed, these quick amplitude changes are reduced and become more stable. The conditions are similar as in single phase water conditions due to a shift towards the lower side of the spectra. This same behaviour is visible in Cao et al. (2019) CFD model outcomes.

keywords: Dredging, centrifugal (dredge) pump, particle trajectories, multi-phase flow, slurry transport, slurry pump, mixture pump, dredge pump, open impeller blades, PIVlab, mixture flow, unsteady head.

Contents

1 Introduction

At the 22^{nd} World Dredging Congress, Cao et al. (2019) was awarded with an IADC Young Author Award for her outstanding paper on "Numerical investigation of the head and unsteady flow characteristics of a dredge pump loading high-concentration sands". By chance, a similar unfinished empirical research on particle trajectories near impeller blades had been conducted by Hofstra et al. (2008) at the Technical University of Delft (TU Delft). The similarity between these research, arose the interest of Dr. Ir. S.A. Miedema to conduct an experimental study, within the facilities of the dredging laboratory, to validate (visually) the numerical outcomes of Cao et al. (2019) for unsteady head and particle trajectories near impeller blades.

With the support of Prof. Dr. Ir. C. van Rhee, a special TU Delft research budget could be made available to fund the cost of such an experimental setup. The funding has been used to build a small scale version of a transparent centrifugal dredge pump to generate the necessary experimental data for such a verification study on the numerical outcomes of Cao et al. (2019).

1.1. Problem specification

Transportation of slurries over a distance has always been one of the main objectives for the dredging industry. To accomplish a transport, centrifugal dredge pumps and mixture pipelines need to be perfectly intertwined. On the slurry transport side, an extensive amount of research has already been conducted towards flow assurance and plugging. This transport related research can easily be accessed in books such as; "Dredge pumps and slurry transport" by Matoušek (2004), "Slurry transport using centrifugal pumps" by Wilson et al. (2006), "IHC Merwede Handbook for Centrifugal Pumps and Slurry Transportation" by Van den Berg (2013) and "Slurry Transport" by Miedema et al. (2019).

For the centrifugal dredge pump on the other hand, available information is relatively scattered or confidential. The performance of a centrifugal pump is mainly determined by conducting experiments with actual slurries or estimated on the performance characteristics obtained from water (Gandhi et al., 2002). However, these performance characteristics are based on model pump experiments and scaled through the known affinity laws to the desired scale (Van Rhee, 2009). Over the years, many researchers have tried to adjust these affinity laws in such a way that these are applicable for mixtures below 20 percent or match the outcomes from scale research with mixtures (McElvain, 1974; Wilson et al., 2006). Holzenberger (1980) and Engine et al. (2003) did an investigation report on these adjusted relations and concluded that a large scatter due to the semi-empirical nature of the equations is present. Although, most investigations where based on performance tests and showed certain points of agreement below mixture concentrations of 20 percent. For higher concentrations of above 20 percent, Wilson et al. (2006) defined a solids-effects diagram that is dependent on multiple input criteria such as: impeller diameter, particle size d_{50}, delivered concentration corrections, relative density of solids and content of fine particles. In this experiment, measurements on flow rate, delivered concentration, head and input power are recorded. None of the research above payed specific attention to why and/or how the particle trajectories internally may have an influence on the outgoing concentration or flow characteristic. Although, Hofstra et al. (2008) made an attempt to specifically study particle trajectories in pumps experimentally. Also, Gandhi et al. (1998) concluded from experiments that the water affinity laws

for specific head and specific capacity are not valid for slurries. It has also been noted that the output pressure value of a dredge pump when loading a mixture is constantly vibrating around an equilibrium value and thus follows an unsteady head characteristic (Cao et al., 2019).

Besides empirical research in laboratories and field studies, numerical Computational Fluid Dynamics (CFD) simulations have become an interesting asset in creating models for multiphase situations. This mainly due to the increasing computational power that is currently available. Multiple (partly) CFD research from Wu et al. (2015), Cao et al. (2019), Hofstra et al. (2010) and Baocheng et al. (2015) show interesting results regarding streamline patterns, concentration profiles, impeller tongue interaction and particle behaviour and/or trajectories alongside the impeller blades.

Although, the CFD research dictated above give interesting results regarding the specific performance of a centrifugal dredge pump, none has conducted an experimental verification on their internal numerical outcomes or looked into internal particle behaviour experimentally. Most of these performed a verification on the in and out going pressures based on adjusted affinity laws, a generalized scheme or numerical CFD outcomes and created a solution for a specific condition. These head and discharge predictions, from either empirical formulas or CFD models, deviate quickly in accuracy when design parameters such as: particle size, fine concentration and relative density are changed. These changes occur constantly in an operating system due to unsteady head characteristics and product properties inflow fluctuations at the pump inlet. Altogether, it can be stated that deviations on measurement accuracy reveals uncertainties towards known information on mixture behaviour in a centrifugal dredge pump. These are in other-words not well understood and require more investigation.

1.2. Research objectives

The goal of this literature study is to gather information on the centrifugal dredge pump to formulate hypotheses for the upcoming experiments. The key focus is placed on the internal particle behavior and its trajectories near impeller blades. The literature study consist out of empirical models, CFD simulations, an analytical description of particle behaviours along impeller blades, (dimensionless) pump characteristics and impeller/shell designs. The objective of the literature study is to clarify the aforesaid problems of affinity law accuracy, unsteady head characteristics and CFD model understanding before actual experiments are conducted.

Following this literature research, experiments are conducted in order to obtain data that includes: pressure head, flow rate, delivered concentrations, high speed recording (PIV analyses) and power input. This data will then be analysed and processed together with the literature research to gain a better understanding of its internal particle trajectory alongside the impeller blades and the streamlines of Cao et al. (2019) CFD model outcomes is verified. An open source Matlab program called PIVlab is used for analysing the high speed recordings (Thielicke et al., 2014).

The obtained information and data is used to clarify the following main question;

- **"Can an experimental study on particle trajectories near impeller blades of a (transparent) centrifugal dredge pump, verify the CFD model of Cao et al. (2019) and explain the unsteady head characteristics while loading a high-concentration sand water mixture?"**

With its corresponding sub-questions;

- *"Are existing mathematical, physical and semi-empirical models regarding centrifugal pumps applicable to a centrifugal dredge pump?"*
- *"Does a single phase flow experiment in the dredge pump gives the same streamline patterns as the CFD simulation and delivers the expected pump characteristics?"*
- *"Does a mixture flow experiment, at different speeds, flow rates and concentration, shows the same particle behavior as the CFD model?"*
- *"Does the experiments show unsteady characteristics of head? If so, when does this happen and which factor(s) mainly cause these?"*

- *"Does the mixture flow experiment show different areas in the pump where the distribution of concentration significantly deviates?"*

With the outcomes of the above main-question and its sub-questions, a verification on Cao et al. (2019) CFD model will be made and an explanation for the origin of unsteady head characteristics while loading high-concentration sand is given. This should fully conclude all questions and provides a recommendation for further research.

1.3. Methodology

This report has been structured in the following manner. In chapter 2, the conducted literature research can be consulted. Followed by the experimental setup explanation and test protocol in chapter 3. Chapter 4 discusses the outcomes of the conducted experiments and their verification. The conclusion of this report can be found in chapter 5 and followed by recommendation regarding future research in chapter 6.

2

Theoretical background

This literature research is intended to explain the theoretical background required to substantiate the upcoming chapters, conclusions and recommendations. Firstly, a collection of basic knowledge regarding a centrifugal pump for single phase conditions is described, followed with information on hydraulic design and internal behaviour on flow and (particle) trajectories. Thereafter, the effect of solids on dredge pumps is further examined to compare empirical models and formula. Followed by a collection of literature research on CFD simulations that specifically focus on particle behavior near impeller blades of a centrifugal dredge pump. Finally, the expected hypotheses of this research are discussed.

2.1. Basic centrifugal pump theory

As the name already describes, a centrifugal pump uses the centrifugal force of its impeller blades to transport kinetic energy, originating from a drive shaft, towards a fluid of density ρ_f $[kg/m^3]$. This pushes the fluid from the centre towards the outer wall of the pump and forces it into the exit pipe. To overcome internal friction and its associated pressure head H_B $[m]$, a minimum amount of energy is needed. If this minimum amount is reached, a certain flow rate, of discharge Q $[m^3/s]$ is created. With the use of Bernoulli's equation, the needed energy can be expressed in three separate terms as shown in equation 2.1. By dividing the Bernoulli equation with the (water) fluid density, the added energy originating from the pump is made density independent and is expressed as the total dynamic head (TDH), or simply "head" (Wilson et al., 2006).

$$H_B = TDH = \frac{(v_p^2 - v_s^2)}{2 \cdot g} + \frac{(p_p - p_s)}{\rho_f \cdot g} + (h_p - h_s) \tag{2.1}$$

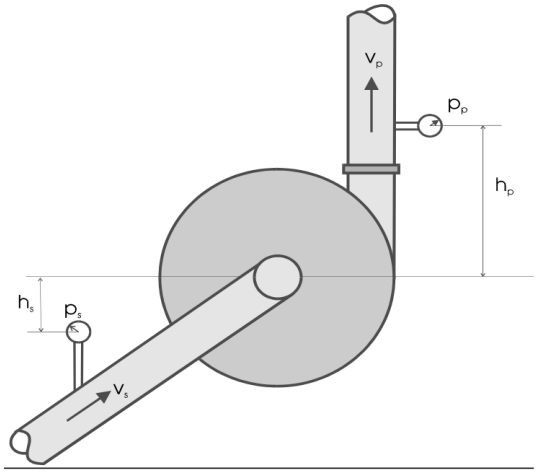

Figure 2.1: Schematic drawing of a centrifugal pump with impeller blades in counterclockwise direction, obtained from Vlasblom (2004)

Figure 2.1, a schematic cross-section, shows the different definitions that are used to calculate the head, discharge and efficiency η [−]. It should be noted that the figure refers to a single fluid phase situation. Subscripts p & s denote to the pressure and suction side of the pump, v_p, v_s are the velocities of the fluid $[m/s]$, p_p, p_s are pressures $[N/m^2]$, h_s, h_p the height different from the center level $[m]$ and D_p is the diameter $[m]$ of the outlet pipe. When known, these values can be used to determine; head H_B with equation 2.1, the adjusted Bernoulli equation, and the discharge capacity Q with equation 2.2.

$$Q = \frac{\pi \cdot D_p^2 \cdot v_p}{4} \tag{2.2}$$

When the $H-Q$ values are available for a constant shaft speed (RPM), a power output P_{out} $[kW]$ of the pump can be determent with equation 2.3 below.

$$P_{out} = \rho_f \cdot g \cdot Q \cdot H_B \tag{2.3}$$

The input power, P_{in} $[kW]$ can be calculated by multiplying the torque T $[Nm]$ on the pump shaft and the angular velocity ω $[rad/s]$. Preferably, the industry defines the shaft speed as "revolutions per minute" (RPM) N, this adds a conversion term to equation 2.4. Engine input power can also be obtained from an electric motor characteristic, supplied by the manufacturer, with known engine slip, mechanical losses, engine efficiency and starting torque.

$$P_{in} = \omega \cdot T = \frac{2\pi \cdot N \cdot T}{60} \tag{2.4}$$

A pump can be defined as ideal when the efficiency reaches 100%. However, such a value can never be reached in real life situations due to losses, friction and back-flow. According to Wilson et al. (2006), efficiencies of over 90% can be achieved for large water pumps. Thus, efficiencies tend to be somewhat less in mixture applications, for reasons to be discussed in subsection 2.3. For calculating the overall efficiency of a pump, equation 2.5 is used.

$$\eta = \frac{P_{out}}{P_{in}} = \frac{60 \cdot \rho_f \cdot g \cdot Q \cdot H_B}{2\pi \cdot N \cdot T} \cdot 100\% \tag{2.5}$$

2.1.1. Pump characteristics

By operating a pump with a constant RPM and throttling a valve at the pressure outlet, a series of data points regarding Q, H and T can be obtained. By throttling, an artificial head is generated to influence Q and T. When the head is then directly plotted against discharge, a pump head characteristics arises for this specific RPM. If also the power P_{in}, efficiency η and limiting suction performance (NPSH) (to be discussed in section 2.2.7) curves are plotted with the use of equation 2.3 and 2.5 in the same figure, a complete pump characteristic as in figure 2.2 is shaped.

In all pump characteristics, the efficiency shows a zero value when the valve is fully closed, $H > 0$, $Q = 0$ and when $H = 0$, $Q \gg 0$. Between these extremes, a maximum of the efficiency is shown and is defines as the "best efficiency point" (BEP). Simultaneously, at the maximum of the efficiency curve, the optimal discharge value Q_{BEP} with respect to power input can be determined. Further, where the efficiency curve intersects with the $H-Q$ curve, the optimal head H_{BEP} is located. By changing the RPM and keeping geometry constant, different Q, H and T values are acquired. However, obtaining multiple sets of data is not necessary due to the existing of scaling relations.

2.1.2. Scaling relations

When geometric shape is kept constant and RPM is changed only, the discharge shift in direct proportion to N, while head shift in proportion to N^2. Further, when RPM is kept constant but the geometric shape of the pump is changed, similar shifts are found. The external diameter of the impeller D $[m]$ is commonly used as the guiding dimension regarding geometric shape scaling, where head scales with respect to D^2 $[m^2]$ and the discharge with D^3 $[m^3]$.

These scaling proportions are the so called affinity laws, or affinity relations, which allow for evaluation of obtained prototype pump performance with three parameters displayed in equation 2.6, 2.7 and 2.8 (Gandhi et al., 2002). It follows from equations, that curves of all members on a set of geometrically similar pumps

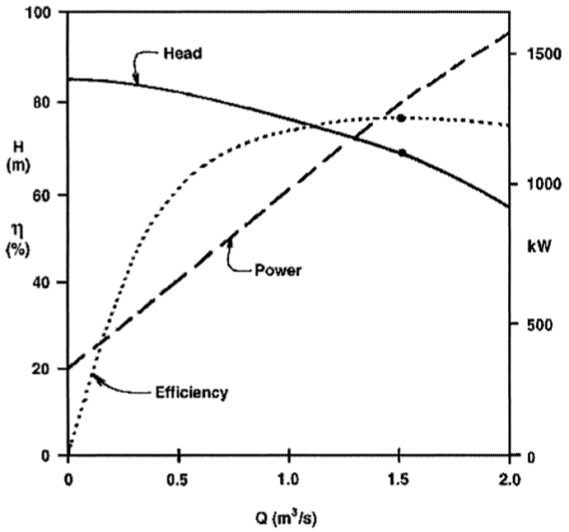

Figure 2.2: Pump characteristic curves, obtained from Wilson et al. (2006)

operating at different RPM can be collapsed into a single entity by using an appropriate system of dimensionless axes (Wilson et al., 2006). White (1986) introduced such a system where the dimensionless discharge is defined with;

$$\Phi = \frac{Q}{n \cdot D^3} \tag{2.6}$$

For dimensionless head;

$$\Psi = \frac{g \cdot H_B}{n^2 \cdot D^2} \tag{2.7}$$

And dimensionless power;

$$\Pi = \frac{P_{in}}{\rho_f \cdot n^3 \cdot D^5} \tag{2.8}$$

White (1986) used these dimensionless numbers to created a dimensionless axis system where dimensionless discharge Φ is plotted against dimensionless head Ψ. To convert head and discharge into their dimensionless version, equation 2.6 and 2.7 are used. Efficiency η can be directly plotted in this dimensionless system, as it is already dimensionless and a dimensionless power input Π curve can be made with use of equation 2.8. Where, n is in angular rotations per second. Both, efficiency and dimensionless power, are plotted against dimensionless discharge.

In figure 2.3, the same set of data as in figure 2.2 is used to plot their dimensionless version. According to Wilson et al. (2006), all points for a geometrical similar pump with varying RPM and pump sizes are indeed on a single line. The same uniformity applies for plotting the efficiency curve, but for smaller pumps the efficiency is slightly lower. This efficiency reduction originates from a greater relative significance of friction (Wilson et al., 2006).

The dimensionless pump characteristics from figure 2.3 can be written as a power series of the second degree. Where for dimensionless head;

$$\Psi = \alpha_0 + \alpha_1 \cdot \Phi + \alpha_2 \cdot \Phi^2 \tag{2.9}$$

And for dimensionless power;

$$\Pi = \beta_0 + \beta_1 \cdot \Phi + \beta_2 \cdot \Phi^2 \tag{2.10}$$

When a pump is scaled through the affinity laws, one can use the dimensionless characteristic as a starting point. A pump specific point is chosen to carry out the point-to-point transfer. To plot a characteristic curve from one pump size and shaft speed towards a different size or speed. These laws apply for all pumps that are in a similar set of geometrically shapes. However, this method is rather cumbersome and Cooper et al. (2001) suggested a different approach. Since, data points of all similar shaped pump plots on the same line at the

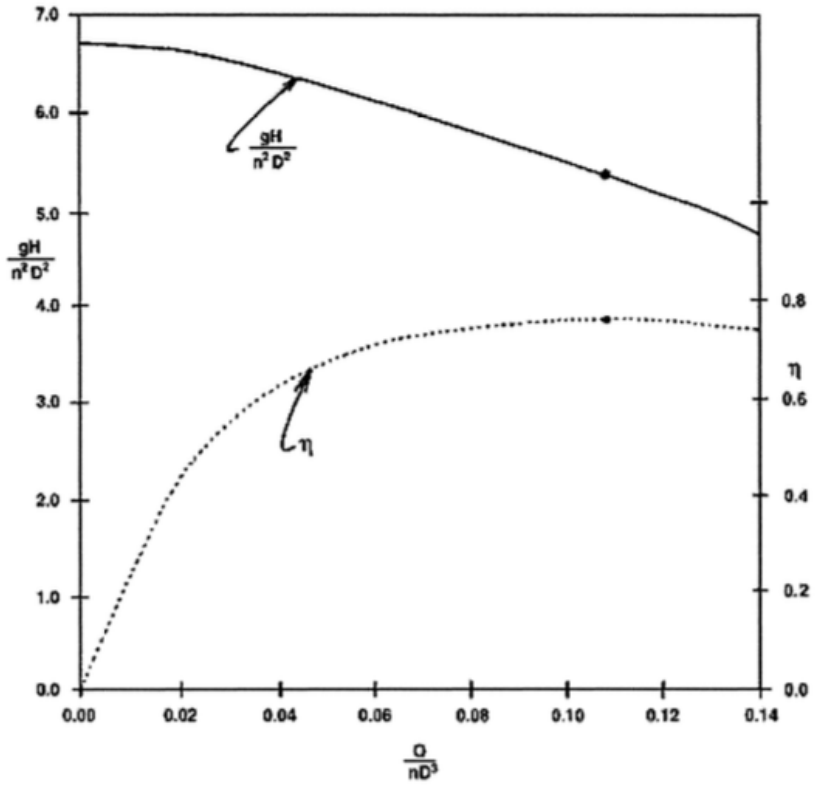

Figure 2.3: Dimensionless pump characteristics, obtained from Wilson et al. (2006)

dimensionless characteristic, it can be said that any point from a prototype pump with impeller diameter D_1 $[m]$ and a RPM of N_1, can be transferred to the curve of the desired pump with diameter D_2 and speed N_2.

For discharge, the affinity law demands that the scale point $\frac{Q}{n \cdot D^3}$ (Φ) has the same value as the prototype in the dimensionless characteristic. This can be done with the use of equation 2.11. Likewise, when dimensions are kept constant and an estimation of discharge at a varying RPM is desired, this equation holds.

$$Q_2 = Q_1 \cdot \left(\frac{N_2}{N_1}\right) \cdot \left(\frac{D_2}{D_1}\right)^3 \tag{2.11}$$

Simultaneously, the same aspects as of discharge are valid for head. Only here the affinity law assures that the scale point $\frac{g \cdot H}{n^2 \cdot D^2}$ (Ψ) has the same value.

$$H_2 = H_1 \cdot \left(\frac{N_2}{N_1}\right)^2 \cdot \left(\frac{D_2}{D_1}\right)^2 \tag{2.12}$$

The affinity law regarding power simply depends on the values of discharge and head. This has also been stated in section 2.1. The power input can be scaled with;

$$P_2 = P_1 \cdot \left(\frac{N_2}{N_1}\right)^3 \cdot \left(\frac{D_2}{D_1}\right)^5 \tag{2.13}$$

An important aspect should be noted when using affinity laws is the scaling dependency of discharge and head. When RPM is changed, it has influences on all three laws in different ratios originating from their superscript values.

2.2. Hydraulic design and internal behaviour

In section 2.1, the centrifugal pump was mainly described as a device where power is converted into a pressure head through its blades. Only external measured values were used to explain the pump behaviour. However, to gain a better understanding of what happens internally, Euler's equation can be used to describe the

2D impeller motion and partly their internal velocities. For clarification purposes, a cross-sectional view of a dredge pump is shown in figure 2.4 with their corresponding part names.

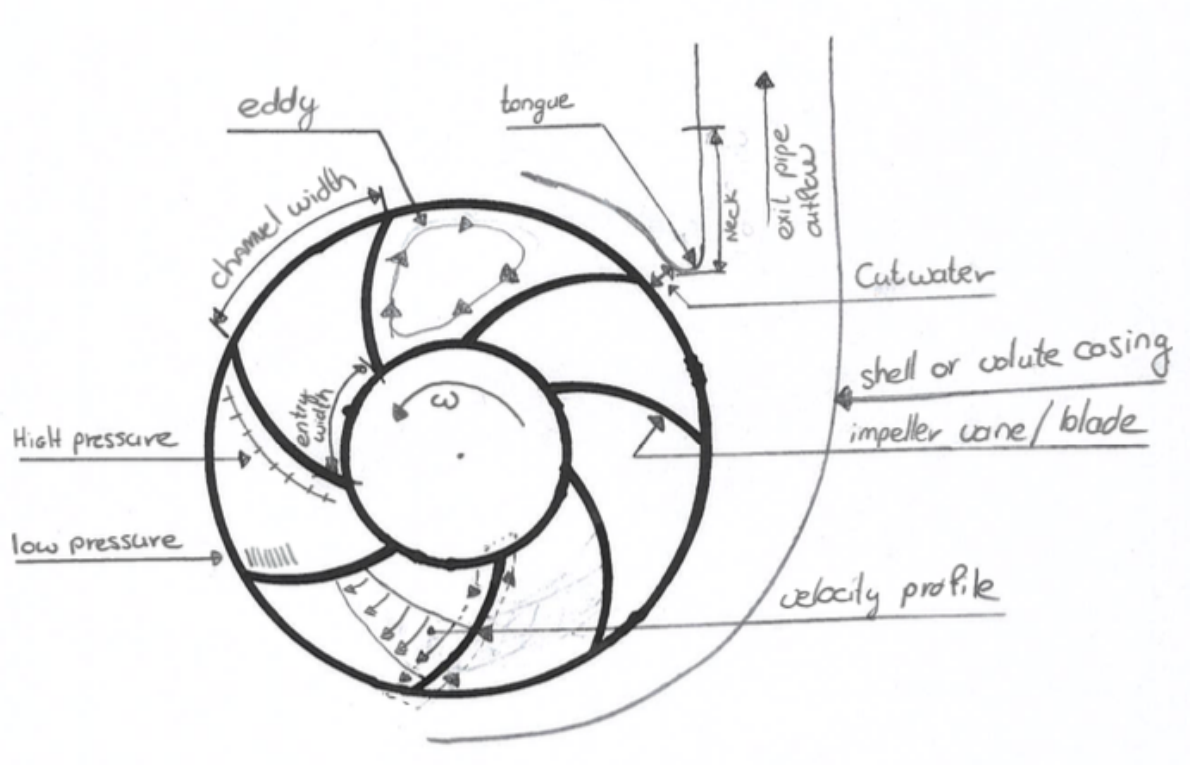

Figure 2.4: Schematic cross-section of a centrifugal dredge pump with corresponding part names and effects.

2.2.1. Euler's pump equation

As a result of Newton's second law, which states that the rate of change in momentum is directly proportional to the force applied and also changes the momentum following the direction of the applied forces. In figure 2.5, these momentum directions are marked as a path through the impeller. The applied torque force, or change in momentum for a rotating bodies is expressed with;

$$T = \frac{d(m \cdot u \cdot r)}{dt} \tag{2.14}$$

Where, m is the mass $[kg]$, r the radius $[m]$ and u the rotational velocity $[m/s]$.

A schematic drawing of an impeller with two imposed velocity triangles is displayed in figure 2.5. The first velocity triangle (centered) includes the entering relative velocity w_1 $[m/s]$ and absolute velocity c_1 $[m/s]$ with its corresponding true particle direction α_1'. The origin of this velocity triangle lays in the change of momentum due to the applied torque force. The evolved velocities and angle are displayed at the outer circle. Note that these have been changed in vector length as an effect of blade curvature, energy transmission and surface increasement. Until now, effect due to friction and shock are neglected and are further discussed in section 2.2.3.

Since only the shift in energy from blade torque into fluid is seen as a velocity difference. The difference "$c_2 - c_1$" can be stated as the full contribution of torque. Velocity vectors, c_1 and c_2, needs to be converted with trigonometry into a tangent vector at the circle boundary for simplification. The velocity difference can then be substituted into equation 2.14. Which results in;

$$T = \frac{d}{dt}\left[m \cdot r_2 \cdot c_2 \cdot cos(\alpha_2') - m \cdot r_1 \cdot c_1 \cdot cos(\alpha_1') \right] \tag{2.15}$$

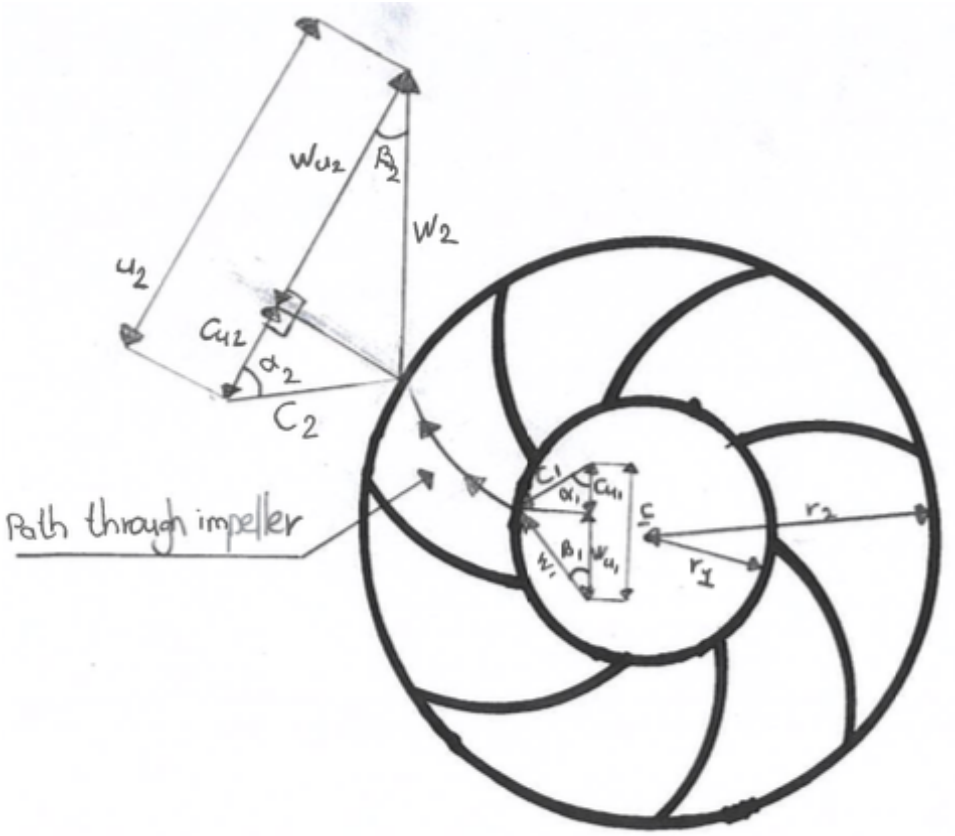

Figure 2.5: Internal velocity triangles at impeller channel entry and channel exit. Impeller rotation in counterclockwise direction.

Equation 2.15, consist out of a time derivative depending torque value that is not favored due to its solve complexity. One may assume that stationary discharge takes place and thus the time derivative is a constant. The full power generation of the impeller can then be calculated with equation 2.4 in a slightly different form. It is stated that the required power P_{in} equals the delivered power P_{out} due to friction losses being neglected. Where the mass is expressed with, $m = Q \cdot \rho_f$. Substituting mass, into equation 2.16, results in a power estimation based on the theoretical delivered pump head H_{th} $[m]$. Note that this is not a measured value as it is in equation 2.4.

$$P_{out} = T \cdot \omega = Q \cdot \rho_f \cdot \omega \cdot (r_2 \cdot c_2 \cdot cos(\alpha_2') - r_1 \cdot c_1 \cdot cos(\alpha_1')) = \rho_f \cdot g \cdot Q \cdot H_{th} \tag{2.16}$$

The peripheral velocity of the impeller can be expressed in $\omega \cdot r = u$, so the expression leads to a further simplification of equation 2.16. Further trigonometry is applied to convert $c \cdot cos(\alpha')$ into c_u, where c_u represents the component in the direction of the peripheral velocity at the absolute velocity. This results in the final equation for H_{th}.

$$H_{th} = \frac{\omega \cdot (r_2 \cdot c_2 \cdot cos(\alpha_2') - r_1 \cdot c_1 \cdot cos(\alpha_1'))}{g} \approx \frac{(u_2 \cdot c_{u_2} - u_1 \cdot c_{u_1})}{g} \tag{2.17}$$

When actual velocities and directions are known, equation 2.17 can provide an outcome. However, these values are unknown in practice and therefore equation 2.17 is rewritten and expressed into vane angles β_1 and β_2. These angles β are known from impeller design and with the use of trigonometry and figure 2.6, Euler's pump equation H_E $[m]$ can be established;

$$H_E = \frac{1}{g} \cdot \left(u_2^2 - u_1^2 - \left(\frac{u_2 \cdot c_{r_2}}{tan(\beta_2)} - \frac{u_1 \cdot c_{r_1}}{tan(\beta_1)} \right) \right) \tag{2.18}$$

Due to stationary conditions, the discharge Q in the blade channel is a constant with a known radius increasement from $r_1 \rightarrow r_2$ and a blade height b from impeller design. By dividing the discharge with the cross-

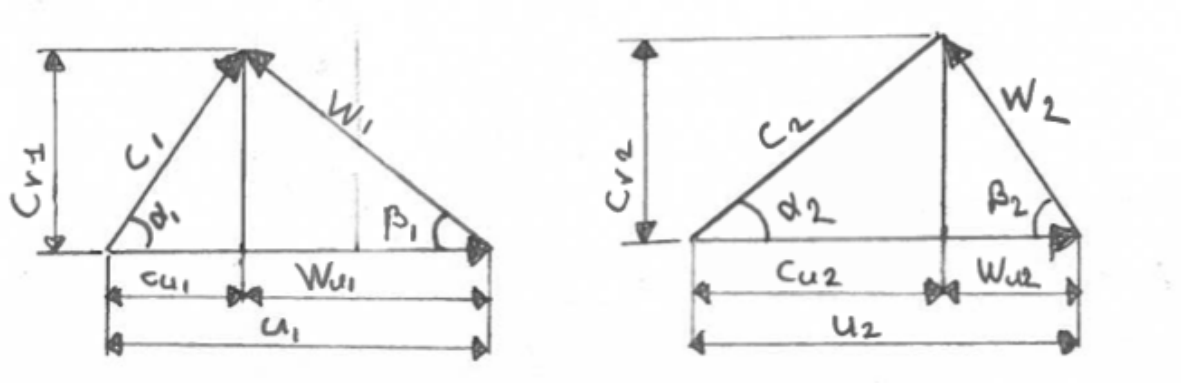

Figure 2.6: Velocity triangles, with angle β, from the impeller channel entry (left) and channel exit (right).

sectional area between the blades, defined as $2\pi \cdot r \cdot b$, the magnitude for c_{r_1} and c_{r_2} are obtained. As an increase in diameter and thus an increase of the r_2 magnitude, the magnitude of c_{r_2} is smaller than c_{r_1}.

$$c_{r_1} = \frac{Q}{2\pi \cdot r_1 \cdot b} \quad c_{r_2} = \frac{Q}{2\pi \cdot r_2 \cdot b} \tag{2.19}$$

Euler's pump equation can then be extended by substituting equation 2.19 into equation 2.18.

$$H_E = \frac{1}{g} \cdot \left(u_2^2 - u_1^2 - \frac{Q}{2\pi \cdot b} \cdot \left(\frac{u_2}{r_2 \cdot tan(\beta_2)} - \frac{u_1}{r_1 \cdot tan(\beta_1)} \right) \right) \tag{2.20}$$

To simplify Euler's equation even further, the following situation may be applicable. One may consider that the liquid enters the impeller without any tangential component and thus the motion in the centrifugal pump is fully radial. This results in a $c_{u_1} = 0$ and Euler's equation becomes;

$$H_E = \frac{1}{g} \cdot \left(u_2^2 - \frac{Q \cdot u_2}{2\pi \cdot b \cdot r_2 \cdot tan(\beta_2)} \right) \tag{2.21}$$

Actually, such condition does not apply in reality and the liquid does have prerotation, this results in a $c_{u_1} \neq 0$ before approach and does not simplify equation 2.20.

2.2.2. Velocity distribution between blades

As stated in the previous section, the true direction angles α_1' and α_2' cannot be obtained and are thus presumed to be the same as the vane angle β_1 and β_2. These real vane angles β originate from impeller design and makes it easier to calculate flow velocities based on those values rather than actual flow velocities.

In reality, a derivation of the fluid with respect to the β vane angle occurs, called β', displayed in figure 2.7. This is a direct reduction in the peripheral component of the absolute velocity c_{u_2} and as a result, a head reduction is noticed. This is called "slip" and has direct consequences on the non-uniform velocity distribution along the impeller blade channel. The input power roughly stays equal due to a constant capacity.

The difference between these β and β' angles is, besides known as slip, also called head reduction factor μ (Vlasblom, 2004). Euler's pump equation H_E is fully expressed on the velocity angles β, while for the theoretical delivered pump head H_{th} is expressed in true velocity angles β'. This result in a μ that can be expressed as follows;

$$\mu = \frac{H_{th}}{H_E} = \frac{\frac{1}{g} \cdot \left(u_2^2 - u_1^2 - \frac{Q}{2\pi \cdot b} \cdot \left(\frac{u_2}{r_2 \cdot tan(\beta_2')} - \frac{u_1}{r_1 \cdot tan(\beta_1')} \right) \right)}{\frac{1}{g} \cdot \left(u_2^2 - u_1^2 - \frac{Q}{2\pi \cdot b} \cdot \left(\frac{u_2}{r_2 \cdot tan(\beta_2)} - \frac{u_1}{r_1 \cdot tan(\beta_1)} \right) \right)} = \frac{\beta'}{\beta} \tag{2.22}$$

2.2.3. Slip factor

To gain an energy transmission from the impeller vanes towards the liquid, a pressure difference is generated at the leading front. This leading front creates a balance to assures a force exertion from vanes onto fluid, with

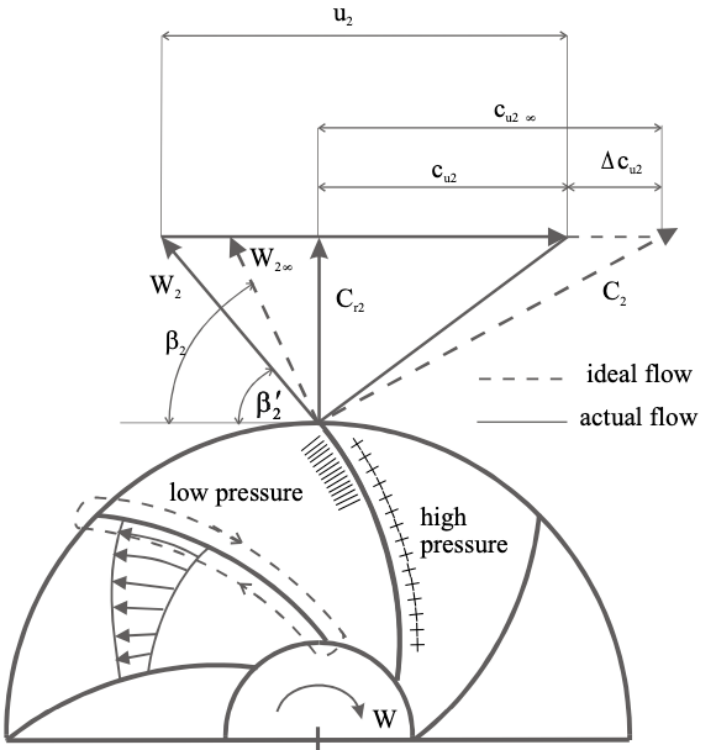

Figure 2.7: Actual and ideal velocities at pump outlet with β' and β, obtained from Vlasblom (2004)

an equal and opposite reaction. As a result, a higher relative velocity between vane and (water) flow is created at the back of the vane compared to the leading front. This creates a velocity profile that can be regarded as the through flow, the flow from channel entry to channel exit, on which a eddy is created. The origin of this eddy can be found in the flow orientation of the fluid along the vanes, see figure 2.7.

Fluid particles enter the channel between the vanes and fail to turn around their axes due to their relative motion being in opposite direction with the impeller rotation. Resulting in an eddy that has the same but opposite velocity compared to the impeller rotation direction, see figure 2.8a. These counter effects result in an inclination of the flow direction at the outlet, figure 2.7 and figure 2.8.

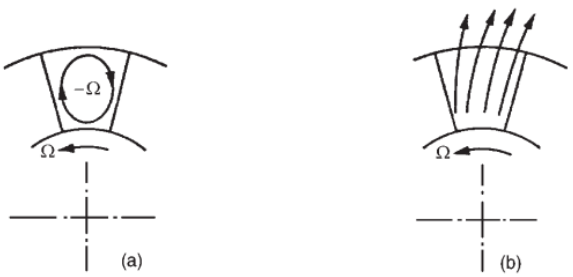

Figure 2.8: (a) Relative eddy without any through flow. (b) Relative flow at impeller exit (through flow added to relative eddy) , obtained from Dixon (1998)

When ideal conditions for the through flow are assumed, it receives less than perfect guidance from the impeller and results in a slip. Assuming that the impeller consist out of an infinite number of infinitesimally thin vanes, creates an ideal flow velocity $c_{u_2\infty}$ that leaves the vanes with angle β, see figure 2.8b. Dividing the tangential component of the absolute velocity c_{u_2}, related to the relative angle β', by the ideal flow velocity, results in a slip factor defined as;

$$\mu = \frac{c_{u_2}}{c_{u_{2\infty}}} \tag{2.23}$$

Since the tangential velocity component $c_{u_{2\infty}}$ is related to the vane angle β, the slip velocity $\triangle c_{u_2}$ can be defined as; $\triangle c_{u_2} = c_{u_{2\infty}} - c_{u_2}$, see figure 2.7 at the velocity triangles. When the slip velocity is then substituted into equation 2.23, this results in;

$$\mu = \frac{\beta'}{\beta} = \frac{c_{u_2}}{c_{u_{2\infty}}} = \frac{c_{u_{2\infty}} - \triangle c_{u_2}}{c_{u_{2\infty}}} = 1 - \frac{\triangle c_{u_2}}{c_{u_{2\infty}}} \tag{2.24}$$

The slip factor from equation 2.24 is still depending on an input value for β', which is unknown. Stodola (1945) defined the slip velocity as a product of the relative eddy and the radius $\frac{d}{2}$ of a circle that is within the channel width. An estimation for the mean channel velocity is made with;

$$\triangle c_{u_2} = \frac{\omega \cdot d}{2} \tag{2.25}$$

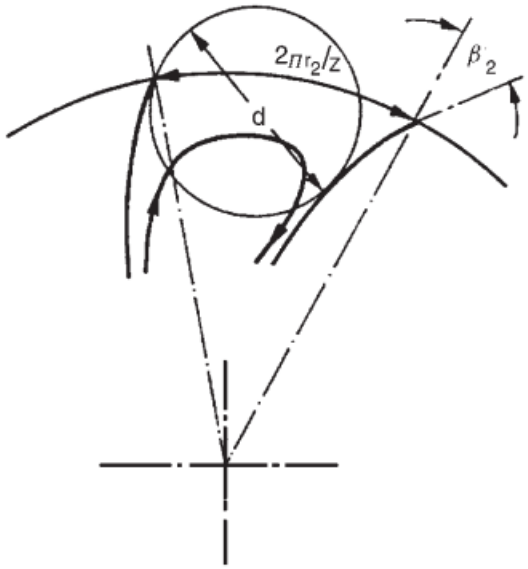

Figure 2.9: Flow model for Stodola slip factor for a counterclockwise rotating impeller, obtained from Dixon (1998)

Where d represents the channel width $[m]$ at the impeller outlet and can be defined with;

$$d = \frac{2\pi \cdot r_2 \cdot sin(\beta_2)}{z} \tag{2.26}$$

With z, the number of vanes of thickness zero $[-]$. Substitute equation 2.26 into 2.25 results;

$$\triangle c_{u_2} = \frac{\pi \cdot \omega \cdot r_2 \cdot sin(\beta_2)}{z} = \frac{\pi \cdot u_2 \cdot sin(\beta_2)}{z} \tag{2.27}$$

Further $c_{u_{2\infty}}$ can be defined with;

$$c_{u_{2\infty}} = u_2 - \frac{c_{r_2}}{tan(\beta_2)} \tag{2.28}$$

Where c_{r_2} is the component of the absolute velocity $[m/s]$ normal to the peripheral velocity. This results in;

$$\mu = 1 - \frac{\pi \cdot u_2 \cdot sin(\beta_2)}{z \cdot \left(u_2 - \frac{c_{r_2}}{tan(\beta_2)}\right)} \tag{2.29}$$

With

$$H_E = \frac{1}{g} \cdot \left(u_2^2 - \frac{u_2 \cdot c_{r_2}}{tan(\beta_2)} \right) \tag{2.30}$$

Gives,

$$\mu = 1 - \frac{\pi \cdot u_2 \cdot sin(\beta_2)}{z \cdot \frac{H_E \cdot g}{u_2}} = \frac{H_{th}}{H_E} \tag{2.31}$$

$$\mu = 1 - \frac{\pi \cdot u_2^2 \cdot sin(\beta_2)}{z \cdot H_E \cdot g} = \frac{H_{th}}{H_E} \tag{2.32}$$

or;

$$1 - \frac{H_{th}}{H_E} = \frac{\pi \cdot u_2^2 \cdot sin(\beta_2)}{z \cdot H_E \cdot g} \tag{2.33}$$

$$H_E - H_{th} = \frac{\pi \cdot u_2^2 \cdot sin(\beta_2)}{z \cdot g} \tag{2.34}$$

2.2.4. Specific speed

In the selection process for a desired centrifugal dredge pump, commonly the discharge, head and RPM (power) are known. As prediscussed, these parameters have a set of dimensionless numbers related to pump scaling. When a combination of these is made, the so called specific speed n_s at the BEP is defined. This parameter is used as a reference number to compare different impeller designs and dimensions with respect towards blade height b, perpendicular to the impeller surface, impeller diameter D and inlet D_{in} over outlet D_{out} diameters. White (1986) suggested to eliminate the impeller diameter with the following equation for specific speed n_s.

$$n_s = \frac{n \cdot \sqrt{Q}}{(g \cdot H_B)^{\frac{3}{4}}} \tag{2.35}$$

Where n, is in rounds per second, Q in m^3/s and H in m. A variation on this equation exist and was proposed by Cooper et al. (2001). This variation is based on angular speed ω rather than rounds per second.

$$n_s = \frac{\omega \cdot \sqrt{Q}}{(g \cdot H_B)^{\frac{3}{4}}} \tag{2.36}$$

Moreover, a derivation on this specific speed exist. Especially defined for engineering practises and is widely used there. This variation consists of removing the gravitational acceleration from equation 2.35 and replacing the rounds per seconds into RPM. However, this variation is inconsistent in units and thus non-dimensionless. This variation in the so called, customary specific speed N_s and is denoted by;

$$N_s = \frac{N \cdot \sqrt{Q}}{H_B^{\frac{3}{4}}} = \frac{s^{-1} \cdot m^{1.5} \cdot s^{-.5}}{m^{.75}} = \frac{m^{.75}}{s^{1.5}} \tag{2.37}$$

When a certain increase/decrease of head or discharge is desired, the specific speed values of an impeller can help. For instance, when a high discharge is needed, an impeller with a high specific speed is most suitable. This applies vice-versa with head, but then a low specific speed impeller is chosen. Naturally, every impeller shape and vane curvature has its own maximum efficiency point and thus adds an extra criteria to impeller selection. These shape criteria are further discussed in the next section. In the figure 2.10, the different characterises of impellers are displayed that inform about these operating areas.

According to Vlasblom (2004), in the dredging industry only centrifugal and half-axial pumps are used. Since on-board of trailing suction hopper dredgers, where the pumps are submerged, the need of low head and high capacity is a requirement.

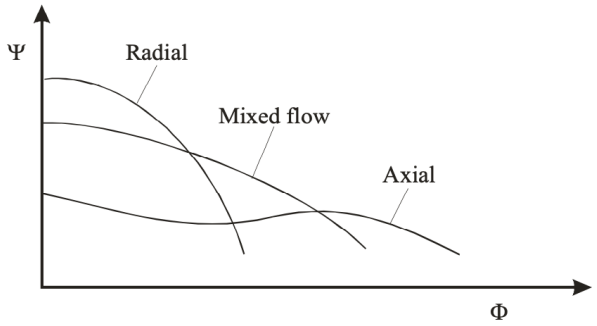

Figure 2.10: Specific Head vs specific Discharge, obtained from Vlasblom (2004)

2.2.5. Dredge shell shape and impeller design

The internal volute of the pump and the curvature of the blades has a great influence on pump performance and thus a wide range of variation exist. The specific speed is used to categorize impellers into different sets with respect to dimensionless discharge and dimensionless head. It should be noted that the impeller diameter is not needed for calculating the specific speed. A further clarification on blade curvature, shell shape and impeller trimming is discussed here.

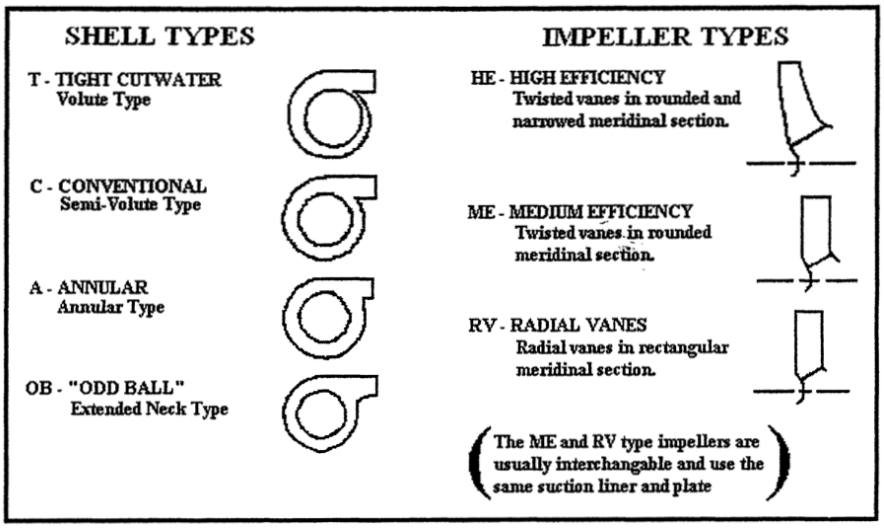

Figure 2.11: Volute and impeller curvature, obtained from (Wilson et al., 2006)

The shell shape of the pump has as purpose to convert the kinetic energy of the fluid leaving the impeller into a pressure head. Multiple shell types are displayed in figure 2.11 and are all perfectly suitable for single and multiphase conditions. Naturally, one is more efficient than others and thus a selection on type is made. This is fully dependent on the mixture that needs to be transported. For instance, when big particles (gravel or debris in sewer application) are expected, one should pick shell type A or OB for its large tongue clearance and special extended neck to limit its wear due to excessive re-circulation (Wilson et al., 2006). If situation are expected with smaller particles, like sand, commonly for a mixture pump, type T is chosen. An off-centric shell that improves particle removal while loading.

Depending on the to be transported mixture, a similar set of selection criteria apply towards impeller types. When a mixture is transported, an impeller with thick vanes and a large impeller channel, which is more capable of handling large particles to assure flow, is needed. This results in different head and discharge values with respect to single phase conditions. Also, some manufacturers adjust the meridional section into a more concave version on top of the impeller spacing. In figure 2.12, three cross-sections of impellers are shown with different designs, from left to right, with an increasing vane thickness and meridional section width.

This modification is applied, so a double inward spiral flow pattern is introduced which reduces wear of the casing (Wilson et al., 2006).

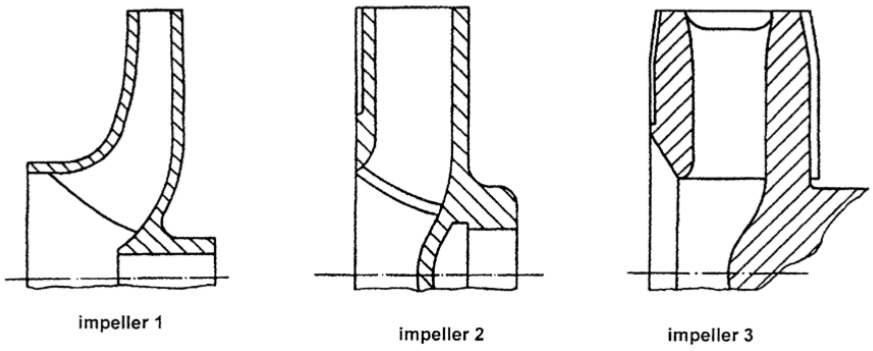

Figure 2.12: Meridional cross-section of three impeller kinds, obtained from (Wilson et al., 2006)

Regarding the vanes shape, Worster (1968) showed that a larger than normal impeller outlet widths for mixture transports tends to shift the discharge capacity at BEP towards a larger value. However, a change in the geometry of the shell can compensate for this shift. Generally, a mixture impeller is of simple shape and lacks complex twisted vanes. This is a compromise between lifespan, maintenance intervals and production cost. Although, this compromise has a large negative effect on the pump's efficiency.

An impeller with a large number of infinitely-thin friction-less (no slip) vanes would produce, in an ideal situation, the highest efficiency. For a centrifugal water pump in practice, this number ranges from five to nine. Compared to a water impeller, a mixture impeller consist out of three to five impeller blades. These blades are relative short due to a compromise between a large bore and pump efficiency. The origin for this compromise lays in the vane shape, so the channel width increasement is minimized to prevent a great velocity gradient of the mixture flow in the channel. A large clearance between the cutwater and the impeller is also desired to prevent large particles from blocking the flow in the shell.

According to Wilson et al. (2006), a lower number of vanes result in a steeper $H-Q$ curve and a reduction in efficiency. This reduction is around 1 to 2 percent in most mixture cases with a shape angle β set to 30 degrees. Again this may vary depending on mixture and performance.

Trimming

The $H-Q$ curve can also be adjusted by trimming the impeller dimensions. By trimming, a certain amount of material is removed to change the diameter of the impeller. This way, the rule of keeping geometric similarity is ignored, as discussed in section 2.1.2, for dimensionless head and dimensionless discharge. Since it has been proven that u_2 varies in directly proportional to the impeller diameter, the value for dimensionless head Ψ does not change due to a small amount of material removal. This means that the scaling law for head still applies in its original form. However, this does not apply for discharge, resulting in a different scaling law required. It is assumed that such a trimming operation is of relatively minor change in diameter so outlet angle β and outlet diameter D_2 remain fixed. Although, the dimensionless discharge value Φ changes proportional scaled from D^3 to D^2 (Wilson et al., 2006). This trimming is all done to accomplish a dimensionless discharge value that shifts closer towards the optimal Q_{BEP}.

2.2.6. Internal head loss corrections

In previous sections, losses due to slip have been extensively described, although other losses have a certain contribution on the real total dynamic head. These other contributors are friction and shock losses, which are expressed in an empirical correction form. For a correction on friction losses, when it is stated that $C_{u_1} = 0$, the contribution is defined as;

$$\triangle H_{friction} = \frac{C_1 \cdot Q^2}{g} \tag{2.38}$$

Where, C_1 [−] is a correction value origination from equation 2.21 defined as;

$$H_E = \frac{1}{g} \cdot \left(u_2^2 - \frac{Q \cdot u_2}{2\pi \cdot b \cdot r_2 \cdot tan(\beta_2)} \right) = \frac{1}{g} \cdot (C_1 - C_2 \cdot Q) \tag{2.39}$$

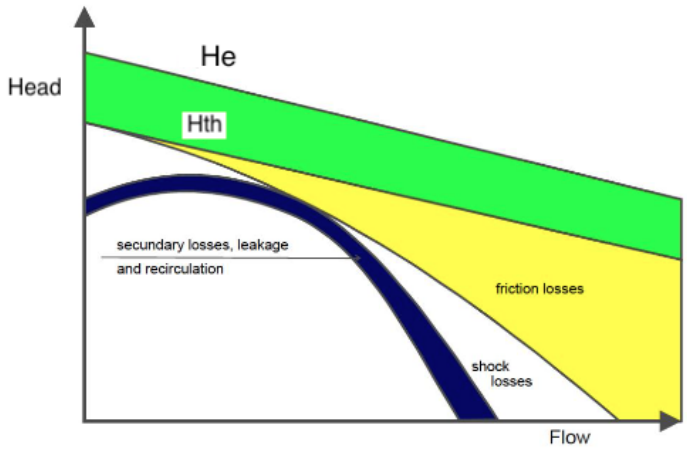

Figure 2.13: Pressure head flow curves, obtained from (Miedema, 2019)

As a result of mixture flow impact at the impeller blades, shock losses are present. These shock losses result in a flow direction change with respect to the blade angle path and are estimated with;

$$\triangle H_{shock} = \frac{C_2 \cdot (Q - Q_s)^2}{g} \tag{2.40}$$

Where, Q_s represent the discharge reduction due to shock losses and C_2 [−] is, as C_1, a correction value from equation 2.39.

Above described shock losses estimation is not valid at the best efficiency point, since it is stated that the inflow is fully radial. Other losses like, internal leakage and re-circulation in pump casing are present but are commonly neglected due to their low contribution.

With all the losses combined, an estimation of the theoretical manometric pressure head H_{mano} can be obtained, where internal leakage and re-circulation are neglected. In figure 2.13, a schematic overview of this contribution of losses is shown. The theoretical manometric pressure head represents the calculated magnitude or actual pressure, expected from an experimental verification test, at the pump outlet.

$$H_{mano} = H_{th} - \triangle H_{friction} - \triangle H_{shock} = \left(\frac{(u_2 \cdot c_{u_2} - u_1 \cdot c_{u_1})}{g} - C_1 \cdot Q^2 - C_2 \cdot (Q - Q_s)^2 \right) \tag{2.41}$$

2.2.7. Cavitation and NPSH

A pump configuration must be chosen such that the suction side of the pump never reaches the vapor pressure of the liquid, otherwise cavitation occurs. Cavitation is a phenomena where liquid starts to boil due to local temperature and pressure achieving its corresponding vapor pressure. This boiling of liquid creates gas bubbles in the mixture and when such a bubble reaches a higher pressure field, where the vapor pressure is not achieved, it implodes and creates a shock wave. This implosion results in a drop of manometric head and efficiency curve. This also negatively influences the impeller blades by increasing the corrosion rate and pitting of the surface. The cavitation location for centrifugal dredge pumps is mainly situated at the entrance of the impeller vanes according to Vlasblom (2004). Cavitation can be predicted by defining the so called Net Positive Suction Head (NPSH) in the following manner;

$$NPSH = h_s - h_v + \frac{v_s^2}{2 \cdot g} \tag{2.42}$$

Where, h_s is the measured absolute pressure head $[m]$ at the suction side, h_v the vapour pressure head $[m]$ of the liquid, obtained from figure 2.14 and v_s the velocity $[m/s]$ at the inlet. This NPSH is the total head available at the pump above the vapour pressure head of the liquid, or in other-words, the depth below the centre of the pump, where water can be extracted from without cavitation.

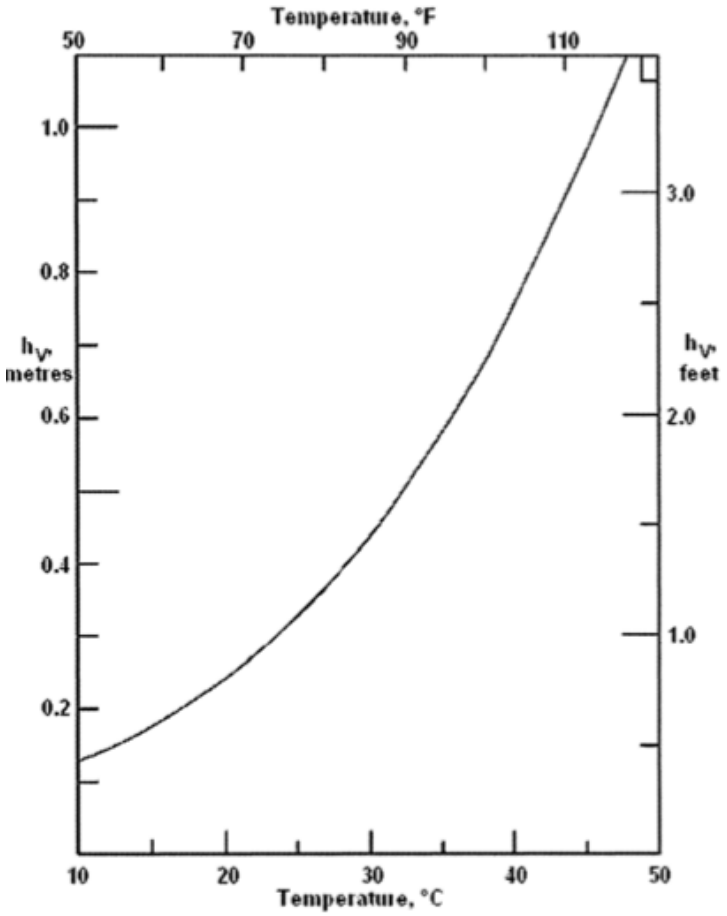

Figure 2.14: Vapor pressure head of water as a function of temperature, obtained from (Wilson et al., 2006)

2.3. Solids effects on dredge pumps

Only single phase situations have been discussed regarding pump performances so far. But when solid particles start to be present in a flow, single phase conditions and/or affinity laws do not (fully) apply anymore. Particles start to produce adverse effects on pump performances and then directly shift the $H-Q$ curve. Since the analysis of solids effect on pump performance is not yet "state of the art", mostly empirical corrections on the single phase situations are available. In present day, CFD techniques have gradually become a research hotspot (Wu et al., 2015) and started to increase significantly in accuracy compared to (semi-) empirical models. CFD models are further discussed in section 2.4. Non-Newtonian fluids are not in the research scope of this report and thus not discussed.

It is assumed that solids in suspension are not able to posses or transmit any fluid energy, so the liquid needs to account for it. To acquire kinetic energy for acceleration, solids subtract energy from the liquid phase and return this partly on deceleration. While decelerating, the kinetic energy is transformed into potential energy from which a significant potential part is transformed back into fluid pressure (Vlasblom, 2004). Overall, (empirical) analysis on solids effects have been focused on two phenomena, varying density effects and varying viscosity effects of Newtonian fluid.

2.3.1. Pump performances with low concentrations of particles

When the assumption is made that a slurry mixture is seen as a single phase fluid with a certain fluid density and is only changed while the viscosity remains constant, the affinity laws can provide a direct method for evaluation. If at a certain discharge, the assumption is made that the internal flow characteristics within the pump are not affected by the influence of particles, the efficiency is unaffected, the head stays steady and the pressure head is measured in terms of water-column. The relative density S_f of the "mixture" fluid, with the same viscosity as water, can then be used as a scaling number and is defined with;

$$S_f = \frac{\rho_m}{\rho_w} \tag{2.43}$$

The required power $P_{m,out}$ for the pump $[kW]$, at an equal water discharge, can then be estimated with;

$$P_{m,out} = S_f \cdot P_w = P_w \cdot \frac{\rho_m}{\rho_w} \tag{2.44}$$

Where, P_w is the power consumption at similar water conditions $[kW]$, ρ_w the water density $[kg/m^3]$ and ρ_m the mixture density $[kg/m^3]$.

An phenomena that has been widely researched is the assumption to see a mixture as a fluid with a higher viscosity than water. When the viscosity of the fluid increases and the fluid density is kept constant, the head and efficiency are lowered and the power needed to maintain a constant discharge is increased (Wilson et al., 2006). When higher flow rates are present, the effect of viscosity decreases significantly. If the research focus lays on small pumps the opposite applies and the viscosity effects are of greater influence.

The head and efficiency reduction ratio due to mixture transport performance compared to clear water is expressed for head reduction ratio H_r $[-]$ in;

$$H_r = \frac{H_m}{H_w} \tag{2.45}$$

Where, H_m is the head production in mixture conditions $[m]$ and H_w the head in water conditions $[m]$.

And for efficiency reduction ratio η_r $[-]$ in;

$$\eta_r = \frac{\eta_m}{\eta_w} \tag{2.46}$$

These reduction ratio's can be converted in fractional reductions R_H $[-]$, R_η $[-]$ to directly calculate the expected head and efficiency values with;

$$R_H = 1 - H_r \; and \; R_\eta = 1 - \eta_r \tag{2.47}$$

These quantities needs to be connected to certain mixture properties that consist out of relative density of solids S_s, C_{vd} as the delivered volumetric concentration $[-]$ and S_{md} as the relative density of the mixture $[-]$ (Wilson et al., 2006). Where S_{md} can be defined with;

$$S_{md} = 1 + (S_s - 1) \cdot C_{vd} \tag{2.48}$$

To define the expected power requirement, multiple method exists. One can estimate the power in similar matter as for head and efficiency above with (Gandhi et al., 2002);

$$P_r = \frac{P_m}{P_w} \rightarrow R_P = 1 - P_r \tag{2.49}$$

Where, P_r is the power reduction ratio $[-]$, R_P the fractional power reduction $[-]$, P_m the power consumption in mixture conditions $[kW]$ and P_w the power consumption in water conditions $[kW]$.

Research by Holzenberger (1980) and Engine et al. (2003) suggested a power requirement P_{in} prediction based on the relative density of the mixture. Thus, this only hold for delivered volumetric concentrations below 20 percent.

$$P_m = S_{md} \cdot P_w \tag{2.50}$$

In their research, a large scatter of data points was found due to the semi-empirical nature of the equations used. Nevertheless, almost all research data was based on real performance test while handling a specific mixture showed a certain agreement that lead to equation 2.50.

When the discharge, torque and RPM are kept constant, equation 2.50 holds and the efficiency reduction fraction equals the head reduction fraction due to an equivalent reduction;

$$H_r = \eta_r \tag{2.51}$$

McElvain (1974) proposed a custom head reduction factor called R_{HMc} and efficiency reduction factor $R_{\eta Mc}$ that is directly proportional to the delivered concentration C_{vd}.

$$R_{HMc} = R_{\eta Mc} = K \cdot \left(\frac{C_{vd}}{0.20} \right) \tag{2.52}$$

McElvain (1974) related this K factor to a specific relative density of solids (S_s = 2.65 from sand) and on an average particles size d_{50}. In figure 2.15, this K factor value is plotted against particle size so a reduction curve is shown as a solid line.

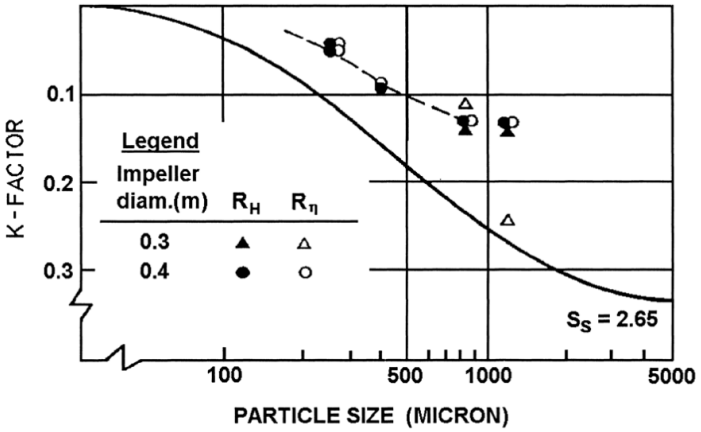

Figure 2.15: Reduction factor K from McElvain (1974), obtained from (Wilson et al., 2006)

Stepanoff (1948) also came up with a similar generalised solid approach where the viscosity difference, particle d_{50} and delivered volumetric concentration are input values. The kinetic energy that is partially transported through solids and transforms to pressure energy is according to Stepanoff expressed by;

$$P_{Stepanoff} = P_w \cdot \frac{\rho_m}{\rho_w} \cdot f_c \tag{2.53}$$

Where f_c is the efficiency reduction [−] originating from;

$$f_c = \frac{\eta_m}{\eta_w} = \eta_r \tag{2.54}$$

And can be expressed from experimental data further into (Vlasblom, 2004);

$$f_c = (1 - C_{vd} \cdot (0.8 + 0.6 \cdot log(d_{50}))) \tag{2.55}$$

Research in the laboratory of Dredging Technology of the TU Delft has shown that equation 2.55 does not fully hold. In figure 2.16, it can be seen that the influence of particle size on pump performance increase linearly which is not true in reality. The research concluded that for fine and medium sand, efficiency is less than Stepanoff's predictions and P_m is more or less equal to P_w. However, this efficiency reduction increased more than linear at high concentrations. For coarse sand, efficiency is lower although the power increases strongly with delivered concentration.

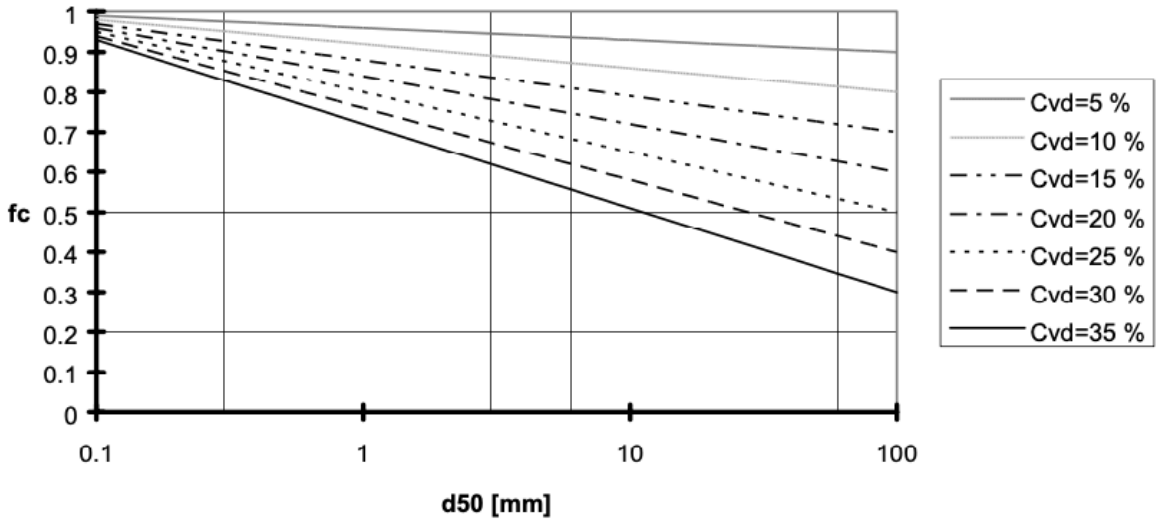

Figure 2.16: Influence on particle size on pump performance by Stepanoff, obtained from Vlasblom (2004)

An important note should be made regarding above discussed reduction factors for head, power and efficiency. Above equations found their origin in the early day of mixture pump research and (almost) all mixture pumps where then employed with inefficient radial-vane impellers. Nowadays, the impellers have been evolved into twisted vanes with the most optimal inlet angles and vane shape. The modern adjustment result in an increase towards efficiency and thus a power requirement reduction. Figure 2.15 shows some modern data points above the solid curved line. The origin of these shifted points from experimental measurements can be found in the use of "modern" curved and twisted vanes in the research of Sellgren et al. (1993). That concludes, solids effects are reduced in more modern equipment.

2.3.2. Effects due to pump scaling

As previously noted, viscosity effects reduce in large pump scales, this also applies for the particle effects towards the reduction factors, R_H, R_μ and R_P. Sellgren et al. (1989) did research on mixture pumps with an impeller of 1.1 to 1.2 meters to extend the available data range regarding mixture head and efficiency curves. A relatively big data scatter was found for the reduction factors compared with small pump data sets. As of this scatter, Sellgren et al. (1989) proposed a new criteria for R_H that is impeller diameter dependent for impellers bigger than 0.35 meters.

$$R_H = R_{H_0} \cdot \left(\frac{D}{D_0}\right)^{-0.9} \tag{2.56}$$

Where, R_{H_0} originates from a reference pump with diameter D_0 larger than 0.35 m and D is the impeller diameter, of the to be examed pump, that is in equivalent shape with respect to the scaling laws.

In a research of Van den Berg et al. (1999) and Vercruijsse et al. (2002), large scale pump experiment have been evaluated with an impeller diameter of 2.5 m. Although, both concluded that the effects of particles on head and efficiency reduction are practically negligible for particles sizes from 200 to 1100 microns. One can then say that the results of Sellgren et al. (1989) are slightly conservative for very large pumps.

2.3.3. Pump performances on high concentrations

Reduction ratio's, R_H, R_η and R_P, only apply for delivered concentrations below 20 percent and are defined in a linear manner. When concentration are starting to be higher than 20 percent, this linear approximation does not hold anymore. Sellgren et al. (1986) already concluded that the fractional reduction of efficiency R_η is more than that of the fractional head reduction R_H. This result in a larger power consumption compared to equation 2.50.

$$P_m > S_{md} \cdot P_w \tag{2.57}$$

And for the head reduction ratio changes to;

$$H_r > \eta_r \tag{2.58}$$

In higher concentrations, the effects of particle properties start to play a way more important role. Ni et al. (1999), Van den Berg et al. (1999), Vercruijsse et al. (2002) all used different delivered volumetric concentrations, impeller sizes and particle size distribution (PSD) in their research. That resulted in a wide variety of results which cannot be expressed in one simple equation. All came up with correction models that are specifically applicable to their tested mixture with certain particle properties. It can be concluded that the determination of required power on an single empirical formula, independently of particle properties and increasing C_{vd} is a hard to predict and thus an unclear situation.

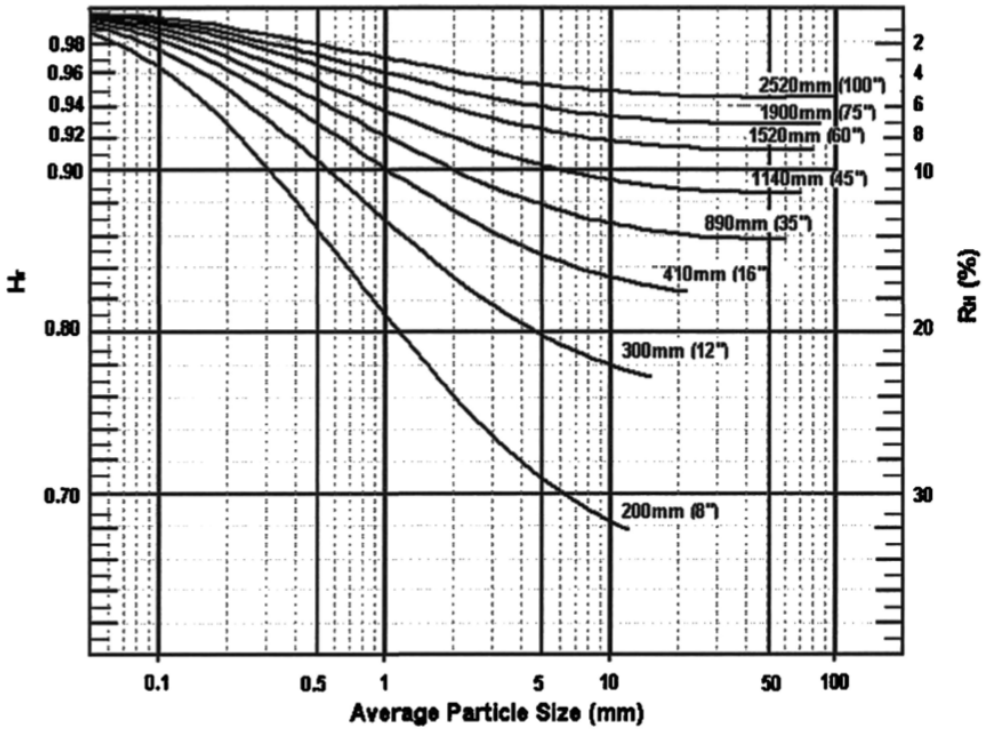

Figure 2.17: Generalised solids-effect diagram for pumps of various impeller diameters. For solids concentration by volume, C_{vd} = 15% with relative density of solids, S_s = 2.65 and a negligible amount of fine particles, obtained from (Wilson et al., 2006)

As a respond on this ambiguity, Wilson et al. (2006) created a generalised solids-effect diagram for settling slurries based on 15 years of testing at the GIW hydraulic laboratory. Figure 2.17 gives R_H and H_r based on impeller diameter and particle size d_{50} at a delivered concentration C_{vd} of 15 percent. Corrections for delivered volumetric concentration C_{vd}, relative density of solids S_s and content of fine particles X_h is given in equation 2.59, if these differ from 15%, 2.65 and zero. Fines are defined as particles smaller than 40 microns.

$$R_{H_{Cvd}} = R_H \cdot \frac{C_{vd}}{15} \cdot \left(\frac{S_s - 1}{1.65}\right)^{0.65} \cdot (1 - X_h)^2 \tag{2.59}$$

Where, C_{vd} is in percent.

2.3.4. Particle influence on cavitation

As in section 2.2.7 described, cavitation is something that needs to be prevented. However, due to the present of particles, a larger pressure drop is present as a result of the higher density of the mixture. The vapor pressure criteria are achieved earlier and the only way to prevent early cavitation is by adjusting one of the following parameters; delivered volumetric concentration, fluid velocity and pump location with respect to the inlet height.

2.4. CFD studies on internal flow patterns and trajectories

CFD models start to play an extensive contribution towards flow behavior explanation in centrifugal pumps due to their big advantage on data acquisition, at every specific point, with respect to pressure and trajec-

tories. However, the CFD model deployed still needs to be verified against known recorded data points for validation. Sadly, this needed verification data is relatively unavailable or non existing since most research focused on external measurement of the pump. Resulted in pump models for head, discharge and efficiency predictions, as discussed in section 2.1, 2.3.1, 2.3.2 and 2.3.3. The aspects regarding internal solids effect on streamlines or the overall local effects of solids has not been studied extensively. Nevertheless, an extensive amount of research on single phase (water) streamlines has been conducted and outcomes of these are assumed to be the same for mixture situation. Gandhi et al. (2002) concluded that an in-depth analysis of the head and efficiency losses taking place in the pump during model research should form an integral part of any scaling of the data for speed and size of the pump. Due to absence of any reliable methodology, the data on model research for centrifugal slurry pumps is still scaled up through "old" affinity laws, as discussed in section 2.1.2. According to Hofstra et al. (2008), there is no known full theoretical explanation on how pump geometry influences pump performance as a function of density, the transported material and the homogeneity of the flow in comparison with the flow of water. Due to these statements, modern technologies like CFD are coming in handy and naturally increase in popularity for solving these uncertainties.

2.4.1. Unsteady head characteristics

In single phase flow situations with a conventional centrifugal pump, a head fluctuation is noted. Small fluctuation originates from the impeller-tongue interaction that has a high pressure field passing by at the leading front as discussed in section 2.2.3. Cao et al. (2019) proved that the head has a periodically fluctuation over time and the pattern is similar when different discharges are used. An illustration of these head fluctuations are shown in figure 2.18A at different design discharges Q_d. In figure 2.18A, for recorded head at $0.5Q_d$, an other low frequency is present, which results in a higher peak-to-peak fluctuating amplitude.

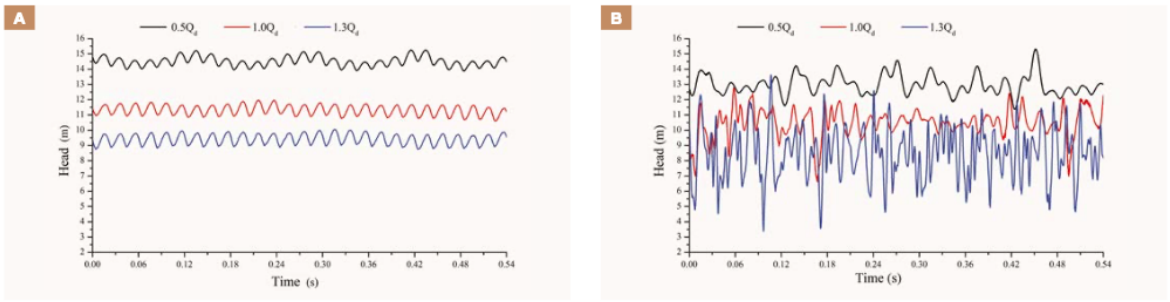

Figure 2.18: Head fluctuation over time for water and mixture flow, obtained from Cao et al. (2019)

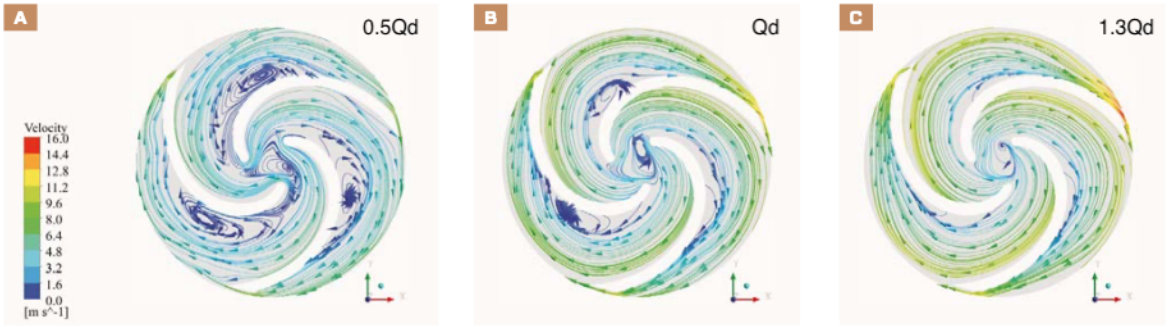

Figure 2.19: Instantaneous streamlines between a counterclockwise rotating impeller in water conditions, obtained from Cao et al. (2019)

According to Cao et al. (2019), the main cause of the unsteady head is the variation of inner flow fields in the pump, which is induced by the impeller tongue interaction. These instantaneous flow streamlines are shown in figure 2.19A with three low velocity separation vortexes, that are respectively displayed in each blade channel and are more or less symmetrical. These vortexes are displayed with blue lines and are located at the pressure side of the blade. The separation vortexes may be the origin of the extra low frequency variation at

$0.5Q_d$ according to Cao et al. (2019). When the flow rate is increased, these vortexes shrink and as in 2.19B, one of these vortexes disappears. Due to this more symmetrical distribution, the impeller-tongue interaction decreases. In 2.19C, the vortexes totally disappear and the unsteady characteristics of the flow field is not affected by the vortexes. The low frequency distortion on the unsteady head has been eliminated.

When the unsteady head characteristics for mixture loads is monitored, a large scatter of frequencies is noted where a main frequency cannot be distinguished with the naked eye, figure 2.18B. Cao et al. (2019) used Fast Fourier Transform (FFT) analyses to determine the main frequency shift in the unsteady head for mixture flow and concluded that the amplitude increases by 3 to 10 times. Figure 2.18B displays the recorded head values for different discharges such as in 2.18A. It can be seen that when a higher discharge is reached, there are more frequency components in each condition and the amplitude of many subdominant frequencies is much higher compared to the water flow situation. Cao et al. (2019) suggested that this may be the result of the complicated interactions between the two phases and the turbulent enhancement from sands.

For the increased frequency components at higher discharge in sand water mixture conditions, the shell shape design and its interaction with the exit tongue can be seen as an other source of origin. When discharge is increased significantly, the flow impact at the downstream of the tongue with the sands increases in impact region and magnitude (Cao et al., 2019). This increasement strengthens the mismatch of the volute casing in overload conditions $1.3Q_d$ and as a result increases the complexity of the unsteady head.

In research of Kadambi et al. (2004), it was concluded that this tongue blade interaction mainly occurred at the suction side of the blade while the pressure blade does not appear to substantially affect the flow velocity. The interaction was mainly detectable due to an increase in kinetic energy at the tongue.

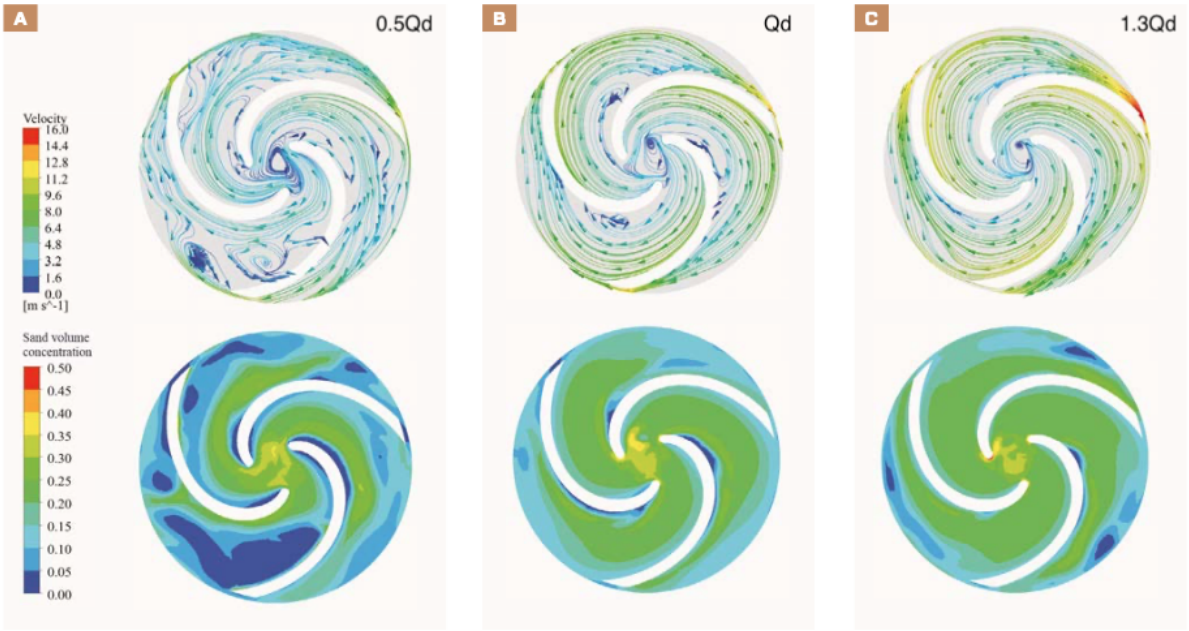

Figure 2.20: Instantaneous streamlines in a counterclockwise rotating impeller in mixture conditions, obtained from Cao et al. (2019)

2.4.2. Deviating streamlines in a centrifugal pump

The instantaneous streamlines that exist between the impeller blades are affected by multiple phenomena. As in chapter 2.2.3 discussed, the slip ratio plays a roll in bending the outlet flow β' of the impeller angle β. Eddies exist due to failure of particle rotation and are eliminated with increasing discharge. Though, this is valid for single (water) phase conditions and has not been expressed for mixture situations yet.

In mixture situations, these effects increase or decrease with a shift in particle size and/or concentration. Due to these facts, every situation gives a (slightly) different outcome when these parameters are adjusted. Cao et al. (2019) used $d_p = 0.3mm$ and a $C_{vd} = 0.20$ for calculation the instantaneous streamlines in the research. In

figure 2.20, again three situations at a specific discharge are shown with also their volumetric concentration distribution. For situations lower than the design discharge $0.5Q_d$, figure 2.20A, the separation vortex tends to concentrate in one blade channel rather than (more or less) evenly distributed as seen in figure 2.19A. In this concentrated blade channel, the vortex moves outwards the blade channel. In the other channels, there are until some degree "straight" flow patterns without the presence of vortexes. In part-load conditions, at velocities below Q_d, the particle velocity is relatively low and as a result, particles pile up. Cao et al. (2019) concluded that this leads to extensively growth of vortexes in lower concentration spots and the vortexes then prevent new particles from entering and increase the local concentration of others. This results in an uneven concentration distribution and creates an extra effect of tongue vortex interaction onto the impeller-tongue interaction. This is a so called stall phenomenon, which causes large hydraulic losses in the pump. When the discharge is increased to design specifications and the flow velocity increases, the concentration profile start to be more evenly distributed and result in more symmetric streamlines. Cao et al. (2019) stated that in comparison with water flow, the degree of flow separation decreases. Although, this does not imply that vortexes do not exist since streamlines are not as smooth as in the water flow.

2.4.3. Boundary layer and particle bouncing

Until this point, focus was directed on particles interaction with streamlines of the flow and their concentration distribution. Two other effect, called boundary layer and particle bouncing, also have a significant contribution in deviating the streamlines and are strongly dependent on each other.

The boundary layer is determined by a number of factors. Besides the local flow velocity and fluid viscosity, the impeller shape where the flow passes alongside are important. Since the boundary layer needs a certain length to fully develop, the channel length is an influence factor. Commonly, a centrifugal pump impeller does not have the needed length for a boundary layer to fully develop which results in an elimination of the use of velocity profile derivations for fully developed flow. Hofstra et al. (2010) suggested to model the impeller blade as an immersed plate where the flow passes along. The boundary layer thickness is set to zero at the trailing edge of the impeller blade and expands along the length of the blade towards the leading front. Initially, a small laminar boundary layer start to develop at the start of the blade and at further propagation, a transition towards a turbulent layer follows.

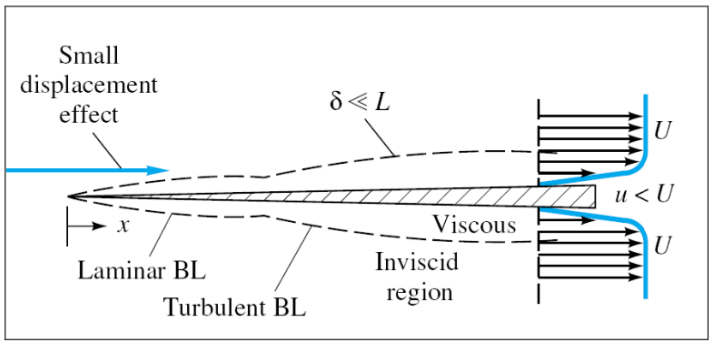

Figure 2.21: Boundary layer on an immersed plate, obtained from White (1986)

Figure 2.21, gives a representation of this boundary layer propagation on the impeller blade. To define the thickness of the layer two formula's exist that are both based on the (local) Reynolds number locating alongside location 'x' in the figure.

$$Re_x = \frac{x \cdot U}{\nu} \tag{2.60}$$

$$\frac{\delta}{x} = \frac{5}{\sqrt{Re_x}}, \text{ valid for Laminar Flow} \tag{2.61}$$

$$\frac{\delta}{x} = \frac{0.16}{Re_x^{1/7}}, \quad \text{valid for Turbulent Flow } Re_x \approx > 10^6 \tag{2.62}$$

Where, ν represent the viscosity $[m^2/s]$, δ the boundary layer thickness $[m]$, U is the 99% value of the fully developed flow speed $[m/s]$ and L the distance $[m]$ between the immersed plate and the next one.

The velocity of the fluid u_b $[m/s]$ in the laminar boundary layer can be determined with a parabolic function that is defined by Prandtl with;

$$u(y) = U \cdot \left(\frac{2y}{\delta} - \left(\frac{y}{\delta} \right)^2 \right) \tag{2.63}$$

Where, y is the height of the boundary layer $[m]$ and u the local velocity $[m/s]$.

For a situation where the boundary layer is turbulent due to a Reynolds number above 10^6, equation 2.63 reduces to;

$$u(y) = U \cdot \left(\frac{y}{\delta} \right)^{1/7} \tag{2.64}$$

Hofstra et al. (2010) did a CFD model calculation in ANSYS with the above boundary layer criteria for an impeller with a diameter of 0.5 meter, blade angel of 30 degree, discharge Q of 2.8 l/s and 1000 RPM. Hofstra et al. (2010) concluded that on the suction side, close to the blade surface, the flow velocities are very low, in an order of 0-2 m/s. The flow velocities at this location do not vary significantly during impeller rotation. On the other-side of the blade, the pressure side, larger velocity fluctuations are noticed in a range of 1-5 m/s. An interesting effect can be noticed regarding a low velocity field passing along the blade from the leading edge of the blade towards the trailing edge. Although, this field does not reach the impeller outlet. It is very unlikely that single continuous boundary layers exits on either the suction or pressure side.

In further extension of above described CFD analyse by Hofstra et al. (2010), particles are added with a variable drag coefficient, an added mass coefficient and a lift coefficient dependent on the drag coefficient. Since, the drag coefficient is a function of the Reynolds, just as with the boundary layer, it varies depending on location and flow velocity. It was concluded that the effect of the boundary layer significantly depends on their laminar or turbulent state, particle size, angle of attack and release height.

In a laminar boundary layer situation, the influence on the streamlines is bigger when compared to a turbulent situation. This originates from a large velocity gradient to deflect the original path of the particles when the angle of attack is small. Hofstra et al. (2010) also noted a clear influence of slip on the particles here. When particles move faster than the surrounding fluid, these tend to deflect towards the wall, figure 2.22, whilst deflect away when these are slower, figure 2.23. Same effect happen in the turbulent layer but are less strong due to only a steep velocity gradient close to the wall surface, figure 2.24 and figure 2.25.

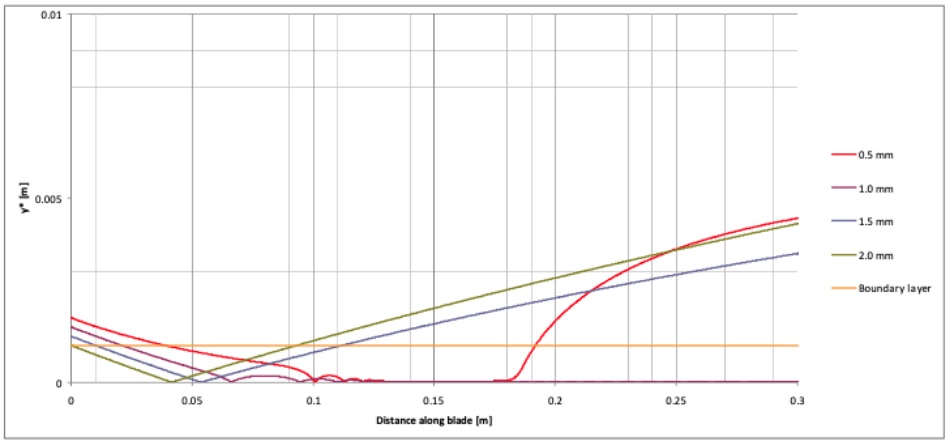

Figure 2.22: Particle trajectories in a laminar boundary layer, the particle velocity is higher than the fluid velocity. (δ=1 mm, U=3 m/s, attack angle 1.4°), obtained from Hofstra et al. (2010)

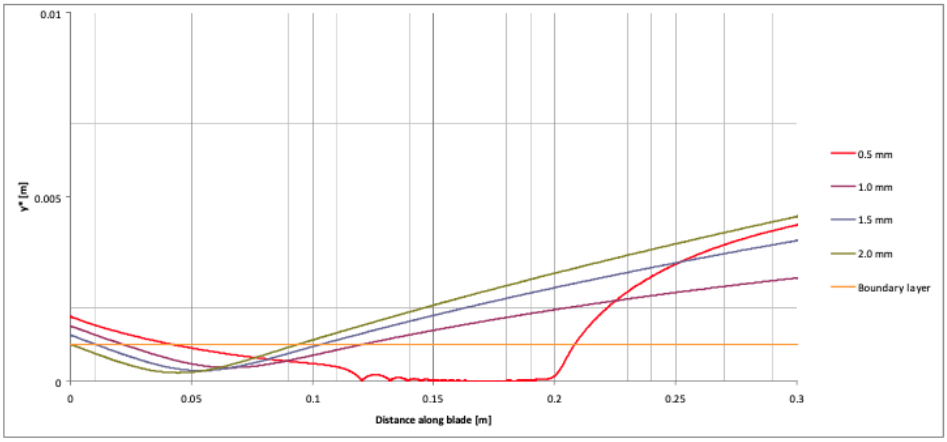

Figure 2.23: Particle trajectories in a laminar boundary layer, the particle velocity is lower than the fluid velocity. (δ=1 mm, U=3 m/s, attack angle 1.4°), obtained from Hofstra et al. (2010)

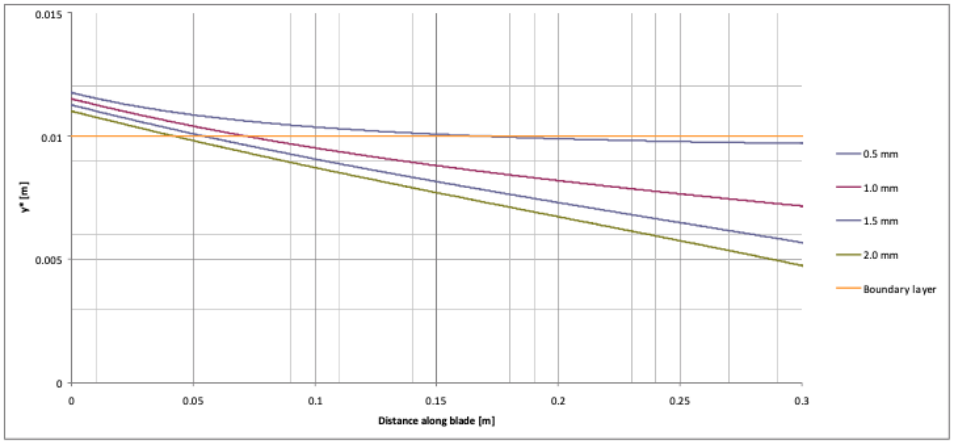

Figure 2.24: Particle trajectories in a turbulent boundary layer, the particle velocity is higher than the fluid velocity. (δ=10 mm, U=3 m/s, attack angle 1.4°) – slip 1.0, obtained from Hofstra et al. (2010)

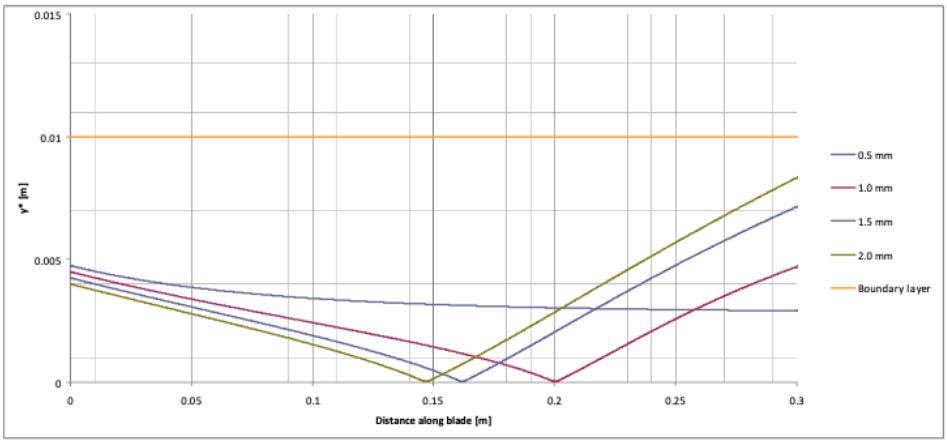

Figure 2.25: Particle trajectories in a turbulent boundary layer, the particle velocity is lower than the fluid velocity. (δ=10 mm, U=3 m/s, attack angle 1.4°) – slip 1.0, obtained from Hofstra et al. (2010)

Overall, it can be said that the boundary layer model/CFD approach of Hofstra et al. (2010) gives promising results. In an experimental verification, it was shown that particles do not penetrate the boundary layer

at the researched low concentration. (No experimental specific concentration C_{vd} value present in Hofstra et al. (2010) paper.) The particles that do interact with the boundary, exhibit behavior depending on the side of the impeller blade (suction or pressure side). Results of these effect can be seen in the experimental observed particle trajectories and be compared with the laminar boundary layer calculation outcomes by Hofstra et al. (2010). Cao et al. (2019) concluded something similar and stated that the bounce of sands and the instantaneous interaction between sands and water causes random fluctuations. The larger the flow rate, the stronger the interaction effect is.

2.5. Hypothesis

In conclusion of the conducted literature research, multiple questions from section 1.2 have been answered or clarified.

Existing models to predict head, discharge and power values of a centrifugal pump are applicable to some extend in mixture situations. When delivered volumetric concentration values below 20 percent are present, linear models as of Stepanoff (1948) and the reduction factor K by McElvain (1974) give basic design parameters. Although, it should be noted that the researched pump is in size and geometry shape similar as where these models are derived from. For higher concentration, the generalised solids-effect diagram by Wilson et al. (2006) may be used. More basic parameters of the mixture should be known then, such as; average particle size d_{50}, relative density of the solids, impeller diameter, delivered volumetric concentration and the content of fines. Due to a constant fluctuations in feed, concentration and change in material properties, the expected head can quickly deviate.

Multiple CFD models have been examed that try to improve these existing empirical models. However, these models did not conduct an internal experimental validation and may thus not be used independently as a replacement for existing empirical models. Conclusively can be said, that these models are not yet "state of the art" and should only be used as an extra tool besides proven models and adjusted affinity relations.

Originating from the obtained knowledge, an expectation regarding the to be conducted experiments can be made. When a single phase flow experiment is conducted, it is indeed expected to see the same streamline patterns as CFD simulations provided. This can be stated due to the extensive amount of single phase research available (Cao et al., 2019; Kadambi et al., 2004; Ni et al., 1999; Wu et al., 2015). For mixture flow experiments, this cannot be stated due to the lack of available data and research. Although, for low concentration experiments it is expected to show big similarities due to the low influence of particles on head and discharge. For higher concentrations above 20 percent, a streamlines verification is going to be challenging due to PIV analysis limitations in particle distinguishing. A verification study on head, discharge and power input can offer a conservative solution then.

Regarding the unsteady head characteristics, the origin can be found partly in the tongue blade interaction as pointed out by Cao et al. (2019); Kadambi et al. (2004); Wu et al. (2015). Due to passing of a high pressure field, at the pressure side of the blade, these unsteady head fluctuations are present in single phase situation. When mixture situations are examed, the angular velocity of the impeller is of greater importance. Due to certain design discharges, vortexes may or may not form in the impeller channels and influence particle capture. Boundary layer effect and particle bouncing start to play a role. In the to be conducted experiments, it is therefore expected to see particle bouncing, concentration field fluctuations, a boundary layer and vortexes at half the design discharge of the pump (Cao et al., 2019).

3

Experimental setup

This chapter explains the details and reasoning of the implemented equipment in the experimental setup. All equipment is discussed individually with their corresponding specifications, way of use, calibration, positioning and data acquisition. Further, an overall experimental protocol is given for consistency in experimental data collection. Followed up with a data processing explanations and verification.

3.1. Overview experimental setup

A custom experimental setup could be realised due to the special budget made available by Prof. Dr. Ir. C. van Rhee. This custom setup is a variation on the existing transparent flow loop in the TU Delft Dredging Laboratory. The full design process and fabrication has been conducted in-house and is further partly discussed in this chapter. In figure 3.1, a 3D overview of the setup is displayed with corresponding part numbers that refers to the implemented sensor(s) and/or equipment. The part numbers are used for further explanation in the upcoming sub-sections. The order of these numbers correspond with the path that the mixture follows through the flow loop.

The mixture flow starts at the so called "particle loading compartment", particles are here added slowly to the running flow in the main loop (1). Next, the mixture enters the centrifugal dredge pump (2) followed up by two 90 degree turns that, in an ideal situation, creates a homogeneous particle distribution at the pump inlet. The mixture passes along the absolute pressure transmitter (3), a (pressure control) valve (4) and the temperature sensor (5) towards the flow meter at location (6). Followed by a bifurcation piece (7), for emptying the flow loop and the U-loop (8) for concentration measurements. The U-loop consists out of four pressure taps that are connected to two differential pressure transmitters. After the U-loop, the mixture reaches the bottom of the "particle loading compartment" at another bifurcation piece for a secondary flow line. This secondary flow line feeds the mixture tank with water for further mixture injection into the main flow loop but also acts as a volume relief to compensate for the added particle volume. At location (9), a (pressure control) valve is located to regulate the pump inlet pressure and mixture injection, the pressure value generated by this valve is recorded with an absolute pressure transmitter at location (10). The secondary flow can be adjusted with two independent valves at (11,12) to regulated the particle injection speed.

3.1.1. Centrifugal dredge pump

Since the centrifugal dredge pump is the key player in this research, it must meet the requirements of a "real" dredge pump stated by Wilson et al. (2006), page 229. Finding such a dredge pump, on small scale, has been a complex task. A small pump had to be found with an open impeller and a flat surface on the suction side as an extra criteria. In a quick market search, the results quickly converged towards single (water) phase centrifugal pumps with a closed impeller, thus a real small dredge pump could not be found. As a compromise, an old vertical-submersible sewage pump was chosen to be converted. This sewage pump had a perfect flat surface on the suction side for a PolyMethyl MethAcrylate (PMMA) window, see figure 3.2 and 3.4. Also, an off-centric open three bladed impeller, with respect to the outer shell, was present and thus fulfilled the criteria, according to Wilson et al. (2006), to classify as a dredge pump. This sewage pump had only one technical drawback regarding suction inlet, it was designed to be vertically semi-submersible in position. For a more easy usable

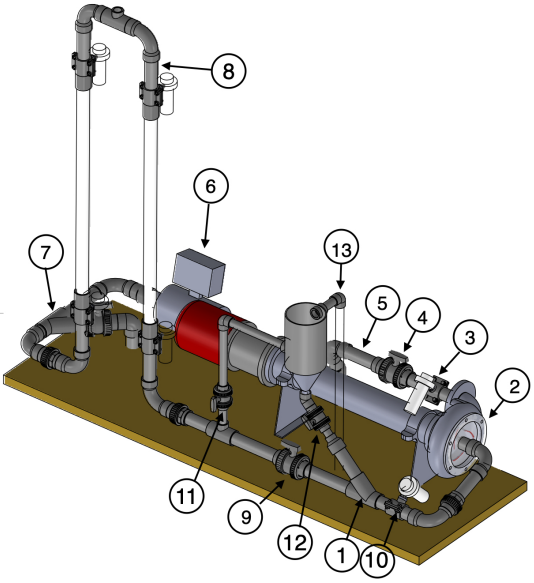

Figure 3.1: Schematic overview of the setup

Figure 3.2: Image overview of the setup

setup, horizontal operations are desired to keep the PMMA window, at the suction side, concentric with the horizontal (high-speed) camera position, see figure 3.9. These setup requirements have been acquired during the refurbishment of the pump, an extra oil seal has been added to prevent water spillage into the drive axle shaft at horizontal position. The final layout of the pump design is shown in figure 3.3. The complete centrifugal dredge pump configuration, including electric engine and drive shaft, is marked as (2) in figure 3.1.

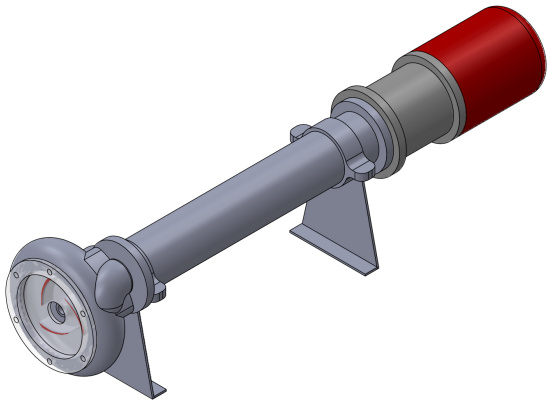

Figure 3.3: Schematic overview of the pump

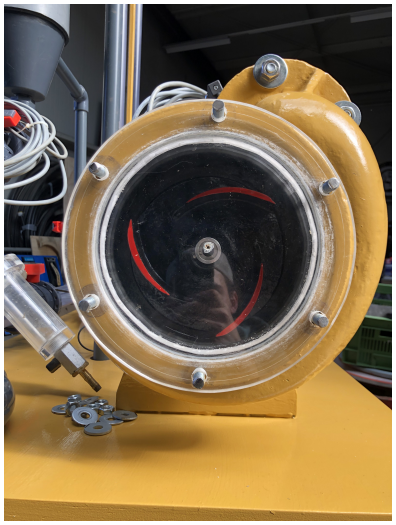

Figure 3.4: Front view of the pump with an counterclockwise rotating impeller

In figure 3.4, the actually impeller of the setup is shown with its corresponding specifications in table 3.1. A note should be made that the impeller used in the experimental setup already has an unknown amount of operation hours and thus has been exposed to a significant amount of wear and degradation on impeller length. This degradation can be seen at the leading front of the blades, where a reduction of around 15% is noticeable. The electric motor used, that is connected with a direct shaft onto the impeller, has its specifications displayed in table 3.2. Due to the age of the pump, limit to none information is available on the shell and a design change, at the suction inlet, that leads to the need of a pump characteristic in single phase conditions.

From experiments, in single phase water situations, a pump characteristic has been created. The acquiring of this characteristic is further explained in chapter 4.2.1.

Three bladed impeller		
Outer diameter	155	[mm]
Inner diameter	100	[mm]
Hole diameter	13	[mm]
Thickness body	8	[mm]
Thickness full	45.5	[mm]
Blade height	32.5	[mm]
Blade length	90	[mm]
Blade length orig.	105	[mm]
Blade thickness	2-6	[mm]
Blade curvature dia.	100-104	[mm]

Table 3.1: 3 bladed impeller

Electric motor		
Company:	Rotor.nl	
Model:	4AP90S-4	
$\cos\phi$	0.8	[-]
Max. RPM	1410	[-]
Efficiency	74	[%]
Power	1.1	[Kw]
Current	2.7	[A]
Voltage	400	[V]

Table 3.2: Electric motor - Rotor.nl - 4AP90S-4

3.1.2. Pressure and flow regulating valves

As denoted with number (4) and (9) in figure 3.1, two main valves are present to regulate discharge and pressure. By throttling these valves, an artificial head or NPSH at the pressure/suction side of the pump can be created/enhanced. By doing so, situations with different head and discharge values can be created to obtain multiple pump characteristics and internal impeller streamline patterns. For emptying the flow loop, location (7), a discharge valve is located. Further, location (11) and (12), smaller valves are located for regulating the secondary flow loop for particle injection. This particle injection is further explained in section 3.1.3. Note that all valves in the experimental setup are operated manually and thus indirectly influence the data output accuracy. All implemented valves consist out of "screw VDL PVC ball valves", this to keep the flow loop detachable for thoroughly cleaning, flushing and repairing of the system.

3.1.3. Particle loading compartment

The "particle loading compartment" has been implemented in the experimental setup to add, in a controlled manner, particles for a desired volumetric mixture concentration. The compartment consist out of a loading tank, that is capable of storing preweighed submerged particles before these are added. This preweighed amount, corresponds to the desired delivered volumetric concentration C_{vd} in the flow loop with respect to internal volume. Particles can be added by opening valve (11) and (12) partly, so the secondary flow loop is opened and starts to inject and compensate for their volumetric concentration shift. To speed up this process, the valve at location (9) can be throttled to create a vacuum and increase the secondary flow discharge. As of safety precautions, the compartment has a build in overflow to dispose excess water into the discharge system if necessary.

3.1.4. U-loop and preweighed particles

For measuring the delivered volumetric density of the mixture, multiple measurement equipment exists. One may determine the internal volume and uses a preweighed amount of particles to gain an averaged C_{vd}. The U-loop is another way to determine the local C_{vd} by defining the pressure difference between an upstream and downstream flow. These pressure difference are a result of higher sedimentation velocities in the downstream end compared to the upstream end. As of availability and budget management, the decision was made to implement an U-loop in combination with the preweighed particles method for C_{vd} determination and cross-data validation.

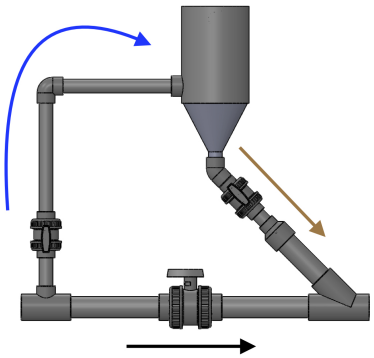

Figure 3.5: Side view of the "particle loading compartment".

The U-loop, located at (8) in figure 3.1, is schematically displayed in figure 3.6 with four pressure taps and their dimensions. These pressure taps are individually connected onto two differential pressure transmitters, that are further detailed in section 3.1.5.

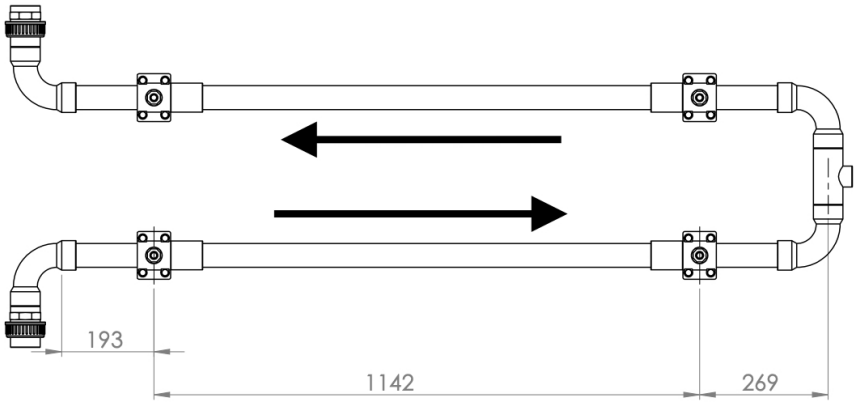

Figure 3.6: Schematic drawing of the U-loop with dimensions.

Defining the delivered volumetric solids concentration based on the U-loop principal was firstly proposed by Clift & Clift in 1981 and later fully explained/described by GIW Hydraulic laboratory (Wilson et al., 2006). The method proposed includes four pressure taps and two differential pressure transmitters, that are parallel connected on the upwards and downwards flow taps. The differential pressure transmitters record a value for $\triangle P_{up}$ and $\triangle P_{down}$ $[Pa]$. To assure a homogeneously distributed mixture flow, the taps should be located at least five times the pipe diameter away from a corner. The mixture density can be defined with;

$$\rho_m = \frac{\triangle p_{up} + \triangle p_{down}}{2 \cdot g \cdot z} + \rho_w \tag{3.1}$$

The delivered volumetric concentration C_{vd} can then be defined with equation;

$$C_{vd} = \frac{\rho_m - \rho_w}{\rho_s - \rho_w} \tag{3.2}$$

Where, ρ_f, ρ_s and ρ_m are the densities of the fluid, solids and mixture $[kg/m^3]$, g the gravitational force $[m/s]$

and z the distance between the pressure taps [m].

As a verification method on the accuracy of the U-loop, preweighed particles can be used to define the delivered concentration with the following formula;

$$C_{vd} = \frac{preweighed\ particles}{internal\ volume \cdot \rho_p} \tag{3.3}$$

Where, the preweighed particles values [kg] and the internal volume [m^3] are obtained during/from experiments. The origin of the 'internal volume' value is further discussed in section 3.3.1.

3.1.5. Sensors

Multiple sensors are implemented in the experimental setup and are briefly discussed independently. The following tables, includes information regarding manufacture, model, signal outputs etc. More specific details regarding signal outputs, connectivity and conversions are given in section 3.1.6. All pressure sensors and transmitters in the setup are indirectly connected to the flow loop, except the temperature sensor. A special air and sedimentation collection/removal compartment is located in between, to prevent particles and air from blocking the sensor and influences its accuracy. Further on, these compartments are called "pressure taps".

Absolute and differential pressure transmitters

Four pressure transmitters are included that consist out of an absolute and a differential version. The absolute pressure transmitters are located at point (3) and (10), to allow direct pressure measurements of the NPSH and head created by the centrifugal dredge pump. As discussed in section 3.1.4, the differential pressure transmitters are both connected on the U-loop for concentration determination. The differential pressure transmitters supply a 4-20 mA output signal, while the absolute pressure transmitters supplies a 0-5 Volts output signals. Further reasoning regarding signal output conversions and connectivity is expressed in section 3.1.6.

Differential pressure transmitter		
Company:	Rosemount DP3	
Model:	1151DP3S22 SMART	
Temperature range	-40 - 85	[°C]
Pressure range	±7	[kPa]
Measurement range (Up)	0 - 7	[kPa]
Measurement range (Down)	-1 - 6	[kPa]
Max input voltage	45	[V]
Output signal	4 - 20	[mA]

Table 3.3: Differential pressure transmitter Rosemount 1151DP3S22 SMART

Absolute pressure transmitter		
Company:	RS	
Model:	461-272	
Accuracy	±0.25	[%]
Temperature range	-20 - 125	[°C]
Pressure range	-1 - 9	[Bar]
Output signal	0 - 5	[V]

Table 3.4: Absolute pressure transmitter RS 461-272

Electromagnetic Flow meter and temperature sensor

To determine the discharge capacity of the centrifugal pump, an electromagnetic flow meter has been installed at location (6). Wilson et al. (2006), stated that such a sensor should be placed in vertical direction to assure a homogeneous distribution of the mixture in the flow. This vertical position assures a transition, from bed form and/or a concentration profile, into a homogeneous distribution of the mixture flow. Otherwise, the accuracy of the sensor decreases significantly due to a higher density layer that deflects the electromagnetic waves. However, in the setup, the flow meter has been placed in horizontal direction just after the centrifugal pump, based on the following motive. As a result off a relative short distance from the pump and a high engine speed, that results in a high turbulent flow, bed and/or concentration profile forming are highly unlikely

to develop. This high turbulent flow automatically result in an homogeneous distribution of the mixture flow.

The temperature sensor, at location (5), is the only one in direct contact with the mixture flow. This direct contact assures an accurate temperature measurement of the mixture flow. If the temperature sensor should have been connected onto a pressure tap first, the water inside the pressure tap has a delay in temperature response with respect to time due to minimal circulation. The implemented temperature sensor is a basic PT100 probe, connected to a temperature converter (PXT-10.230) with an output signal of 0-10 Volts. Further detail regarding the output signal conversion is discussed in the next section.

Electromagnetic Flow meter		
Company:	Flowtec Variomag	
Model:	Discomag DMI 6531	
Input voltage	220	[V]
Temperature range	150	[°C]
Internal diameter	45.3	[mm]
Max range	250	$[dm^3/m]$
Output value	(0-4)/20	[mA]

Table 3.5: Electromagnetic Flow meter, Flowtec Variomag Discomag DMI 6531

Temperature sensor		
Model:	PT100	
Temperature range	-50 - 150	[°C]
Output value	0 - 10	[V]
Output signal	15*U - 50	[V]
Input voltage	230	[V]

Table 3.6: PT100 Temperature sensor

3.1.6. Connectivity and data collection

As multiple sensor and equipment are implemented that all supply different signal outputs, a conversion board is needed to acquire the necessary data in a readable format. An Arduino Uno board for data collection is used due to its freely programmable features. Although, it has some technical drawback due to 0-5 Volt analogue data input limitations, as the sensors implemented, supply output voltages of 10-24 Volts (Except the absolute pressure transmitter). Making these sensors Arduino compatible, a separate PCB was designed to convert the voltages to usable values. In figure 3.7, a schematic is shown on how the output signal of the differential pressure transmitters and flow meter are converted into a readable 0-5 Volt analog signal. This is done by using Ohms law from equation 3.4. For the temperature sensor, a so called 'voltage thief' was implemented to divide the incoming voltage by 2, see figure 3.8 for an electric drawing. By doing so, also here the Arduino 0-5 Volts criteria are met.

$$U = I \cdot R \tag{3.4}$$

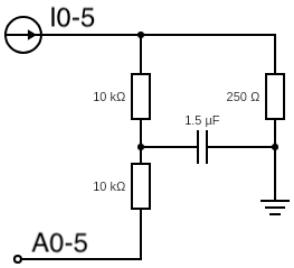

Figure 3.7: 4-20 mA conversion schematic towards Arduino compatibility.

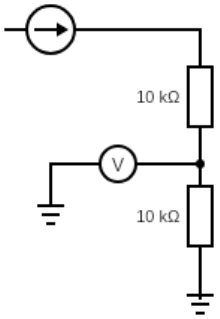

Figure 3.8: 10 Volts to 5 Volts conversion schematic towards Arduino compatibility.

Where, U is the voltage $[V]$, I the ampere $[A]$ and R the resistance $[\Omega]$. This results in a 250 Ohm resistor value over the ground line for a 24V input, with two 10K resistors and a capacitor in between. The high resistor value is used for over-voltage protection and the capacitor is used for signal filtering. For the "voltage thief" or voltage divider, the total 20K high precision resistor limits the amount of current. A voltmeter is connected over one of the resistors, as of Ohms law, it gives halve the total voltage value.

After signal input voltage conversion, the voltage enters the Arduino analog input pins in a certain order that needs to be indicated. In table 3.7, the corresponding input signals and their channel is displayed. This channel indication is needed for correct data string forwarding within the Arduino code.

Arduino channel indication		
Sensor:	**Pin Number:**	**Channel:**
Differential Down	1	0
Differential Up	2	1
Absolute Head	3	2
Absolute NPSH	4	3
Flow meter	5	4
Temperature	6	5

Table 3.7: Arduino analogue channel indication

The Arduino forwards the data through a serial connection to a storage device in the same order as the channel indication. This storage device runs a live script to convert the analogue input values into real information and stores these in a CVS file. This conversion script can be found in appendix D together with the base code for the Arduino. The CVS file is loaded into a Matlab script to process these data string into use-full graphs and figures.

High speed video recorder

Simultaneously, while the Arduino collects sensor data, high speed video recordings are made of every executed experiment. In figure 3.9, a schematic top view of the camera position and it's dimensions are shown. In table 3.8, the camera and lens specifications are presented. The internal camera setting that are consistent for every experiment can be found in table 3.9.

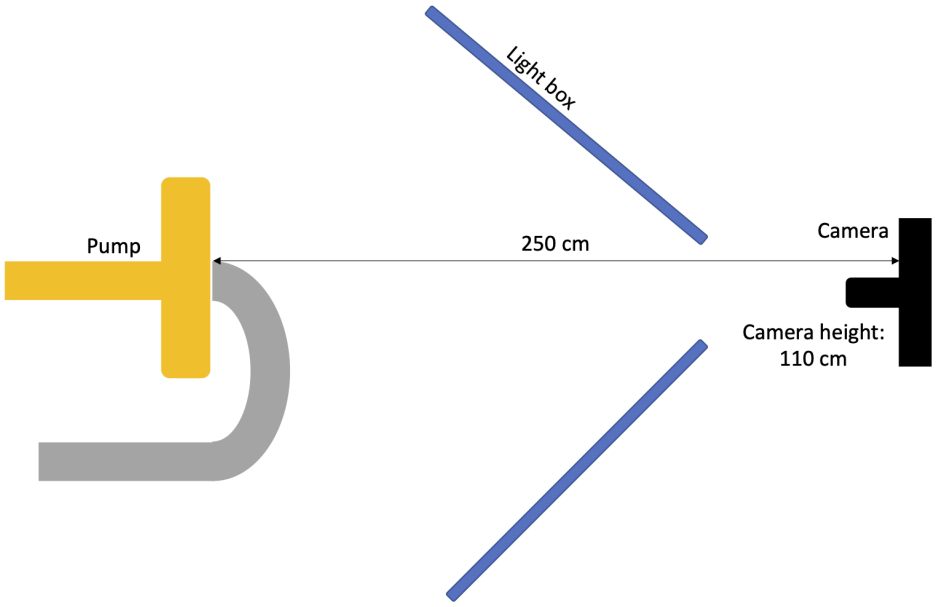

Figure 3.9: Schematic top view of the high speed camera line out.

High speed video recorder			
Camera		**Lens**	
Brand:	Fastec Imaging	Brand:	Navitar
Model:	IL5HM8512D	Model:	DO-5095
Storage:	16GB SD 45 MB/S W	F-stop:	0.95-16
FPS:	634 max	Length:	50mm

Table 3.8: High speed camera specifications

Software settings	
Function	**Value**
LR Mode:	Enable
ROI Width:	750
ROI Height:	750
Offset X:	600
Offset Y:	250
Frame Rate (FPS):	636
Shutter speed:	500

Table 3.9: High speed camera software settings

3.2. Test (mixture) material

The material that is used, to conduct flow pattern verification for the CFD model and gain water and mixture test data, consist out of two materials and three particle sizes. For single phase flow pattern verification, polystyrene particles are used with a density near that of water. The polystyrene particles have a varying density of 1000-1050 kg/m^3 with a mean density of 1025 kg/m^3. For "real" mixture experiments, glass particles are used to simulate sand particles with a fixed diameter of 1 and 3 mm. The specifications of these two materials are;

Experimental particles					
Brand:	**Material:**	**Density:**	**Unit:**	**Diameter:**	**Unit:**
RPG-Balls	Polystyrene	1000-1050	$[kg/m^3]$	2	$[mm]$
SiLi beads	Polished Glass - Soda Lime Glass	2500	$[kg/m^3]$	1	$[mm]$
SiLi beads	Polished Glass - Soda Lime Glass	2500	$[kg/m^3]$	3	$[mm]$

Table 3.10: Experimental particles and its specifications

3.3. Experimental layout and protocol

This subsection explains the experimental protocol used that consist out of three phases, "pre-", "peri-" and "post-". These phases create a guideline protocol to increase consistency in experiment execution and assures nothing is left out on individual experiments. As a result, the overall accuracy on data collection is also significantly improved.

3.3.1. Experiments and settings

Referring back to the main question of this research, multiple experiments on particle trajectories needs to be executed at a wide variation of concentration and speed (RPM). Nevertheless, these main experiments can only be conducted if firstly three base experiments are performed. These base experiments are necessary for data validation, calibration and delivered volumetric concentration estimation/validation. The complete overview of the executed experiments is displayed in table 3.11.

The base experiment that needs to be conducted is a measurement on the internal volume of the setup. This volume is needed for equation 3.3, so the C_{vd} can be defined manually. This volume also gives an inside on the amount of test material needed in kilograms. Five repetitions are conducted where the setup has been topped up until the water overflow was reached. As the overflow is reached, the secondary flow valves are closed. This way the water volume in the overflow is not being accounted for during drainage. The system was then fully drained into a bucket and measured on a weighting scale, likewise five times repeated. The overall average of these experiments lead to an estimation of the internal volume expressed in kilograms of water.

Due to the design change at the pump inlet, a new pump characteristic for water flow conditions has been defined. This characteristic is needed to create a base value for further particle trajectories test in mixture situation and compare it to other existing (water) characteristics. The base values are also used to distinguish certain data trend shifts during concentration loads.

Before the main experiments are conducted, a streamline verification of the impeller blades in the pump is desired. These streamlines give more inside on the behaviour during pure water loading conditions and thus also create a base reference for mixture conditions. These verification experiments are conducted at multiple discharge values and concentrations to distinguish any change in streamlines with respect to internal flow speed. Also, these streamlines can be used to directly verify the first part of Cao et al. (2019) CFD model. In this first part, an outcome on streamline patterns during pure water loading conditions was given.

To gather a wide set of data points for particle trajectories analysing, multiple experiments with a varying discharge, based on input power and concentration was conducted. On these experiments, the head valve has also been throttled to gain a pump characteristic for mixture situations. For experiments with concentration levels above 12%, the individual particle distinguishing started to be complex due to multiple particle 'layers' in depth between the blades. This complexity resulted in a white blur of particles on the image recordings. For the complete text matrix, table 3.11 can be found.

Executed experiments					
Experiment:	C_{vd}**:**	**RPM:**	**Material:**	**Number of tests:**	**High speed recordings:**
Defining internal volume	[-]	[-]	[-]	5	-
Define pump characteristic	[-]	564/846/1128/1410	[-]	3	-
Verifying streamlines	1%	564/846/1128/1410	[Polystyrene]	1	4
Verifying streamlines	3%	564/846/1128/1410	[Polystyrene]	1	4
Verifying streamlines	5%	564/846/1128/1410	[Polystyrene]	1	4
Particle trajectories	3%	564/846/1128/1410	[Glass 1/3 mm]	1	8
Particle trajectories	5%	564/846/1128/1410	[Glass 1/3 mm]	1	8
Particle trajectories	8%	564/846/1128/1410	[Glass 1/3 mm]	1	8
Particle trajectories	12%	564/846/1128/1410	[Glass 1/3 mm]	1	8
Particle trajectories	15%	564/846/1128/1410	[Glass 1/3 mm]	1	8
Particle trajectories	20%	564/846/1128/1410	[Glass 1/3 mm]	1	8

Table 3.11: Executed experiments

3.3.2. Pre-test phase

This pre-test phase describes the proceedings that have been conducted to prepare the setup prior to experimentation. If these proceedings are followed repeatably correct, every experiment should have the same base values and results in an increases of consistency. A blockage at the pressure taps and/or defective measurement instrument can also be detected at an early stage before initial experiments have been started. Every step explained, should be followed up in the same order as these are written down in this pre-test phase.

Filling and air removal

To assure a setup that is fully cleaned from particles before any filling/refill of the system is conducted. All coupling flanges are tided up completely, the overflow valve is closed and the air removal valve of the U-loop has been opened. For filling the setup, the particle loading compartment should be used to prevent any damage from pressure build up origination from a quick valve close in the tap water network. (Originally, a different filling approach has been used but resulted in a blow out of the PMMA window due to water hammer.) When the overflow level has been reached, the U-loop air removal valve should be closed and the electric motor can be connected onto a 230V power supply through a 50HZ frequency regulator.

Start the electric motor and keep filling up the setup until again the overflow has been reached. Reduce the frequency towards 20HZ (564 RPM) for a discharge reduction and an increase in air bubble removal at the particle loading compartment. Run the motor for another 3-5 minutes for full air removal. An air bubble removal on the absolute pressure transmitters and pressure taps can be conducted by closing valve (7), so a high pressure is created. The valves on the taps and absolute pressure transmitters can be opened to press out any air bubbles.

Sensor calibration

After air removal, all measurement equipment can be connect onto a 230 Volt power source. A personal computer should be connected onto the outgoing serial port of the data logger through a USB-B cable and be assessed with the data collection script. For the data collection script and the data logger code, see appendix D.

When a stable connection between the computer and the live script has been established, a validation on the bases values is conducted. These base values are represented in table 3.12. For verification of these base values, the system should be turned off completely and the discharge is set to zero.

Base values on flow verification		
Sensor	**Value**	**Unity**
Differential pressure transmitter Down	[322]	[bits]
Differential pressure transmitter Up	[201]	[bits]
Absolute pressure transmitter Head	[123]	[bits]
Absolute pressure transmitter NPSH	[119]	[bits]
Flow meter	[201]	[bits]
Temperature sensor	[201]	[bits]

Table 3.12: Base values for sensor validation, for more details about "bits" see section 3.4

Sediment weighting and loading

Depending on the desired concentration needed in the experiment, a certain amount of preweighed particles needs to be added thought the particle loading compartment. This preweighed amount can be defined with formula 3.3 explained earlier. Also, the data-logger script supplies automatically the amount of particles needed depending on the desired concentration.

Loading of the preweighed (dry) amount of particles is done by adding them into the loading compartment. Then slowly, the secondary flow loop is turned on by throttling valve (11) and (12). Due to the availability of an overflow, the amount of excess water, created due to the added volume, can be disposed and the overall concentration is not affected.

3.3.3. Peri-test phase

As of above described base values are met, the next phase of an experiment can be started, the so called peri-test phase. In the peri-test phase, the proceedings for every experiment should be followed up in the same order as written down.

Frequency regulator settings

Depending on the speed requirement of the experiment, the frequency regulator can be adjusted manually. However, at particle loading, the maximum speeds (1410 RPM) is needed to prevent blockage. This blockage may exist due to a high density wave due to inconsistent loading. The discharge capacity is limited by throttling the head valve to stay in measurement range (at full speed) of the flow meter and suction is created at the inlet side of the pump for more enhanced loading of particles.

Mixture spreading

After particle loading, a certain density wave exist that result in a concentration fluctuation in the pump. This fluctuation does affect the final particle trajectory study since the mixture flow is not constant. Mixture

spreading or concentration distribution can be flatted out by throttling valve (9) so a certain internal flow loop resistance is created. This resistance creates an uniformly distributed concentration profile after 2-3 minutes.

Sensor data collection and video records

If the concentration profile from particle loading has been spread evenly and the desired speed is set, the data logger can be run to store the sensor data. The duration of this data logging is set to 30 sec at default. Simultaneously, a high speed recording of 3 seconds is made for particle trajectory analysing. At experiments with glass beads, also a 30 second pump head recording is executed to define a pump characteristic at mixture conditions.

When experiments are conducted with an increasing concentration, the peri-test phase can be repeated. This repetition consist out of adding the extra preweighted amount of particles for experiments with a higher concentration. By doing so, the system does not need to be cleaned between these experiments.

3.3.4. Post-test phase

In this phase, called post-test phase, the setup needs to be thoroughly cleaned and prepared for the next test run. The data-logger, flow meter and temperature sensor can be disconnected from their host and/or power-supply if there is no direct experiment afterwards. The written down proceedings are again followed up in the same order as these are written down.

System flushing and cleaning

After completing the desired experiment(s), the system needs to be cleaned and flushed to prevent "contamination" at successive experiments. This contamination exist out of different particle sizes and/or "dirty" water. This "dirty" water is a result of degradation at the PVC material and "sand blasting" of the cast-iron impeller and its shell/volute. This "dirty" water is not a problem for sensor measurement data but greatly reduces the observability of particles in the high speed video recordings.

Before the water from the setup can be disposed through valve (7), the electric motor should be kept on to prevent particle blockage at the impeller in the pump. The frequency regulator should be set to a speed of 50Hz (1410 RPM) and the air removal valve of the U-loop should be opened to prevent a vacuum. Directly after opening the air removal valve, valve (7) is opened to dispose the water into the sewer system. If a catchment of particles is desired for reuse, a bucket can be placed under the discharge opening. For a re-flush, close valve (7) and re-full the setup as described in section 3.3.2. Repeat above flushing method for two to three times, to remove all particles internally without disassembling the setup.

If a completed cleaning of the setup is desired, the full setup can be disassembled through unscrewing all connection pieces between valves, sensors and U-loop. These separate pieces can then be manually flushed. Removing the PMMA window is done by inserting a putty knife between the pump shell and the PMMA corners. Patience and care needs to be taken into account due to vulnerability of PMMA towards scratches and cracks. For reassembly, remove all old white silicon and apply a gentle amount of fresh liquid silicon as a new gasket.

PMMA window polishing

Depending on operation time, particle size, particle sharpness and flow speed. The inside of the PMMA window does scratch as a result of particle interference. This scratching reduces the observability of particles with the video recording and thus need to be "repaired". A polishing machine is used to remove these minor scratches and imperfections to improve the image quality for the next experiment.

3.4. Data processing

From the experiments, two different kinds of data are collected, sensor data and images. The sensor data is converted into readable data by a Matlab script while the images are processed by a special PIV analyse program called PIVlab.

3.4.1. Matlab data conversion

The Arduino Uno board is only able to read input signals of 0-5 Volts DC. These input signals are internally split up in 1024 bit parts and give a certain Voltage per bit value. Converting these bit values into user readable data, the formulas below have been integrated into the data logger script. Where, x is defined as $x = \frac{5 \cdot bit}{1024}$ that represent a Voltage conversion.

Bit data conversion formula		
Sensor	**Formula**	**Unit**
Differential Down	$y = 1.7563 \cdot x - 2.7778$	[kPa]
Differential Up	$y = 1.7511 \cdot x - 1.7201$	[kPa]
Absolute Head	$y = 2.0060 \cdot x - 0.0863$	[bar]
Absolute NPSH	$y = 2.0182 \cdot x - 0.0807$	[bar]
Flow meter	$y = 62.034 \cdot x - 60.174$	$[l/m]$
Temperature sensor	$y = 30 \cdot x - 50$	[°C]

Table 3.13: Bit conversion formula as implemented in data logger script

3.4.2. PIVLab image processing and data extraction

Image processing is conducted with the program called PIVlab. PIVlab is an open-source Matlab add-on to analyse particle image velocimetry (PIV) and is able to display the flow/stream patterns, designed by Thielicke et al. (2014). The images originating from the high speed camera recordings are used by PIVlab as an input value for trajectory and streamline determination. After tuning the setting of PIVlab for this specific situation, the following base settings are determined.

PIVlab base settings	
Tab	**Settings:**
Image settings	Manual mask selection per image
	Enable CLAHE (20)
	Auto contrast stretch
Analysis	FFT window deformation
	Pass 1, Interrogation area 64
	Pass 2, Interrogation area 32
	Sub-pixel estimator, Gauss 2x3 -point
Calibration	Real distance 10 [mm]
	Time step 1.572 [ms]
	Distance calibration on 10 [mm] sticker
Post-processing	Vector validation around high density scatter plot
	remove the extreme velocities
Plot	Display Parameter in Velocity magnitude
	Smooth data ON
	Colourmap limits ON autoscale
	Autoscale vectors ON
	Colourmap "Parula" legend "West"
	Streamlines manually added with line rake of 10
Extractions	Polyline in Velocity magnitude
	Nr. of interpolated points: 300

Table 3.14: PIVlab (Version 2.36) base values for a consistent image processing.

For every PIV analysis on images, a certain base mask needs to be drawn. This base mask sets the boundary conditions/contour lines and specifies the region of interest. In figure 3.10, a base base mask is shown that is constant over all analysis. Besides this base mask, every impeller blade has to be masked manually for every image as these boundary conditions move along time. If all masks are drawn for a certain set of images, mostly ten pieces, PIVlab can be run with the base values settings from table 3.14. If the analysing is completed, Post-processing and plot settings are tuned to create a trajectories image with streamlines. These outcomes can be found in appendix C and are further discussed in section 3.4.

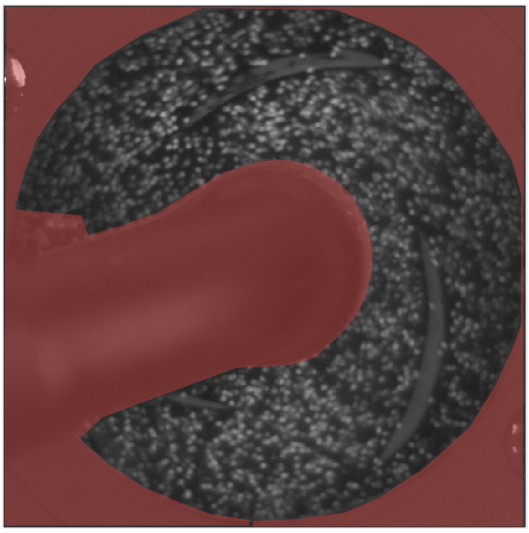

Figure 3.10: Base mask as boundary conditions for PIVlab, which are the same for every image.

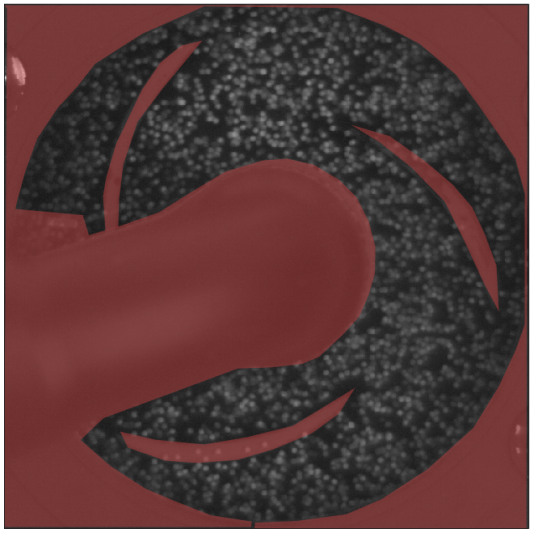

Figure 3.11: Full mask as boundary conditions for PIVlab, which is image dependent.

For comparing multiple local velocities at different speeds and concentrations, four regions of interest are specified. In figure 3.12, four lines are drawn and numbered that represent these regions. Number 1 and 2 are crossing the local eddy that is present at the suction side of the blade. Number 3 and 4 present the local velocities at the pressure side of the blade. This data is extracted from the PIVlab analyse by a so called "Polyline in Velocity magnitude". These velocity magnitude plots are included in appendix C and are further discussed in section 3.4.

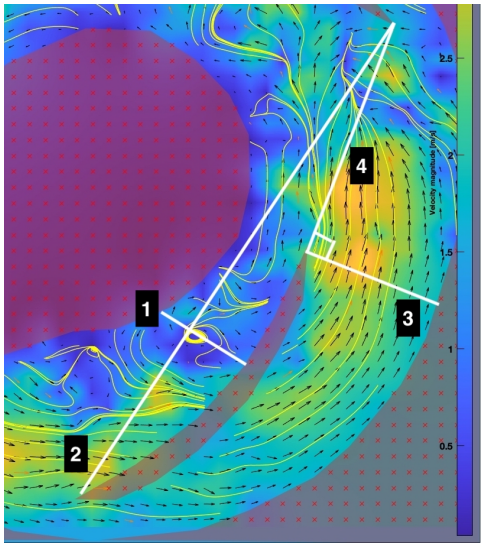

Figure 3.12: PIVlab local velocity plot locations.

4

Experimental outcomes and data analysing

This chapter is a summary of the most notable experimental research outcomes. Firstly, the internal volume determination is discussed to create a base value for delivered volumetric concentration validation. Followed by the (unsteady) head behaviour at single phase characteristics with its streamlines and trajectories. These same aspects, (unsteady) head, characteristics, streamlines and trajectories, are also discussed for the mixture phase situation. The conclusions on a visual comparison for density distribution is given next. Finally, an overall comparison/validation with the CFD paper of Cao et al. (2019) is made.

4.1. Internal volume determination and particle preweighed

As discussed in the previous chapter, the internal volume had to be defined to determine the needed amount of particles. An internal volume measurement has been conducted 5 times and resulted into an average internal volume of 16.52 liters based on a water density of 998 kg/m^3.

Executed volume experiments				
Test:	**Average weighted:**	**Unit:**	**Average volume:**	**Unit:**
Volume loop 1	15.46	$[kg]$	15.41	$[l]$
Volume loop 2	15.32	$[kg]$	15.27	$[l]$
Volume loop 3	15.57	$[kg]$	15.52	$[l]$
Volume loop 4	15.42	$[kg]$	15.37	$[l]$
Volume loop 5	15.47	$[kg]$	15.42	$[l]$
Total loop average			15.40	$[l]$
Volume shell			1.115	$[l]$
Total volume average			16.52	$[l]$

Table 4.1: Internal volume determination of the setup.

With the average internal volume determination, a list of preweighed amount of particles could be made with the use of equation 3.3. In table 4.2, these needed amounts are given with the "to be added amount" for continuing experiments with higher concentrations.

Particles preweighed				
	Cvd:	**Weight:**	**Weight-added:**	**Unit:**
Polystyrene	0.01	170.8		$[gram]$
	0.03	512.4	341.6	$[gram]$
	0.05	854.0	341.6	$[gram]$
Glass	0.03	1249.7		$[gram]$
	0.05	2082.9	833.2	$[gram]$
	0.08	3332.7	1249.8	$[gram]$
	0.12	4999.9	1667.2	$[gram]$
	0.15	6248.7	1248.8	$[gram]$
	0.20	8331.7	2083.0	$[gram]$

Table 4.2: Weight determination regarding the needed amount of particles per C_{vd}.

4.2. Single phase experiments

In this section, conducted experiments and their outcomes/analyses for single phase situation are discussed. Firstly, the "single phases characteristic" is defined. Followed by the "unsteady (water) head" recordings at multiple situations. Lastly, the water streamlines and trajectories obtained with PIVlab analysis are discussed.

4.2.1. Single phase characteristic

As the geometry of the pump has been changed, a new pump characteristic for referencing at mixture conditions is needed. Due to the age of the pump and shell, no existing pump specifications could be sources from the manufacturer as a certain base reference. By throttling, the discharge valve after the pump outlet, a wide range of discharges could be created with their corresponding head value. This data is plotted in figure 4.1, with in the top left graph on the x-axis "Discharge" and on the y-axis the corresponding "Head" value. On the top right graph, the NPSH value shows an exponential increase with discharge. In the bottom left graph, the pump efficiency with respect to an increasing discharge is displayed. The bottom right graph shows the power absorption by water with increasing discharge. All experiments are conducted at four different engine speeds, 564, 846, 1128 and 1410 RPM respectively. In comparison with the discussed theory in chapter 2, the head does indeed reduce with an increase in discharge. The efficiency curve is a parabolic function with a certain maximum that can be used to distinguish the BEP for single phase situation of this pump specifically.

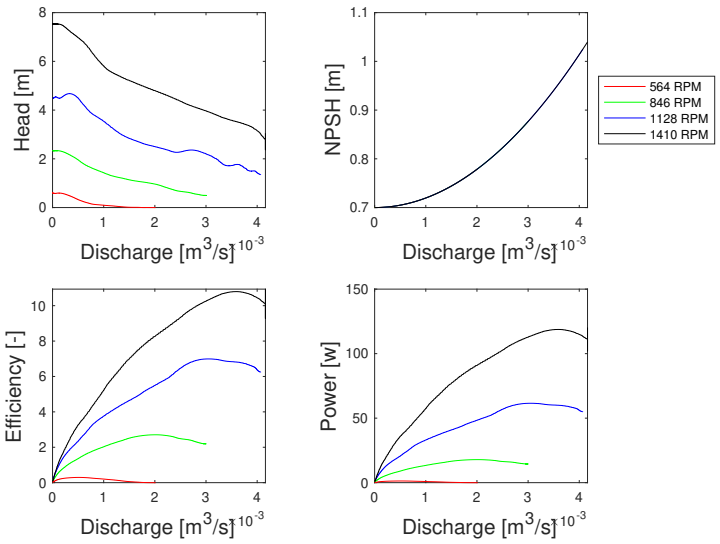

Figure 4.1: Pump characteristic, speed dependent with corresponding head vs. discharge, NPSH vs. discharge, efficiency vs. discharge and power conversion vs. discharge at 564, 846, 1128 and 1410 RPM. The discharge ranges from 0 - $4 \cdot 10^{-3} m^3/s$

4.2.2. Unsteady (water) head

As discussed in the literature research and the paper of Cao et al. (2019), the impeller creates a fluctuating head due to impeller interaction with the exit tongue. In single phase water condition, as shown in figure 4.2A that originates from Cao et al. (2019), the unsteady head is a constant occurring phenomena with a relative steady frequency peak. This fluctuation is a result of the multiplication of the local impeller frequency (f_n) with the number of blades present. In this research, CFD and experimental impeller have the same number of blades, three. In figure 4.2[B], a FFT analysis (f) from the data in [A], divided by the local impeller frequency (f_n), results in the relative frequency ratio (f/f_n). This shows that indeed the peek frequencies are a function of three times the local impeller frequency. A side note should be made regarding the FFT at $0.5Q_d$, a peak frequency ratio of 0.44 can be distinguished in the graph. This low frequency peak ratio is discussed further in the coming up sections.

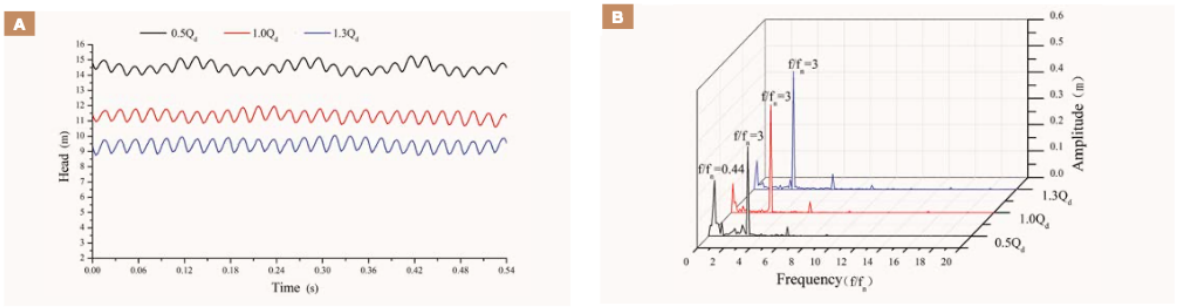

Figure 4.2: Head fluctuation over time for water [A] and the spectrogram of head shown for water flow [B], obtained from Cao et al. (2019)

Verifying the CFD model outcomes for single phase situations have been conducted with experiments at multiple engine speeds and sampling frequencies. To gain a wide set of head data, see figure 4.3 as an example. As well, some easy hand calculations are conducted to define the local rounds/seconds or local frequency of the impeller (RPM/60) and for a single blade, the impeller frequency is multiplied by the number of blades. In table 4.3, these hand calculations are compared with the measured frequencies obtained from experiments by a FFT analysis, figure 4.4, based on the head fluctuations, visualized in figure 4.3. The FFT peak frequencies are, as in figure 4.2[B], divided by the local impeller frequency that result in a relative frequency ratio (f/f_n), displayed in figure 4.5.

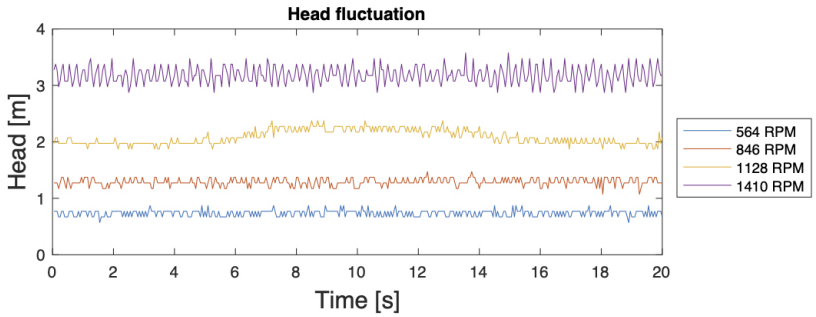

Figure 4.3: Unsteady head fluctuations in water conditions at 564, 846, 1128 and 1410 RPM, sample frequency 20HZ, Head valve 50% opened.

Unsteady head frequencies from FFT (experiments)								
Engine freq.:	**RPM/60: (f_n)**	**Blade freq.:**	**Engine freq. FFT**	**Impeller freq. FFT:**	**Eigen freq.:**	**Unit:**	**Impeller FFT / f_n:**	**Blade FFT / f_n:**
20	9.4	28.2	10.12	30.40	51.18	$[Hz]$	1.08	3.23
30	14.1	42.3	15.13	45.46	51.71	$[Hz]$	1.07	3.22
40	18.8	56.4	20.29	60.85	52.29	$[Hz]$	1.08	3.24
50	23.5	70.5	25.52	76.49	53.44	$[Hz]$	1.09	3.25

Table 4.3: Frequency comparing of calculations vs FFT from measurement.

The unsteady head measurements needed for the FFT graphs, in figure 4.4, originate from absolute pressure transmitter recordings at the exit pipe of the pump. Different sampling frequencies are used for noise mitigation and an increase in measurement accuracy for higher frequency distinguishing. Figure 4.4, consists out of four graphs with a variation in engine speed and sampling frequency. From left to right, 564RPM/125Hz, 846RPM/125Hz, 1128RPM/167Hz and 1410RPM/250Hz. From these graphs, it can be concluded that in water conditions with an increase in engine speed, there is a frequency shift from the right side of the spectra towards the left side. This means that the overall pump gets more stable in head, as less high frequencies are present. In other words, this energy shift towards the lower spectra side results in a reduction of head amplitude variation.

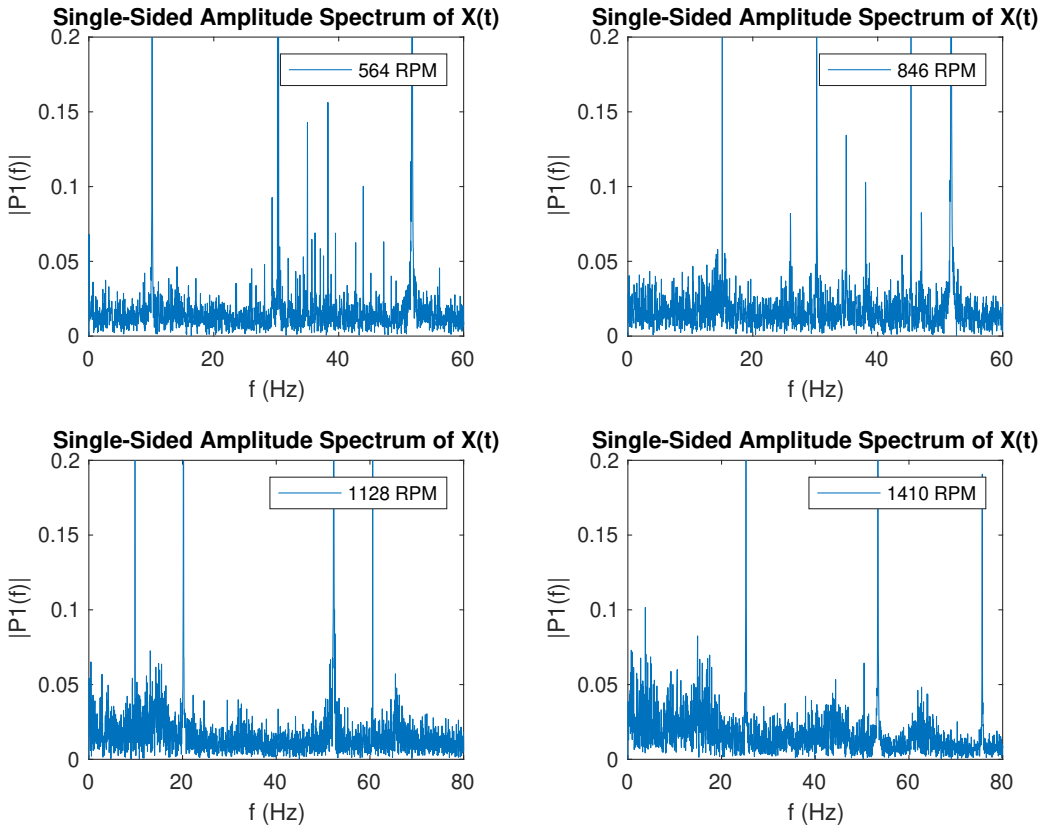

Figure 4.4: Unsteady head fluctuations at 564, 846, 1128 and 1410 RPM, sample frequency 125HZ, 167Hz, 250Hz, Head valve 50% opened.

For comparison of the experimental spectra with the spectrogram of Cao et al. (2019), the data in figure 4.4 needs to be divided by the local frequency of the impeller. By doing so, this results in a 3D plot with on the x-axis the relative frequency ratio (f/f_n), on the y-axis the engine speed (RPM) and on the z-axis the spectral

density. One can concluded from comparing this experimental spectrogram to the CFD model, that there is indeed a lot of overlap. The local impeller frequency is indeed present at a ratio of ~1 and the local blade frequency is present at ~3. These values are slightly higher than the hand calculations and the CFD model expectations, most likely, originating from effect that occur during experiments which are not accounted for in calculations.

One should also notice that there are some other interesting peaks present. One shifting peak, along increasing speed, can be easily explained. This peak is a representation of the eigenfrequency of the pump and has a value of ~52 Hz, see figure 4.4. Revering back to the side-note made above, regarding the 0.44 ratio representation at $0.5Q_d$ in the CFD model, a similar peak is also present at the 1128 RPM values at a ratio of 0.52, see the red circle in figure 4.5. Cao et al. (2019) suggested that this low frequency peak originated from eddy separations between the blades. As with an increase in speed, towards 1410 RPM, this spectral peak disappears.

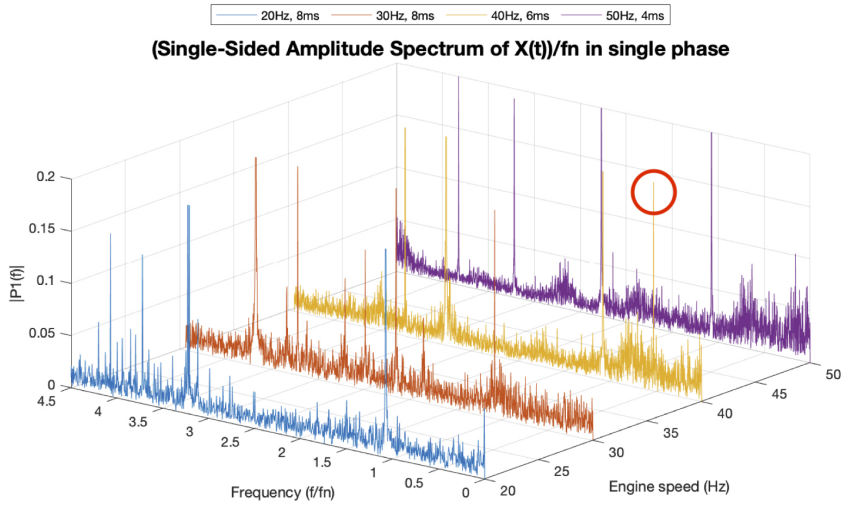

Figure 4.5: FFT head fluctuations divide by the local frequency f_n for comparison with figure 4.2 from Cao et al. (2019)

4.2.3. Water streamlines and trajectories verification

PIVlab has been extensively used to define the absolute particle trajectories and their absolute streamlines along the impeller blades. In appendix C, all PIVlab image analysis are available for every concentration, speed, particle kind and size. Due to a limitation in discussion space for this thesis, a certain selection is discussed here. The selection criteria are based on the 0.52 frequency peak ratio visible in the 1128 RPM engine input situation. This frequency peak is also, in more or less the same magnitude, present in the $0.5Q_d$ data plots given in Cao et al. (2019). A natural consequence is that also 1410 RPM is included for comparison with the Q_d data. Situations for $1.3Q_d$ could not be created due to limitation on the experimental setup as of safety restrictions.

An important side note regarding PIVlab velocity magnitude estimations should be made. The images used for PIVlab are an "unfiltered" image of the particles between the blades. As no laser was used for layer identification that "light up" a specific layer. In other-words, there is no distinguishing in their Z-direction and thus the images show particles on a flat plain at the window front. The consequence is that the absolute velocity magnitude is an approximation and can be partly used for validation of the relative streamlines and trajectories of Cao et al. (2019) CFD model outcomes.

In combination with the pre-defined regions of interest, discussed in section 3 and again displayed in figure 4.7, four local velocity plots could be made from the PIVlab image results. In these local velocity plots, the x-axis displays the distance $[m]$ and the y-axis the velocity magnitude $[m/s]$. In the PIVlab images, displayed in figure 4.8 and 4.9, a colour bar is present at the left side of the image. This colour bar gives an indication on the local absolute velocity magnitude of the fluid $[m/s]$. Furthermore, multiple absolute streamlines are drawn in the images to give an idea on flow direction at that specific time and location. From these streamlines, one can conclude that a large section of the cross-sectional area is in turbulent conditions due to the representation of eddies and acute changes in flow direction due to shearing of opposite velocity magnitudes.

In the four local velocity plots, changes in flow speed as a result of turbulent conditions are easily distinguishable as peaks. By comparing figure 4.10 with figure 4.14, there is no significant change in amplitude size. Though, a small increase in the local velocity magnitude is present at the 1410 RPM water situation. A visual comparison of figure 4.8 and 4.9 shows a reduction in the amount of eddies present and higher absolute local velocities. The reduction of eddies implies that the streamline is less turbulent. This phenomena is also noticeable at the instantaneous relative streamline image from Cao et al. (2019), see figure 4.6A/B. In this figure, the local relative velocities are more or less equal compared to the calculated absolute velocities originating from PIVlab. Both situations have a wide range of velocities between 0 and ±4.8 m/s and are of the same order of magnitude a in the paper of Hofstra et al. (2010).

In an one on one visual comparisons of the conducted flow verification experiment with the CFD model outcomes in figure 4.6, the following can be concluded; with an increase on engine speed, the presents of eddies and acute changes in flow direction do indeed reduce and the local velocity magnitude of the flow speed increases significantly as mentioned in the paper of Cao et al. (2019). The reduction of eddies and acute changes in flow direction are reasoned by Cao et al. (2019) as a reduction in eddy separation between impeller blades.

For the discussed low frequencies ratio of 0.44 in Cao et al. (2019) and the 0.52 ratio at the 1128 RPM experiments, this separation of eddies may indeed be the origin of this frequency. As in both Q_d and 1410 RPM experiments, this frequency disappears with the change in streamlines that are also visible in the PIVlab image comparison.

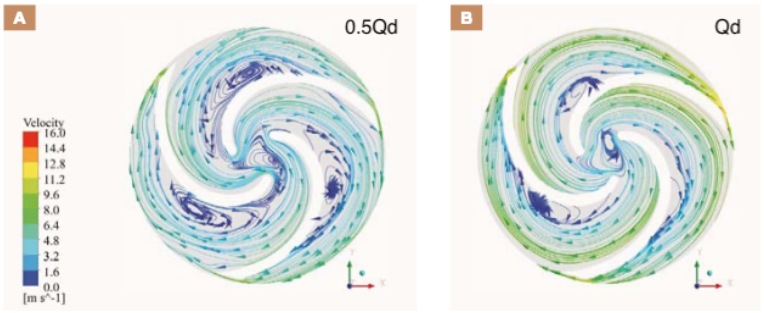

Figure 4.6: Instantaneous relative streamlines between a counterclockwise rotating impeller at water flow. Shown for three conditions: $0.5Q_d$ and Q_d, obtained from Cao et al. (2019)

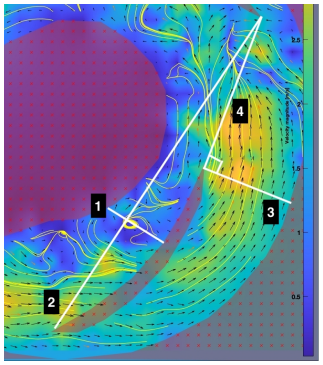

Figure 4.7: PIVlab local velocity plot locations.

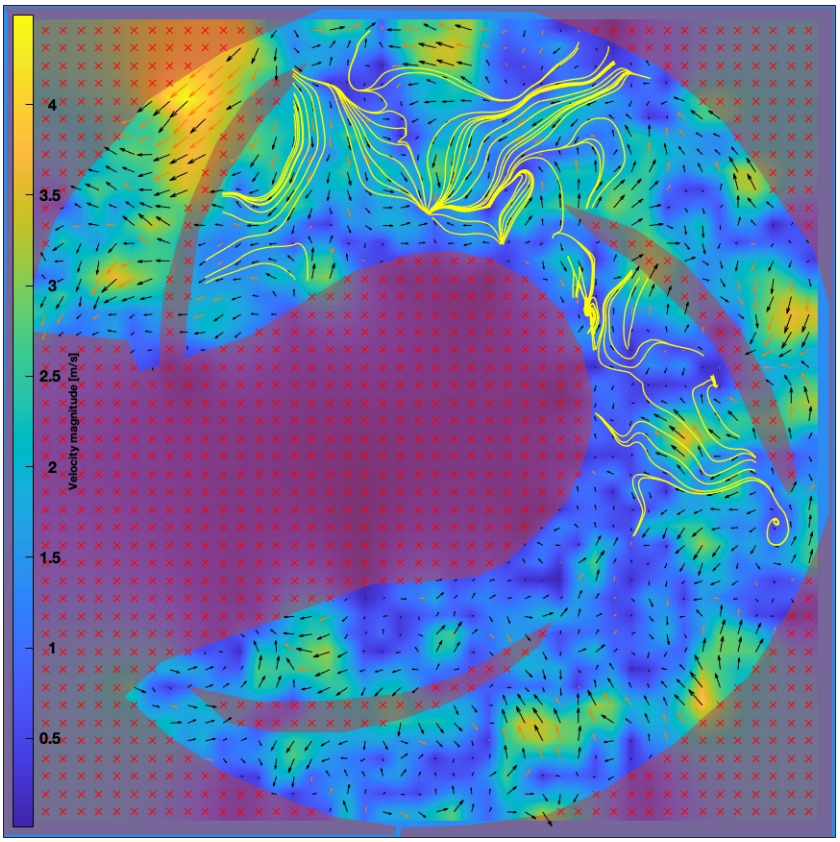

Figure 4.8: PIVlab image analysing in water conditions at 1128 RPM with a counterclockwise rotating impeller and absolute streamlines.

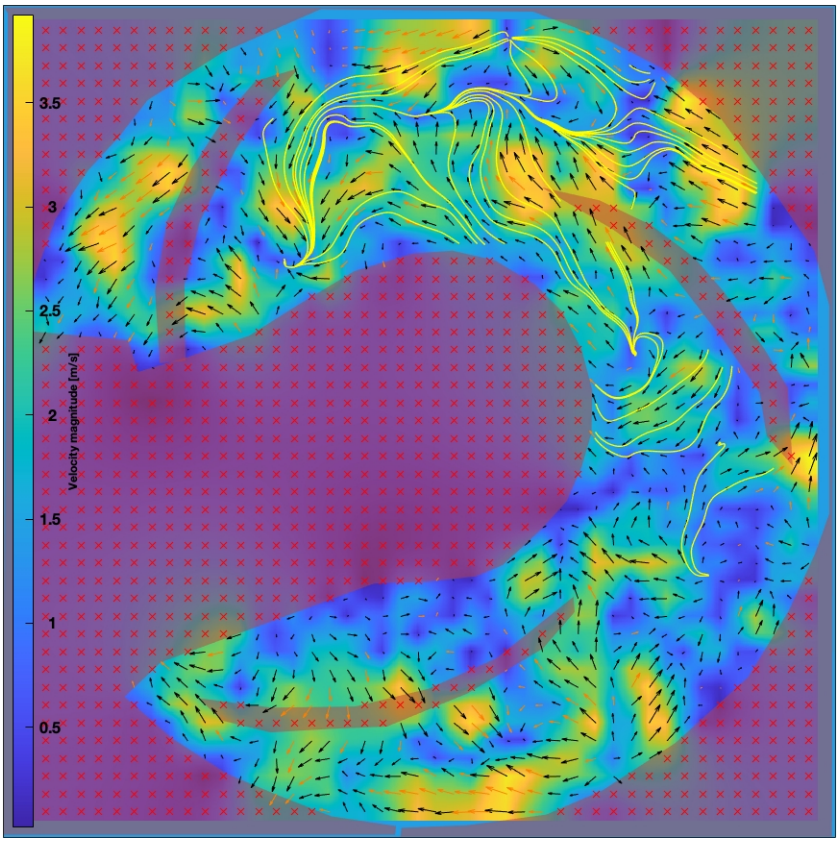

Figure 4.9: PIVlab image analysing in water conditions at 1410 RPM with a counterclockwise rotating impeller and absolute streamlines.

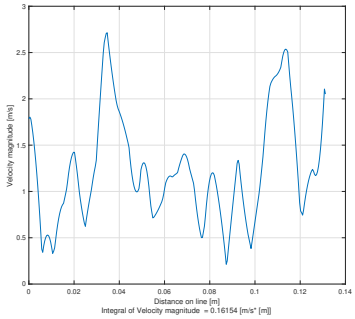

Figure 4.10: Local Velocity line plot of the eddy in longitudinal direction, corresponding to figure 4.8.

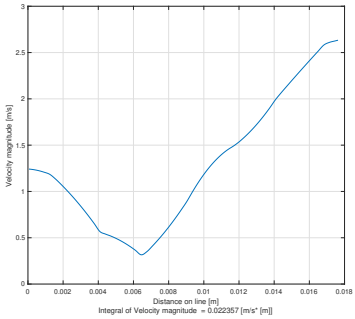

Figure 4.11: Local Velocity line plot of the eddy in transverse direction, corresponding to figure 4.8.

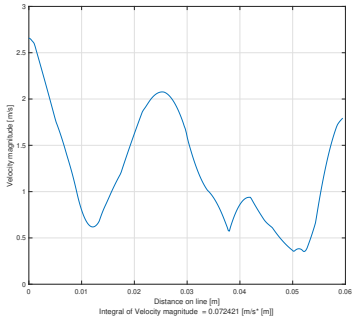

Figure 4.12: Local Velocity line plot between the leading front and tail of two impellers, corresponding to figure 4.8.

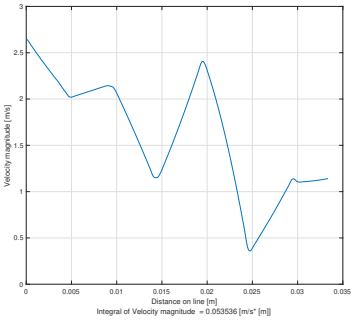

Figure 4.13: Local Velocity line plot perpendicular on the leading front of the impeller, corresponding to figure 4.8.

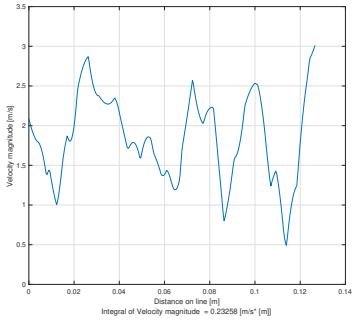

Figure 4.14: Local Velocity line plot of the eddy in longitudinal direction, corresponding to figure 4.9.

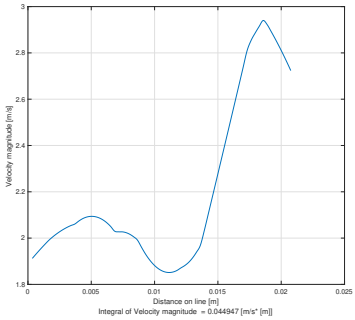

Figure 4.15: Local Velocity line plot of the eddy in transverse direction, corresponding to figure 4.9.

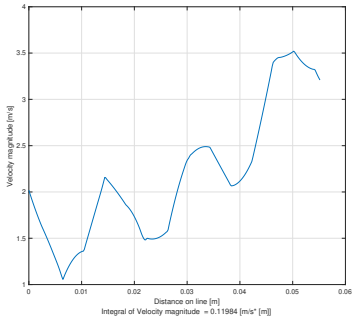

Figure 4.16: Local Velocity line plot between the leading front and tail of two impellers, corresponding to figure 4.9.

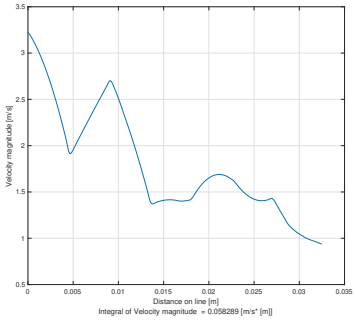

Figure 4.17: Local Velocity line plot perpendicular on the leading front of the impeller, corresponding to figure 4.9.

4.3. Mixture phase experiments

In this section, conducted experiments and their outcomes/analyses for mixture phase situation are discussed. Firstly, the "mixture phases characteristic" is created. Followed by the "unsteady (mixture) head" recordings at multiple situations. Further, the water streamlines and trajectories obtained with PIVlab analysis are discussed. Lastly, the concentration distribution between the blades is analysed.

4.3.1. Mixture phase characteristics

The literature research concluded that particles have a significant influence on head and discharge performance resulting in a shift in pump characteristics. As of these statements, for every conducted experiment a mixture pump characteristic has been obtained. This resulted in a set of twelve different graphs. As of the limitation in size for discussion, a certain selection is made again. On top of the 1128/1410 RPM criteria from water only, a criteria is added to select the experiments with high concentrations, because Cao et al. (2019) created CFD model outcomes for mixture flow concentrations of 20%. The mixture phase characteristic and head vs. concentration measurements for 20%, with 1.5 mm and 3.0 mm glass beads are shown in figure 4.18 and 4.19. All other graphs, figures and tables that are not discussed in this section can be found in appendix A, B and C

In figure 4.18 and 4.19, the mixture pump characteristics are shown for all engine speeds at a C_{vd} = 0.20 with 1.5 and 3.0 mm particles. These figures consists out of four subplot that display the following data; top left graphs shows on the x-axis "Discharge" and on the y-axis the corresponding "Head" value. Top right graphs shows the "Concentration" increase with respect to increasing "Discharge". Bottom left graphs, displays the pump "Efficiency" with respect to "Discharge". The bottom right graphs shows the "Power" absorption by water with increasing discharge.

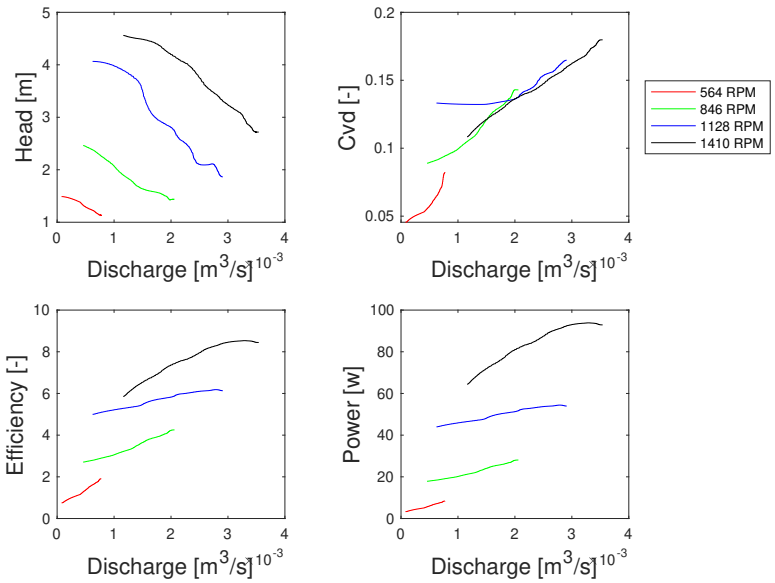

Figure 4.18: Pump characteristic, speed dependent with corresponding head vs. discharge, NPSH vs. discharge, efficiency vs. discharge and power conversion vs. discharge at 564, 846, 1128 and 1410 RPM with a C_{vd} = 0.20 and 1.5mm glass beads.

In figure 4.18, some interesting aspects can be noted compared to the same speeds in single phase conditions. Indeed, as concluded in the literature research, the head values are lower in mixture conditions. Also, the discharge rate at full engine speed is significant lower, combined with a lower head, this results in a lower efficiency and power absorption rate.

The exact C_{vd} of the mixture depends on the flow velocity and particle size, as can be seen in the top right graph. At discharge values of around $1.5 \cdot 10^{-3}$ $[m^3/s]$, the concentrations starts to show a linear approach and slowly reaches the 20% concentration. In other words, the energy transmission from the impeller into

the fluid is high enough to create a transition from moving bed towards homogeneous flow that occurs and is observed in the pipe. In the 564 RPM situation, the discharge is to low too create a sliding bed phenomena and thus the desired concentration for experiments is not reached.

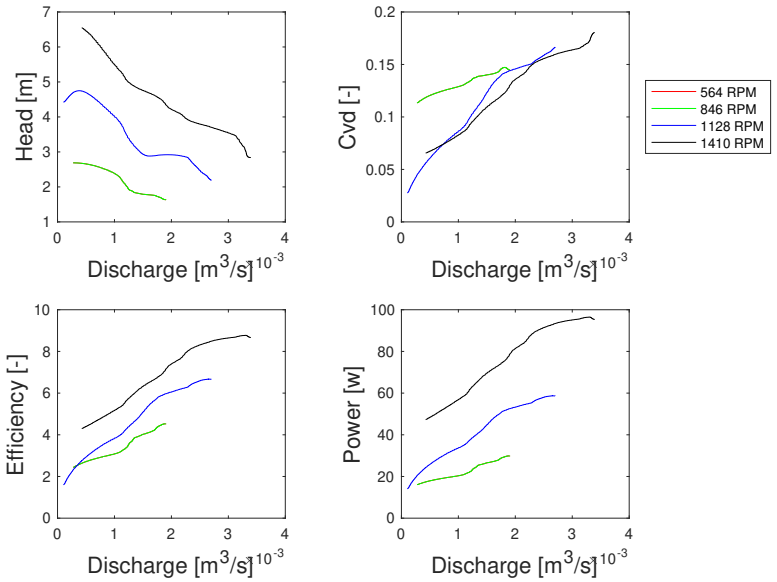

Figure 4.19: Pump characteristic, speed dependent with corresponding head vs. discharge, NPSH vs. discharge, efficiency vs. discharge and power conversion vs. discharge at 846, 1128 and 1410 RPM with a C_{vd} = 0.20 and 3.0mm glass beads.

The mixture pump characteristic for glass beads particles with a diameter of 3.0 mm and a C_{vd} of 20% looks slightly different compared to figure 4.18. A pump curve for 564 RPM situations could not be created, due to blockages of the 3.0 mm glass beads between the impeller and pump shell near the drive axle. As a result of low torque from the low speed setting, the drive axle could not overcome this internal resistant and started to make "dangerous" noises.

A big difference, in comparison with figure 4.18, is the higher head at 1410 RPM with low discharge. Again, at a discharge value of around $1.5 \cdot 10^{-3}$ $[m^3/s]$, the concentrations start to line up and slowly reach the 20% concentration.

4.3.2. Unsteady (mixture) head

In the paper of Cao et al. (2019) for mixture situations, an enhancement on the unsteady head is shown. This enhancement can be clearly seen in figure 4.20[A] with a reduction in head while an increasing of discharge is present. This enhancement can also be clearly seen at the 20%, 1.5 mm and 3.0 mm glass beads experiments. Figure 4.21 and 4.22, show the head and concentration recording of these experiments. In the 1.5 mm particle experiment, a relative small amplitude in head is visible. While at the 3.0 mm particles, even an amplification in head amplitude is noticeable for 846, 1128 and 1410 RPM. In both situations at 1128 RPM, again the low frequency waves is present and is not at the 1410 RPM experiments. Another interesting aspect is the presents of a low frequency waves in the concentration profile. More on this phenomena is discussed in section 4.3.4.

From the CFD model outcomes for mixture loading, a FFT analysis was also made by Cao et al. (2019). The result of this analysis are displayed in figure 4.20[B] and show for $0.5Q_d$ an interesting shift from $f/f_n = 3$ towards $f/f_n = 1$ as main peak frequency ratio. The peak frequency ratio at Q_d has not been changed and thus stays equal to 3. However, in both situation, the amount of "noise" has significantly increased compared to figure 4.2[B]. The origin of this noise can be fully assigned to the unsteady head enhancement as a result of mixture loading.

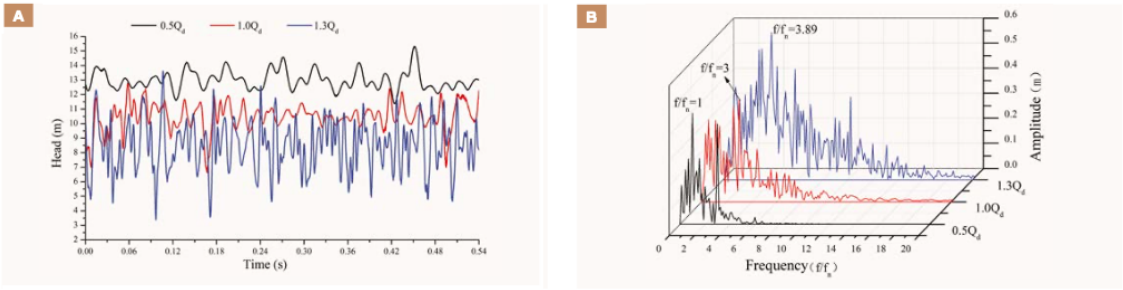

Figure 4.20: Head fluctuation over time for water [A] and spectrogram of head shown for mixture flow [B], obtained from Cao et al. (2019)

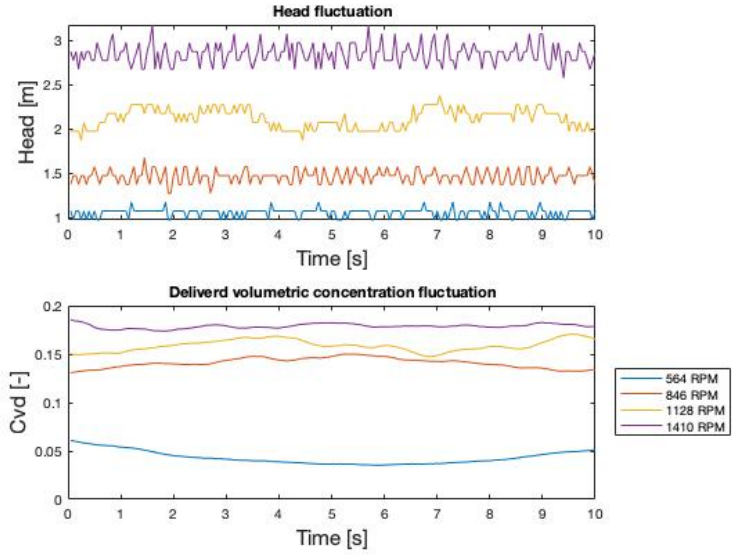

Figure 4.21: Unsteady head fluctuations in mixture conditions at 564, 846, 1128 and 1410 RPM, sample frequency 20Hz, Head valve 50%, Particle size 1.5mm, $C_{vd} = 0.20$

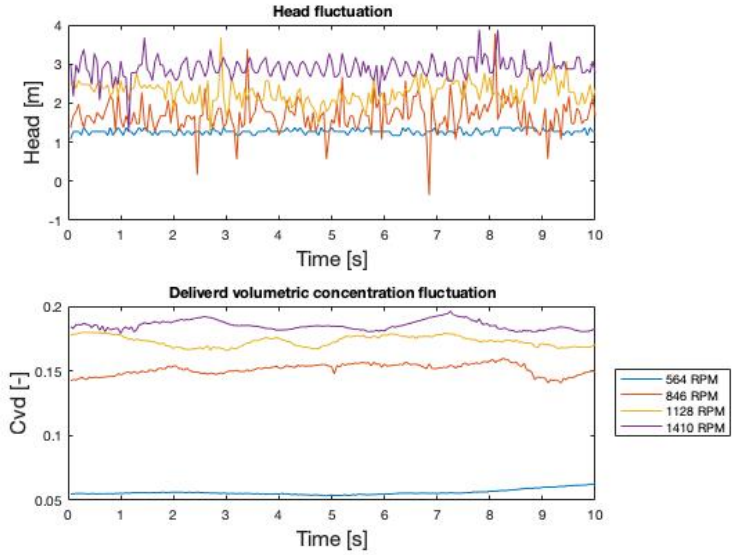

Figure 4.22: Unsteady head fluctuations in mixture conditions at 564, 846, 1128 and 1410 RPM, sample frequency 20Hz, Head valve 50%, Particle size 3.0mm, $C_{vd} = 0.20$

As with the FFT analysis on unsteady head conditions in single phase water conditions, the same FFT analysis have been conducted on data collected from mixture loading experiments. This resulted in a wide range of figures and data, as frequency vs. energy density plots and a table with all the local peak frequencies. Table 4.4, is a collection of all the local peak frequencies origination from either the local impeller or blade frequency present in figure 4.23, 4.24, 4.24, 4.26 and appendix B. One can quickly conclude, that during particle loading, the unsteady head enhancement due to particles does not shift or influences the dominant peak frequencies significantly. As everywhere in table 4.4;

$$\frac{(\text{Engine frequency FFT}) \cdot 60}{RPM} \sim 1 \tag{4.1}$$

And

$$\frac{(\text{Blade frequency FFT}) \cdot 60}{RPM} \sim 3 \tag{4.2}$$

Figures 4.23, 4.24, 4.25 and 4.26 are the result of the conducted FFT analysis from the experimental data of mixture loading at all C_{vd} values with 1.5mm and 3 mm particles at 1128 RPM and 1410 RPM. Again, at the 1128 RPM engine speed situation, the low frequency wave at the 0.52 peak frequency ratio is present during all concentration loading. However, these mixture FFT analysis, at all concentrations and at 1128 and 1410 RPM to water FFT at 1128 and 1410 RPM, do not directly give a reasoning for the unsteady concentration fluctuation.

Unsteady head peak frequencies from FFT at water/mixture.									
Engine freq.:	**RPM/60: (f_n)**	**Blade freq.:**	**Engine freq. FFT**	**Blade freq. FFT:**	**Eigen freq.:**	**Unit:**	**Cvd:**	**Particle Size:**	**Unit:**
20	9.4	28.20	10.12	30.40	51.18	$[Hz]$	0%	-	$[mm]$
"	"	"	10.08	30.14	51.70	$[Hz]$	3%	1.5	$[mm]$
"	"	"	10.15	30.42	51.75	$[Hz]$	5%	1.5	$[mm]$
"	"	"	10.14	30.42	51.79	$[Hz]$	8%	1.5	$[mm]$
"	"	"	10.14	30.23	51.75	$[Hz]$	12%	1.5	$[mm]$
"	"	"	10.13	30.08	51.67	$[Hz]$	15%	1.5	$[mm]$
"	"	"	10.14	30.41	51.70	$[Hz]$	20%	1.5	$[mm]$
"	"	"	12.00	31.95	51.73	$[Hz]$	3%	3.0	$[mm]$
"	"	"	10.10	32.93	51.73	$[Hz]$	5%	3.0	$[mm]$
"	"	"	12.44	30.37	51.72	$[Hz]$	8%	3.0	$[mm]$
"	"	"	10.14	30.38	51.70	$[Hz]$	12%	3.0	$[mm]$
"	"	"	10.15	30.41	51.71	$[Hz]$	15%	3.0	$[mm]$
"	"	"	10.12	30.41	51.08	$[Hz]$	20%	3.0	$[mm]$
30	14.1	42.3	15.13	45.46	51.71	$[Hz]$	0%	-	$[mm]$
"	"	"	15.05	45.19	51.67	$[Hz]$	3%	1.5	$[mm]$
"	"	"	15.09	45.32	51.70	$[Hz]$	5%	1.5	$[mm]$
"	"	"	15.08	45.32	51.73	$[Hz]$	8%	1.5	$[mm]$
"	"	"	15.08	45.25	51.69	$[Hz]$	12%	1.5	$[mm]$
"	"	"	15.08	45.30	51.67	$[Hz]$	15%	1.5	$[mm]$
"	"	"	15.07	45.25	51.71	$[Hz]$	20%	1.5	$[mm]$
"	"	"	16.66	42.34	51.72	$[Hz]$	3%	3.0	$[mm]$
"	"	"	17.89	45.28	51.72	$[Hz]$	5%	3.0	$[mm]$
"	"	"	15.54	45.53	51.72	$[Hz]$	8%	3.0	$[mm]$
"	"	"	15.32	45.34	51.70	$[Hz]$	12%	3.0	$[mm]$
"	"	"	15.11	45.34	51.74	$[Hz]$	15%	3.0	$[mm]$
"	"	"	15.09	45.34	51.70	$[Hz]$	20%	3.0	$[mm]$
40	18.8	56.4	20.29	60.85	52.29	$[Hz]$	0%	-	$[mm]$
"	"	"	20.16	60.35	52.33	$[Hz]$	3%	1.5	$[mm]$
"	"	"	20.20	60.52	52.32	$[Hz]$	5%	1.5	$[mm]$
"	"	"	20.16	60.47	52.27	$[Hz]$	8%	1.5	$[mm]$
"	"	"	20.15	60.30	52.26	$[Hz]$	12%	1.5	$[mm]$
"	"	"	20.12	60.33	52.24	$[Hz]$	15%	1.5	$[mm]$
"	"	"	20.11	60.30	52.28	$[Hz]$	20%	1.5	$[mm]$
"	"	"	20.19	60.57	52.27	$[Hz]$	3%	3.0	$[mm]$
"	"	"	20.18	60.54	52.26	$[Hz]$	5%	3.0	$[mm]$
"	"	"	20.19	60.56	52.24	$[Hz]$	8%	3.0	$[mm]$
"	"	"	20.21	60.54	52.32	$[Hz]$	12%	3.0	$[mm]$
"	"	"	20.13	60.39	52.30	$[Hz]$	15%	3.0	$[mm]$
"	"	"	20.18	60.52	52.23	$[Hz]$	20%	3.0	$[mm]$
50	23.5	70.5	25.52	76.49	53.44	$[Hz]$	0%	-	$[mm]$
"	"	"	24.93	74.86	53.44	$[Hz]$	3%	1.5	$[mm]$
"	"	"	25.11	75.35	53.45	$[Hz]$	5%	1.5	$[mm]$
"	"	"	25.01	75.06	53.44	$[Hz]$	8%	1.5	$[mm]$
"	"	"	24.99	74.96	53.31	$[Hz]$	12%	1.5	$[mm]$
"	"	"	24.95	74.49	53.34	$[Hz]$	15%	1.5	$[mm]$
"	"	"	24.92	74.74	53.41	$[Hz]$	20%	1.5	$[mm]$
"	"	"	25.15	75.50	53,37	$[Hz]$	3%	3.0	$[mm]$
"	"	"	25.16	73.19	53.37	$[Hz]$	5%	3.0	$[mm]$
"	"	"	25.16	75.51	53.41	$[Hz]$	8%	3.0	$[mm]$
"	"	"	25.18	75.50	53.37	$[Hz]$	12%	3.0	$[mm]$
"	"	"	25.12	75.36	53.42	$[Hz]$	15%	3.0	$[mm]$
"	"	"	25.20	75.39	53.41	$[Hz]$	20%	3.0	$[mm]$

Table 4.4: Peak frequency comparing of calculations vs FFT (measured at mixture conditions).

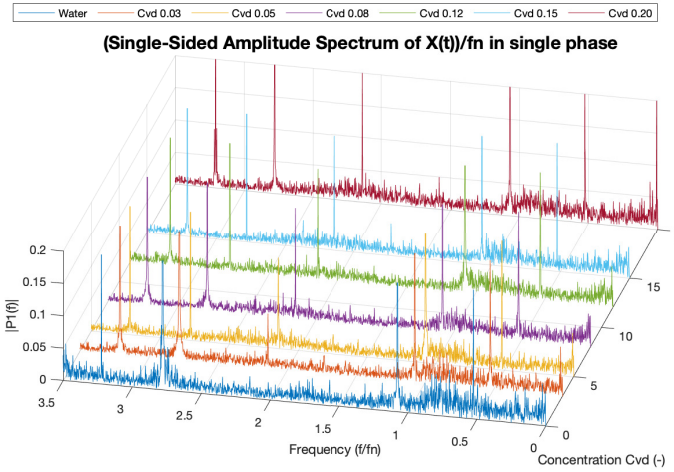

Figure 4.23: 3D plot of multiple FFT analysis from 1128 RPM experiments at all concentrations with a particle size of 1.5 mm.

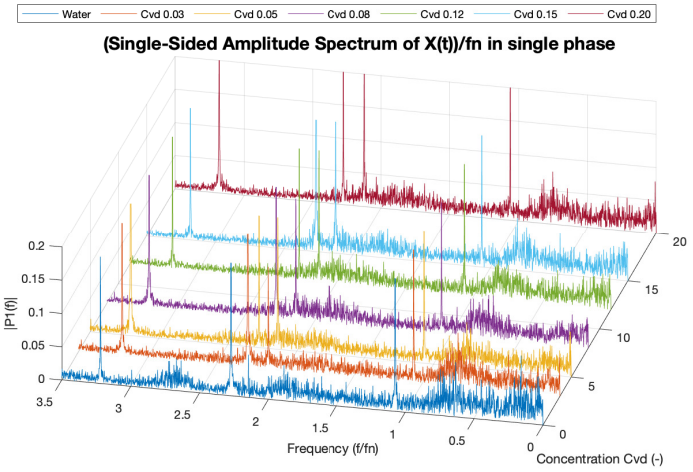

Figure 4.24: 3D plot of multiple FFT analysis from 1410 RPM experiments at all concentrations with a particle size of 1.5 mm.

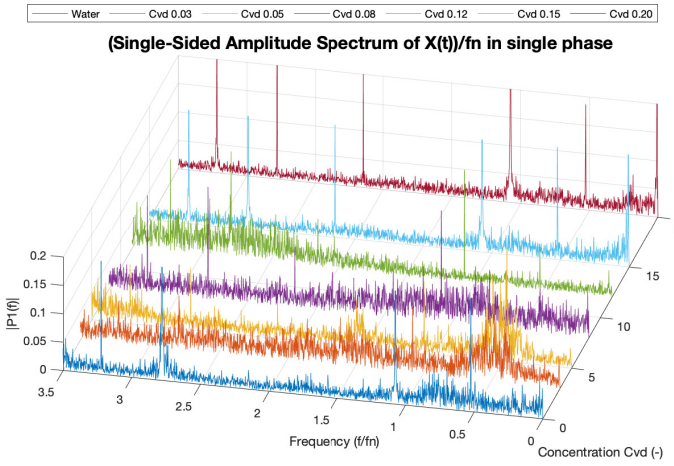

Figure 4.25: 3D plot of multiple FFT analysis from 1128 RPM experiments at all concentrations with a particle size of 3.0 mm.

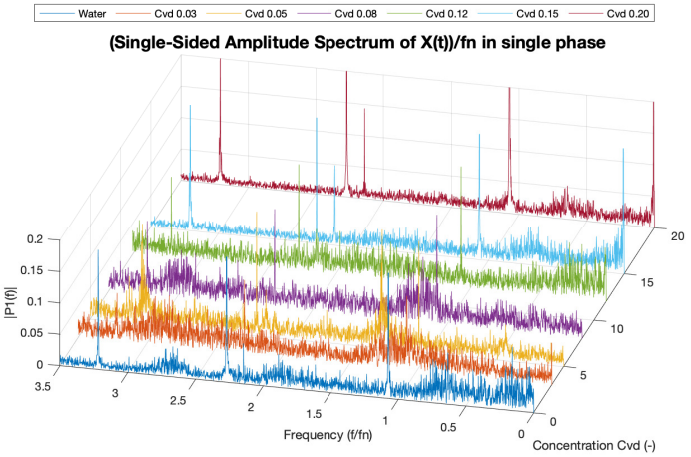

Figure 4.26: 3D plot of multiple FFT analysis from 1410 RPM experiments at all concentrations with a particle size of 3.0 mm.

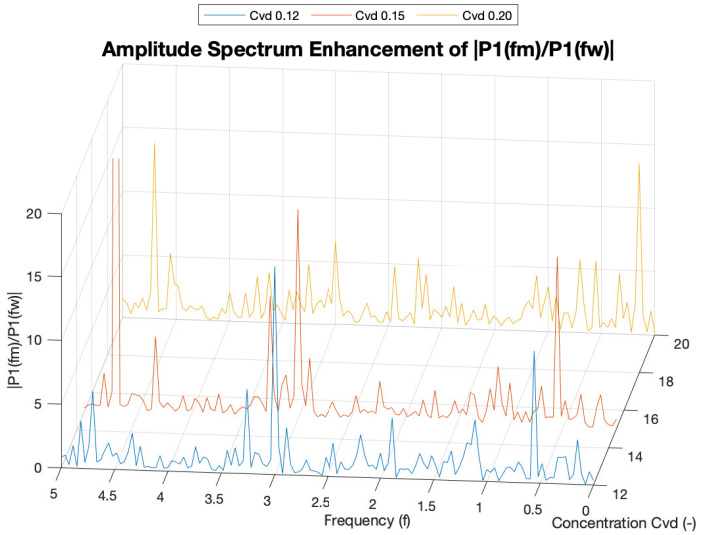

Figure 4.27: 3D plot of mixture FFT divided by water FFT from experiments at 1128 RPM with $C_{vd} = 0.12$, $C_{vd} = 0.15$ and $C_{vd} = 0.20$ and a particle size of 1.5 mm.

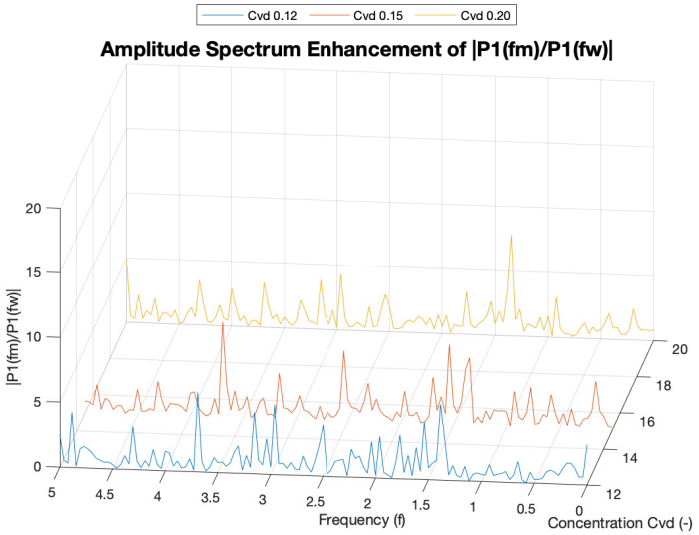

Figure 4.28: 3D plot of mixture FFT divided by water FFT from experiments at 1410 RPM with $C_{vd} = 0.12$, $C_{vd} = 0.15$ and $C_{vd} = 0.20$ and a particle size of 1.5 mm.

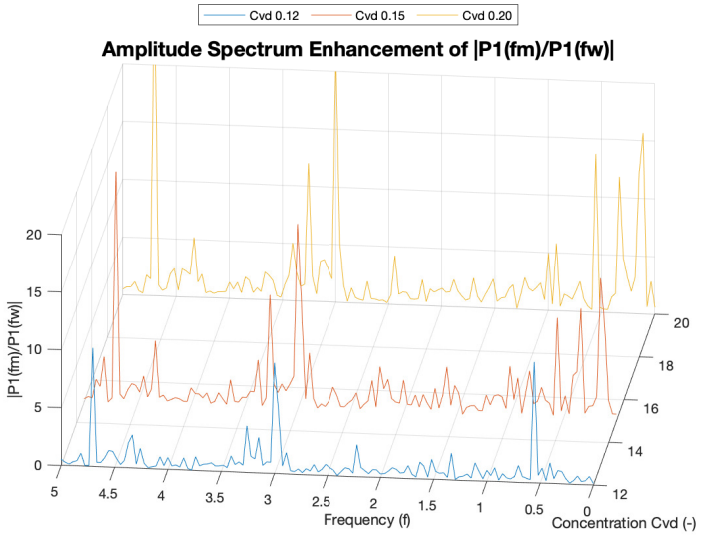

Figure 4.29: 3D plot of mixture FFT divided by water FFT from experiments at 1128 RPM with $C_{vd} = 0.12$, $C_{vd} = 0.15$ and $C_{vd} = 0.20$ and a particle size of 3.0 mm.

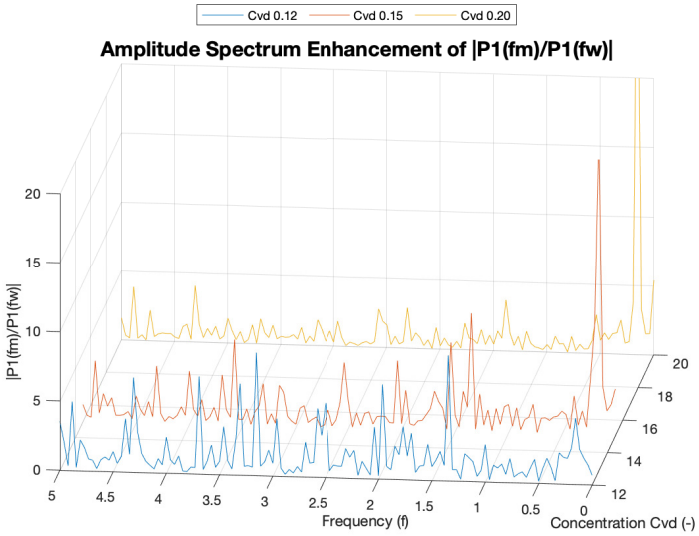

Figure 4.30: 3D plot of mixture FFT divided by water FFT from experiments at 1410 RPM with $C_{vd} = 0.12$, $C_{vd} = 0.15$ and $C_{vd} = 0.20$ and a particle size of 3.0 mm.

By dividing the mixture FFT with the water FFT analysis, the local energy enhancement in the spectra is made visible. Figure 4.27, 4.28, 4.29 and 4.30 are representing this act for the lower part of the spectra. In all these figures, at the lower side of the frequency spectra (0-2 Hz), a local increase in density of the spectra is present. From analysing these frequencies, it is discovered that these are the same as the concentration fluctuations frequency present in figure 4.21 and 4.22. At the 3.0 mm particles with an 1410 RPM and a C_{vd} of 20%, a high peak enhancement of ~ 0.3 Hz is present, see figure 4.30. This higher peak enhancement originates from the greater need of energy to overcome the pick up flux for more heavy particles. For the 1.5 mm particles with an 1410 RPM and a C_{vd} of 20%, a smaller enhancement of the spectral density is visible compared to 1128 RPM. This originates from the higher amount of energy available to overcome the pick up flux for these smaller particles. This reduction in spectral density enhancement is also directly visible in figure 4.21 at 1410 RPM. The concentration fluctuation is here more flattened. One may conclude that the impeller interaction with the particles, create a concentration fluctuation profile directly after the pump outlet. Thus, it should be noted that the experimental setup operates in a closed loop and these effect may be amplified at perfect conditions.

4.3.3. Particle streamlines and trajectories verification

For defining the absolute particle trajectories and their absolute streamlines along the impeller blades in mixture situations, PIVlab was used again. As of limitations in discussion space of this thesis, the same selection criteria applied towards PIVlab outcome image selection. This means only situation of 1128/1410 RPM at a C_{vd} = 0.20 with 1.5 mm and 3.0 mm particles are discussed.

Figure 4.32, 4.33, 4.42, and 4.43 are the outcomes for PIVlab analysis at above described situations. Again, one can concluded from analysing and comparing these images visually that due too the large amount of eddies and acute changes in flow direction, the flow is highly turbulent. The amount of eddies and acute changes are also significantly higher compared to the single phase water streamline situation from section 4.2.3.

All four PIVlab image outcomes have four local velocity plots as discussed and pre-described in section 3 and re-displayed in figure 4.7. The results of turbulent flow can again be easily distinguished with the peaks in figures 4.34, 4.38, 4.44, and 4.48. In comparison with the local velocity plot discussed in section 4.2.3, there is no significant reduction in amplitude size of the velocity fluctuation with an increase in engine speed. This means that no direct correlation, on the low frequency wave at the 0.44 ratio in Cao et al. (2019) and the 0.52 ratio value from experiments, can be given. With an increase in engines speed, at both particle sizes, no reduction in eddies and/or acute changes in flow direction are visible. An increase in eddies and/or acute changes in flow direction are actually noticeable at the absolute streamlines. Cao et al. (2019) suggested that the low frequency wave at the 0.44 ratio, found its origin in the transition from an unevenly distribution of eddies between the blades, to an more evenly distribution at higher speeds. The result from the analysed experiments in mixture contradict this statement of Cao et al. (2019) and is thus in conflict.

As the four PIVlab image outcomes are in conflict with the relative streamlines given by Cao et al. (2019) in figure 4.31. These results can not be used as a direct verification for the streamline pattern outcomes of the CFD model. However, this does not imply that the PIVlab image outcome are wrong and may be used as a steady base for further research.

The conflicting outcomes of the PIVlab analysis may also found its origin in other aspects. These aspects may be, PIVlab iteration limitations, impeller kind, high speed camera limitations and distinguish-ability of the (transparent) glass particles. For PIVlab, the limitation may originates from a minimum amount of particles needed/present per iteration for a reliable trajectory and velocity estimation. The impeller used in experiments is slightly different of to the CFD model one. It has a shorter blade length, so the eddies, on either pressure or suction side, interfere each other less. The high speed camera has a limitation in FPS and shutter speed, especially at higher RPM. At these higher RPM's, the maximum available FPS is not sufficient enough to record a "slow motion video". The shutter speed limits the exposure time for light collection, this reduces the image quality with respect to particle distinguishing and creates blurry images since the image "moves" during exposure. The glass particles used, have a certain transparency that also effects their detect-ability on images. Although, detect-ability is also a result of high speed camera limitations in FPS and shutter speed.

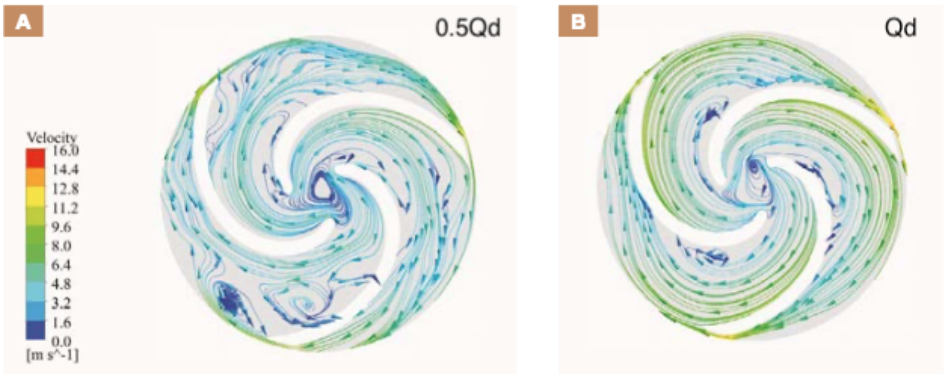

Figure 4.31: Instantaneous relative streamlines between impeller blades with a counterclockwise rotation at mixture flow, obtained from Cao et al. (2019).

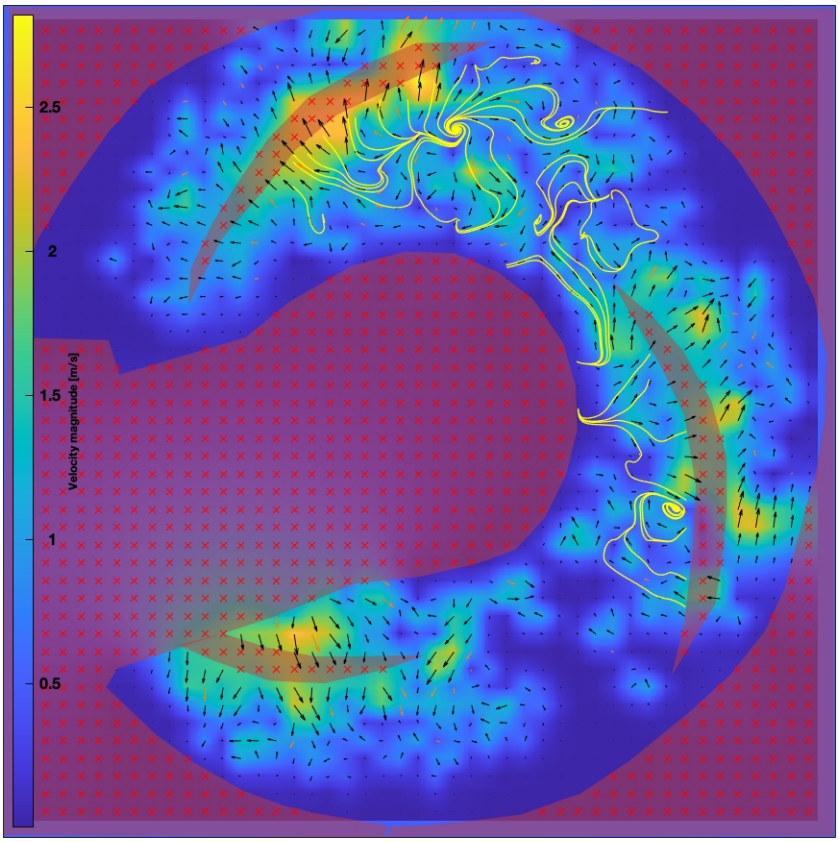

Figure 4.32: PIVlab image analysing in mixture conditions at 1128 RPM experiments with a C_{vd} = 0.20, 1.5 mm glass beads, a counterclockwise rotating impeller and absolute streamlines.

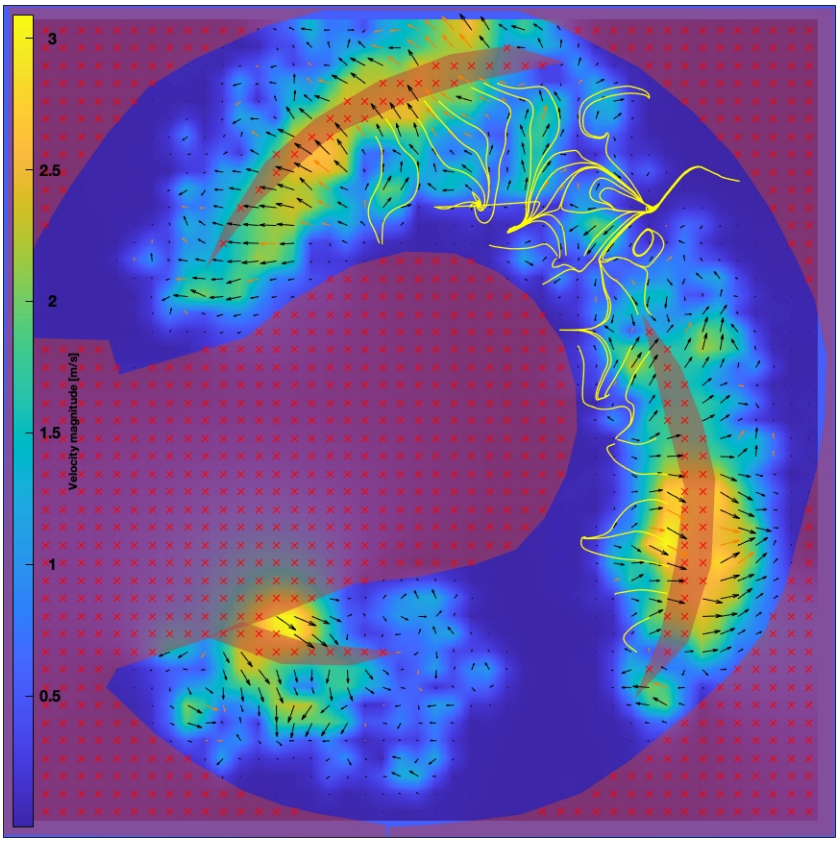

Figure 4.33: PIVlab image analysing in mixture conditions at 1410 RPM experiments with a C_{vd} = 0.20, 1.5 mm glass beads, a counterclockwise rotating impeller and absolute streamlines.

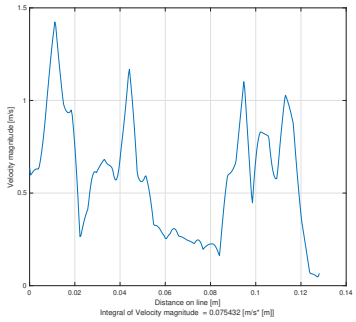

Figure 4.34: Local Velocity line plot of the eddy in longitudinal direction, corresponding to figure 4.32.

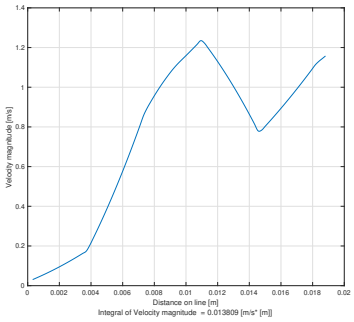

Figure 4.35: Local Velocity line plot of the eddy in transverse direction, corresponding to figure 4.32.

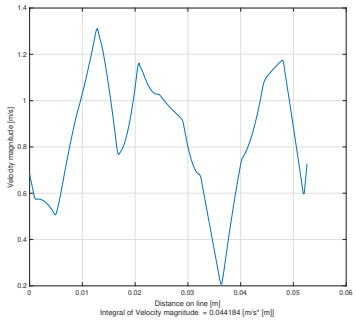

Figure 4.36: Local Velocity line plot between the leading front and tail of two impellers, corresponding to figure 4.32.

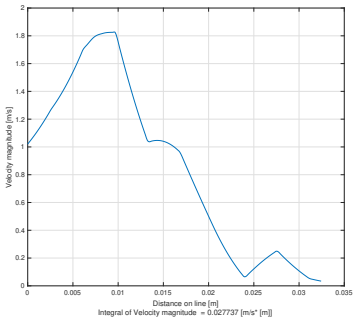

Figure 4.37: Local Velocity line plot perpendicular on the leading front of the impeller, corresponding to figure 4.32.

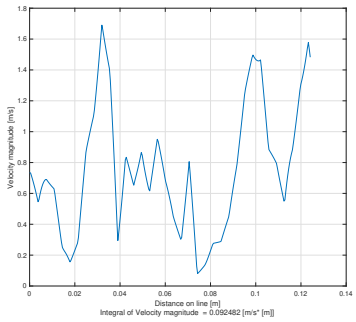

Figure 4.38: Local Velocity line plot of the eddy in longitudinal direction, corresponding to figure 4.33.

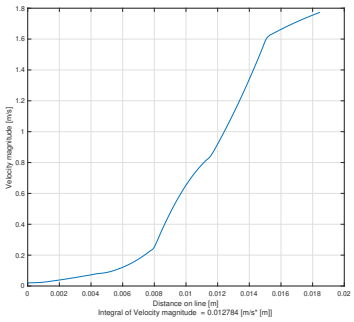

Figure 4.39: Local Velocity line plot of the eddy in transverse direction, corresponding to figure 4.33.

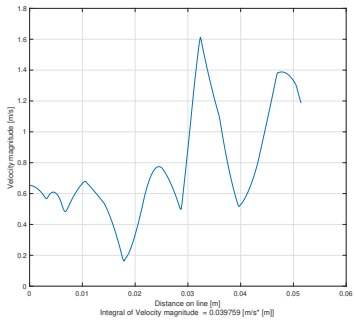

Figure 4.40: Local Velocity line plot between the leading front and tail of two impellers, corresponding to figure 4.33.

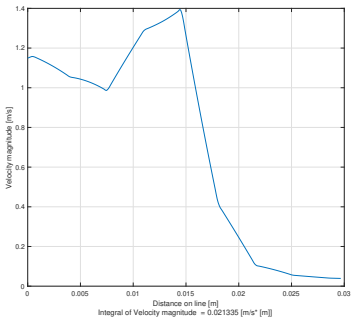

Figure 4.41: Local Velocity line plot perpendicular on the leading front of the impeller, corresponding to figure 4.33.

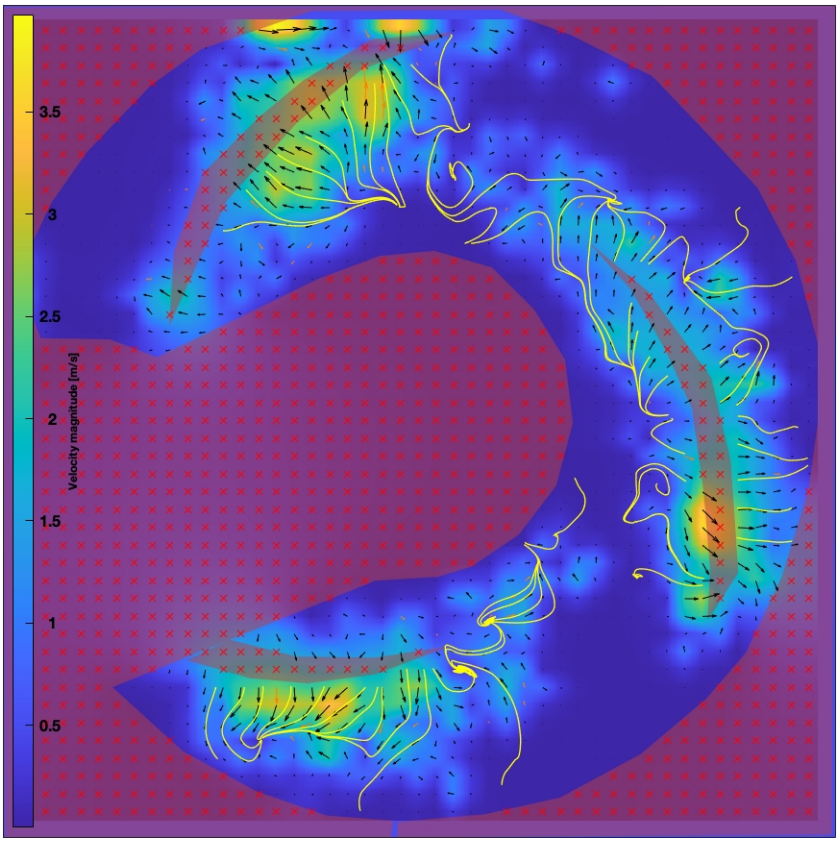

Figure 4.42: PIVlab image analysing in mixture conditions at 1128 RPM experiments with a C_{vd} = 0.20, 3.0 mm glass beads, a counterclockwise rotating impeller and absolute streamlines.

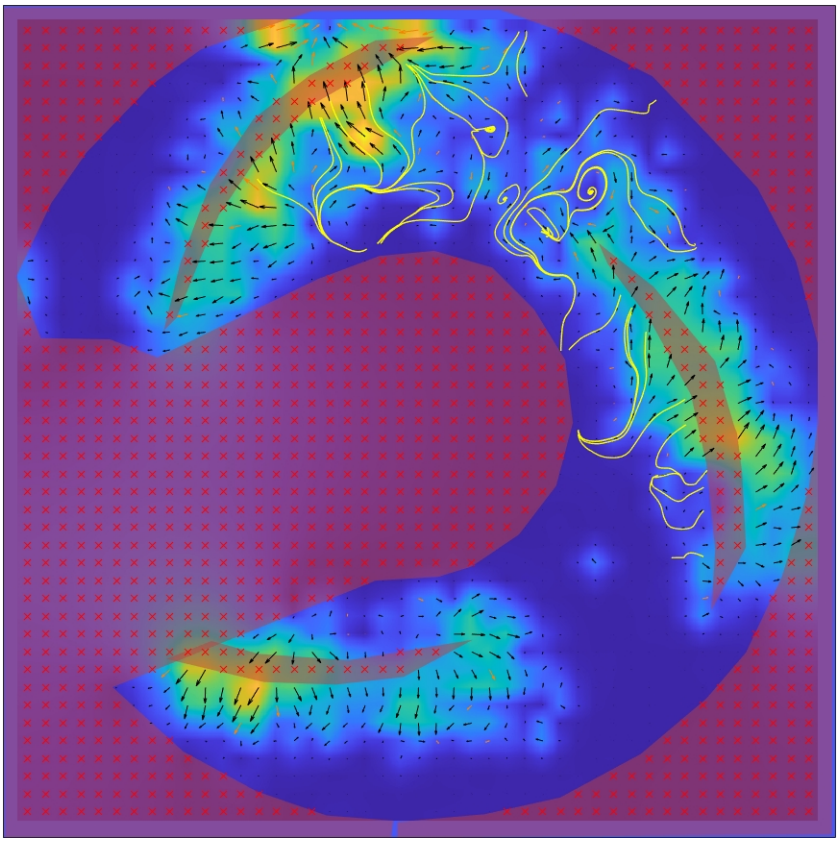

Figure 4.43: PIVlab image analysing in mixture conditions at 1410 RPM experiments with a C_{vd} = 0.20, 3.0 mm glass beads, a counterclockwise rotating impeller and absolute streamlines.

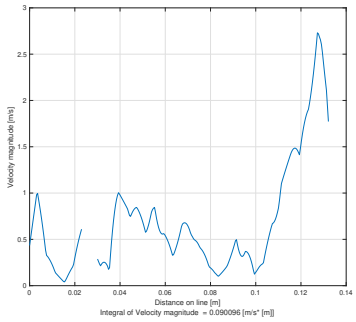

Figure 4.44: Local Velocity line plot of the eddy in longitudinal direction, corresponding to figure 4.42.

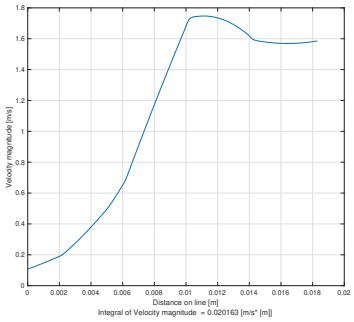

Figure 4.45: Local Velocity line plot of the eddy in transverse direction, corresponding to figure 4.42.

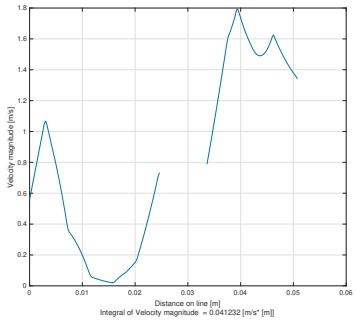

Figure 4.46: Local Velocity line plot between the leading front and tail of two impellers, corresponding to figure 4.42.

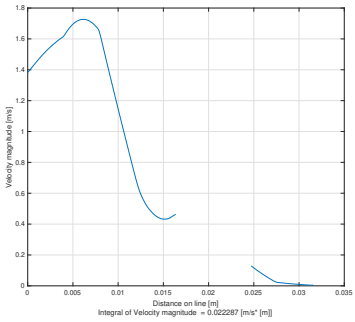

Figure 4.47: Local Velocity line plot perpendicular on the leading front of the impeller, corresponding to figure 4.42.

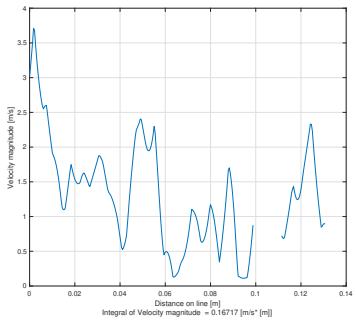

Figure 4.48: Local Velocity line plot of the eddy in longitudinal direction, corresponding to figure 4.43.

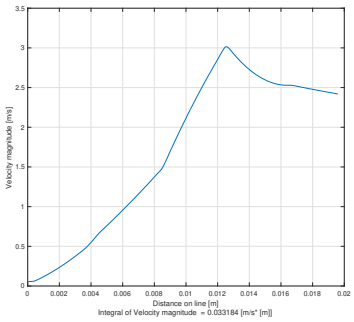

Figure 4.49: Local Velocity line plot of the eddy in transverse direction, corresponding to figure 4.43.

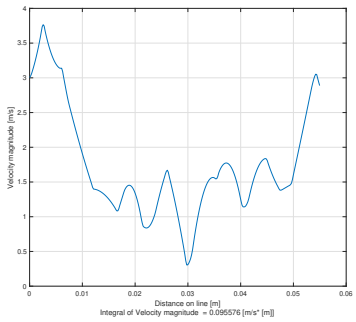

Figure 4.50: Local Velocity line plot between the leading front and tail of two impellers, corresponding to figure 4.43.

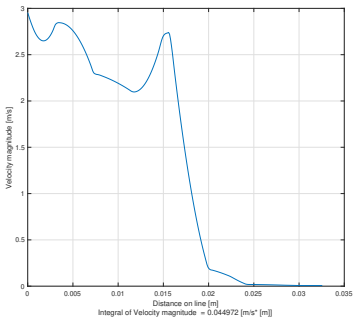

Figure 4.51: Local Velocity line plot perpendicular on the leading front of the impeller, corresponding to figure 4.43.

4.3.4. Concentration distribution between the blades

Sadly, PIVlab is not able to determine a certain concentration profile in any manner like Cao et al. (2019) supplied figure 4.52. As concluded in section 4.3.2, the impeller interaction with the tongue is also affected by the concentration profile fluctuation as visually seen in figure 4.21 and 4.22. As of these reasoning, a small visual inspection on four images obtained from the high speed recordings is conducted. In this visual inspection, the two concentration distributions of Cao et al. (2019) are compared with the experimental images at 1128/1410 RPM with a $C_{vd} = 0.20$ at 1.5 mm and 3.0 mm glass beads.

Figure 4.53 and 4.55 are both "equal" situations in 1128 RPM to $0.5Q_d$. The concentration distribution as displayed in figure 4.52[A] should be visible here. However, in the RAW image of figure 4.53, no such distribution profile can be visually determined. At the suction and pressure side of the blades, an equal concentration distribution of particles can be distinguished only. From the RAW image in figure 4.54, the same equal distribution applies, except a small concentration distribution increase at the suction side of the blade, see the red marker.

For both situations at 1410 RPM, figure 4.54 and 4.56, no large concentration distribution can be determined, either at the suction or pressure side of the blade. Although, a small concentration reduction is visible at the pressure side of the blade, near the tip, see red markers in figure 4.54 and 4.56. The small concentration drop and an equal concentration distribution along the rest of the impeller does line up with figure 4.52[B] of Cao et al. (2019).

Again, it should be noted that the image are a 2D representation of the particles visible at the PMMA window and is thus not able to distinguish particles in Z-direction or identifies more layers of particles inline. A direct consequence is that lined up particles are not detectable and effects the visibility and accuracy of the concentration distribution.

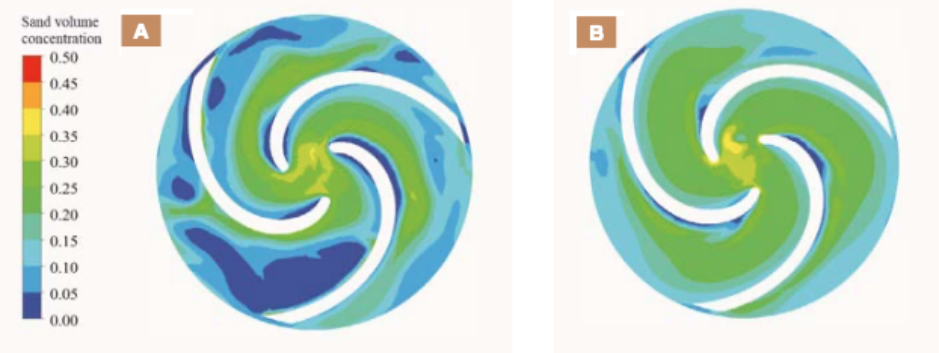

Figure 4.52: Instantaneous concentration distribution in the impeller with mixture flow at a counterclockwise rotation, obtained from Cao et al. (2019)

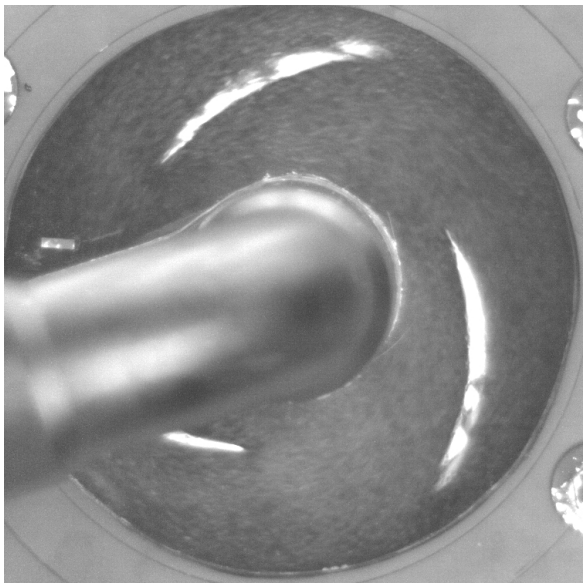

Figure 4.53: RAW image for high speed video recordings at 1128 RPM, at concentration of 20%, 1.5mm glass beads and a counterclockwise rotation.

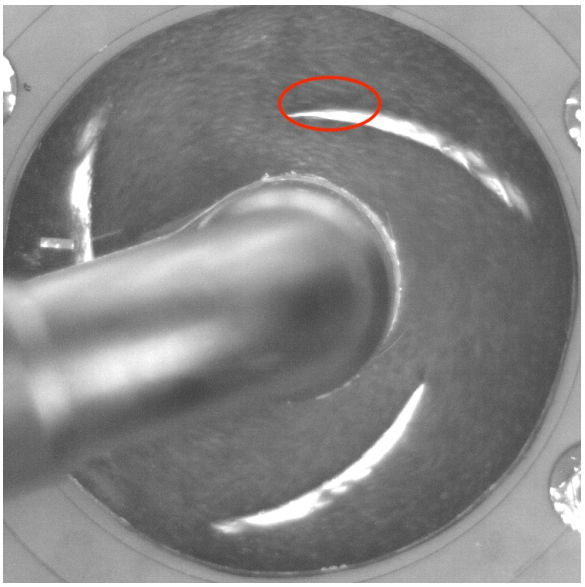

Figure 4.54: RAW image for high speed video recordings at 1410 RPM, at concentration of 20%, 1.5mm glass beads and a counterclockwise rotation.

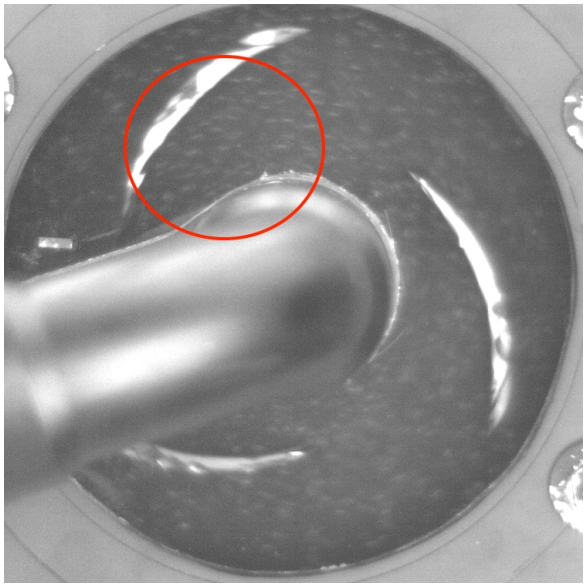

Figure 4.55: RAW image for high speed video recordings at 1128 RPM, at concentration of 20%, 3.0mm glass beads and a counterclockwise rotation.

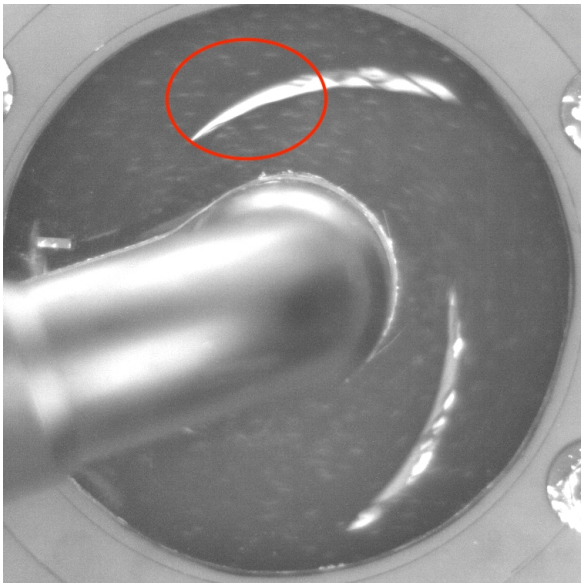

Figure 4.56: RAW image for high speed video recordings at 1410 RPM, at concentration of 20%, 3.0mm glass beads and a counterclockwise rotation.

4.4. Conclusion on experimental analysis

In the sections above, a wide range of notes and conclusions are made from the analysed data compared towards the CFD model outcomes of Cao et al. (2019). This section is dedicated to refer these analysis and outcomes back to the sub questions stated in section 1.2. Every sub question is discussed individually and answered specifically towards the question asked. In section 5, the overall answer on the main question is given.

- *"Does a single phase flow experiment in the dredge pump gives the same streamline patterns as the CFD simulation and delivers the expected pump characteristics?"*

In the experiments regarding single phase flow verification and water pump characteristic, it was concluded that the absolute streamline patterns created in PIVlab are only partly similar with the CFD model outcomes. Although, the range in velocity magnitude (either absolute or relative) are of the same size (0-4.8 m/s). Another similarity is the reduction in visible eddies with an increase of discharge/engine speed that is also visible in the CFD model. Most likely due to the use of a different impeller shape, the streamlines obtained from PIVlab are not matching with the CFD model. Although, the experimental water phase outcomes can be used partly for further verification of the model. As for a full verification a wider set of experiments and studies is needed.

For the single phase pump characteristic, great similarities are found in comparison with the literature research expectations. The pump characteristic shows a BEP in the efficiency curve at a certain discharge and head. But also show a reduction of head with an increase in discharge. This means that the experimental setup shows the same behaviour as a normal centrifugal pump in water conditions with an increase of discharge as found in the literature research.

- *"Does a mixture flow experiment, at different speeds, flow rates and concentration, shows the same particle behavior as the CFD model and delivers the expected pump characteristics?"*

In the previous section, the particle behavior at 1182 and 1410 RPM only have been extensively examed with 1.5 mm and 3.0 mm particles. From these analyses, it can be concluded that the absolute streamlines of the experiment have some visual overlap with the relative streamlines from the CFD model. Further, the obtained data can not be used to directly verify the CFD model outcomes but can be used in further research as a supplement.

For the expected pump characteristics, it can be concluded that these are inline with the expectations gained from literature research. A greater reduction in head with an increase of discharge is noted compared to water situations. This reduction in head is of even greater magnitude in higher concentrations. This concludes that the experimental setup functions also as a centrifugal dredge pump at mixture conditions. As the same effect in head reduction are noted which where expected from the literature research.

- *"Does the experiments show unsteady characteristics of head? If so, when does this happen and which factor(s) mainly cause these?"*

In the experiments conducted, in either single phase water conditions or mixture conditions with multiple concentrations, all experiments show an unsteady head characteristic. For water conditions, this phenomena actually becomes less significant at the higher part of the spectra with a RPM increase. For mixture conditions, with an increase in concentration and a RPM increasement from 1182 RPM to 1410 RPM, a similar shift is noticeable. Only this shift, for mixture conditions, is of greater magnitude in the lower side of the spectra, especially at 0-2 Hz. The increase of spectral density, is most likely the cause of a combination of the 0.52 low frequency peak ratio, figure 4.5 and the concentration fluctuation, figure 4.21 and 4.22.

- *"Does the mixture flow experiment show different areas in the pump where the distribution of concentration significantly deviates?"*

From visual inspection at 1128 and 1410 RPM with 1.5 mm and 3.0 mm particles, no specific areas can be clearly pointed out as a deviating distribution of concentration. Although, at higher speeds of 1410 RPM with 3.0 mm particles, concentration differences at the suction and pressure side of the blade are somewhat visible. These are, to some extend, similar as the expectations obtained from the CFD model at Q_d. Conclusively,

can be said that the visual comparison does not give further details/explanation/verification on the imposed origin by Cao et al. (2019) for the low frequency wave at the 0.44 peak frequency ratio. Cao et al. (2019) imposed as origin that the unevenly distribution is a result of growth in eddy size. These eddies block new particles from entering the channel between the blades and create so this unevenly distribution.

5
Conclusions

This chapter contains the conclusion on the conducted research. The conclusion is separated over three sections that consist out of, literature observations, experimental outcomes and the answer to the main research question.

5.1. Conclusion

The goal of this research is to gather a set of knowledge by conducting a literature research and experiments to clarify the particle trajectories between impeller blades. In short, it can be said that this goal has been reached by comparing the CFD model from Cao et al. (2019) with the experimental analysis. The data needed for this experimental analysis was conducted by performing multiple experiment in a custom designed and manufactured flow loop.

This custom flow loop consist out of a horizontally placed converted dirty water (sewer) pump with multiple sensors implemented. These sensor are multiple absolute (0-10 bar) and differential ($\triangle$ 7 kPa) pressure transmitters for head/NPSH and concentration determinations. A flow meter (max. 250 l/m) and temperature sensor (-50/100 °C) are included for discharge capacity measurements and recording of temperature with respect to viscosity change. Further, the flat side of the pump has been converted to a transparent plate. The transparency is needed to make the internal impeller visual during operation for high speed image recordings.

The executed experiments consist out of head and discharge recording by throttling the exit valve for pump characteristics in single phase water conditions and mixture conditions at 564, 846, 1128 and 1410 RPM. The impeller used has a diameter of 155 mm and is a so called "open impeller". At mixture conditions, delivered volumetric concentration (C_{vd}) of 5%, 8%, 12%, 15% and 20% are reached. High speed image recording are made of the impeller blades at above mentioned situations but with a steady exit valve that is set to 50%. These image are used for PIV image analysis with a program called PIVlab for streamline and particle trajectories determination.

5.1.1. Literature review

In conclusion of the literature research regarding particle trajectories near impeller blades in a centrifugal dredge pump, the following observations are made regarding the existing (CFD) models and the unsteady head characteristics expectations;

- Existing empirical models that predicts, head, discharge and power values of a centrifugal pump in mixture conditions are applicable to some extend. Their applicability strongly depends on the input parameters as C_{vd}, particle size d_{50}, relative density of the solids, impeller diameter and content of fines.
- CFD models exist to improve existing empirical models for a wider range of data. However, these CFD models are not validated and may thus not be used independently. These should be used as an extension on the current models as an extra "tool set".

- For pump characteristics in mixture conditions, it is expected to see a higher decline rate in head with an increase of discharge, likewise with an increase in concentration vs. water conditions.
- At streamline verification of higher concentrations around 20%, it is expected to see a reduction in particle distinguishing from high speed images. The reduction of particle distinguishing results in less reliable and accurate trajectory estimations.
- The unsteady head is present in every experiment, as it is a result of blade tongue interaction. In mixture situation, the unsteady head, is expected to be enhanced as particles start to increase the presents of eddies that disturb the through flow between the impeller.

5.1.2. Experimental outcomes

From experiments conducted in different mixture conditions and speeds, the following observations/conclusion can be made;

- In either a validation of the pump characteristics in water or mixture conditions. The reduction of head with an increase of discharged showed the behaviours as expected from the literature research.
- The unsteady head characteristics is present at all conditions and their peak frequencies are not affected by an increase in concentration. Although, with an increase in concentration, the amount of noise around the head peak amplitude increase significantly. With an increase of engine speed, the higher spectral noises move towards the lower side of the spectra and increases its local density. This results in a more stable unsteady head wave as seen at water conditions.
- In the CFD model and the FFT analysis from experiments, a low frequency wave is detectable at a relative frequency ratio of 0.44 in CFD and 0.52 at experiments. Most probably, this originates from the transition from unevenly distributed eddies between the blades, to an more evenly distribution.
- With an increase in engine speed, at mixture loading conditions, a concentration fluctuation is noticeable. These fluctuations, most likely, finds their origin in the unevenly distribution of concentration between the blades. This unevenly distribution is a result of growth in eddy size that blocks new particles from entering the channel between the blades.

5.1.3. Main research question

In this thesis, the main objective is to gather a set of knowledge and information that is sufficient enough to answer the main question;

- **"Can an experimental study on particle trajectories near impeller blades of a (transparent) centrifugal dredge pump, verify the CFD model of Cao et al. (2019) and explain the unsteady head characteristics while loading a high-concentration sand water mixture?"**

Conclusively, on the main question a full comprehensive answer can not be given. Although, an experimental study on particle trajectories near impeller blades of a centrifugal dredge pump gives an interesting inside on the behaviour of particles internally. On the particle trajectory side, where PIVlab image analysis are conducted, the results can be used partially on the streamline verification from the CFD model of Cao et al. (2019). This especially applies for the single phase situations and partially less for the mixture situation due to problems with particle distinguishing. To sum up, this means that the conducted experimental study is not sufficient enough to verify the CFD model outcomes of Cao et al. (2019) for the instantaneous streamlines and concentration distribution between the impeller blades. Though, it supplies a steady base for further research.

For the unsteady head characteristics that are enhanced during mixture loading at high-concentrations on the other hand, interesting data is collected. The unsteady head characteristics shows an enhancement in noise at the lower side of the spectra with an increase of concentration and engine speed. At low engine speed, the unsteady head amplitude has a wider spread that results in a lot of short quick amplitude changes. For an increase in speed, these quick amplitude changes are reduced and become more stable. The conditions are similar as in single phase water conditions due to a shift towards the lower side of the spectra. For engine speeds at 1128 RPM, at the relative frequency ratio of 0.52, a low frequency wave is noted that is, most likely, originating from a transition between an unevenly distribution of flow between the blades to an even distribution at higher speeds. This unevenly distribution in combination with the shift of unsteady head amplitude to the lower side of the spectra is expected to be the origin of the concentration fluctuation after the pump exit. Though, this last expectation needs further research and is not confirmed.

6

Recommendations

As with every conducted research, none is fully completed and perfect. During this research, multiple aspects are noted that need attention if a follow-up research is desired. These aspects are distinguished in the following three headers, the overall research recommendations, experimental setup and PIVlab.

Overall research recommendations
In the previous section, the main-question and side-questions have been answered as much as possible. However, some answers could be further explained with a follow-up research. These follow-up research could consist out of;

- Redoing the particle experiments with a wider range of particles sizes and a particle size distribution.
- Increase the particle visibility, for instance by changing the glass beads colour, for particle distinguishing enhancement in PIVlab.
- Build a transparent impeller and implement a light sheet for layer distinguishing of particles between impeller blades.
- Redo the current executed experiments but focus on the fluctuation in concentration (density wave) and the low frequency wave at 1128 RPM.

Experimental setup
For the experimental setup, multiple aspects should be changed if a further research is conducted. As for the mechanical side of the setup, the following recommendations are noted;

- Replace the oil seal between the pump shell and drive shaft. As the current oil seal leaks.
- Replace the current impeller for a new one that does not has a blade length reduction of 20%. This increases the efficiency and most-likely increases the visibility of the unsteady head.
- Powder coat the current impeller in either bright yellow or pink to increase the particle distinguishing in the high speed recordings.
- Replace the PMMA window with a custom CNC part for a wider research area in PIVlab. Also, the current PMMA window reached end of life.
- Replace the head valve after the pump outlet. Due to corrosion, the ball valve does not fully closes the flow loop.
- Add an extra pipe strap after the temperature sensor to reduce local pipe vibrations.

For the implemented sensors and external equipment, the following recommendations are noted;

- Replacement or plugging of the temperature sensor, as a small leak is present.
- Move the horizontal flow meter into a vertical direction under the U-loop to enhance its accuracy at higher concentrations and low velocities.
- Extend the U-loop to twice it length to make space for the above stated move of the flow meter.
- Extend the implemented Arduino Uno with a "stack on board" for internal SD data storage capacity. This to eliminated the software limitations of Matlab (student version).

- Replace the current high speed camera with a unit that is capable of make recording at higher FPS and lower shutter time. As in the current situation of 1410 RPM, the particles started to be displayed as lines instead of dots.

Matlab and PIVlab limitations
Besides recommendations for further research and an improvement on the current experimental setup. The following recommendations on data processing and analysing with Matlab and PIVlab are noted;

- Write a small .bat/.sh script to progress/save the serial sensor data, originating from the Arduino, on a PC automatically. As the internal serial logger of Matlab has a clock speed limitation for processing incoming frequencies that results in a runaway of data string.

Abbreviations and Nomenclature

The next list describes the symbols that are included within the body of this document.

Abbreviations

BEP	Best Efficiency Point
CFD	Computational Fluid Dynamics
FFT	Fast Fourier Transform
IADC	International Association of Dredging Companies
NERC	CCCC National Engineering Research Center of Dredging Technology and Equipment Co., Ltd
NPSH	Net Positive Suction Head
PIV	Particle Image Velocimetry
RPM	Rounds per minute
TDH	Total Dynamic Head
TU Delft	Technical University of Delft

Nomenclatures

α_1	Vane angle inlet	$[deg]$
α_1'	True particle angle inlet	$[deg]$
α_2	Vane angle outlet	$[deg]$
α_2'	True particle angle outlet	$[deg]$
β_1	Vane angle inlet	$[deg]$
β_1'	True particle angle inlet	$[deg]$
β_2	Vane angle inlet	$[deg]$
β_2'	True particle angle inlet	$[deg]$
δ	Boundary layer thickness	$[m]$
η	Efficiency	$[-]$
η_m	Efficiency value from mixture situation	$[-]$
η_r	Efficiency reduction ratio from mixture vs. water	$[-]$
η_w	Efficiency value from water situation	$[-]$
μ	Slip factor	$[-]$
ω, n	Angular velocity	$[rad/s]$
ω_1	Relative velocity	$[m/s]$
Φ	Dimensionless discharge	$[-]$

Π	Dimensionless power	$[-]$
Ψ	Dimensionless head	$[-]$
ρ_f	Fluid density	$[kg/m^3]$
ρ_w	Water density	$[kg/m^3]$
$\triangle C_{u2}$	Slip velocity	$[m/s]$
b	Impeller blade height	$[m]$
c	Absolute velocity	$[m/s]$
c_1	Absolute velocity inlet	$[m/s]$
c_2	Absolute velocity outlet	$[m/s]$
c_u	Absolute velocity of the peripheral velocity	$[m/s]$
C_1	Coefficient correction value from Euler's pump equation	$[-]$
C_2	Coefficient correction value from Euler's pump equation	$[-]$
c_{r_1}	Absolute velocity at inlet radius	$[m/s]$
c_{r_2}	Absolute velocity at outlet radius	$[m/s]$
$c_{u_2\infty}$	Tangential velocity component	$[m/s]$
D	Impeller diameter of the to be defined pump	$[m]$
d	Channel width between the vanes	$[m]$
D_p	Diameter of outlet pipe	$[m]$
D_0	Impeller diameter reference parameter set	$[m]$
d_{50}	Average particle size in a sand sample	$[\mu m]$
f_c	Efficiency reduction ratio by Stepanoff (1948)	$[-]$
g	Gravitational acceleration	$[m/s^2]$
H_B	Head based on the Bernoulli equation	$[m]$
h_p	Height difference from center level to pressure side	$[m]$
h_s	Height difference from center level to suction side	$[m]$
H_{BEP}	Best efficiency point with corresponding head	$[m]$
H_E	Euler's pump equation to define head	$[m]$
$H_{friction}$	Friction losses pump and impeller combined	$[m]$
H_{mano}	Theoretical manometric pressure head	$[m]$
H_m	Head value from mixture situation	$[m]$
H_r	Head reduction ratio from mixture over water	$[-]$
H_{shock}	Shock losses pump and impeller combined	$[m]$
H_{th}	Theoretical delivered pump head	$[m]$
h_v	Vapour pressure head of the liquid at the inlet side	$[m]$

H_w	Head value from water situation	$[m]$
K	Scaling factor related to a relative density of solids by McElvain (1974)	$[-]$
m	Mass of particles	$[kg]$
N	Round per minute of engine	$[RPM]$
N_s	Customary specific speed	$[-]$
n_s	Specific speed	$[-]$
p_p	Pressure at pressure side	$[N/m^2]$
p_s	Pressure at suction side	$[N/m^2]$
P_f	Resulting power requirement for the pump at an equal water flow situation	$[kW]$
P_{in}	Engine shaft power input	$[kW]$
$P_{m,Step}$	Power value from mixture situation based on Stepanoff (1948)	$[kW]$
P_m	Power value from mixture situation	$[kW]$
p_m	Pressure output from pump at a mixture situation	$[N/m^2]$
P_{out}	Power output from pump	$[kW]$
P_r	Power reduction ratio from mixture over water	$[-]$
P_w	Power value from water situation	$[kW]$
p_w	Pressure output from pump at a water situation	$[N/m^2]$
Q	Discharge capacity	$[m^3/s]$
Q_{BEP}	Best efficiency point with corresponding discharge	$[m^3/s]$
Q_d	Designed discharge capacity	$[m^3/s]$
Q_s	Discharge reduction due to shock losses	$[m^3/s]$
r	Impeller radius	$[m]$
r_1	Impeller radius inlet	$[m]$
r_2	Impeller radius outlet	$[m]$
$R_{\eta Mc}$	Fractional efficiency reduction ratio based on McElvain (1974)	$[-]$
R_η	Fractional efficiency reduction ratio	$[-]$
R_{H_0}	Fractional head reduction ratio based on H_0	$[-]$
$R_{H_{Cvd}}$	Fractional head reduction ratio based on Wilson et al. (2006)	$[-]$
R_{HMc}	Fractional head reduction ratio based on McElvain (1974)	$[-]$
R_H	Fractional head reduction ratio	$[-]$
R_P	Fractional power reduction ratio	$[-]$
Re_x	Reynolds number based on location x	$[-]$
S_f	Relative density of the mixture fluid with the same viscosity as water	$[-]$
S_{md}	Relative density of the mixture	$[-]$

S_s	Relative density of the solids	$[-]$
T	Torque at engine shaft	$[N \cdot m]$
U	99% of the fully developed flow speed	$[m/s]$
u	Rotational velocity	$[m/s]$
u_1	Rotational velocity inlet	$[m/s]$
u_2	Rotational velocity outlet	$[m/s]$
u_b	Velocity of the fluid in either laminar or turbulent situations	$[m/s]$
v	Fluid viscosity	$[m^2/s]$
v_p	Fluid velocity pressure side	$[m/s]$
v_s	Fluid velocity suction side	$[m/s]$
X_h	Fractional content of fine particles in a concentration load	$[-]$
z	Number of vanes with thickness zero	$[m]$
x	Location alongside immersed plate	$[m]$
y	Height of the boundary layer	$[m]$

List of Figures

List of Tables

Bibliography

Baocheng, S., Wei, J., & Zhang, Y. (2015). Phase discrimination and a high accuracy algorithm for piv image processing of particle-fluid two-phase flow inside high-speed rotating centrifugal slurry pump. *Flow Measurement and Instrumentation*, *45*. doi:10.1016/j.flowmeasinst.2015.05.002

van den Berg, C. H., Vercruijsse, P. M., & van den Broek, M. (1999). The hydraulic transport of highly concentrated sand-water mixtures using large pumps and pipeline diameters. *Proc. 14th Int. Conference on the Hydraulic Transport of Solids in Pipes*.

van den Berg, C. H. (2013). *Ihc merwede handbook for centrifugal pumps and slurry transportation*. MTI Holland BV.

Cao, L., Zhemg-wei, W., & Lin-zhu, Z. (2019). Numerical investigation of the head and unsteady flow characteristics of a dredge pump loading high-concentration sands. *Terra et Aqua*, (155), 6–14.

Cooper, P., Karassik, I. J., Messina, J. P., & Heald, C. C. (2001). *Centrifugal pump theory, section 2.1 of pump handbook*. McGraw-Hill.

Dixon, S. L. (1998). *Fluid mechanics, thermodynamics of turbomachinery*. Pergamon Press LTD 1966.

Engine, & Gur. (2003). Comparative evaluation of some existing correlations to predict head degradation of centrifugal slurry pumps. *ASME J. of Fluids Eng.* (125), 149–157.

Gandhi, B. K., Singh, S. N., & Seshadri, V. (1998). Applicability of affinity laws to centrifugal slurry pumps. *Proc. 3rd National Conf. on Fluid Machinery*, 77–83.

Gandhi, B. K., Singh, S. N., & Seshadri, V. (2002). Effect of speed on the performance characteristics of a centrifugal slurry pump. *Journal of Hydraulic Engineering*, *128*(2), 225–233. doi:10 . 1061 / (ASCE) 0733 - 9429(2002)128:2(225)

Hofstra, F., Miedema, S., & van Rhee, C. (2010). Particle trajectories near impeller blades in centrifugal dredge pumps.

Hofstra, F., Miedema, S., van Rhee, C., & Talmon, A. M. (2008). On the particle trajectories in dredge pump impellers.

Holzenberger, K. (1980). Betriebsverhalten von kreiselpumpen beim hydraulischen feststofftransport. *VDI-Berichte*, (371), 59–66.

Kadambi, J. R., Charoenngam, P., Subramanian, A., Wernet, M. P., Sankovic, J. M., Addie, G., & Courtwright, R. (2004). Investigations of particle velocities in a slurry pump using PIV: Part 1, the tongue and adjacent channel flow. *Journal of Energy Resources Technology*, *126*(4), 271–278. doi:10.1115/1.1786928

Matoušek, V. (2004). *Dredge pumps and slurry transport*. TU Delft.

McElvain, R. E. (1974). High pressure pumping. *Skilling Mining Review*, (63-4), 1–14.

Miedema, S. (2019). *Dredging engineering special topic*. doi:http://doi.org/10.5074/t.2019.004

Miedema, S., & Ramsdell, R. C. (2019). *Fundamentals, a historical overview & the delft head loss & limit deposit velocity framework*. Slurry Transport. doi:http://doi.org/10.5074/t.2019.002

Ni, F., Vlasblom, W. J., & Zwartbol, A. (1999). Effect of high solids concentration on characteristics of a slurry pump. *Proc. 14th Int. Conference on the Hydraulic Transport of Solids in Pipes*.

van Rhee, C. (2009). *Centrifugal pumps*. TU Delft.

Sellgren, A., & Addie, G. R. (1989). Effects of solids on large centrifugal pump head and efficiency. *Proc. The CEDA Dredging Day*.

Sellgren, A., & Addie, G. R. (1993). Solids effects on the characteristics of centrifugal slurry pumps. *Proc. 12th Int. Conference on the Hydraulic Transport of Solids in Pipes*.

Sellgren, A., & Vappling, L. (1986). Effect of highly concentrated slurries on the performance of centrifugal pumps. *Proc. International Symposium on Slurry Flows*, (38), 143–148.

Stepanoff, A. J. (1948). *Centrifugal and axial flow pumps*. John Wiley & Sons Inc.

Stodola, A. (1945). *Steam and gas turbines*.

Thielicke, W., & Stamhuis, E. J. (2014). PIVlab – towards user-friendly, affordable and accurate digital particle image velocimetry in MATLAB. *Journal of Open Research Software*, *2*. doi:10.5334/jors.bl

Vercruijsse, P. M., & Corveleyn, F. (2002). The solids effect on pump and pipeline characteristics- keeping up with present trends in the dredging industry. *Proc. 15th Int. Conference on the Hydraulic Transport of Solids in Pipes*, 711–723.

Vlasblom, W. J. (2004). *Dredge pumps*. TU Delft.

White, F. M. (1986). *Fluid mechanics*. McGraw Hill.

Wilson, K. C., Addie, G. R., Sellgren, A., & Clift, R. (2006). *Slurry transport using centrifugal pumps*. Springer.

Worster, R. C. (1968). *The flow in volutes and its effect on centrifugal pump performance*. BHRA Hydraulic Plant and Machinery Group.

Wu, B., Wang, X., Liu, H., & Xu, H. (2015). Numerical simulation and analysis of solid-liquid two-phase three-dimensional unsteady flow in centrifugal slurry pump. *Journal of Central South University, 22*(8), 3008–3016. doi:10.1007/s11771-015-2837-7

A

Experimental pump characteristics

In this appendix, a collection of the created pump characteristics can be found. These characteristics are obtained from the conducted experiments with different particle sizes and their corresponding concentrations. The first section includes the basic single phase (water) characteristic at different speeds. Followed by multiple mixture characteristics with different concentrations, particle sizes and engine speed.

A.1. Single phase (water) characteristics

In the figure below, 4 plots are displayed that are all referring to the same input data. The top left plot shows a head reduction with an increase in discharge. The top right plot shows an exponential NPSH increasement with an increase in discharge. The bottom left plot shows the efficiency curve alongside the discharge. The bottom right plot shows the power absorbed by the water.

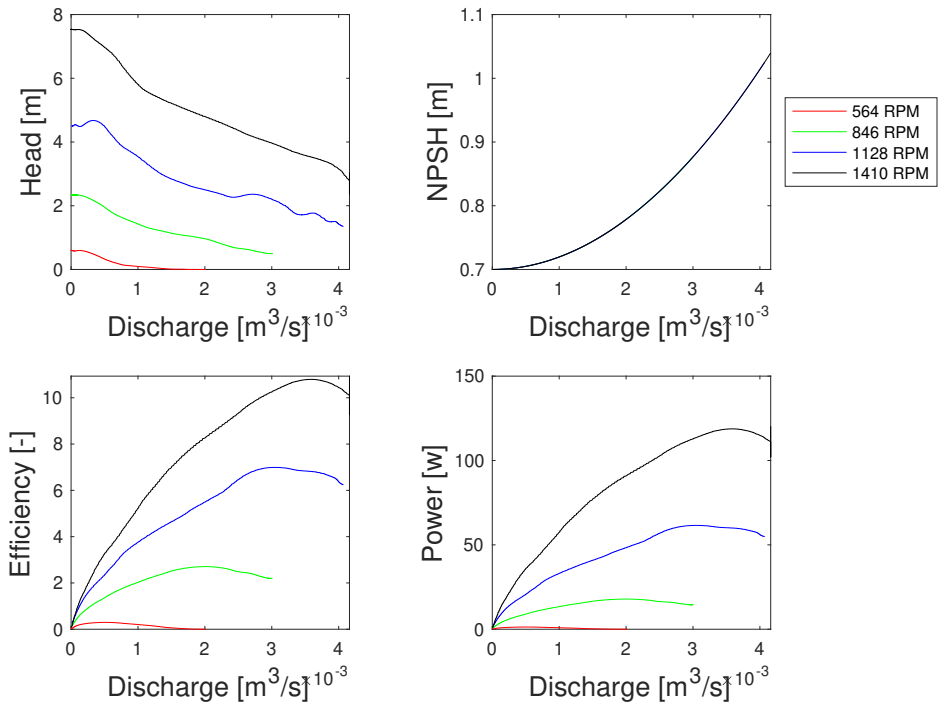

Figure A.1: Single phase (water) characteristics at multiple engine speeds.

A.2. Mixture phase characteristics

The following mixture characteristics also consist out of 4 plots that all refer to the same input data. Only the NPSH plot is changed here with a C_{vd} plot for explanation to drops in head value. The top left plot shows a head reduction with an increase in discharge. The top right plot shows a C_{vd} increase with an increase in discharge. The bottom left plot shows the efficiency curve alongside the discharge. The bottom right plot shows the power absorbed by the water.

A.2.1. Glass beads 1.5 mm, Cvd = 0.03

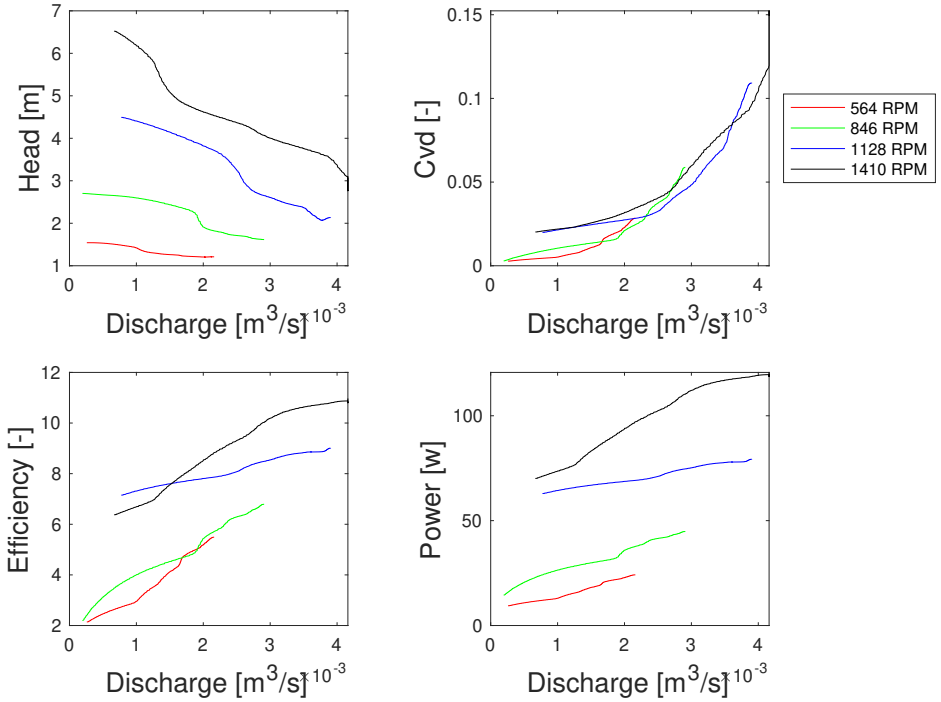

Figure A.2: Mixture characteristics at multiple engine speeds with glass beads of 1.5 mm and a C_{vd} = 0.03.

A.2.2. Glass beads 1.5 mm, Cvd = 0.05

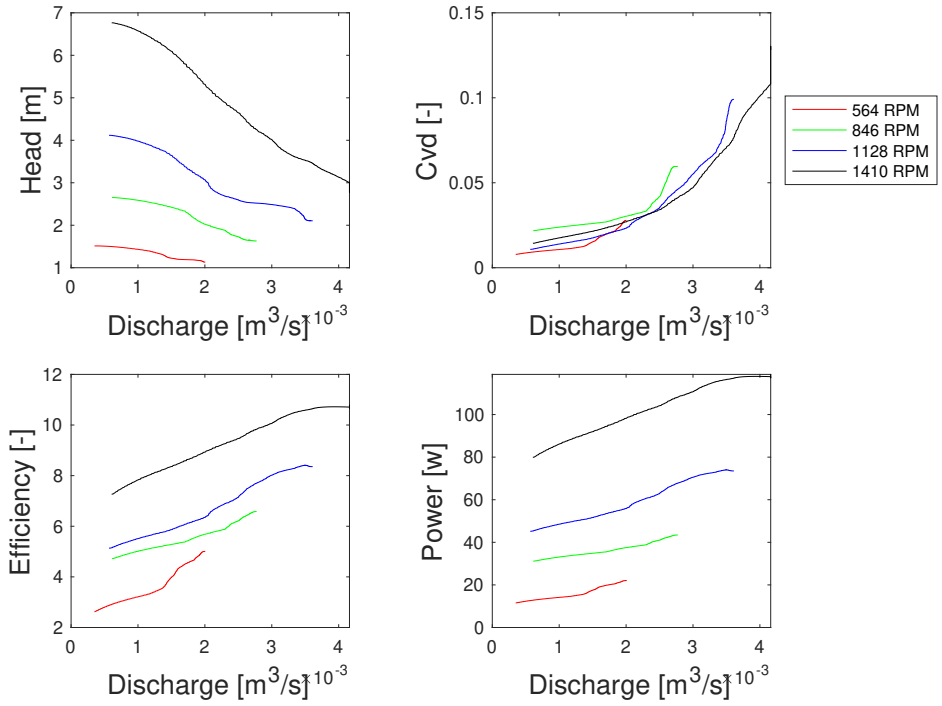

Figure A.3: Mixture characteristics at multiple engine speeds with glass beads of 1.5 mm and a $C_{vd} = 0.05$.

A.2.3. Glass beads 1.5 mm, Cvd = 0.08

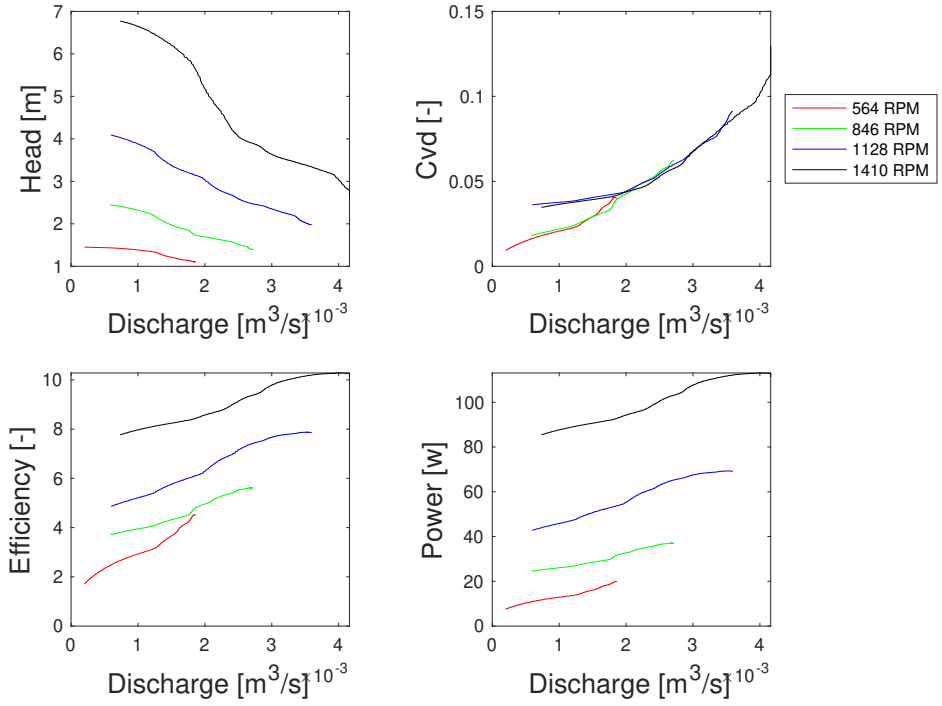

Figure A.4: Mixture characteristics at multiple engine speeds with glass beads of 1.5 mm and a $C_{vd} = 0.08$.

A.2.4. Glass beads 1.5 mm, Cvd = 0.12

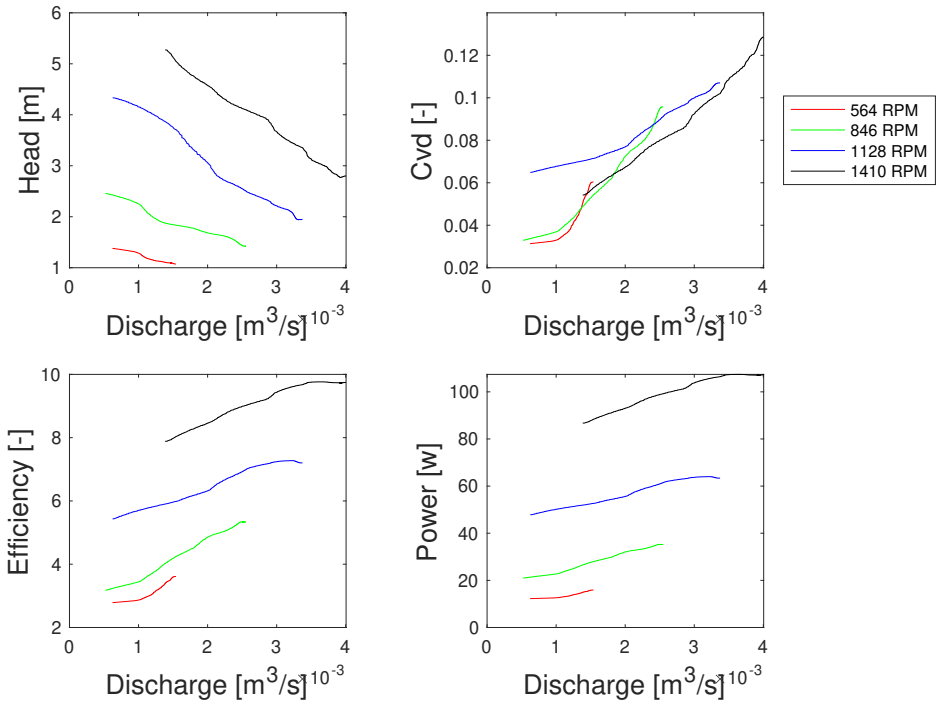

Figure A.5: Mixture characteristics at multiple engine speeds with glass beads of 1.5 mm and a $C_{vd} = 0.12$.

A.2.5. Glass beads 1.5 mm, Cvd = 0.15

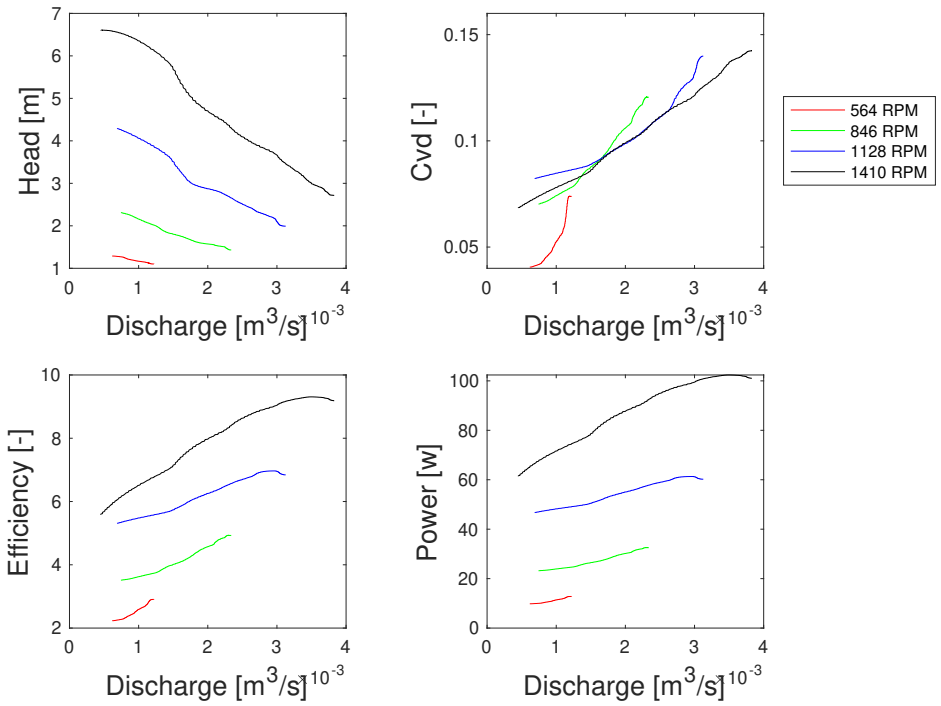

Figure A.6: Mixture characteristics at multiple engine speeds with glass beads of 1.5 mm and a $C_{vd} = 0.15$.

A.2.6. Glass beads 1.5 mm, Cvd = 0.20

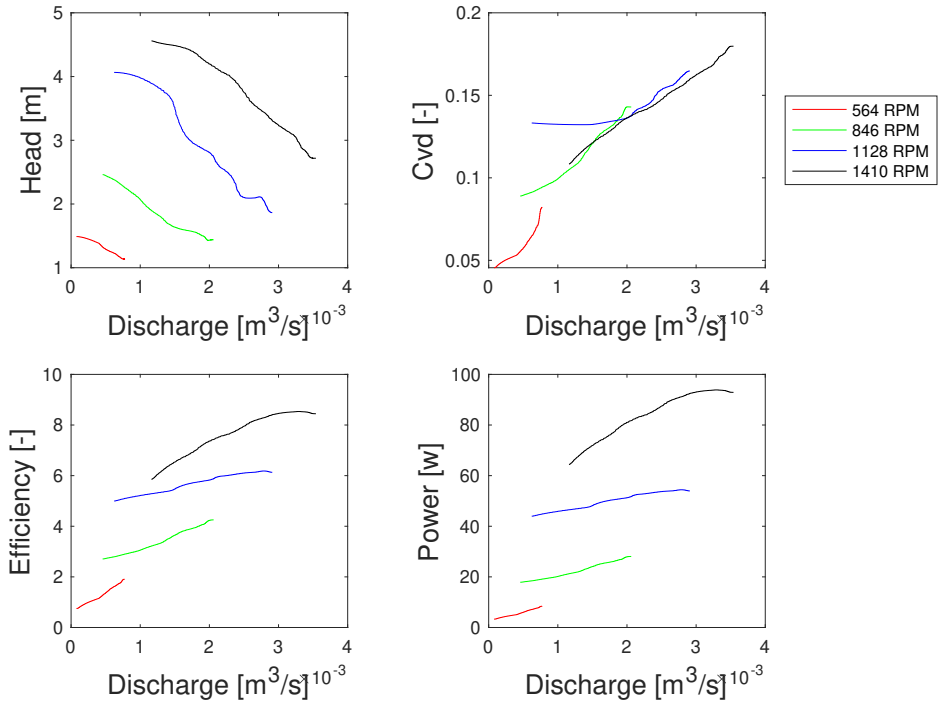

Figure A.7: Mixture characteristics at multiple engine speeds with glass beads of 1.5 mm and a C_{vd} = 0.20.

A.2.7. Glass beads 3.0 mm, Cvd = 0.03

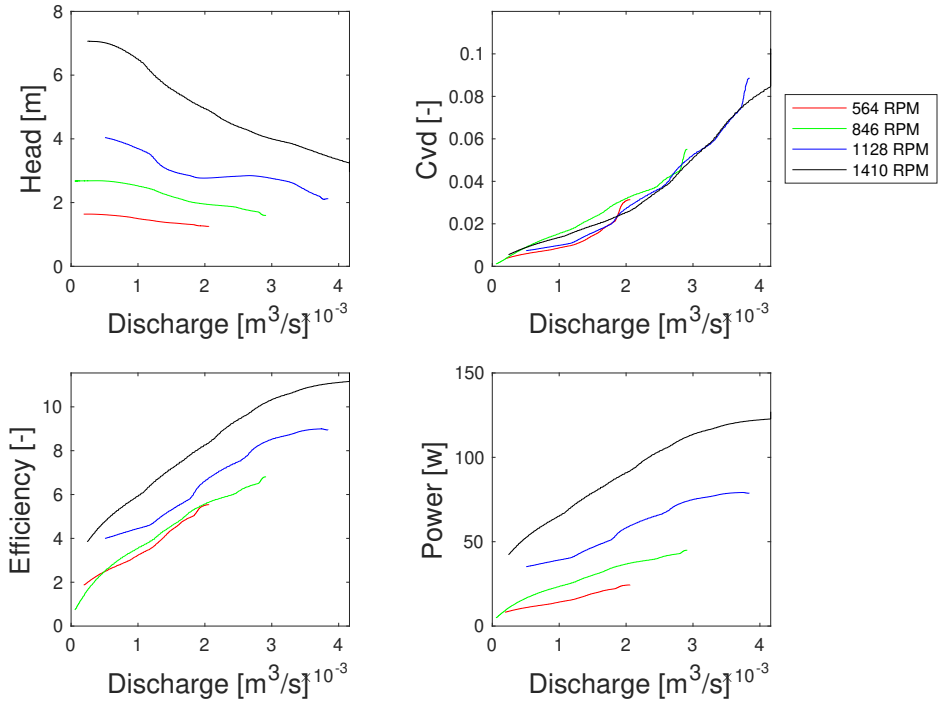

Figure A.8: Mixture characteristics at multiple engine speeds with glass beads of 3.0 mm and a C_{vd} = 0.03.

A.2.8. Glass beads 3.0 mm, Cvd = 0.05

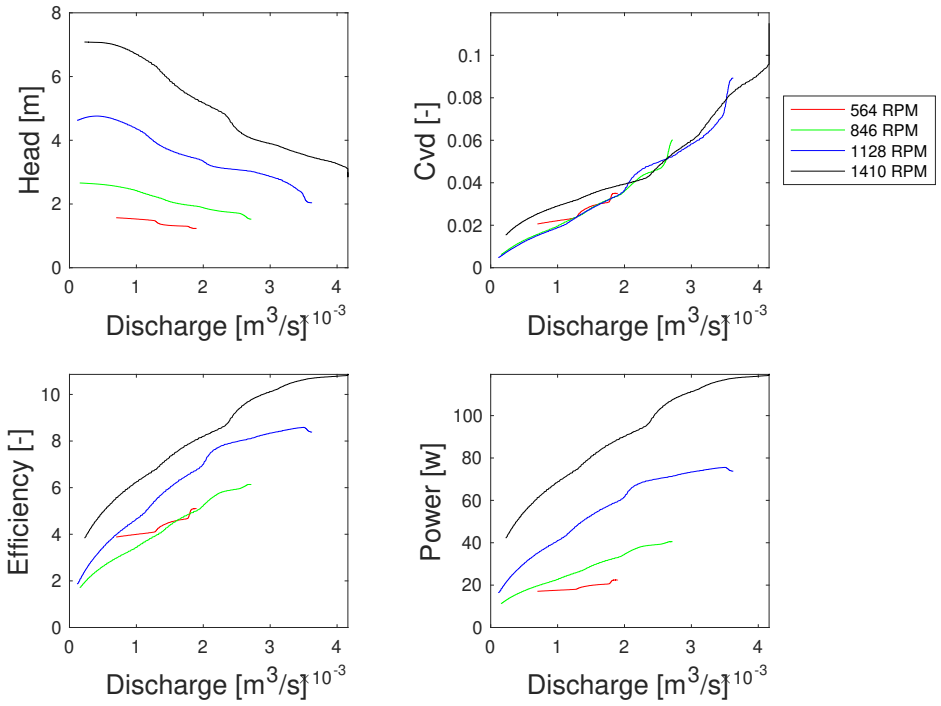

Figure A.9: Mixture characteristics at multiple engine speeds with glass beads of 3.0 mm and a C_{vd} = 0.05.

A.2.9. Glass beads 3.0 mm, Cvd = 0.08

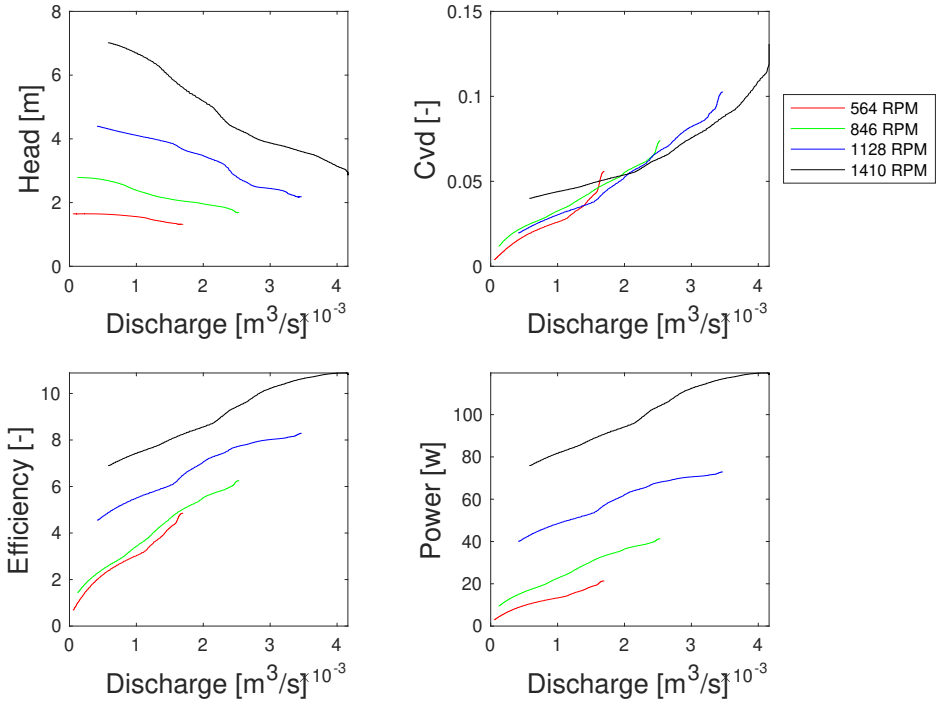

Figure A.10: Mixture characteristics at multiple engine speeds with glass beads of 3.0 mm and a C_{vd} = 0.08.

A.2.10. Glass beads 3.0 mm, Cvd = 0.12

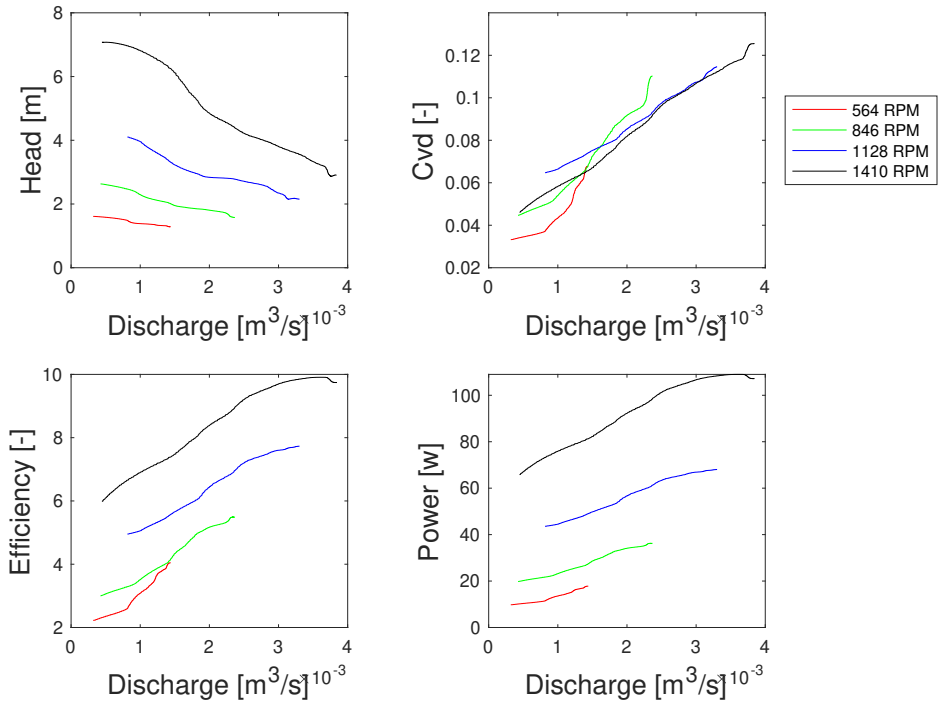

Figure A.11: Mixture characteristics at multiple engine speeds with glass beads of 3.0 mm and a $C_{vd} = 0.12$.

A.2.11. Glass beads 3.0 mm, Cvd = 0.15

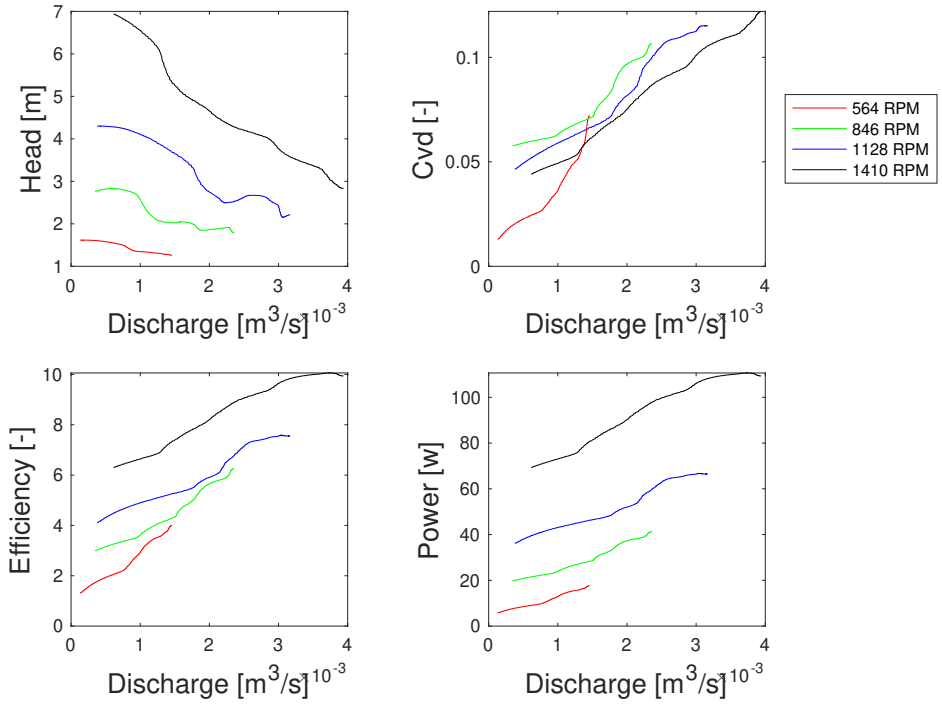

Figure A.12: Mixture characteristics at multiple engine speeds with glass beads of 3.0 mm and a $C_{vd} = 0.15$.

A.2.12. Glass beads 3.0 mm, Cvd = 0.20

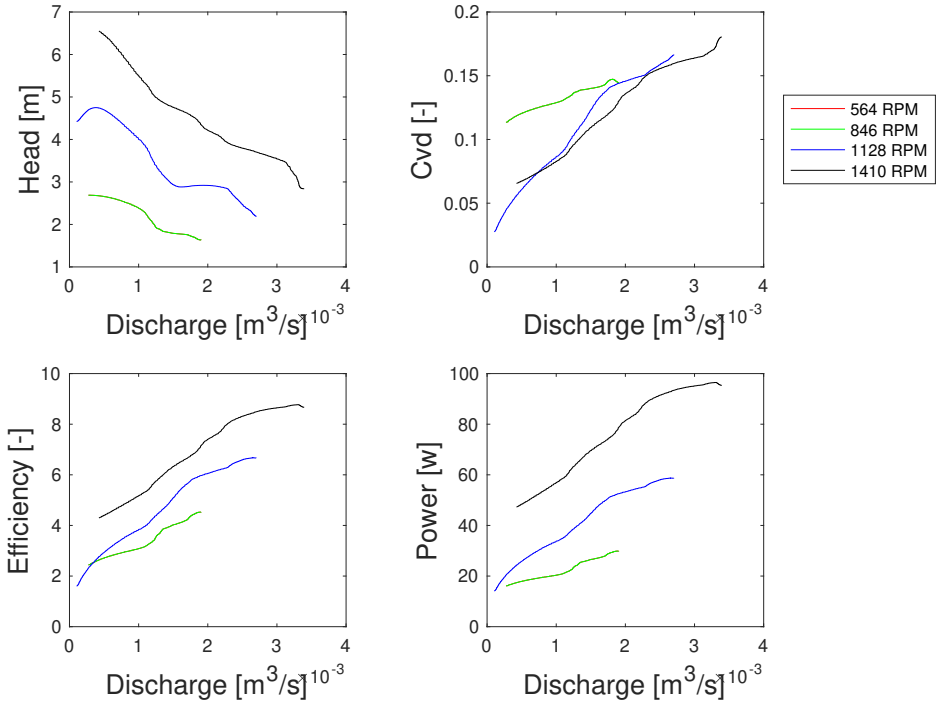

Figure A.13: Mixture characteristics at multiple engine speeds with glass beads of 3.0 mm and a $C_{vd} = 0.20$.

B

Sensor data analyzes from water/mixture experiments

This appendix includes experimental sensor data to analyse the multiple effects of particle concentrations on (unsteady) head and (unsteady) discharge. Also, this data is recorded simultaneously with the high speed images so the data can be used as supportive information on the PIVlab image analyses. The figures gathered in these appendix show head, discharge, concentration and temperature along the duration of the test. Also, on the unsteady head vs time plot, a FFT analyses is done to determine the dominant frequencies to concluded if the impeller interaction is indeed enhanced with an increase in C_{vd}.

B.1. Sensor data at single phase (water) conditions

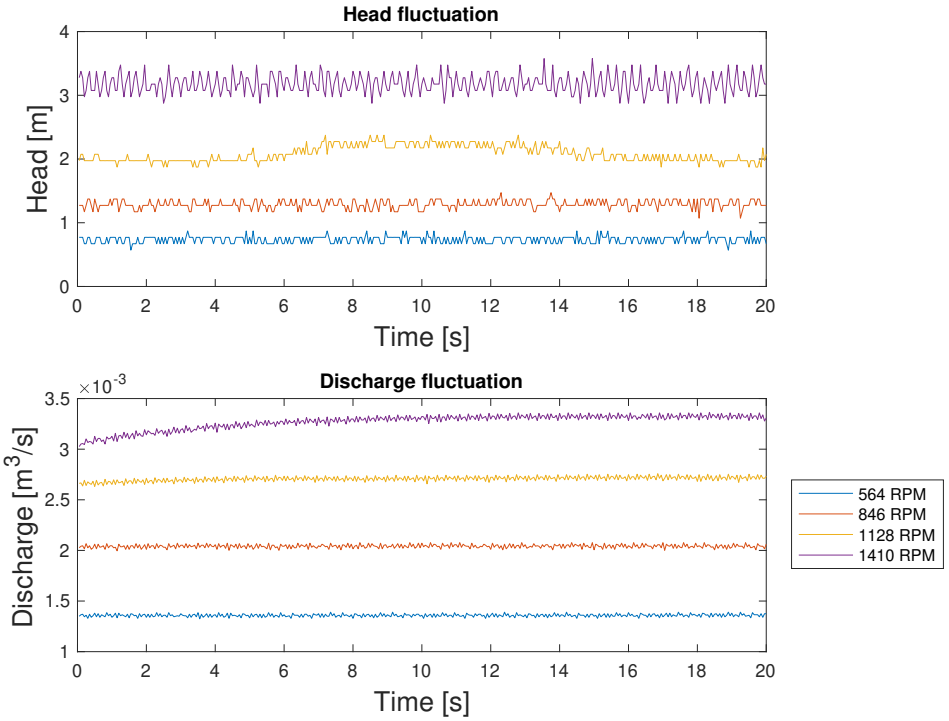

Figure B.1: Head, discharge and concentration plotted against time.

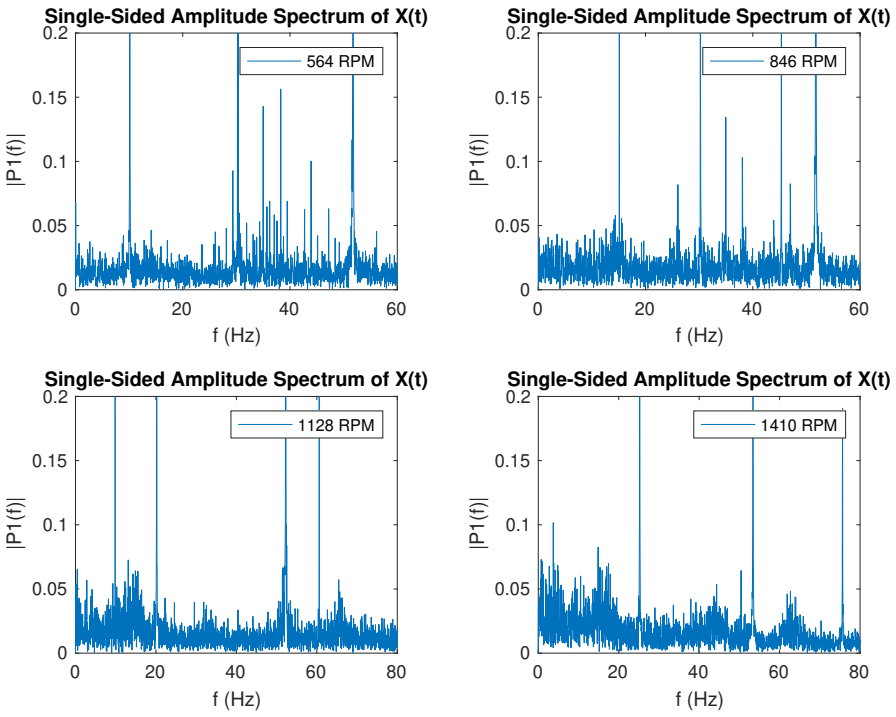

Figure B.2: FFT transformation of the (unsteady) head for impeller head interaction.

B.2. Sensor data at mixture phase conditions

B.2.1. Glass beads 1.5 mm, Cvd = 0.03

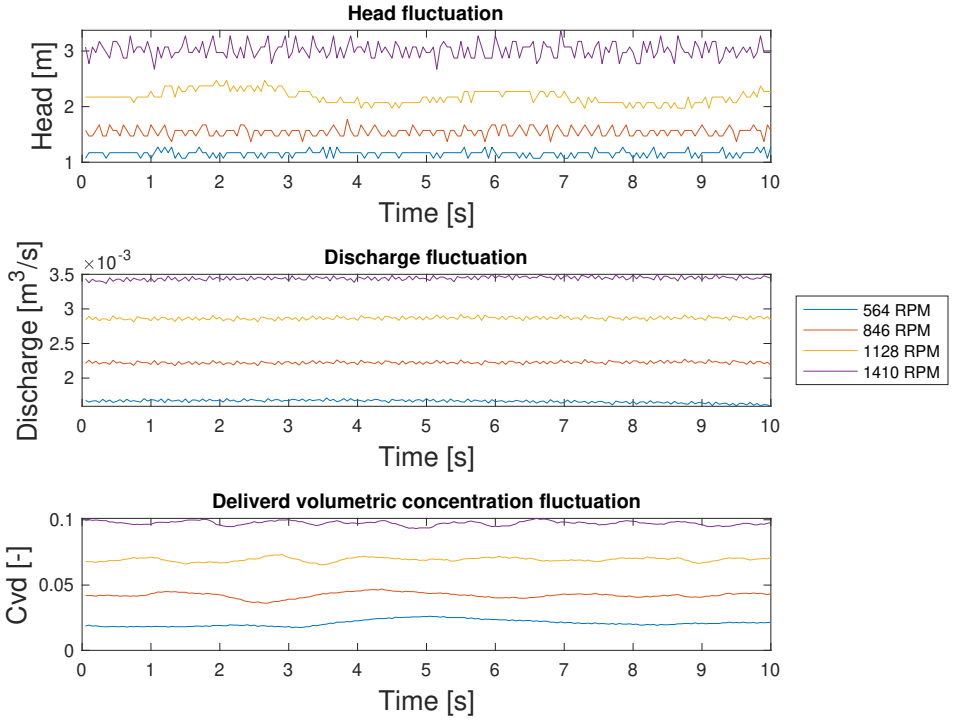

Figure B.3: Head, discharge and concentration plotted against time at water conditions only.

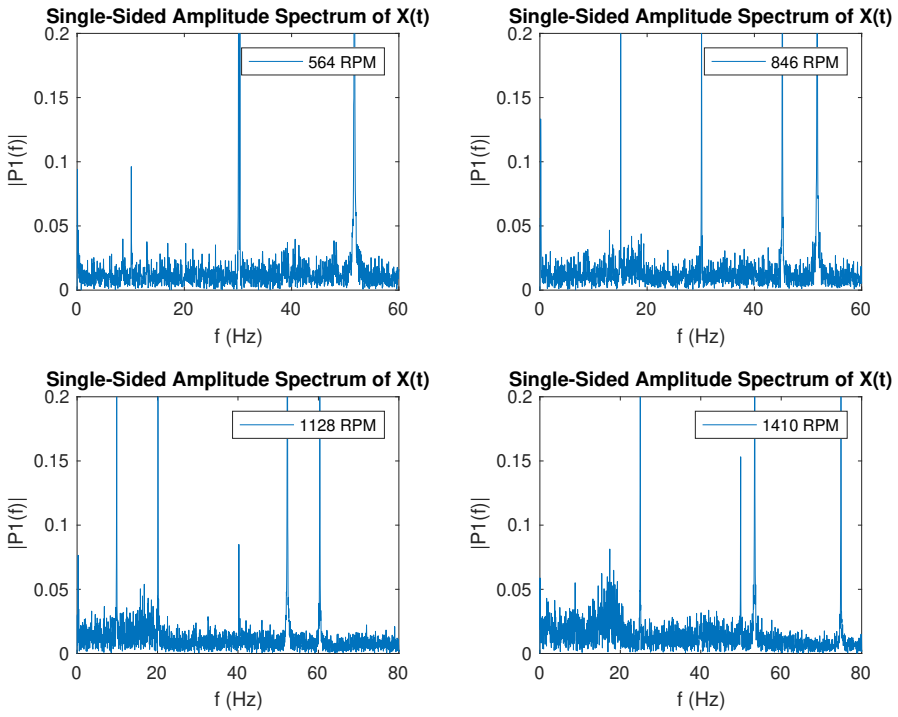

Figure B.4: FFT transformation of the (unsteady) head due to impeller head interaction.

B.2.2. Glass beads 1.5 mm, Cvd = 0.05

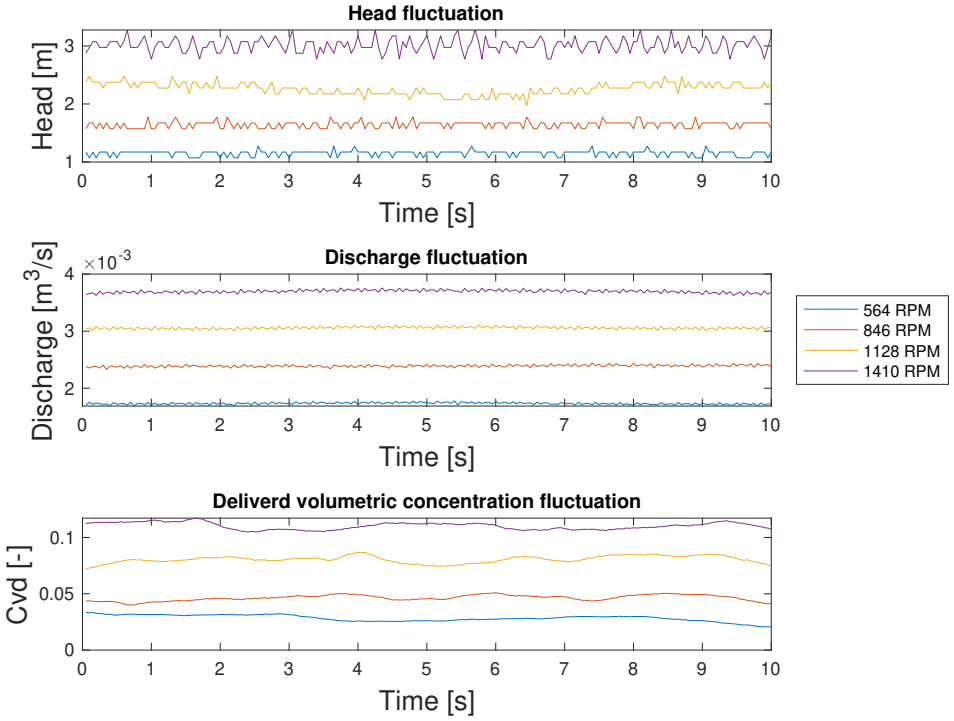

Figure B.5: Head, discharge and concentration plotted against time.

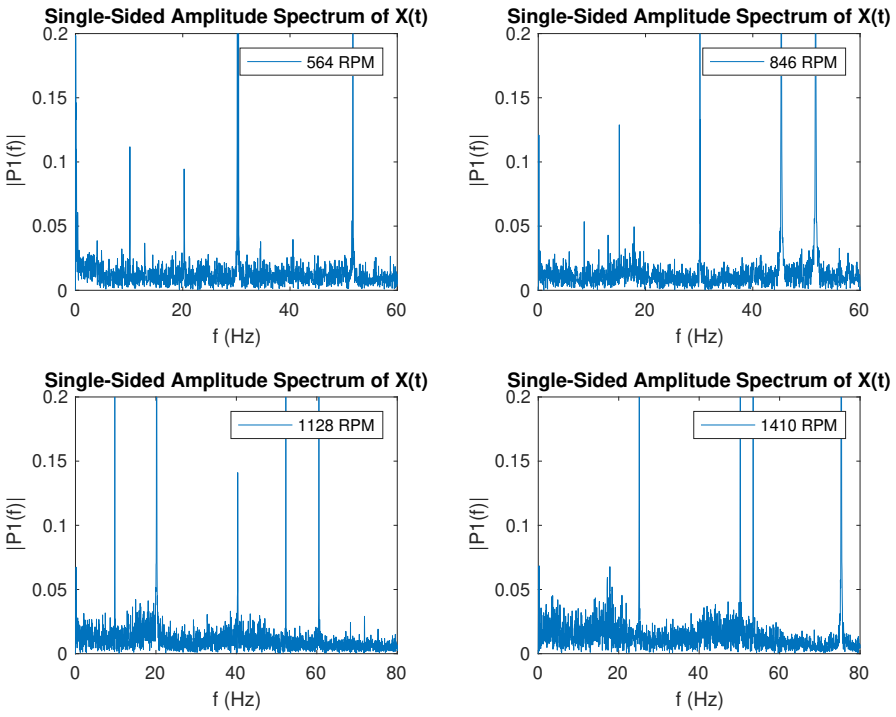

Figure B.6: FFT transformation of the (unsteady) head for impeller head interaction.

B.2.3. Glass beads 1.5 mm, Cvd = 0.08

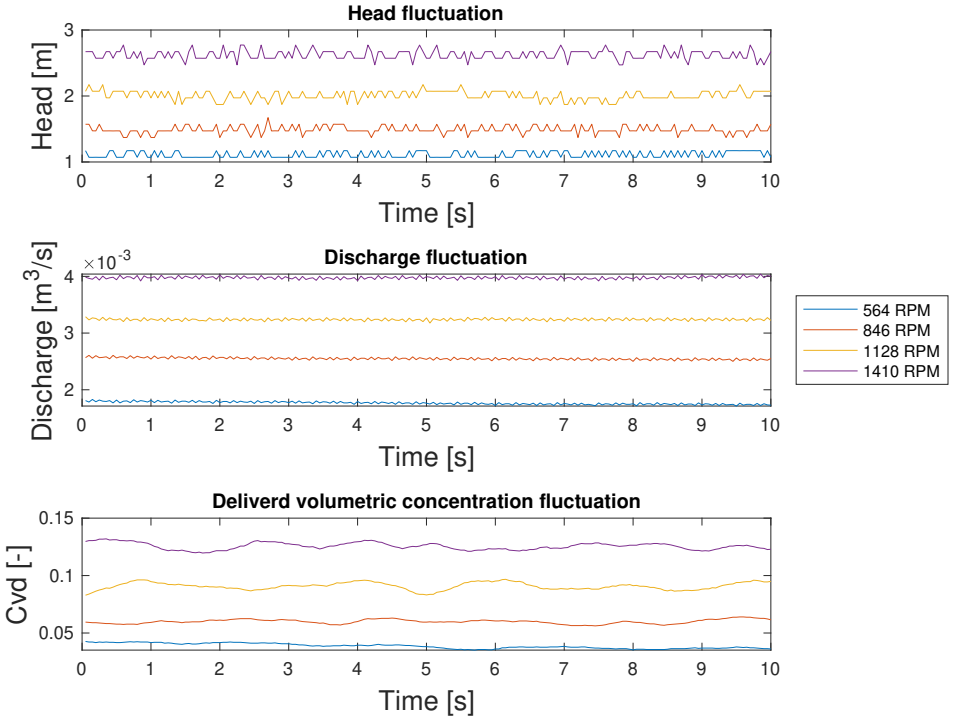

Figure B.7: Head, discharge and concentration plotted against time.

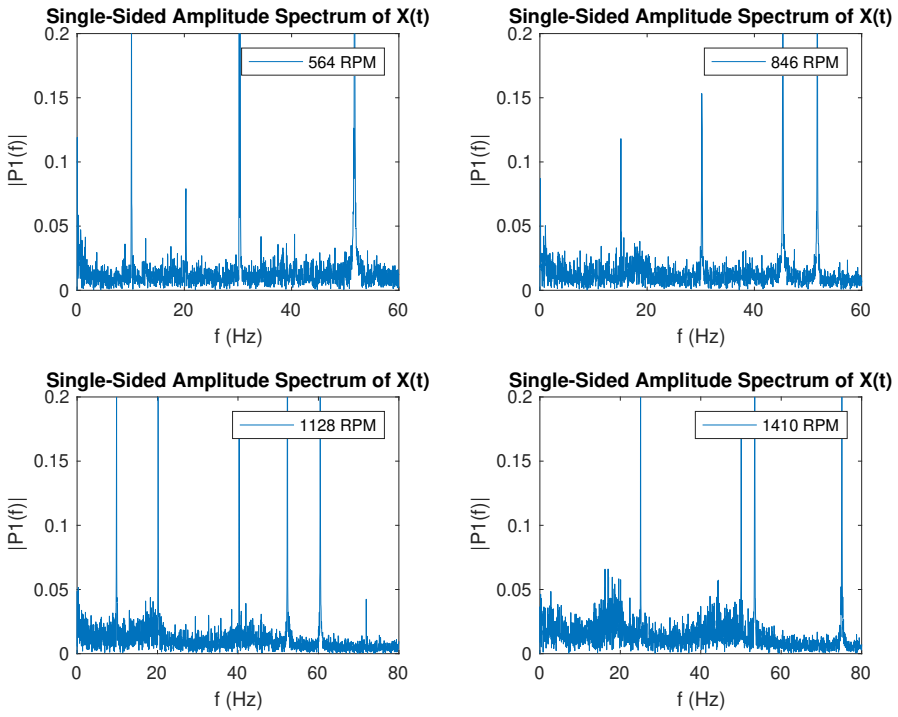

Figure B.8: FFT transformation of the (unsteady) head for impeller head interaction.

B.2.4. Glass beads 1.5 mm, Cvd = 0.12

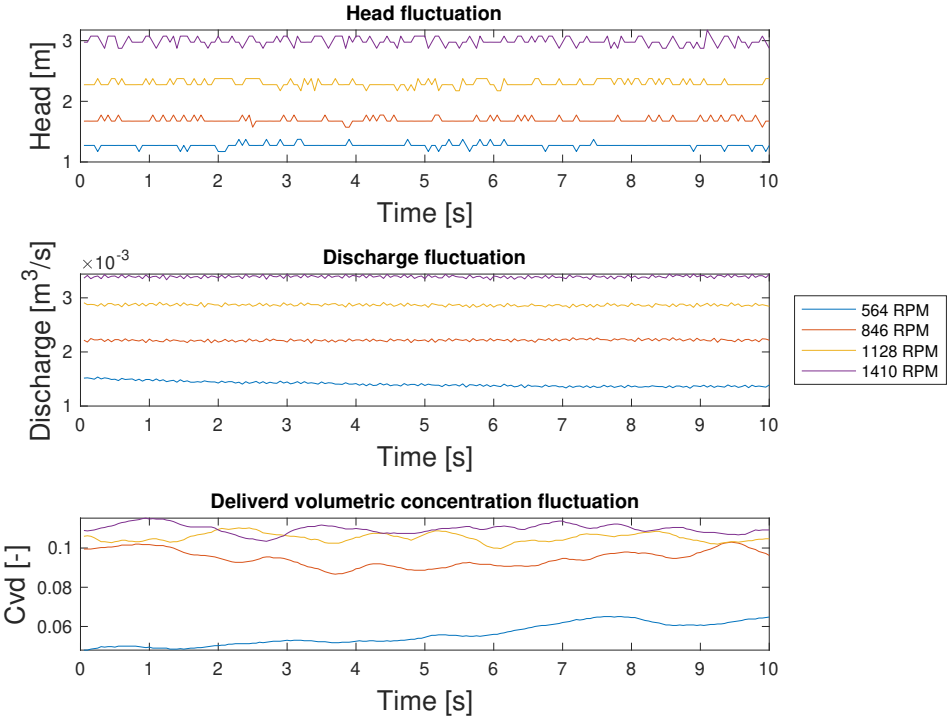

Figure B.9: Head, discharge and concentration plotted against time.

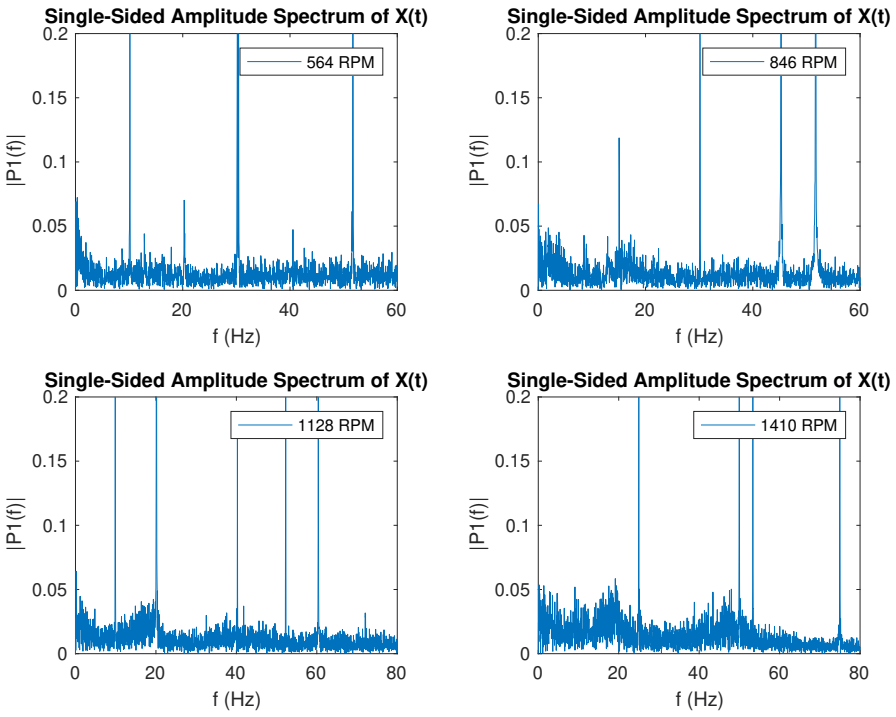

Figure B.10: FFT transformation of the (unsteady) head for impeller head interaction.

B.2.5. Glass beads 1.5 mm, Cvd = 0.15

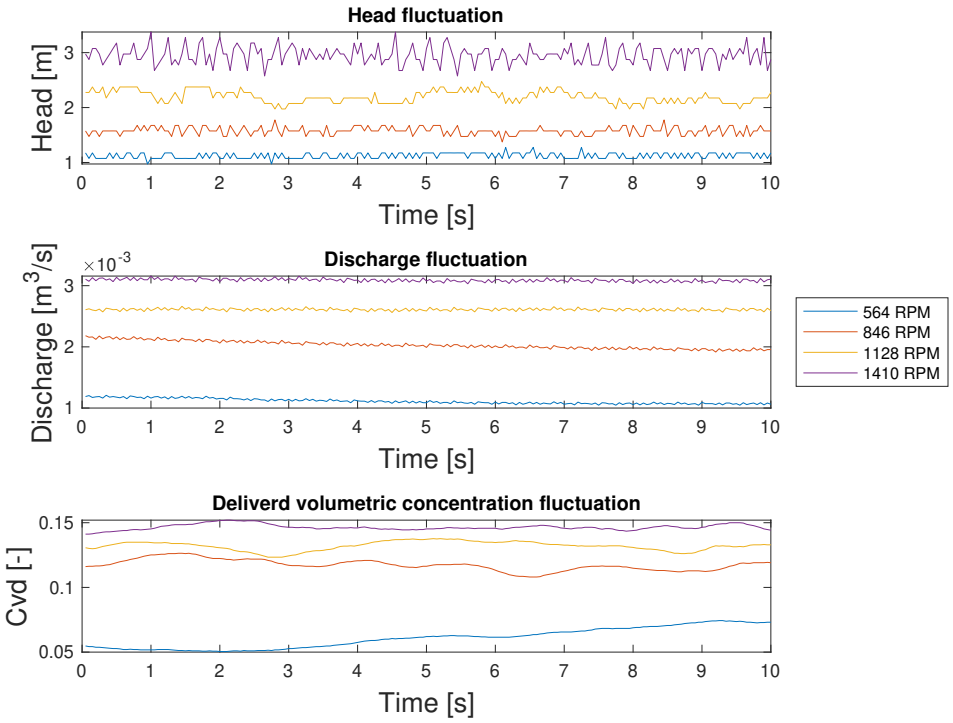

Figure B.11: Head, discharge and concentration plotted against time.

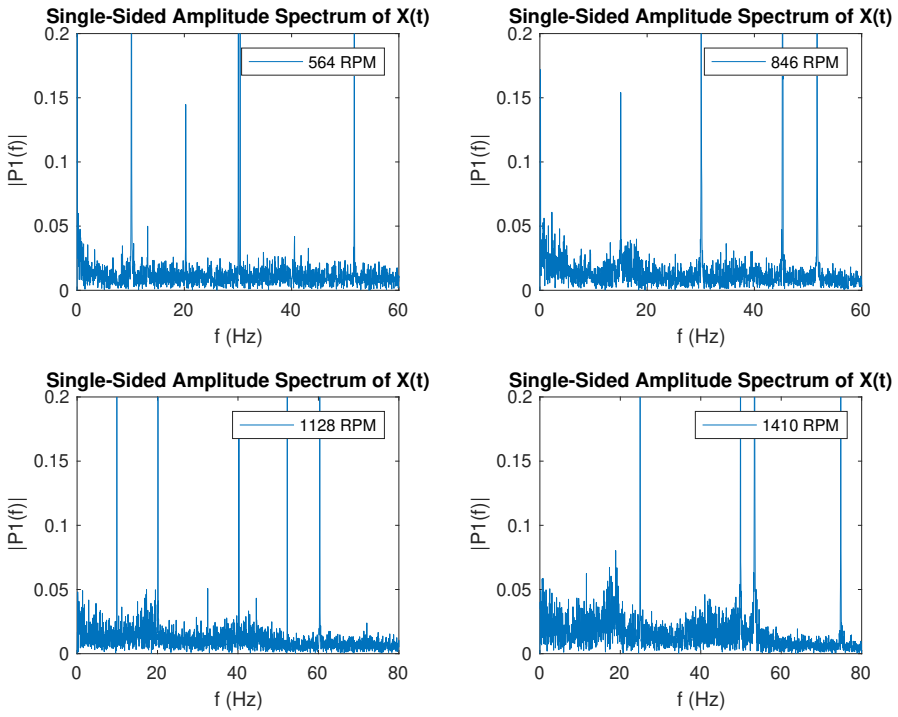

Figure B.12: FFT transformation of the (unsteady) head for impeller head interaction.

B.2.6. Glass beads 1.5 mm, Cvd = 0.20

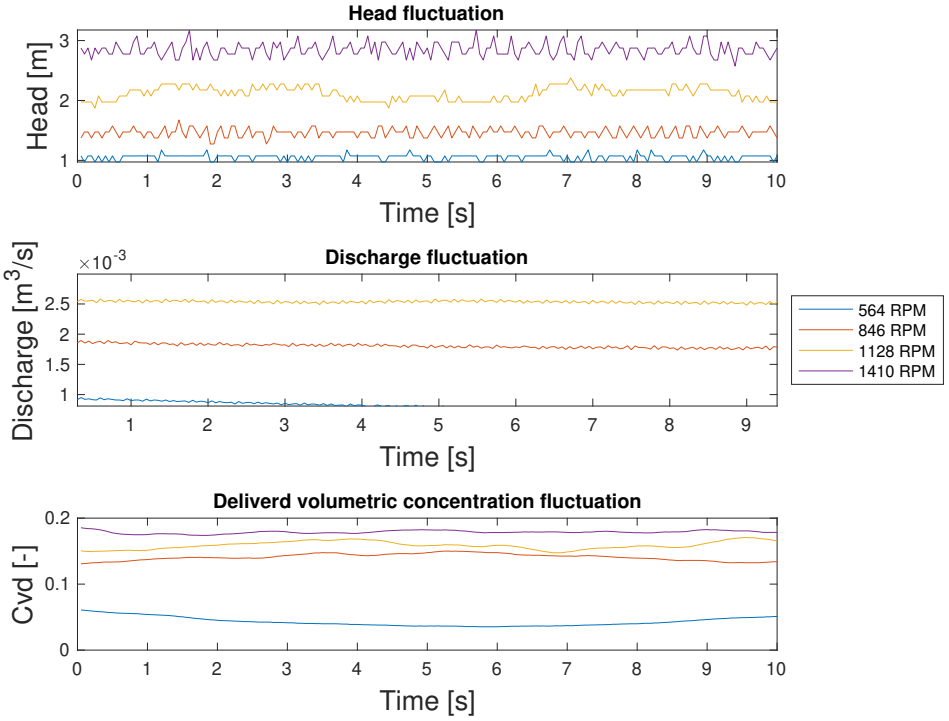

Figure B.13: Head, discharge and concentration plotted against time.

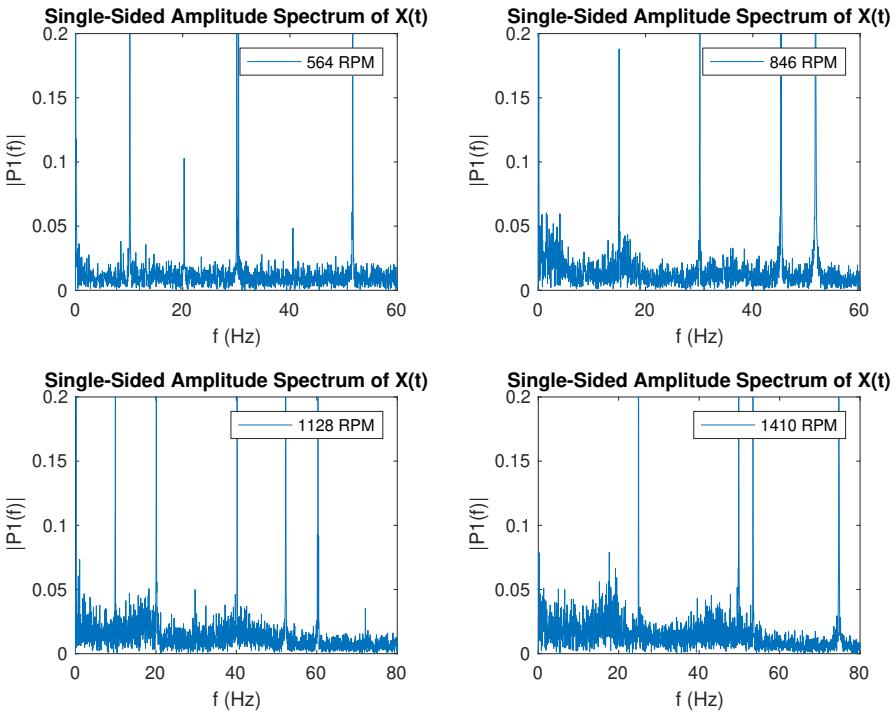

Figure B.14: FFT transformation of the (unsteady) head for impeller head interaction.

B.2.7. Glass beads 3.0 mm, Cvd = 0.03

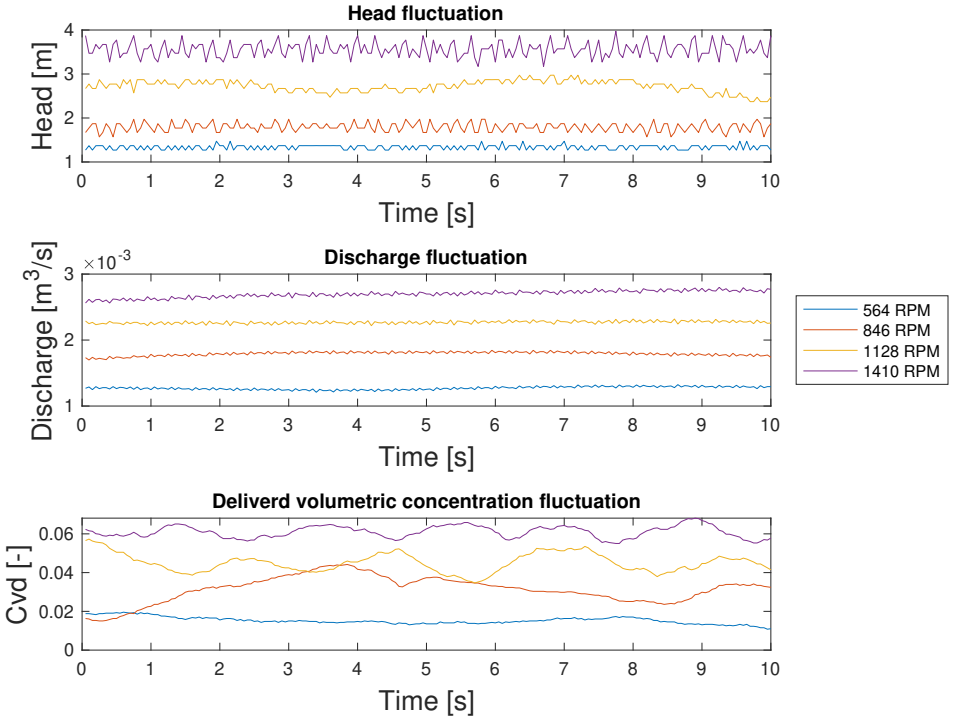

Figure B.15: Head, discharge and concentration plotted against time.

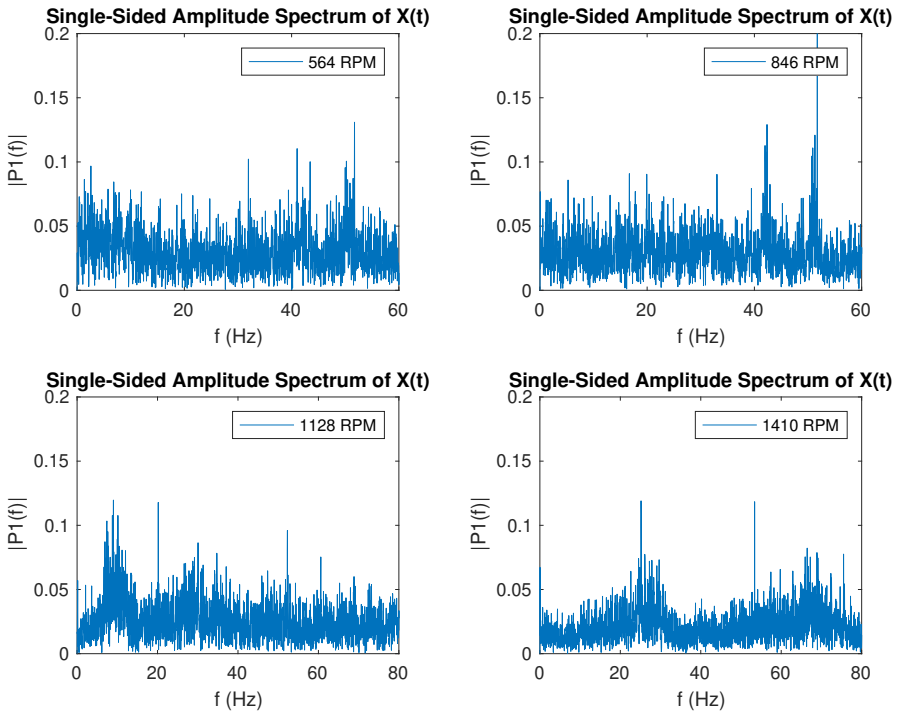

Figure B.16: FFT transformation of the (unsteady) head for impeller head interaction.

B.2.8. Glass beads 3.0 mm, Cvd = 0.05

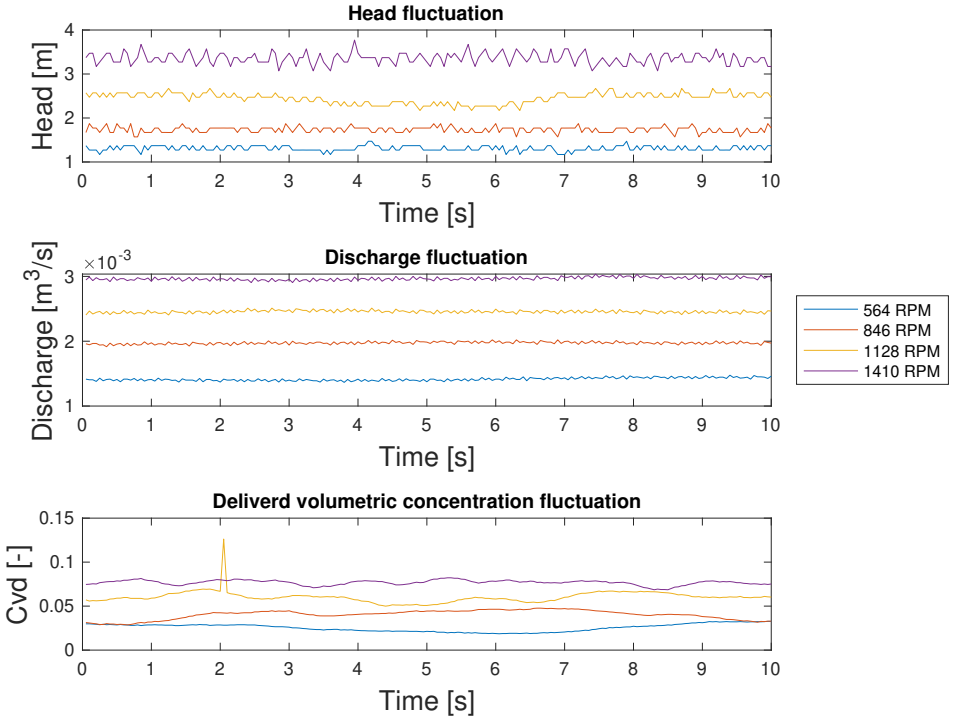

Figure B.17: Head, discharge and concentration plotted against time.

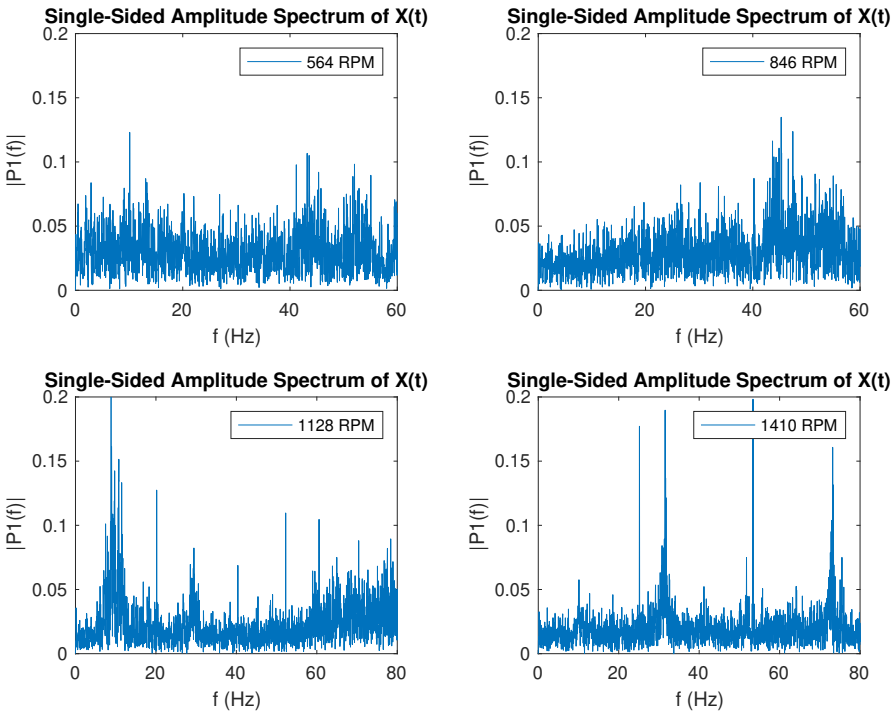

Figure B.18: FFT transformation of the (unsteady) head for impeller head interaction.

B.2.9. Glass beads 3.0 mm, Cvd = 0.08

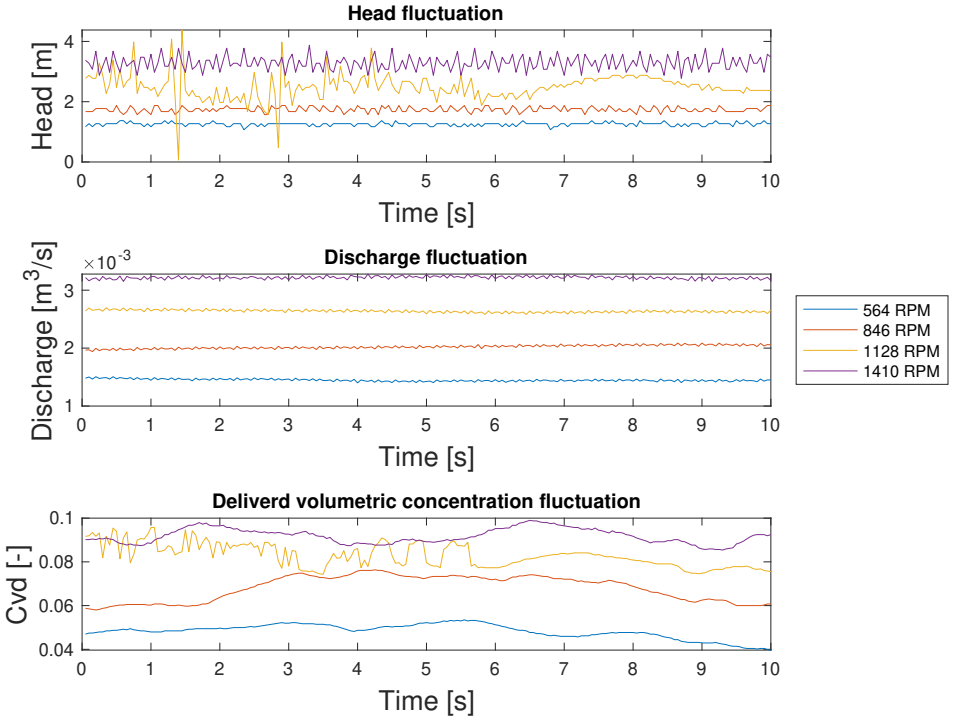

Figure B.19: Head, discharge and concentration plotted against time.

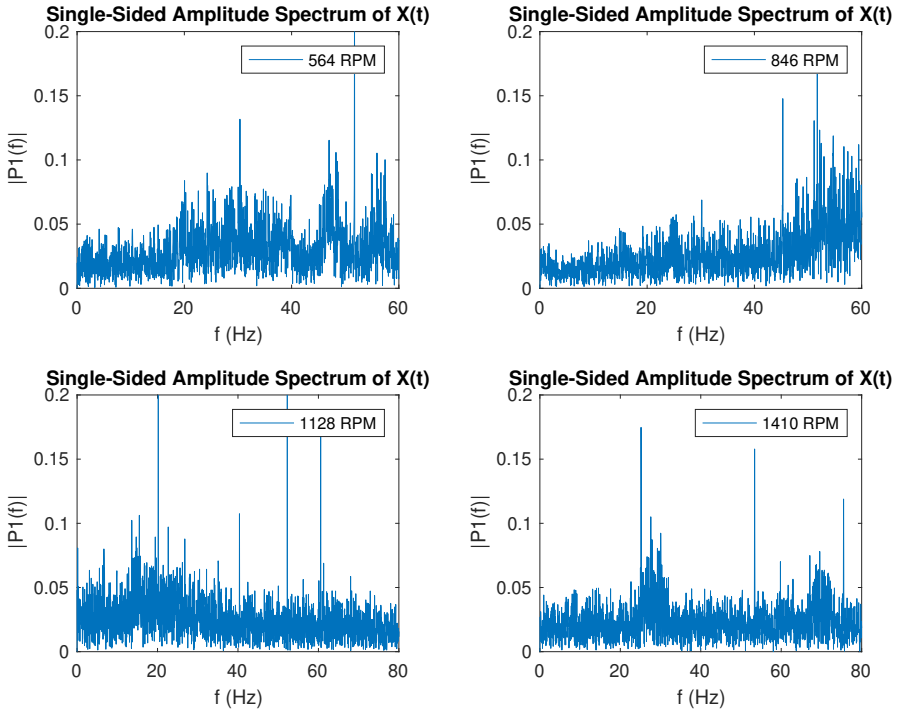

Figure B.20: FFT transformation of the (unsteady) head for impeller head interaction.

B.2.10. Glass beads 3.0 mm, Cvd = 0.12

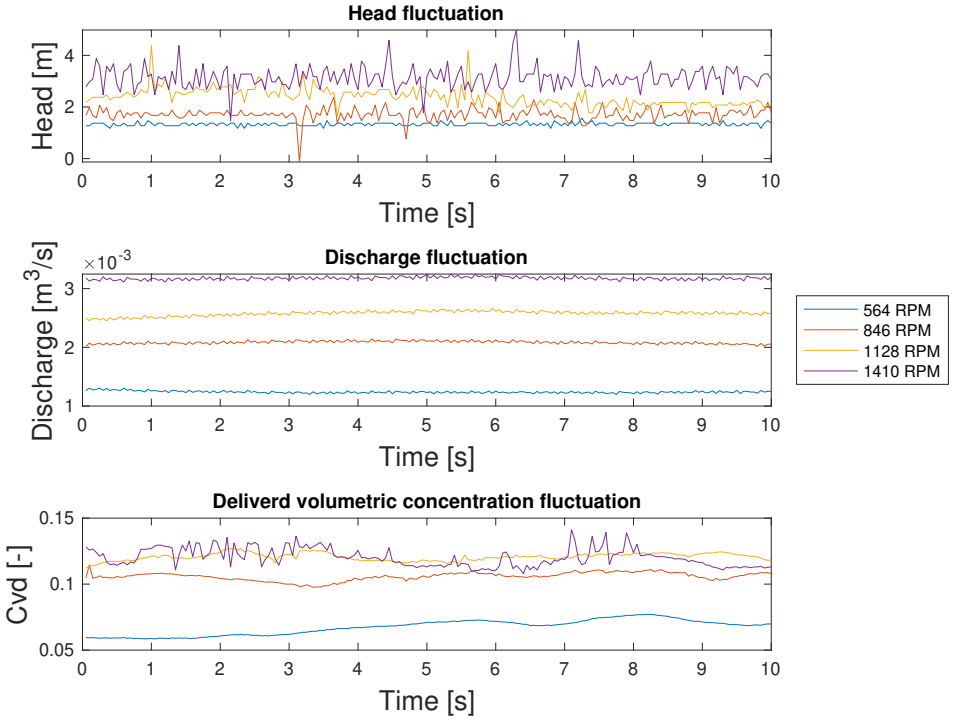

Figure B.21: Head, discharge and concentration plotted against time.

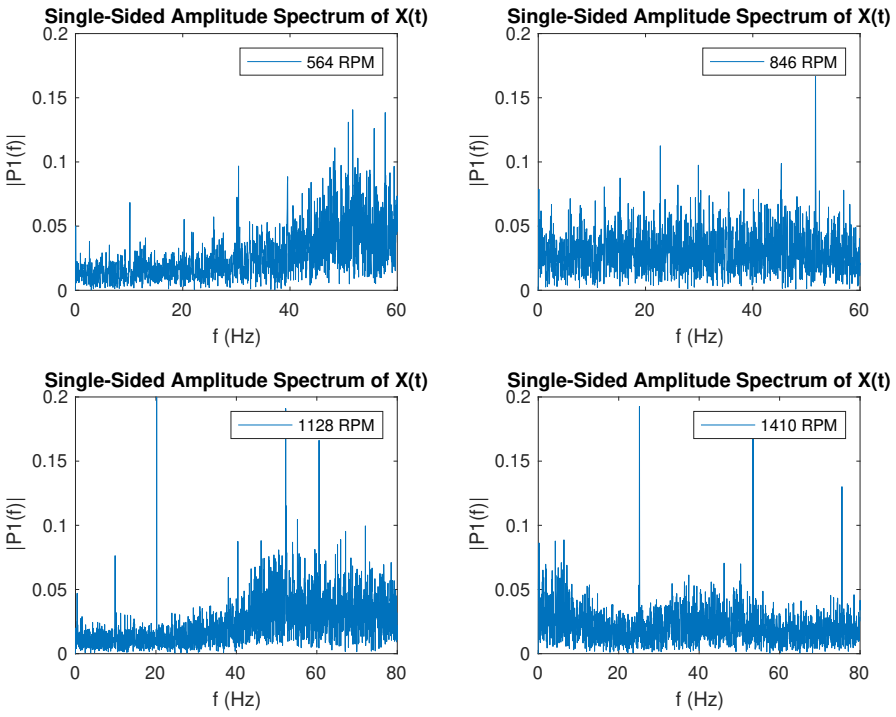

Figure B.22: FFT transformation of the (unsteady) head for impeller head interaction.

B.2.11. Glass beads 3.0 mm, Cvd = 0.15

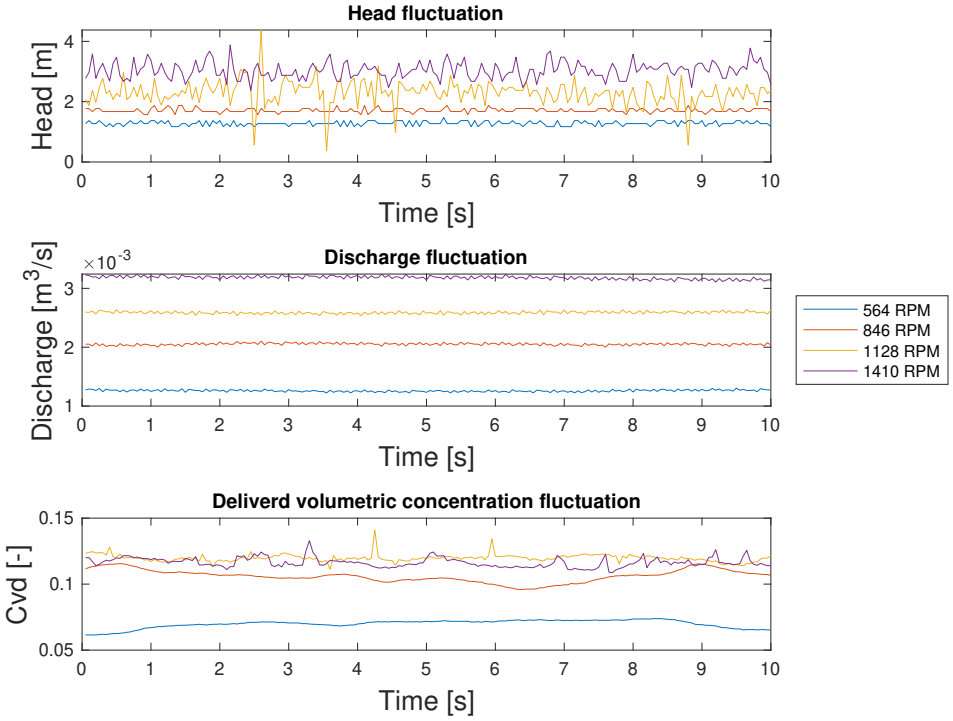

Figure B.23: Head, discharge and concentration plotted against time.

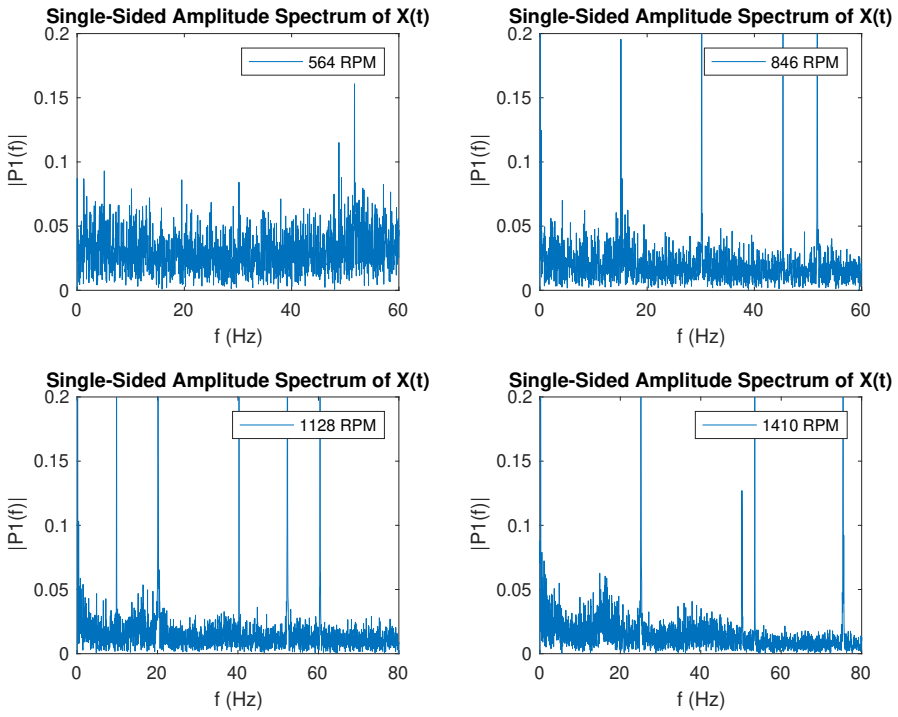

Figure B.24: FFT transformation of the (unsteady) head for impeller head interaction.

B.2.12. Glass beads 3.0 mm, Cvd = 0.20

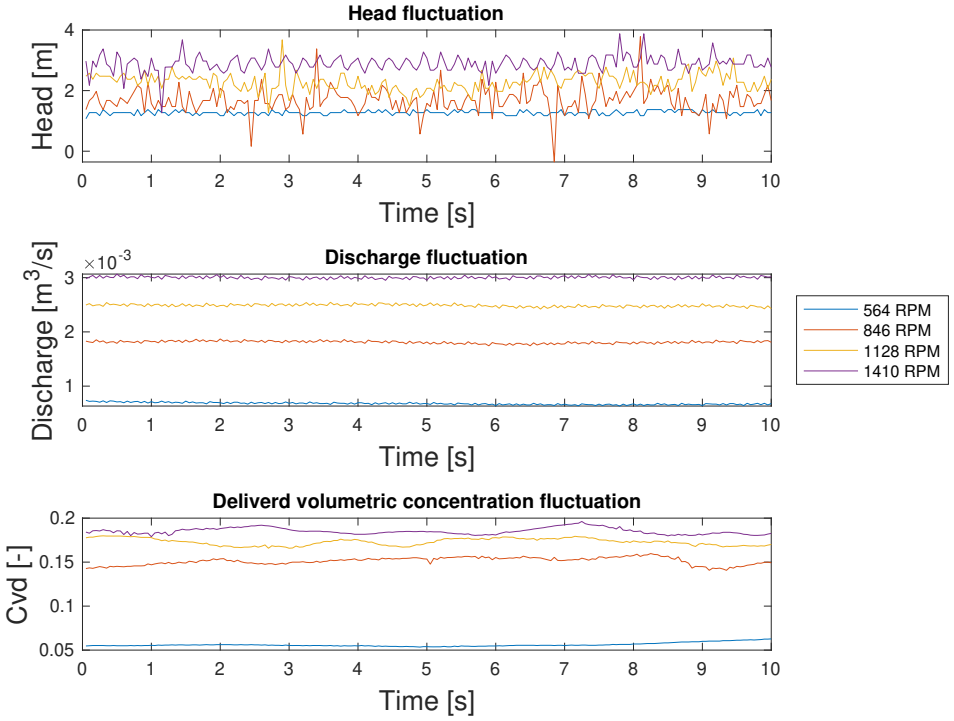

Figure B.25: Head, discharge and concentration plotted against time.

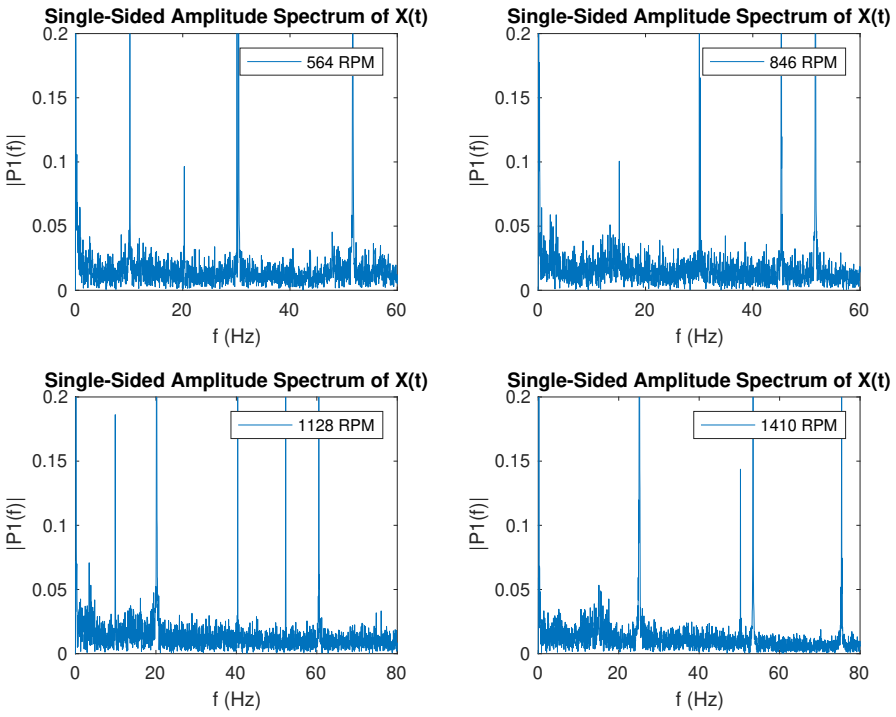

Figure B.26: FFT transformation of the (unsteady) head for impeller head interaction.

C

PIVlab analysis with polystyrene and glass

This appendix includes the PIVlab image analyses outcomes on streamline patterns and trajectories. Also, the local velocities, at multiple points on the impeller, are given for reference on an increase in speed and concentration. In these (water) experiments, polystyrene particles of 2 mm in diameter with a density of 1025 kg/m^3 are used and glass bead particles are used of 1.5/3 mm in diameter with a density of 2500 kg/m^3. (The polystyrene particles have a density deviation of 1000-1050 kg/m^3)

C.1. Single Phase streamline/trajectories verification

In the single phase streamline/trajectories verification experiments with PIVlab, it was concluded that a C_{vd} concentration of 3% gives the most clear results for a "water" streamline verification. Due to these reasoning, this appendix does not include the C_{vd} situations with 1% and 5% concentration. These "missing" video recordings and PIVlab images can be found at the local storage of the Offshore and Dredging department at the TUDelft. Subsections below include the main PIVlab streamline/trajectories image and 4 local velocity plots based on the criteria found in chapter 4, figure 3.12.

C.1.1. Polystyrene 2mm, Cvd = 0.03, Speed 564 RPM

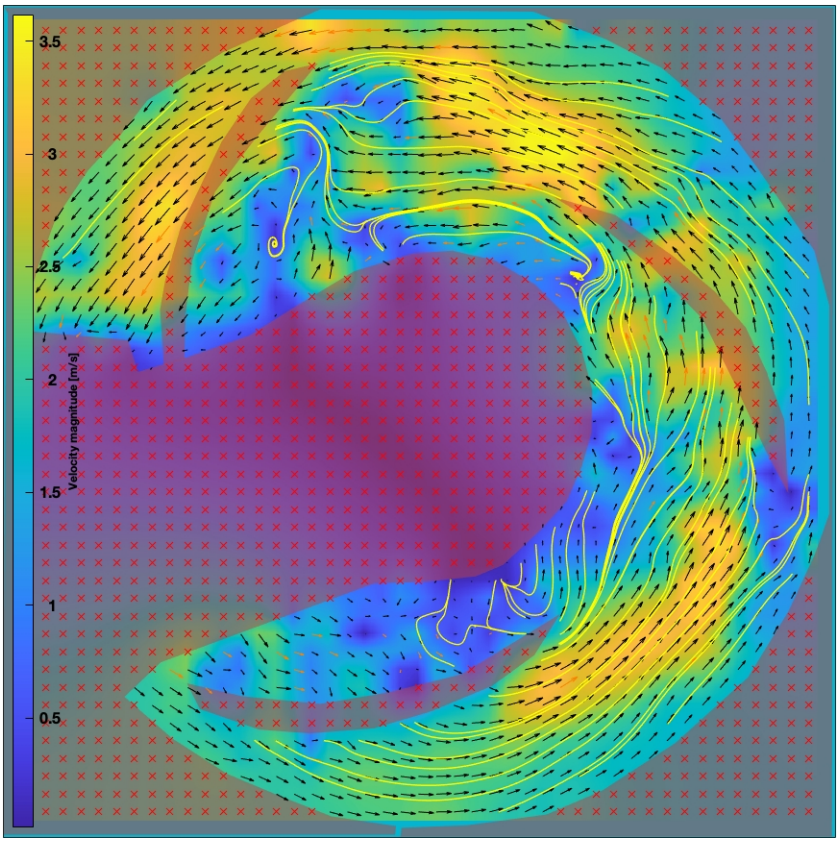

Figure C.1: PIVlab analysis of the streamlines and trajectories.

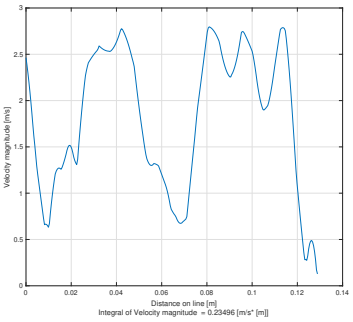

Figure C.2: Local Velocity line plot of the eddy in longitudinal direction.

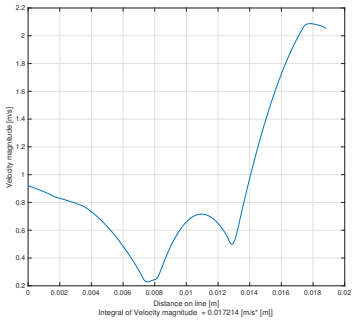

Figure C.3: Local Velocity line plot of the eddy in transverse direction.

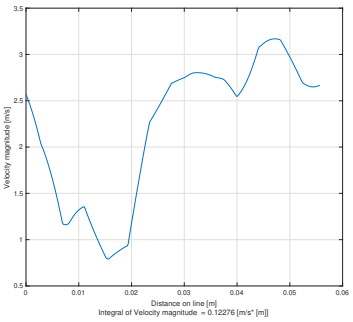

Figure C.4: Local Velocity line plot between the leading front and tail of two impellers.

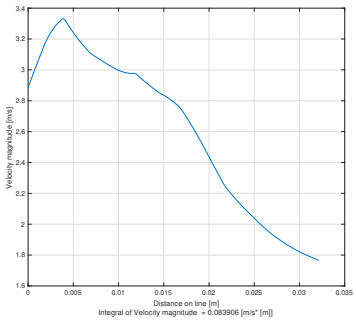

Figure C.5: Local Velocity line plot perpendicular on the leading front of the impeller. See figure 3.12 for clarification.

C.1.2. Polystyrene 2mm, Cvd = 0.03, Speed 846 RPM

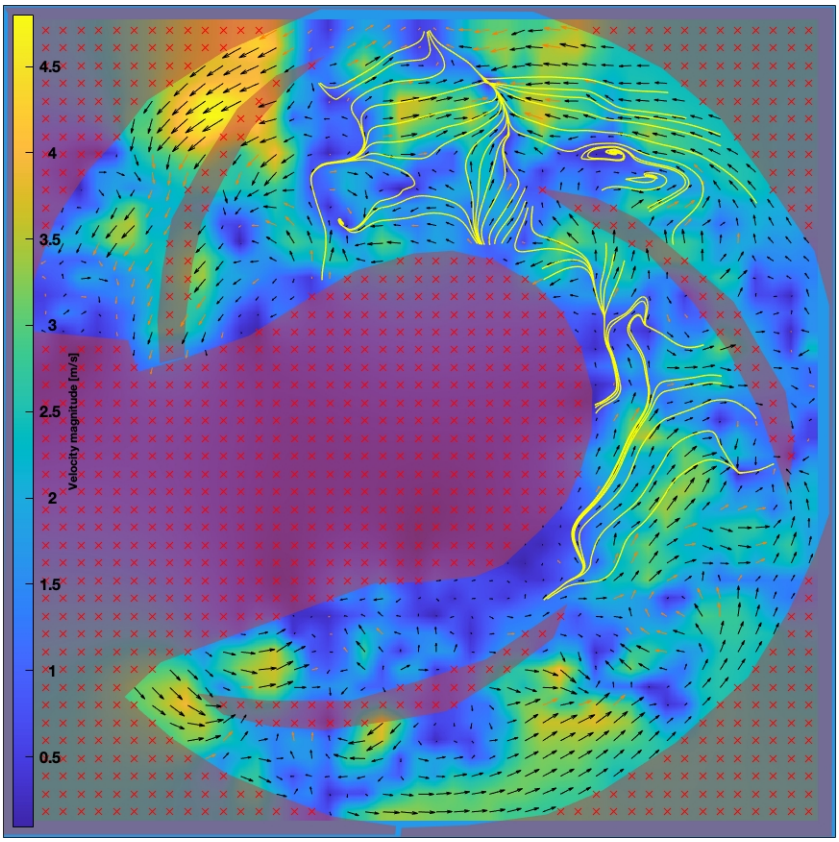

Figure C.6: PIVlab analysis of the streamlines and trajectories.

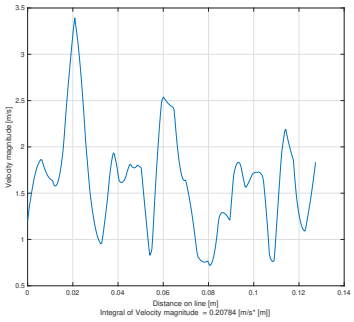

Figure C.7: Local Velocity line plot of the eddy in longitudinal direction.

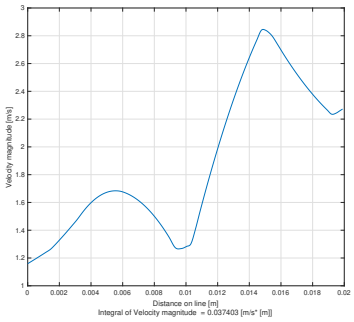

Figure C.8: Local Velocity line plot of the eddy in transverse direction.

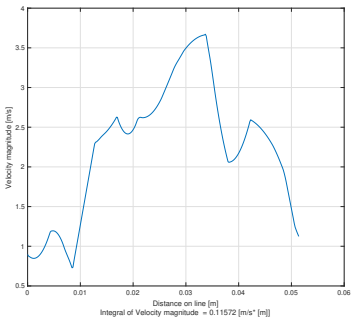

Figure C.9: Local Velocity line plot between the leading front and tail of two impellers.

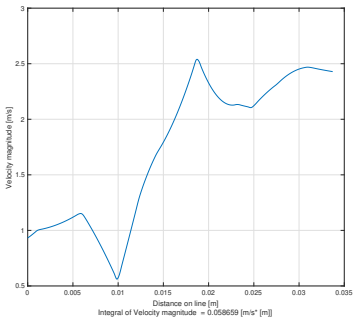

Figure C.10: Local Velocity line plot perpendicular on the leading front of the impeller. See figure 3.12 for clarification.

C.1.3. Polystyrene 2mm, Cvd = 0.03, Speed 1128 RPM

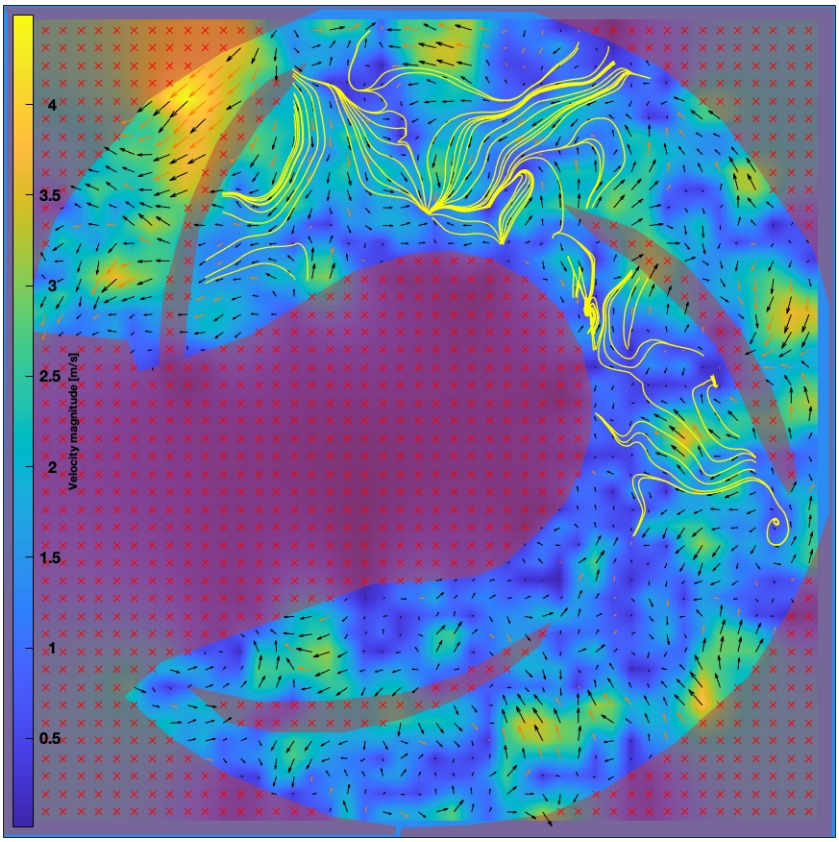

Figure C.11: PIVlab analysis of the streamlines and trajectories.

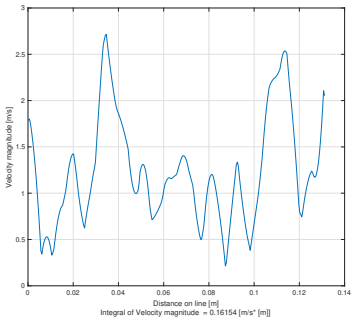

Figure C.12: Local Velocity line plot of the eddy in longitudinal direction.

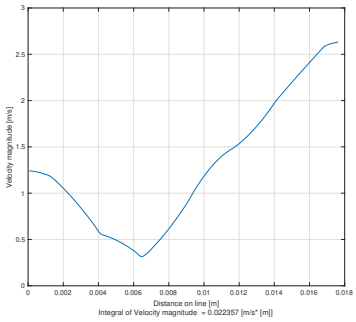

Figure C.13: Local Velocity line plot of the eddy in transverse direction.

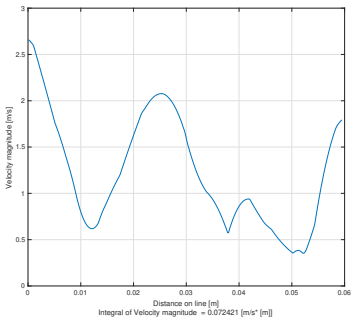

Figure C.14: Local Velocity line plot between the leading front and tail of two impellers.

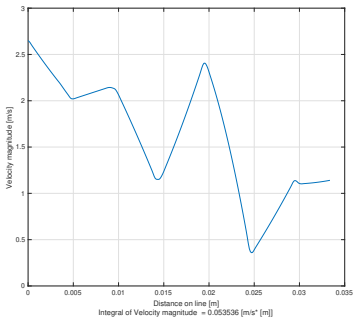

Figure C.15: Local Velocity line plot perpendicular on the leading front of the impeller. See figure 3.12 for clarification.

C.1.4. Polystyrene 2mm, Cvd = 0.03, Speed 1410 RPM

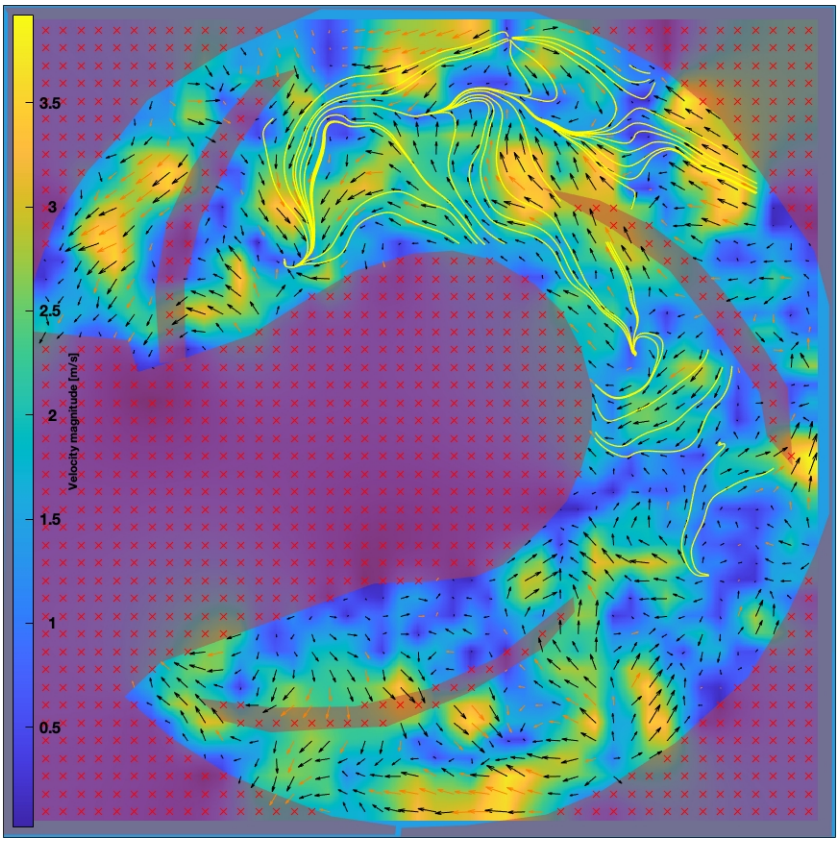

Figure C.16: PIVlab analysis of the streamlines and trajectories.

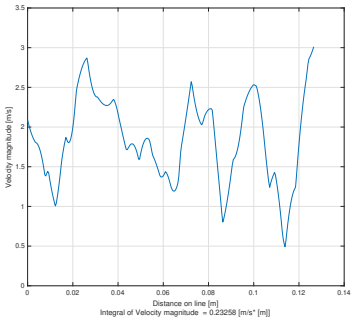

Figure C.17: Local Velocity line plot of the eddy in longitudinal direction.

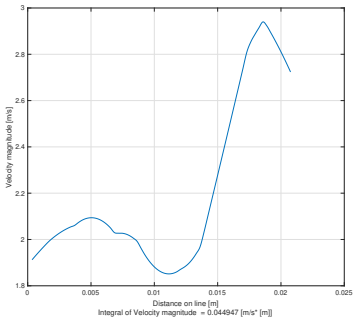

Figure C.18: Local Velocity line plot of the eddy in transverse direction.

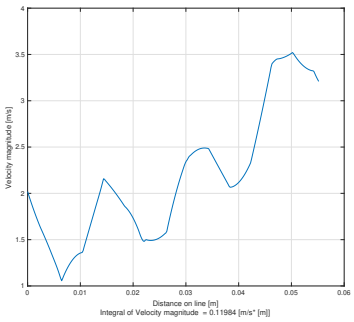

Figure C.19: Local Velocity line plot between the leading front and tail of two impellers.

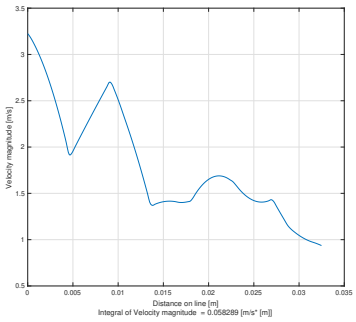

Figure C.20: Local Velocity line plot perpendicular on the leading front of the impeller. See figure 3.12 for clarification.

C.2. Mixture Phase streamline/trajectories verification

C.2.1. Glass beads 1.5mm, Cvd = 0.03, Speed 564 RPM

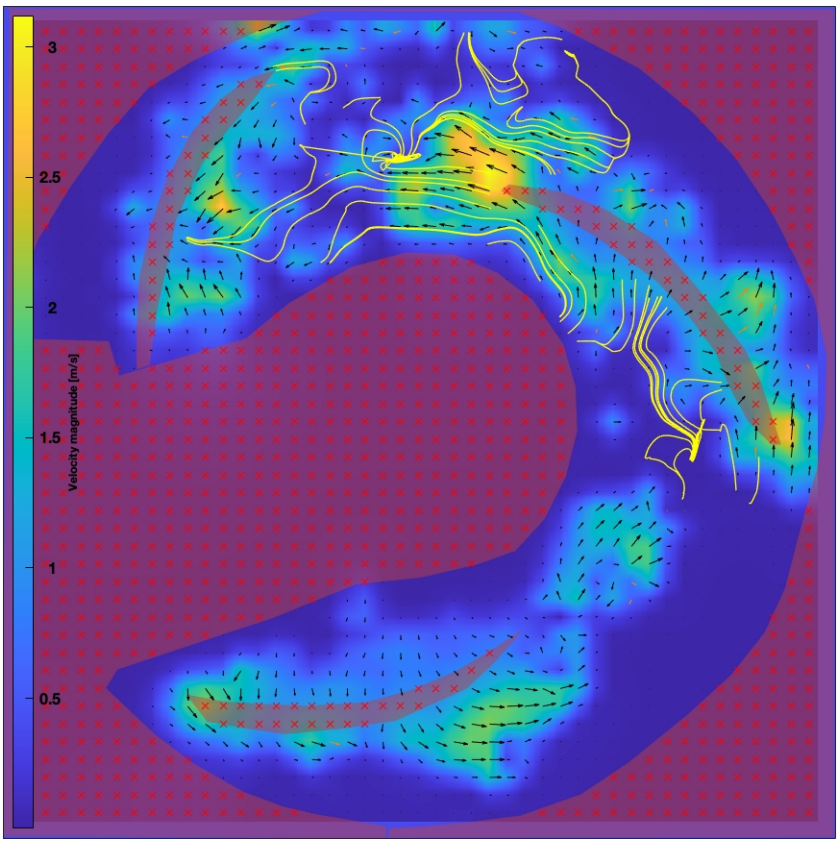

Figure C.21: PIVlab analysis of the streamlines and trajectories.

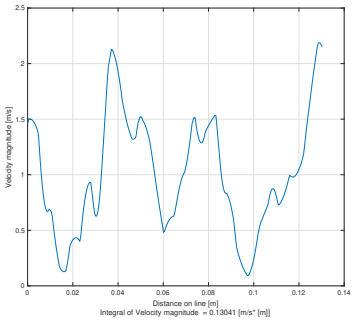

Figure C.22: Local Velocity line plot of the eddy in longitudinal direction.

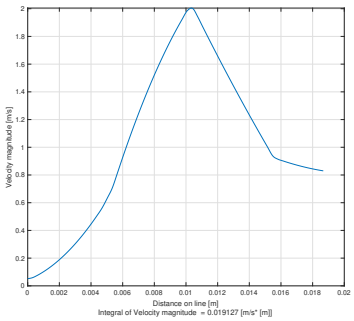

Figure C.23: Local Velocity line plot of the eddy in transverse direction.

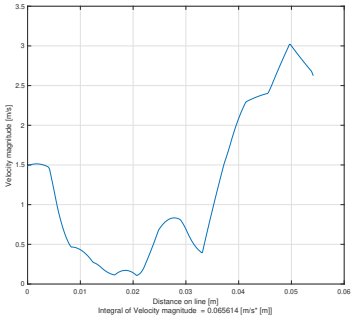

Figure C.24: Local Velocity line plot between the leading front and tail of two impellers.

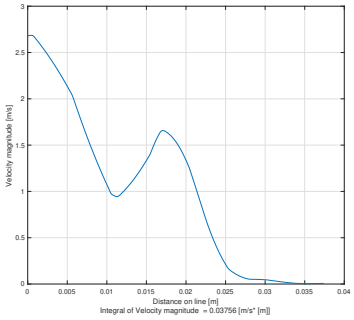

Figure C.25: Local Velocity line plot perpendicular on the leading front of the impeller. See figure 3.12 for clarification.

C.2.2. Glass beads 1.5mm, Cvd = 0.03, Speed 846 RPM

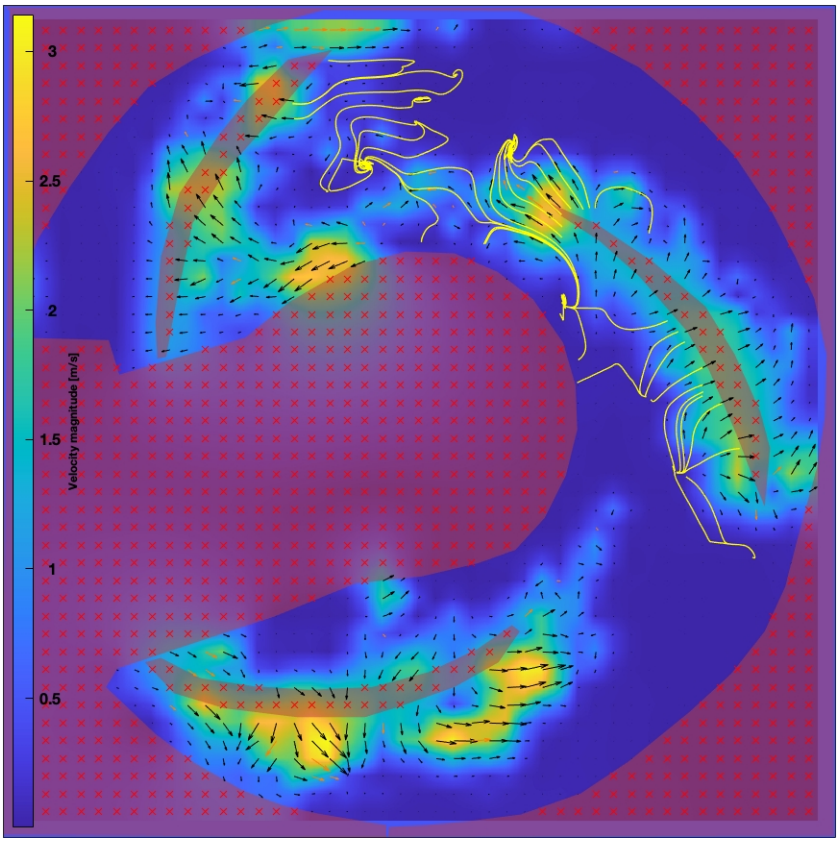

Figure C.26: PIVlab analysis of the streamlines and trajectories.

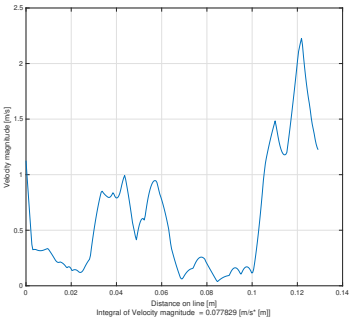

Figure C.27: Local Velocity line plot of the eddy in longitudinal direction.

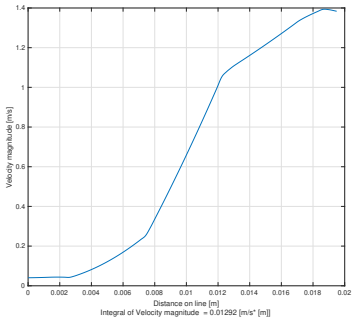

Figure C.28: Local Velocity line plot of the eddy in transverse direction.

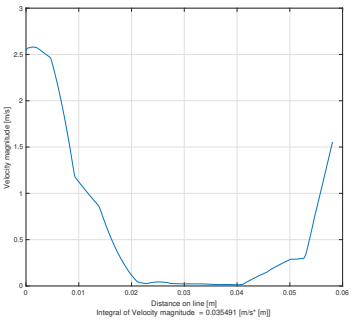

Figure C.29: Local Velocity line plot between the leading front and tail of two impellers.

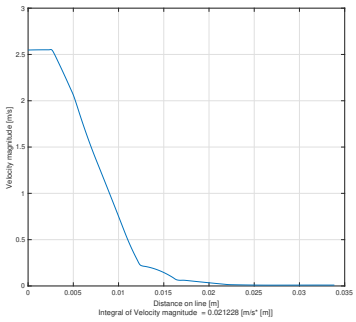

Figure C.30: Local Velocity line plot perpendicular on the leading front of the impeller. See figure 3.12 for clarification.

C.2.3. Glass beads 1.5mm, Cvd = 0.03, Speed 1128 RPM

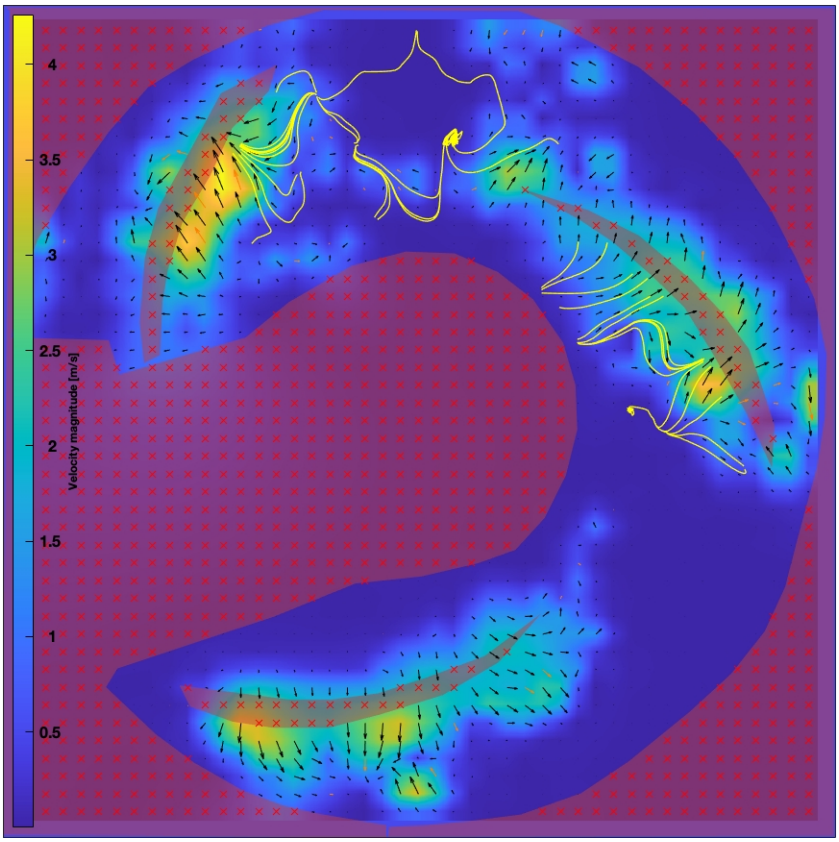

Figure C.31: PIVlab analysis of the streamlines and trajectories.

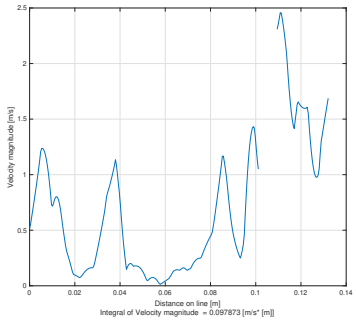

Figure C.32: Local Velocity line plot of the eddy in longitudinal direction.

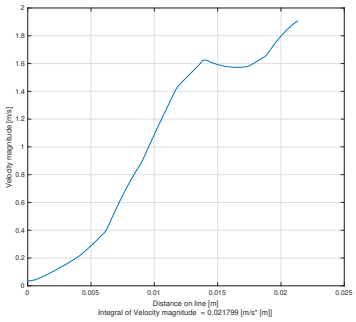

Figure C.33: Local Velocity line plot of the eddy in transverse direction.

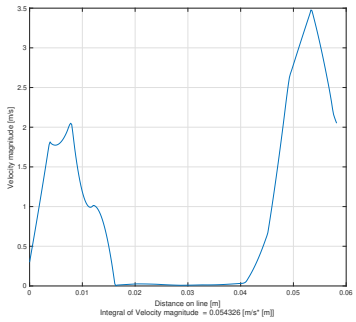

Figure C.34: Local Velocity line plot between the leading front and tail of two impellers.

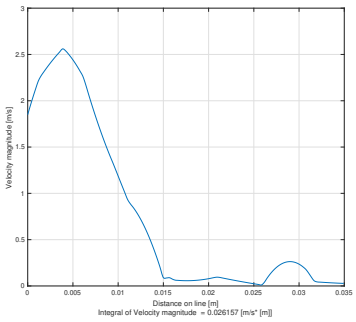

Figure C.35: Local Velocity line plot perpendicular on the leading front of the impeller. See figure 3.12 for clarification.

C.2.4. Glass beads 1.5mm, Cvd = 0.03, Speed 1410 RPM

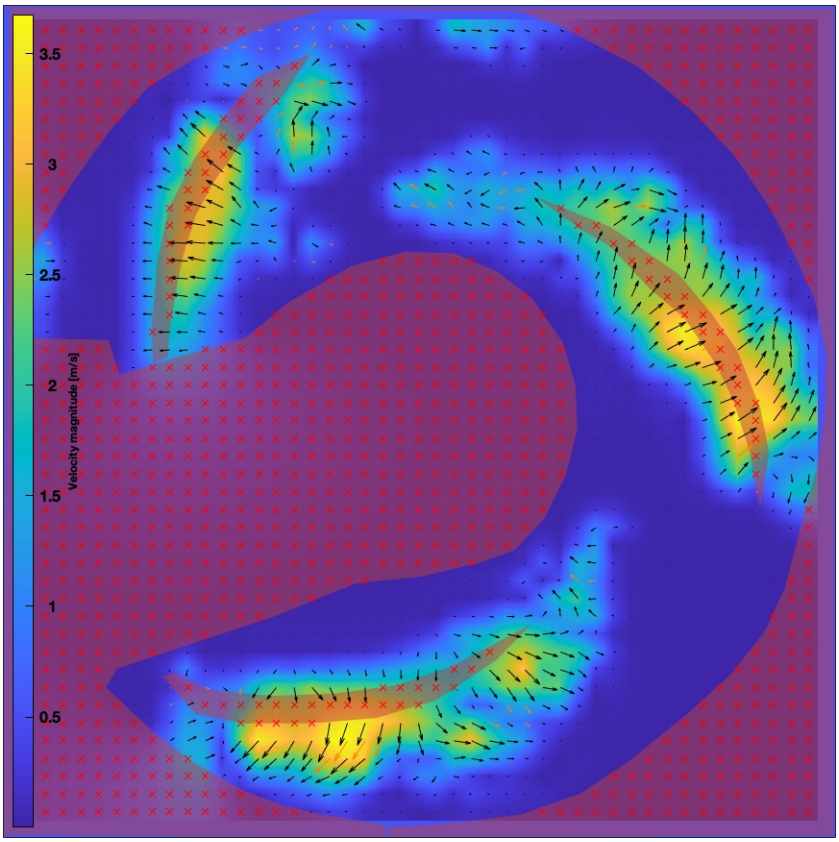

Figure C.36: PIVlab analysis of the streamlines and trajectories.

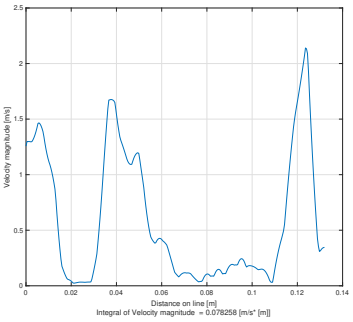

Figure C.37: Local Velocity line plot of the eddy in longitudinal direction.

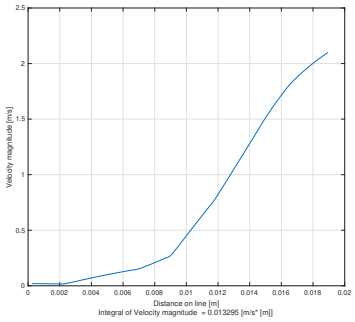

Figure C.38: Local Velocity line plot of the eddy in transverse direction.

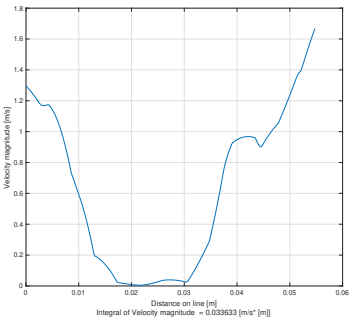

Figure C.39: Local Velocity line plot between the leading front and tail of two impellers.

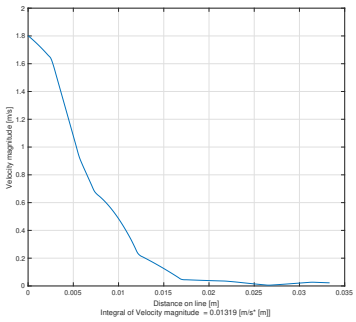

Figure C.40: Local Velocity line plot perpendicular on the leading front of the impeller. See figure 3.12 for clarification.

C.2.5. Glass beads 1.5mm, Cvd = 0.05, Speed 564 RPM

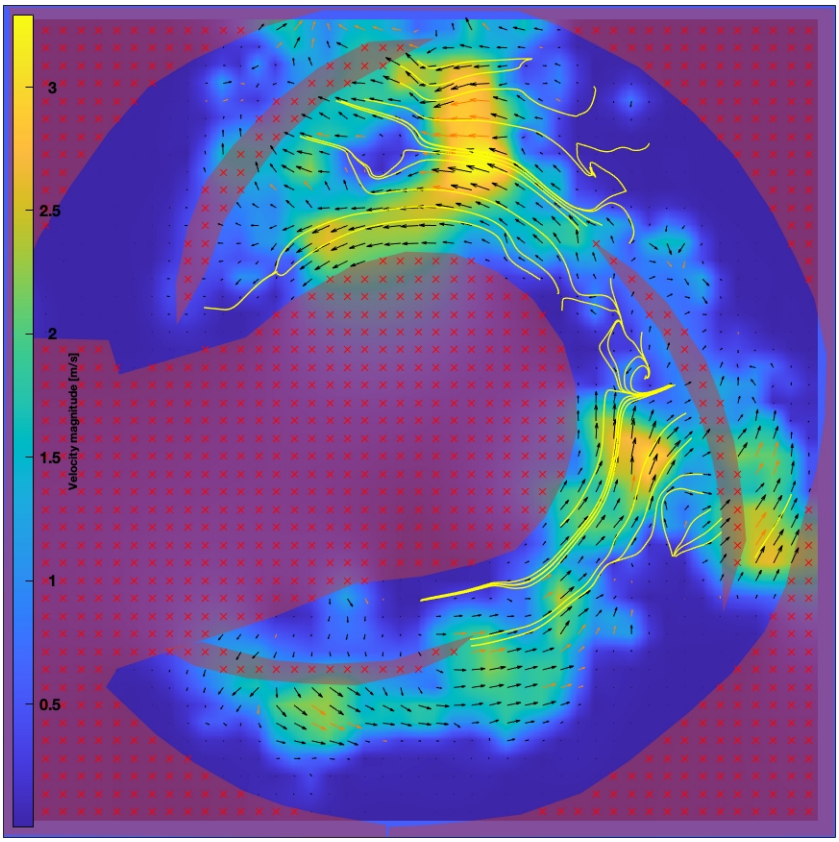

Figure C.41: PIVlab analysis of the streamlines and trajectories.

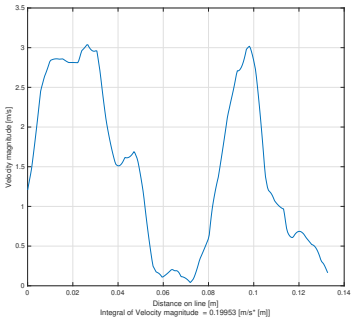

Figure C.42: Local Velocity line plot of the eddy in longitudinal direction.

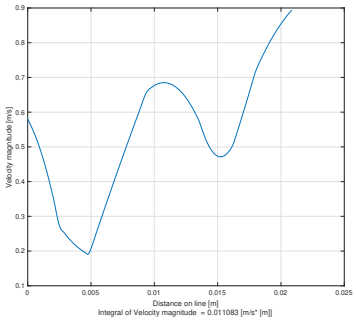

Figure C.43: Local Velocity line plot of the eddy in transverse direction.

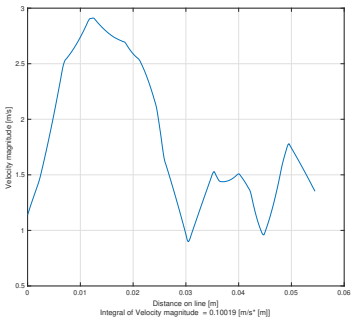

Figure C.44: Local Velocity line plot between the leading front and tail of two impellers.

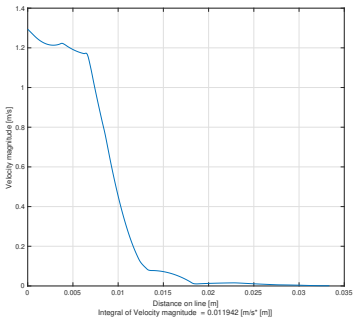

Figure C.45: Local Velocity line plot perpendicular on the leading front of the impeller. See figure 3.12 for clarification.

C.2.6. Glass beads 1.5mm, Cvd = 0.05, Speed 846 RPM

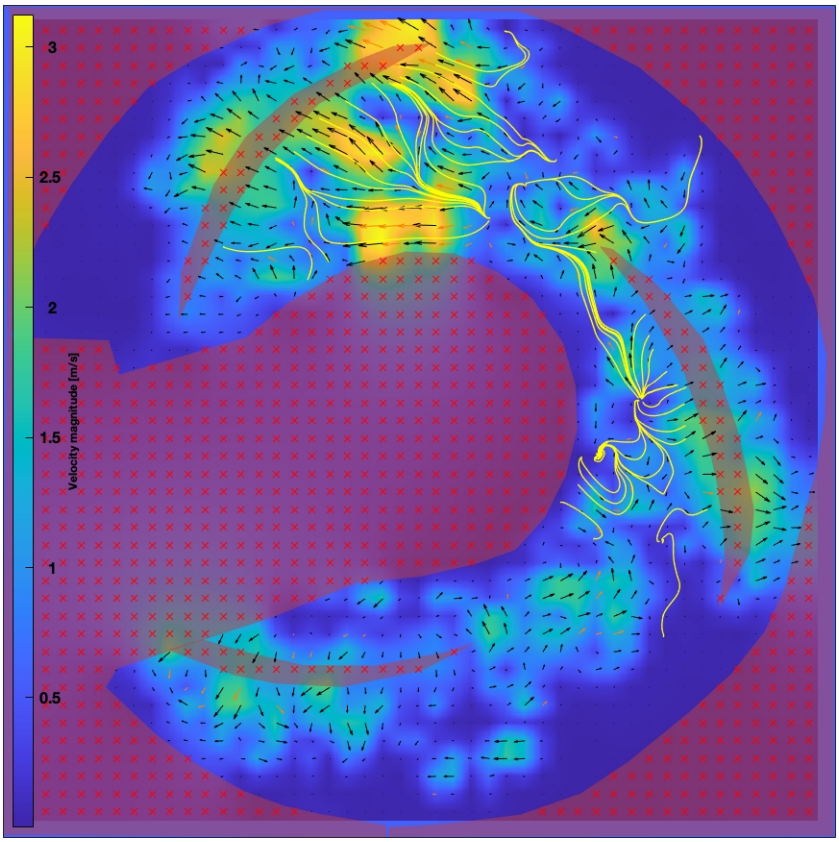

Figure C.46: PIVlab analysis of the streamlines and trajectories.

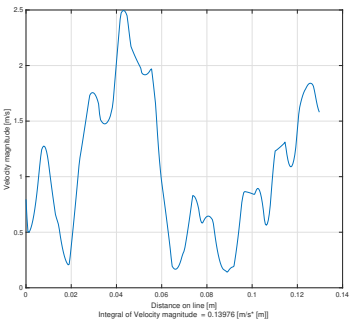

Figure C.47: Local Velocity line plot of the eddy in longitudinal direction.

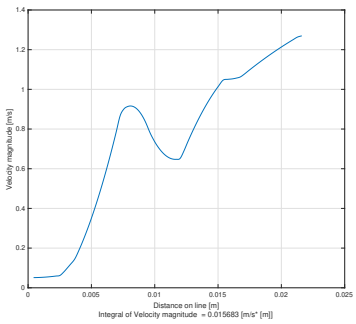

Figure C.48: Local Velocity line plot of the eddy in transverse direction.

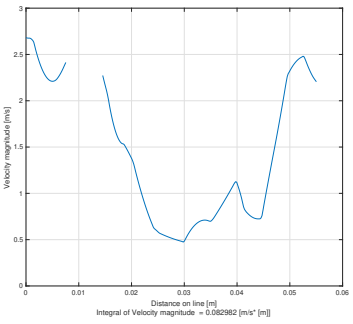

Figure C.49: Local Velocity line plot between the leading front and tail of two impellers.

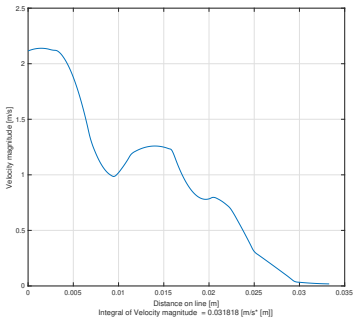

Figure C.50: Local Velocity line plot perpendicular on the leading front of the impeller. See figure 3.12 for clarification.

C.2.7. Glass beads 1.5mm, Cvd = 0.05, Speed 1128 RPM

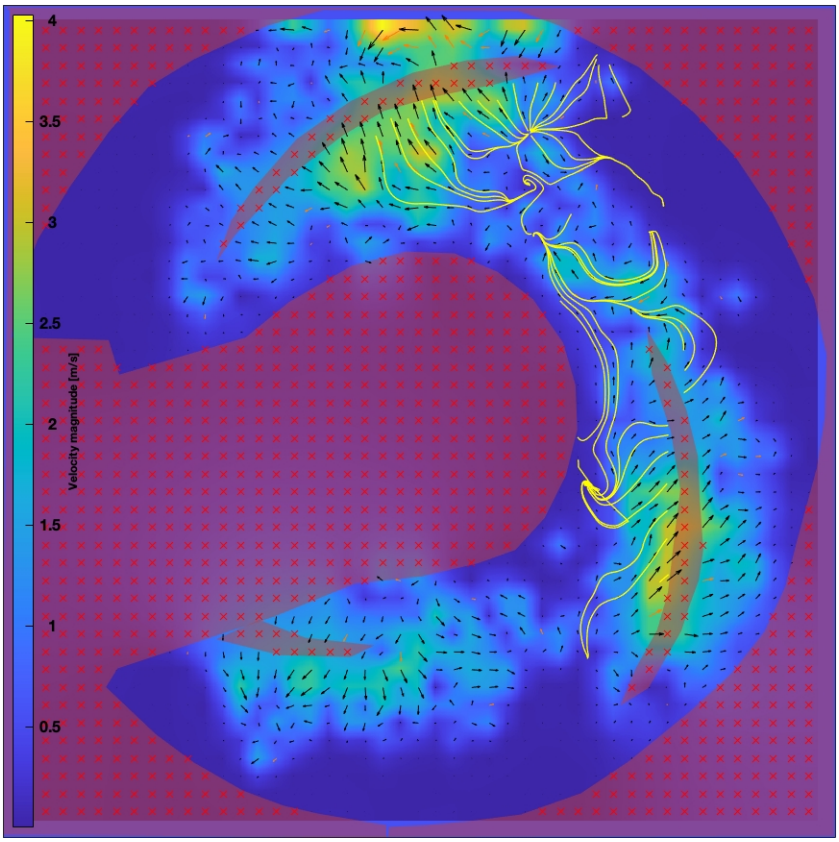

Figure C.51: PIVlab analysis of the streamlines and trajectories.

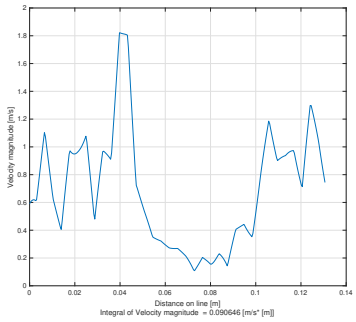

Figure C.52: Local Velocity line plot of the eddy in longitudinal direction.

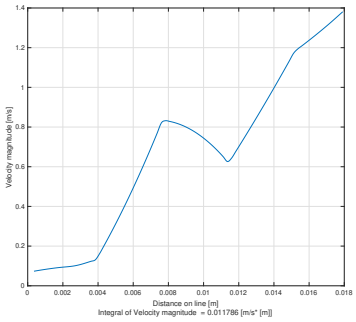

Figure C.53: Local Velocity line plot of the eddy in transverse direction.

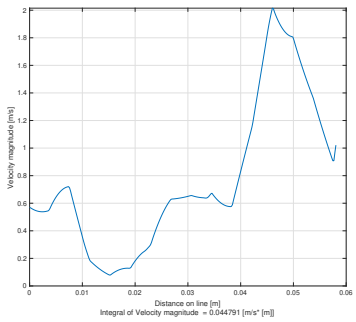

Figure C.54: Local Velocity line plot between the leading front and tail of two impellers.

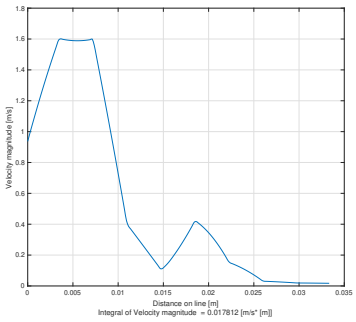

Figure C.55: Local Velocity line plot perpendicular on the leading front of the impeller. See figure 3.12 for clarification.

C.2.8. Glass beads 1.5mm, Cvd = 0.05, Speed 1410 RPM

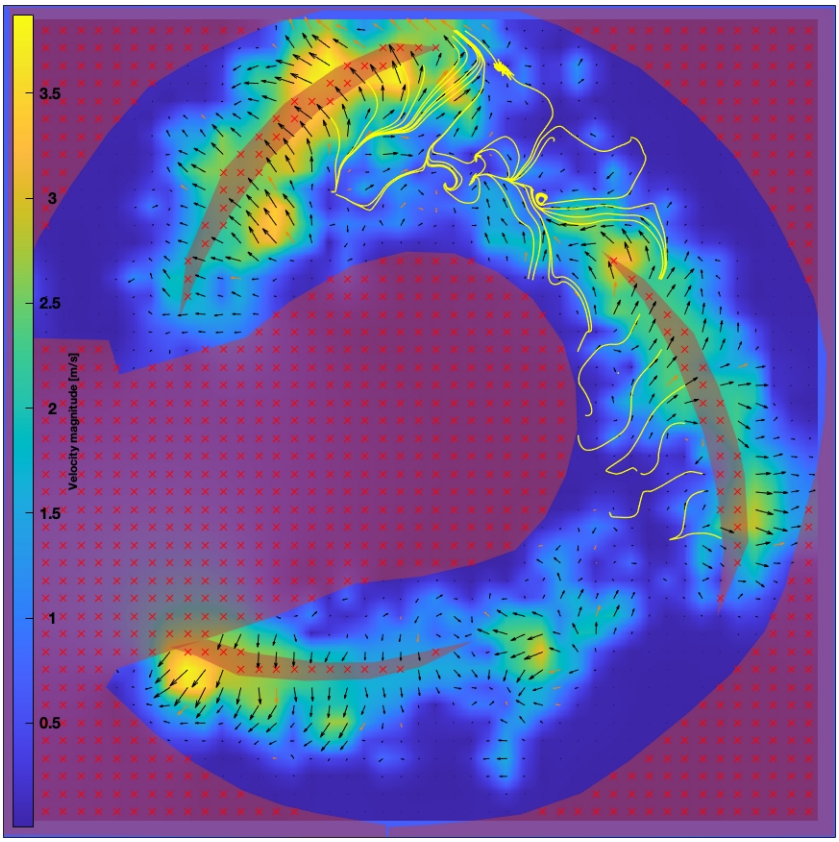

Figure C.56: PIVlab analysis of the streamlines and trajectories.

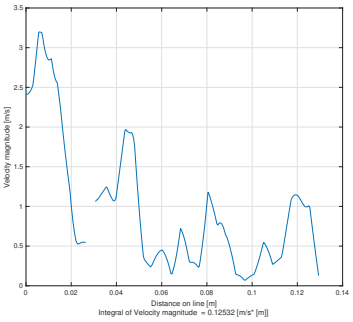

Figure C.57: Local Velocity line plot of the eddy in longitudinal direction.

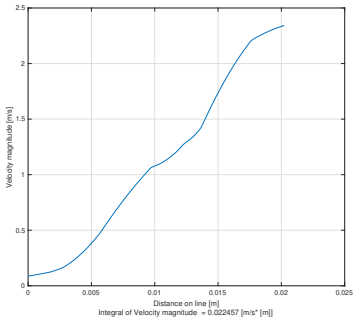

Figure C.58: Local Velocity line plot of the eddy in transverse direction.

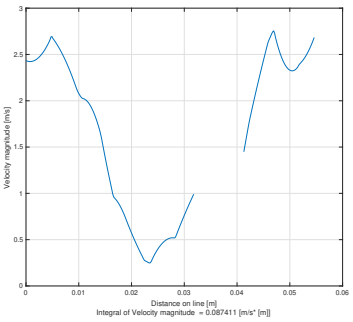

Figure C.59: Local Velocity line plot between the leading front and tail of two impellers.

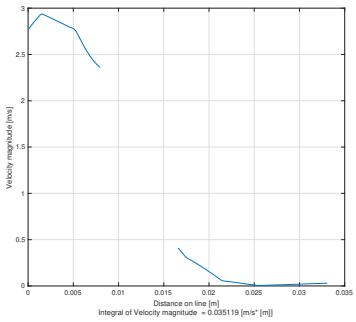

Figure C.60: Local Velocity line plot perpendicular on the leading front of the impeller. See figure 3.12 for clarification.

C.2.9. Glass beads 1.5mm, Cvd = 0.08, Speed 564 RPM

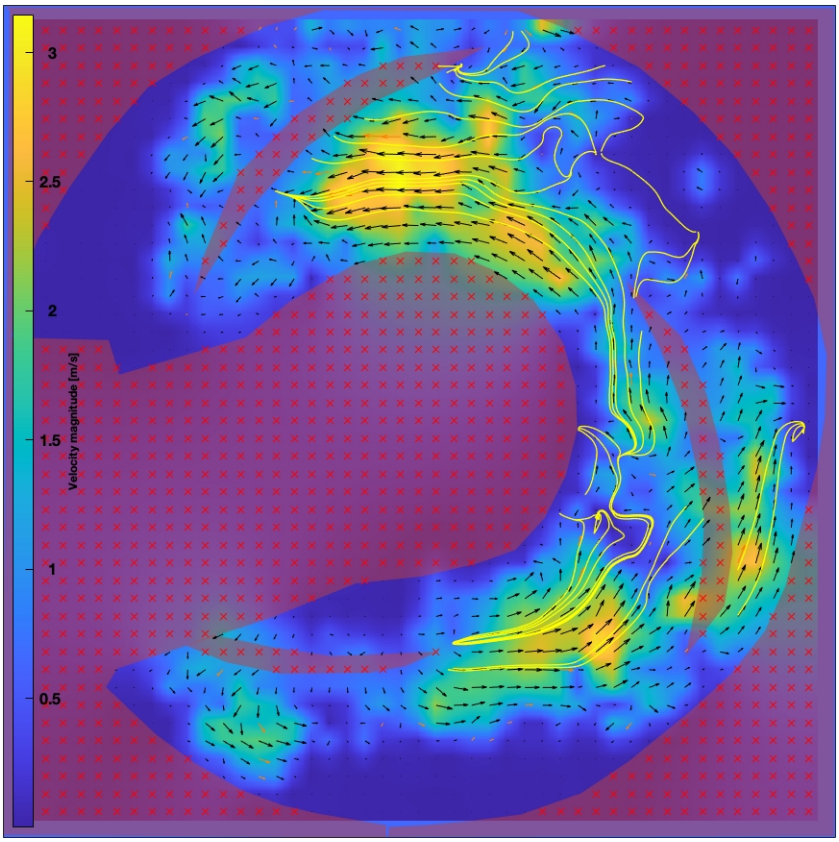

Figure C.61: PIVlab analysis of the streamlines and trajectories.

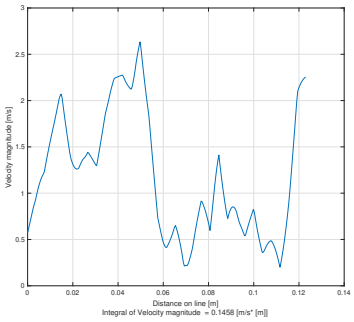

Figure C.62: Local Velocity line plot of the eddy in longitudinal direction.

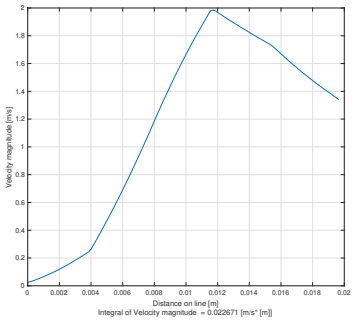

Figure C.63: Local Velocity line plot of the eddy in transverse direction.

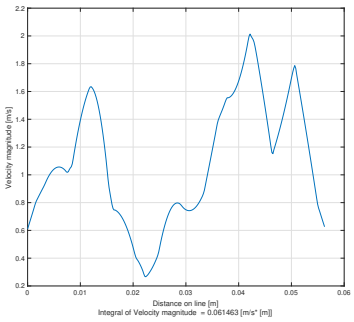

Figure C.64: Local Velocity line plot between the leading front and tail of two impellers.

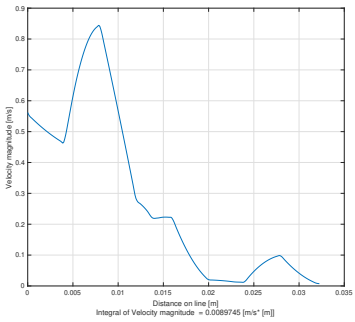

Figure C.65: Local Velocity line plot perpendicular on the leading front of the impeller. See figure 3.12 for clarification.

C.2.10. Glass beads 1.5mm, Cvd = 0.08, Speed 846 RPM

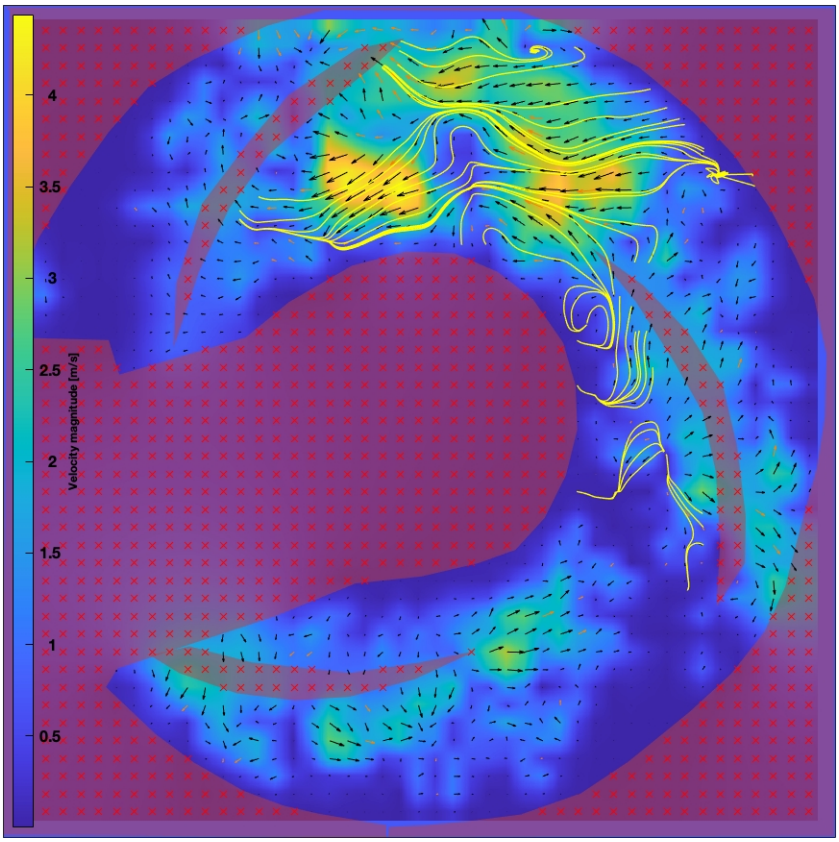

Figure C.66: PIVlab analysis of the streamlines and trajectories.

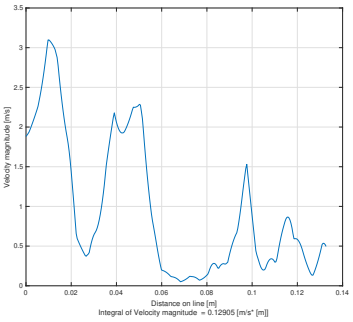

Figure C.67: Local Velocity line plot of the eddy in longitudinal direction.

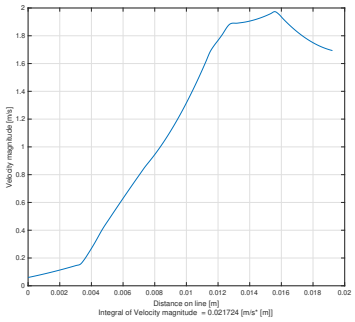

Figure C.68: Local Velocity line plot of the eddy in transverse direction.

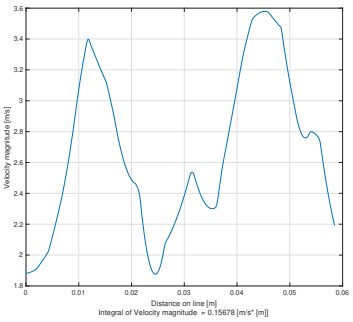

Figure C.69: Local Velocity line plot between the leading front and tail of two impellers.

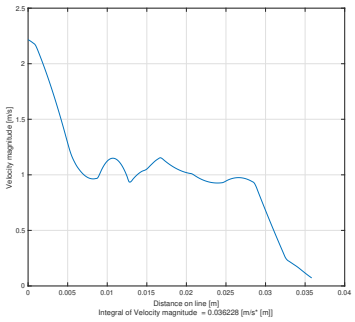

Figure C.70: Local Velocity line plot perpendicular on the leading front of the impeller. See figure 3.12 for clarification.

C.2.11. Glass beads 1.5mm, Cvd = 0.08, Speed 1128 RPM

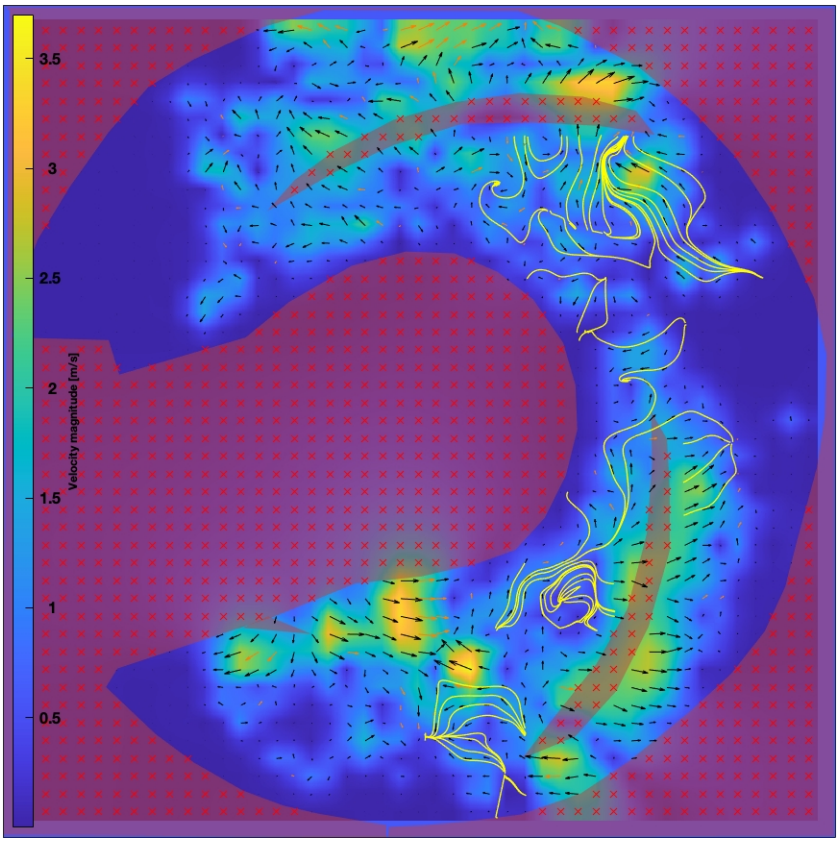

Figure C.71: PIVlab analysis of the streamlines and trajectories.

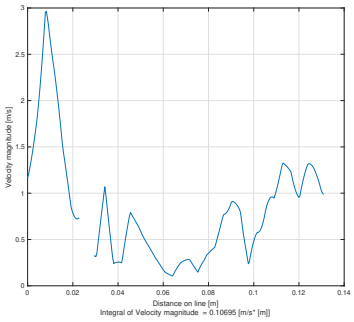

Figure C.72: Local Velocity line plot of the eddy in longitudinal direction.

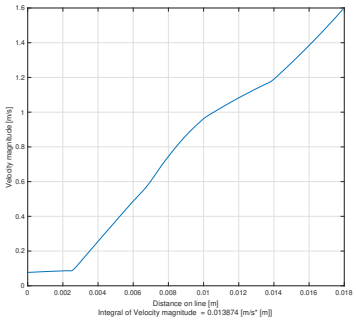

Figure C.73: Local Velocity line plot of the eddy in transverse direction.

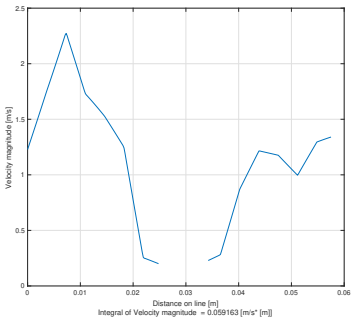

Figure C.74: Local Velocity line plot between the leading front and tail of two impellers.

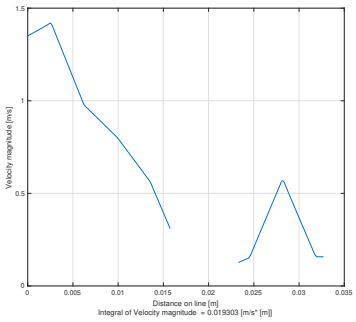

Figure C.75: Local Velocity line plot perpendicular on the leading front of the impeller. See figure 3.12 for clarification.

C.2.12. Glass beads 1.5mm, Cvd = 0.08, Speed 1410 RPM

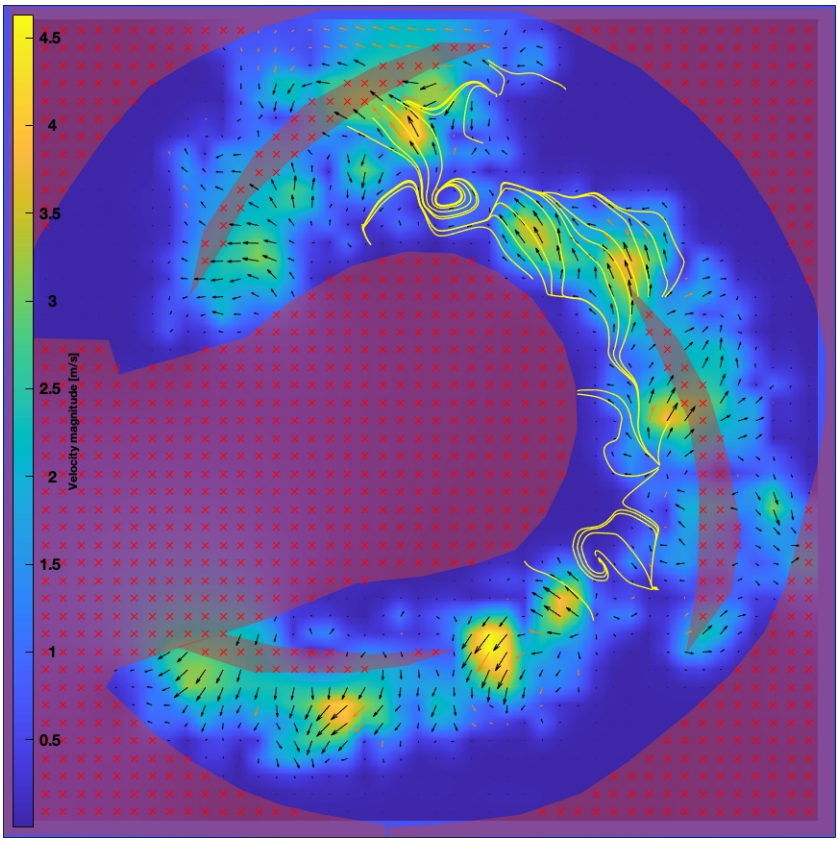

Figure C.76: PIVlab analysis of the streamlines and trajectories.

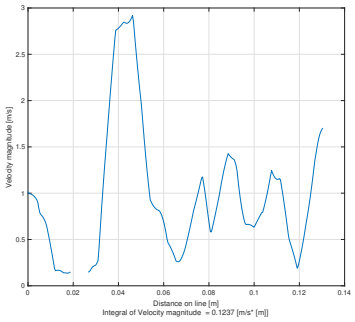

Figure C.77: Local Velocity line plot of the eddy in longitudinal direction.

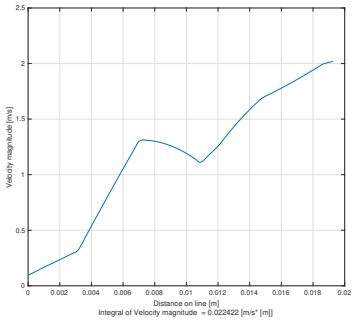

Figure C.78: Local Velocity line plot of the eddy in transverse direction.

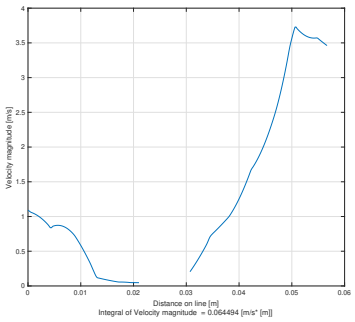

Figure C.79: Local Velocity line plot between the leading front and tail of two impellers.

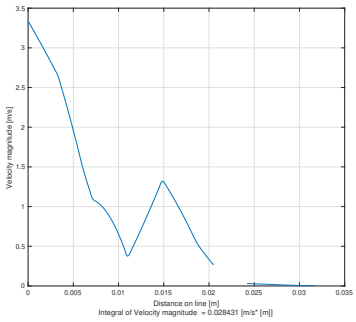

Figure C.80: Local Velocity line plot perpendicular on the leading front of the impeller. See figure 3.12 for clarification.

C.2.13. Glass beads 1.5mm, Cvd = 0.12, Speed 564 RPM

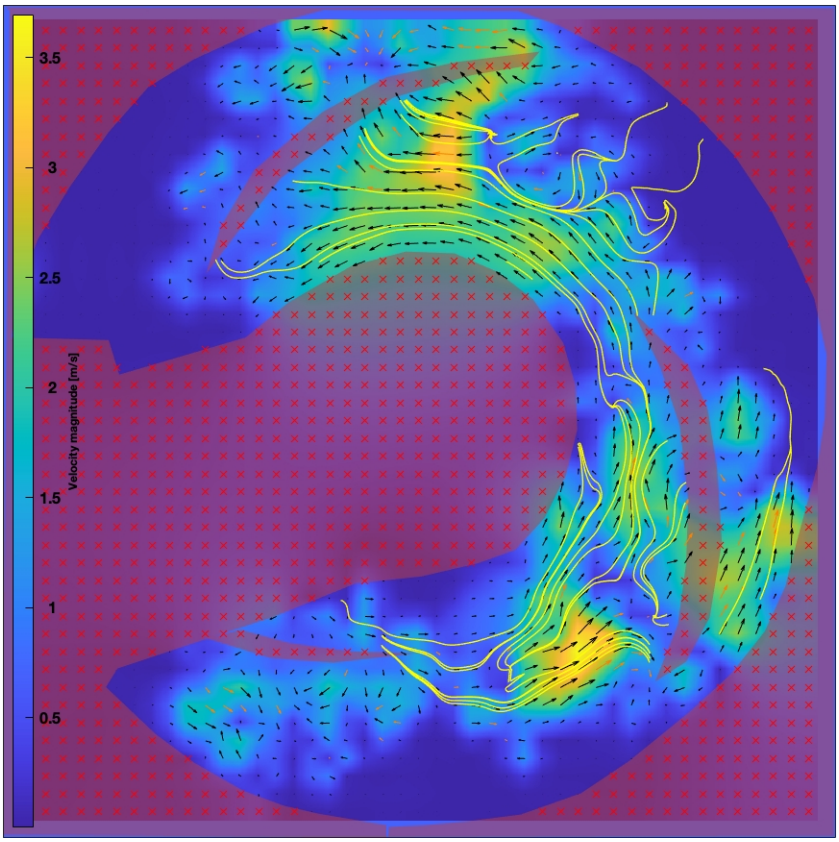

Figure C.81: PIVlab analysis of the streamlines and trajectories.

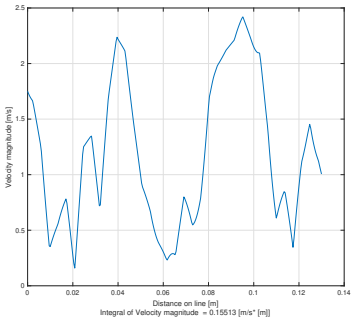

Figure C.82: Local Velocity line plot of the eddy in longitudinal direction.

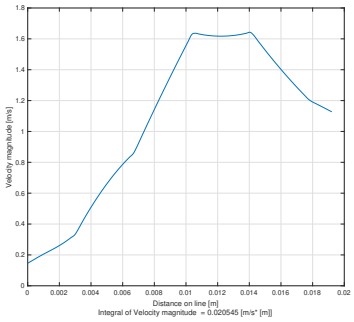

Figure C.83: Local Velocity line plot of the eddy in transverse direction.

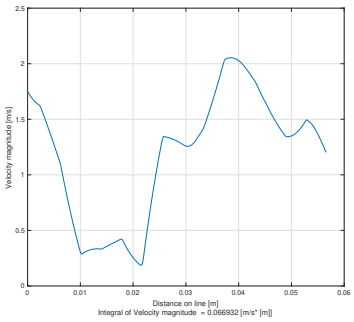

Figure C.84: Local Velocity line plot between the leading front and tail of two impellers.

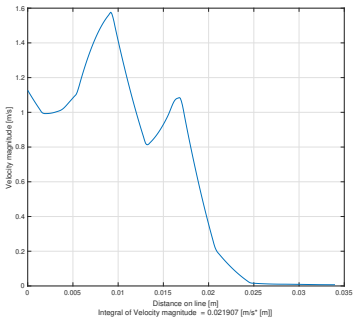

Figure C.85: Local Velocity line plot perpendicular on the leading front of the impeller. See figure 3.12 for clarification.

C.2.14. Glass beads 1.5mm, Cvd = 0.12, Speed 846 RPM

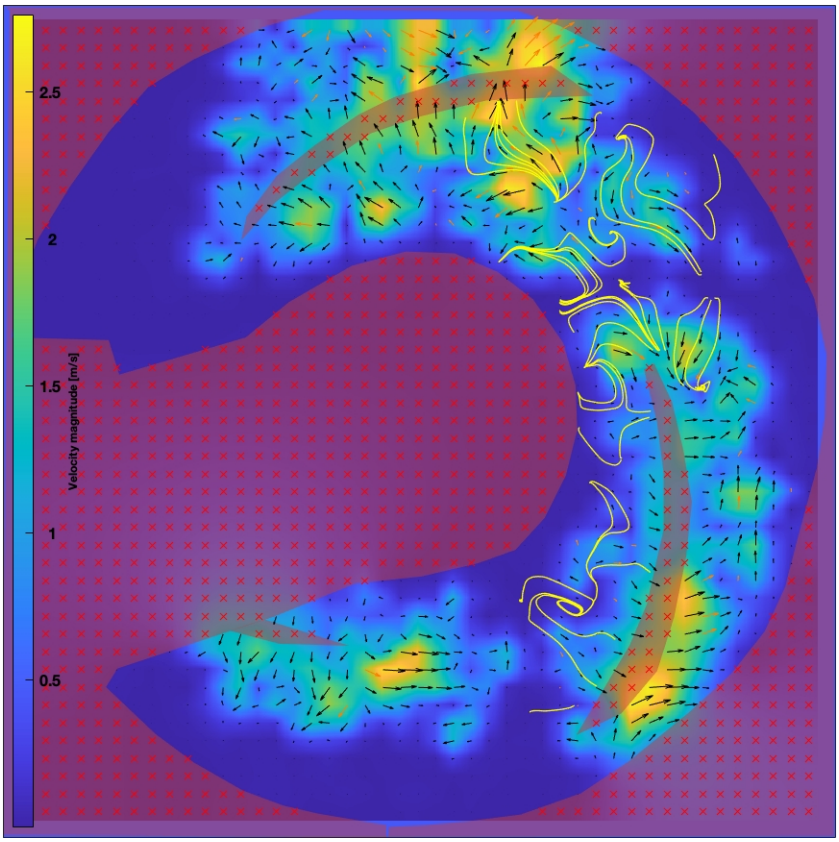

Figure C.86: PIVlab analysis of the streamlines and trajectories.

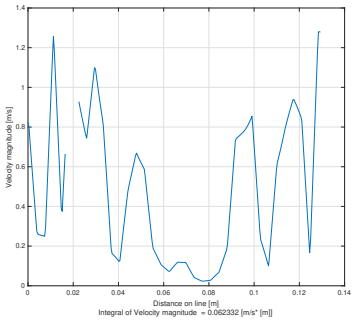

Figure C.87: Local Velocity line plot of the eddy in longitudinal direction.

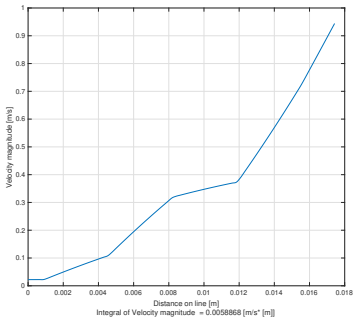

Figure C.88: Local Velocity line plot of the eddy in transverse direction.

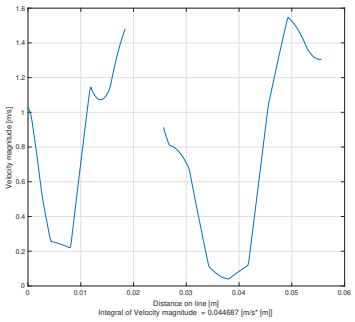

Figure C.89: Local Velocity line plot between the leading front and tail of two impellers.

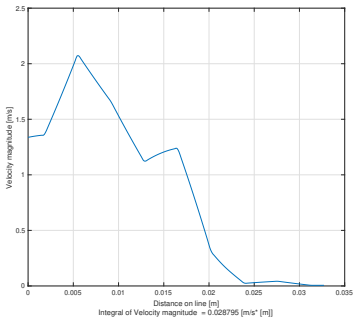

Figure C.90: Local Velocity line plot perpendicular on the leading front of the impeller. See figure 3.12 for clarification.

C.2.15. Glass beads 1.5mm, Cvd = 0.12, Speed 1128 RPM

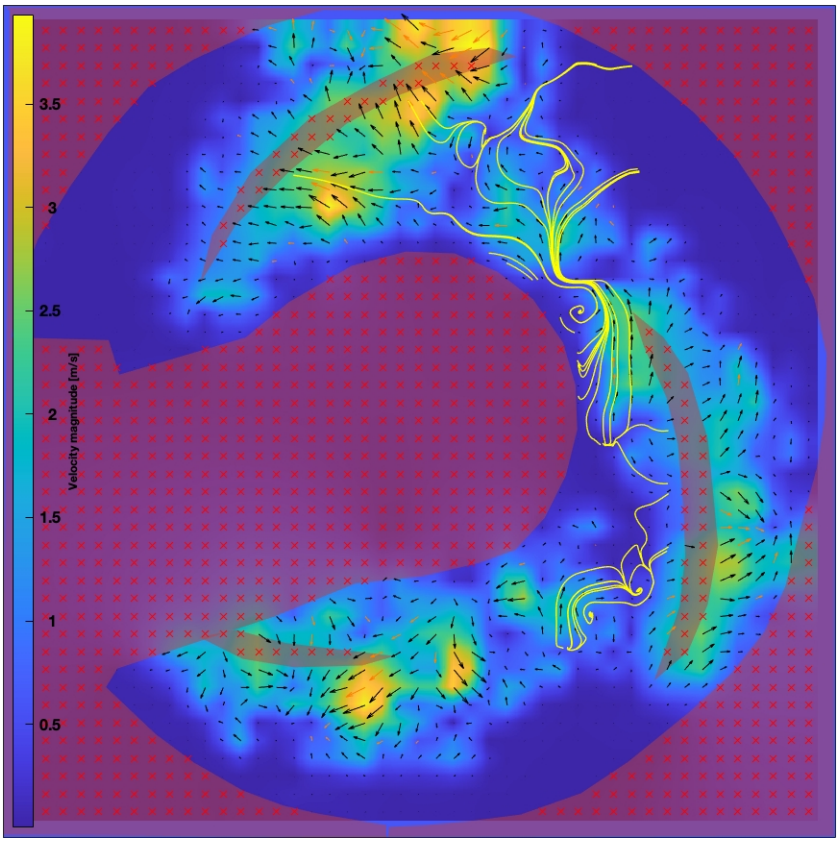

Figure C.91: PIVlab analysis of the streamlines and trajectories.

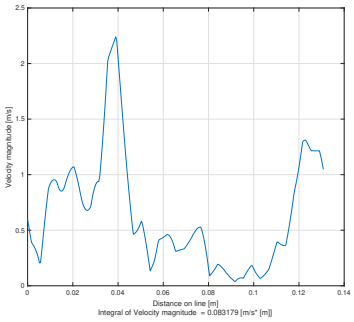

Figure C.92: Local Velocity line plot of the eddy in longitudinal direction.

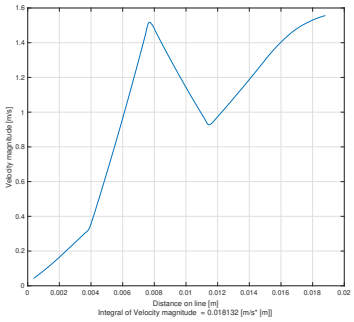

Figure C.93: Local Velocity line plot of the eddy in transverse direction.

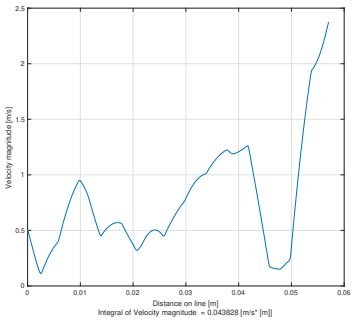

Figure C.94: Local Velocity line plot between the leading front and tail of two impellers.

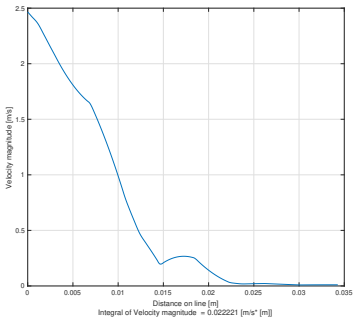

Figure C.95: Local Velocity line plot perpendicular on the leading front of the impeller. See figure 3.12 for clarification.

C.2.16. Glass beads 1.5mm, Cvd = 0.12, Speed 1410 RPM

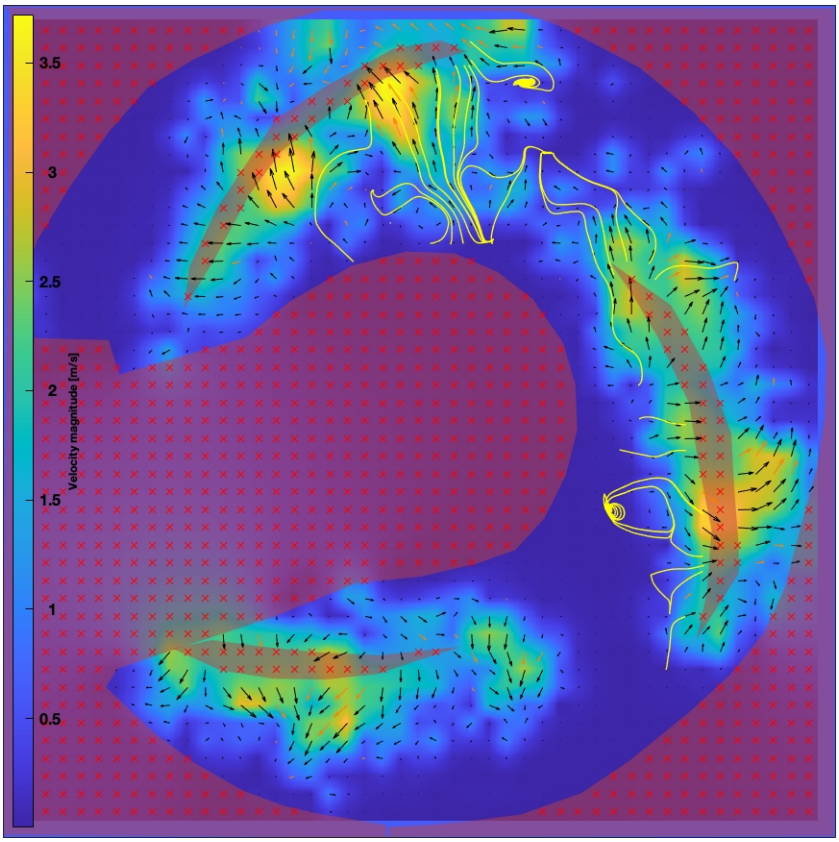

Figure C.96: PIVlab analysis of the streamlines and trajectories.

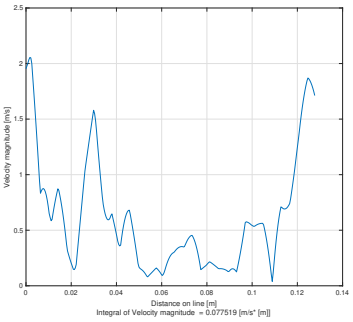

Figure C.97: Local Velocity line plot of the eddy in longitudinal direction.

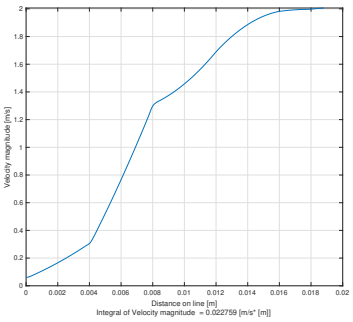

Figure C.98: Local Velocity line plot of the eddy in transverse direction.

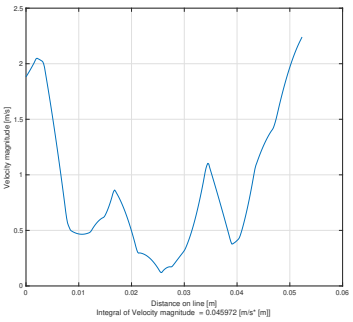

Figure C.99: Local Velocity line plot between the leading front and tail of two impellers.

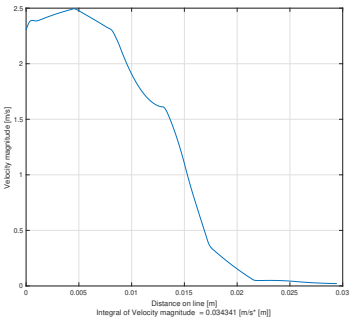

Figure C.100: Local Velocity line plot perpendicular on the leading front of the impeller. See figure 3.12 for clarification.

C.2.17. Glass beads 1.5mm, Cvd = 0.15, Speed 564 RPM

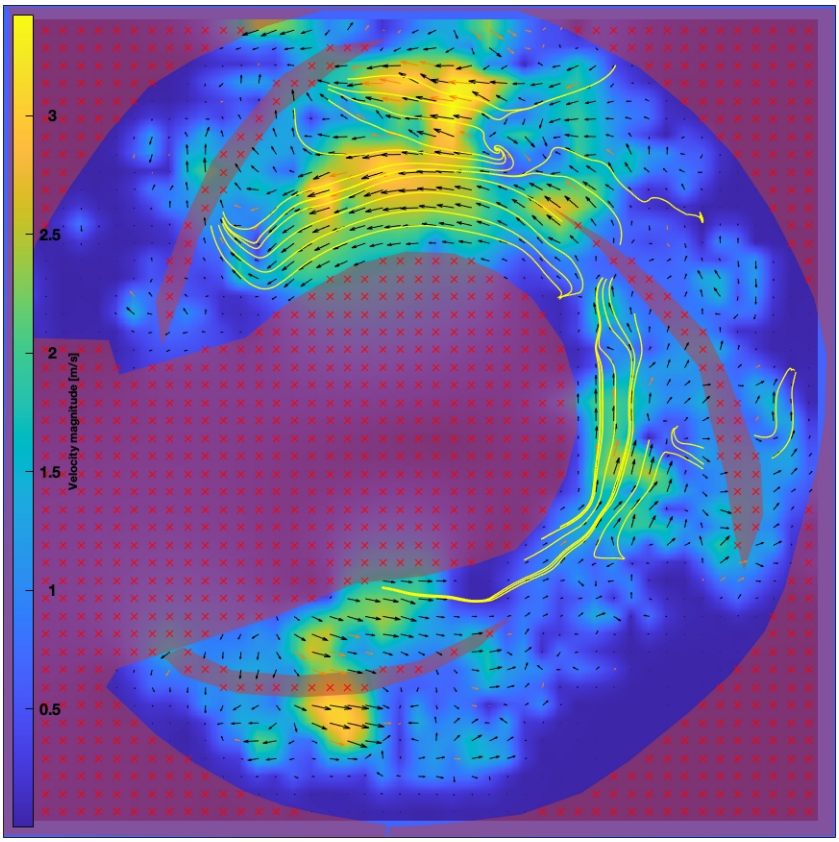

Figure C.101: PIVlab analysis of the streamlines and trajectories.

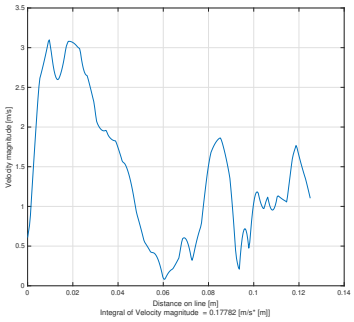

Figure C.102: Local Velocity line plot of the eddy in longitudinal direction.

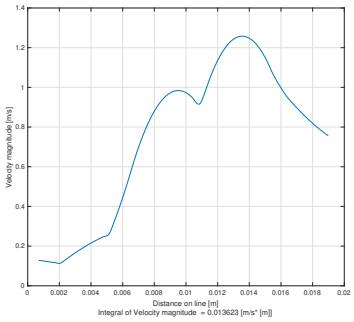

Figure C.103: Local Velocity line plot of the eddy in transverse direction.

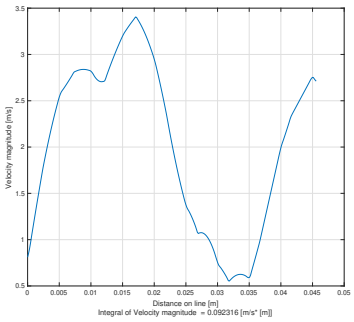

Figure C.104: Local Velocity line plot between the leading front and tail of two impellers.

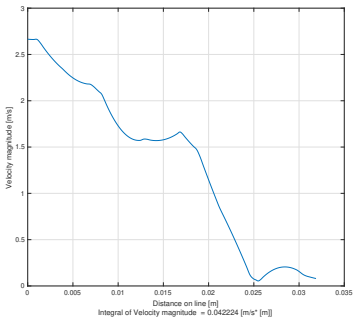

Figure C.105: Local Velocity line plot perpendicular on the leading front of the impeller. See figure 3.12 for clarification.

C.2.18. Glass beads 1.5mm, Cvd = 0.15, Speed 846 RPM

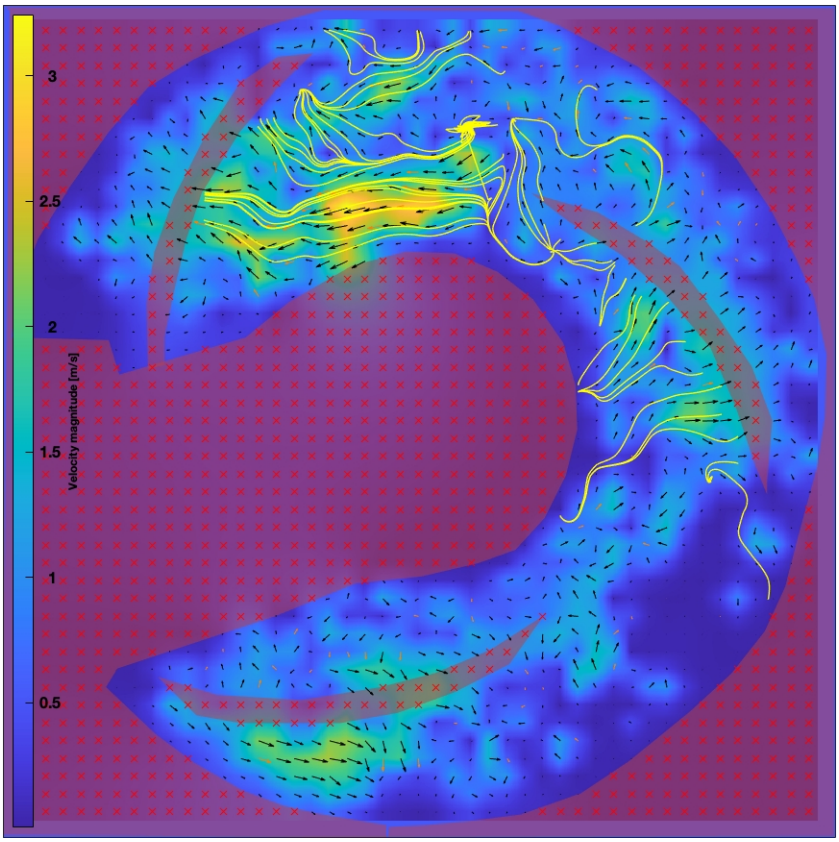

Figure C.106: PIVlab analysis of the streamlines and trajectories.

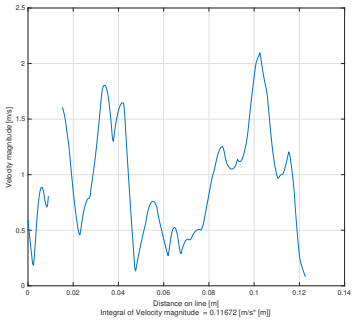

Figure C.107: Local Velocity line plot of the eddy in longitudinal direction.

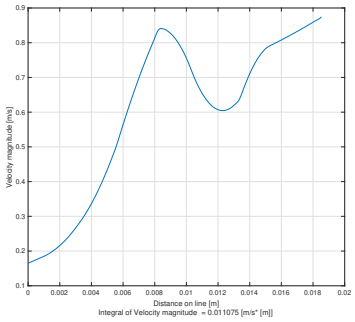

Figure C.108: Local Velocity line plot of the eddy in transverse direction.

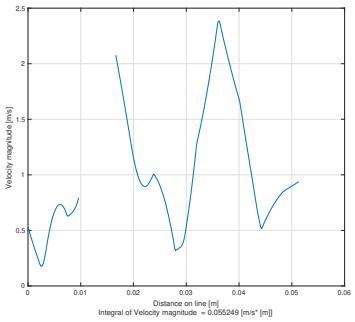

Figure C.109: Local Velocity line plot between the leading front and tail of two impellers.

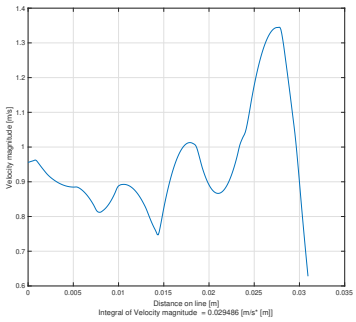

Figure C.110: Local Velocity line plot perpendicular on the leading front of the impeller. See figure 3.12 for clarification.

C.2.19. Glass beads 1.5mm, Cvd = 0.15, Speed 1128 RPM

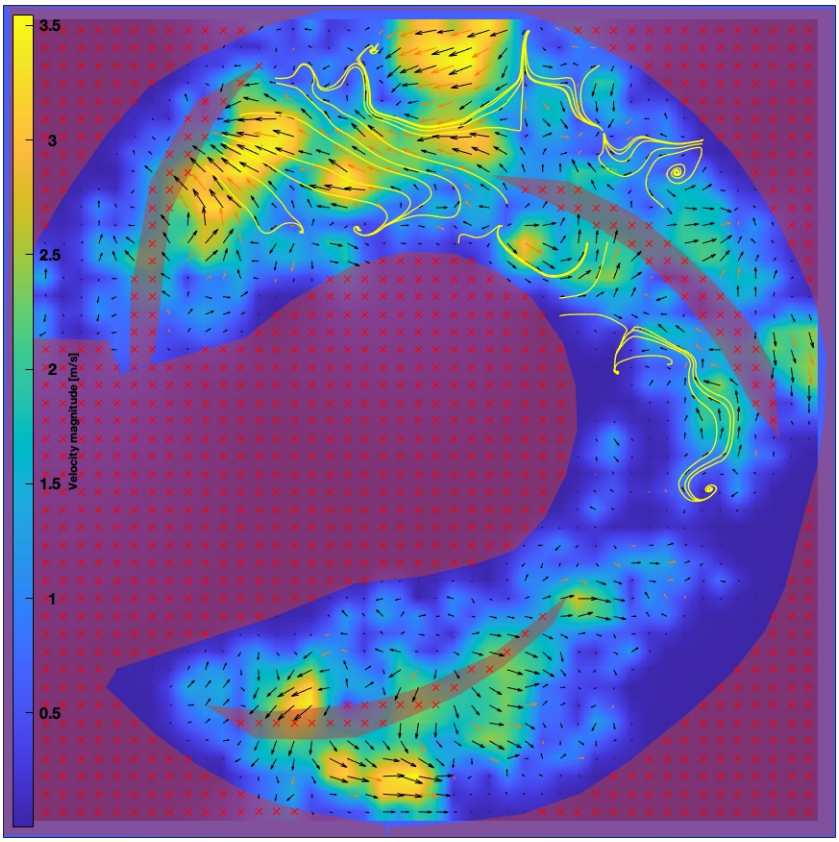

Figure C.111: PIVlab analysis of the streamlines and trajectories.

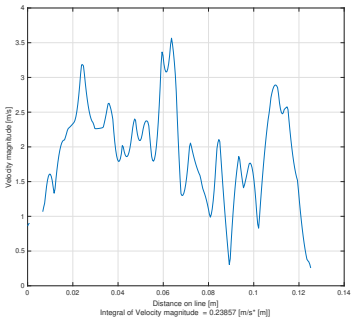

Figure C.112: Local Velocity line plot of the eddy in longitudinal direction.

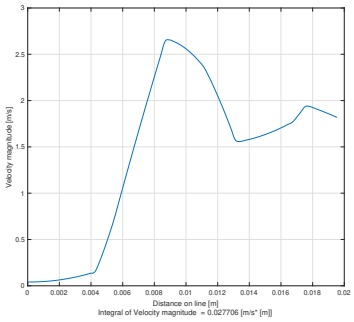

Figure C.113: Local Velocity line plot of the eddy in transverse direction.

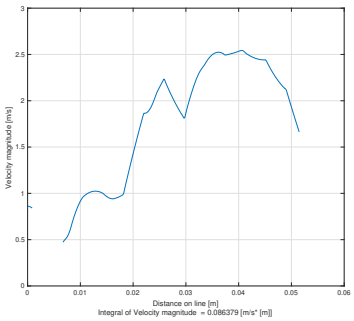

Figure C.114: Local Velocity line plot between the leading front and tail of two impellers.

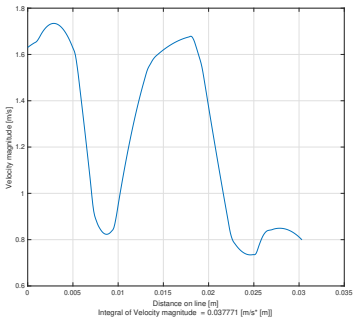

Figure C.115: Local Velocity line plot perpendicular on the leading front of the impeller. See figure 3.12 for clarification.

C.2.20. Glass beads 1.5mm, Cvd = 0.15, Speed 1410 RPM

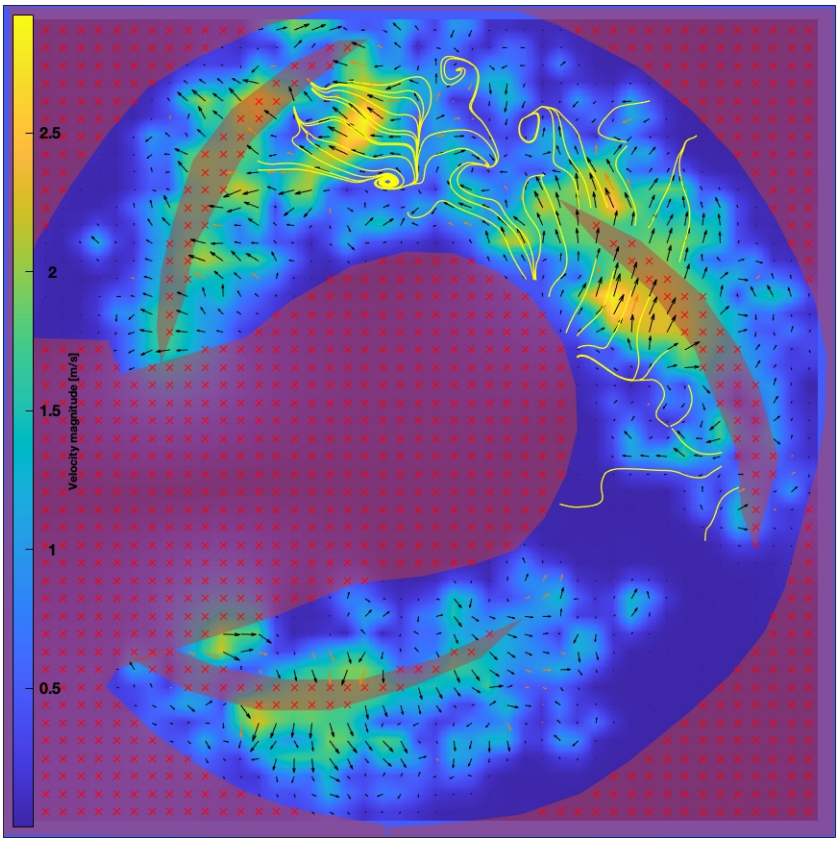

Figure C.116: PIVlab analysis of the streamlines and trajectories.

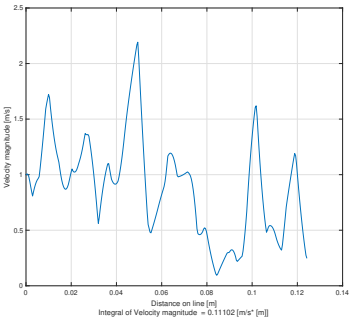

Figure C.117: Local Velocity line plot of the eddy in longitudinal direction.

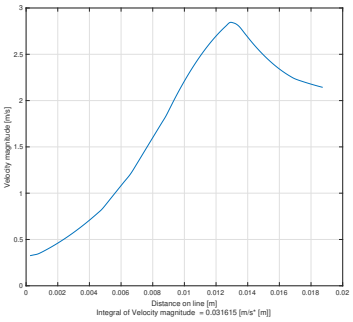

Figure C.118: Local Velocity line plot of the eddy in transverse direction.

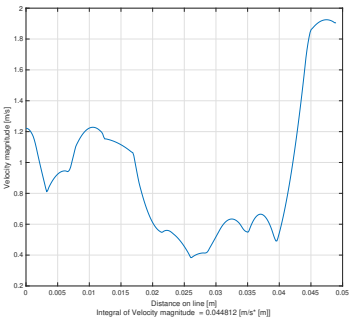

Figure C.119: Local Velocity line plot between the leading front and tail of two impellers.

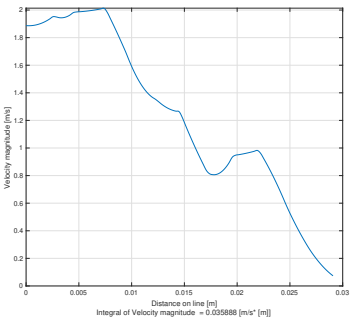

Figure C.120: Local Velocity line plot perpendicular on the leading front of the impeller. See figure 3.12 for clarification.

C.2.21. Glass beads 1.5mm, Cvd = 0.20, Speed 564 RPM

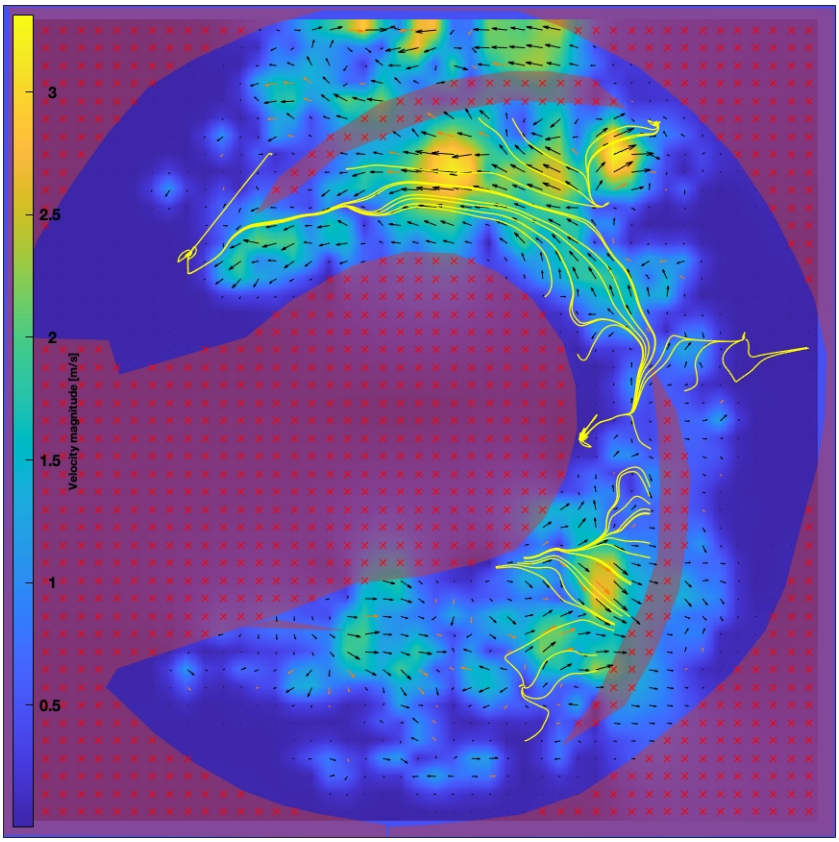

Figure C.121: PIVlab analysis of the streamlines and trajectories.

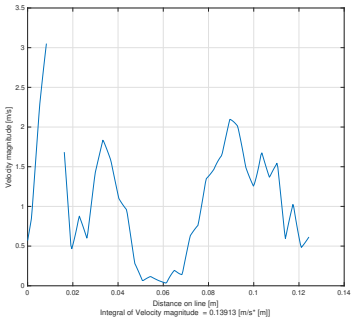

Figure C.122: Local Velocity line plot of the eddy in longitudinal direction.

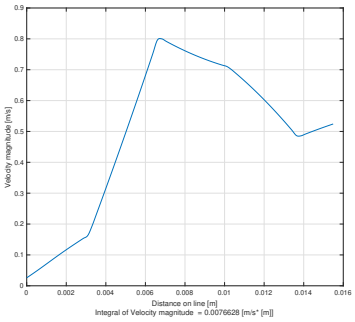

Figure C.123: Local Velocity line plot of the eddy in transverse direction.

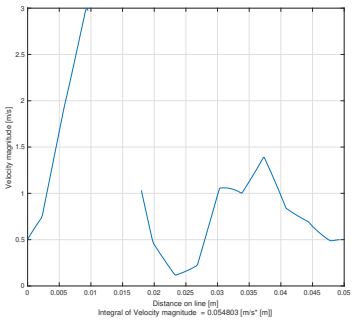

Figure C.124: Local Velocity line plot between the leading front and tail of two impellers.

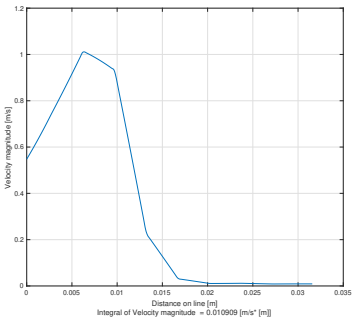

Figure C.125: Local Velocity line plot perpendicular on the leading front of the impeller. See figure 3.12 for clarification.

C.2.22. Glass beads 1.5mm, Cvd = 0.20, Speed 846 RPM

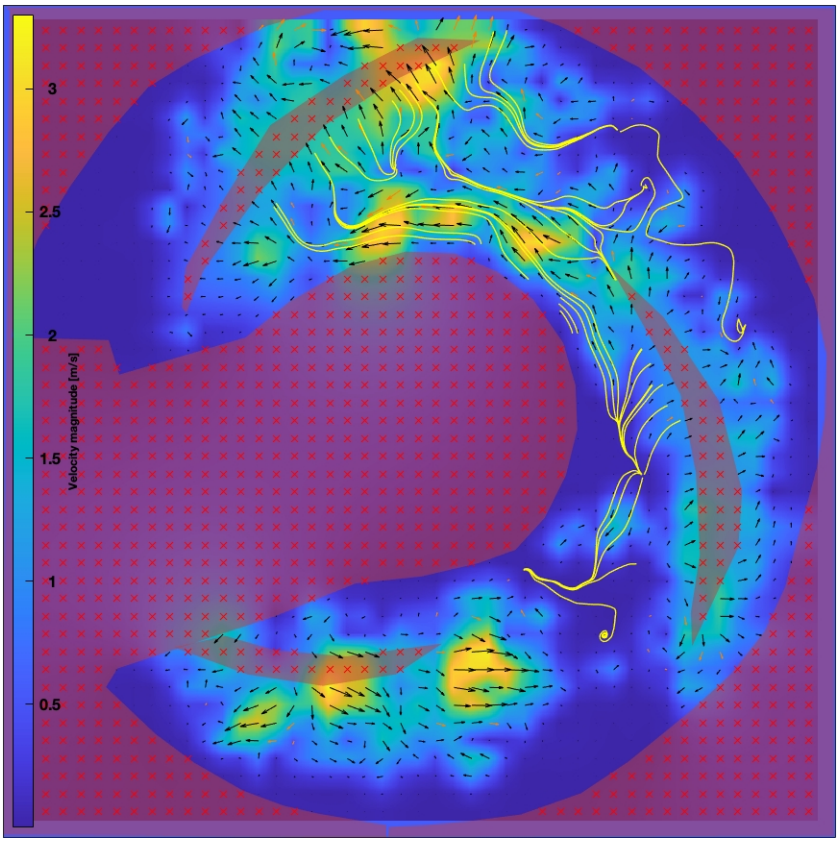

Figure C.126: PIVlab analysis of the streamlines and trajectories.

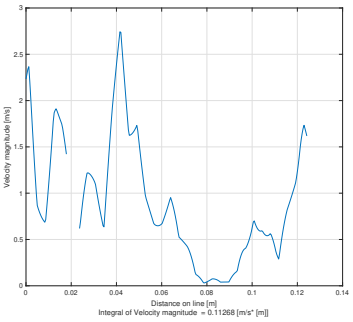

Figure C.127: Local Velocity line plot of the eddy in longitudinal direction.

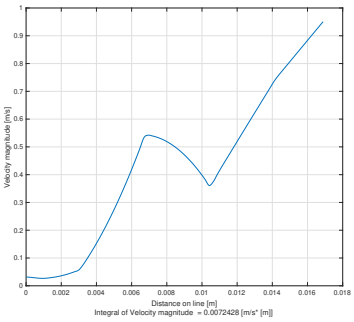

Figure C.128: Local Velocity line plot of the eddy in transverse direction.

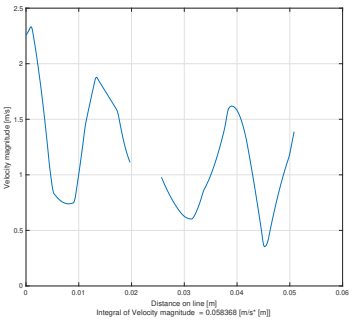

Figure C.129: Local Velocity line plot between the leading front and tail of two impellers.

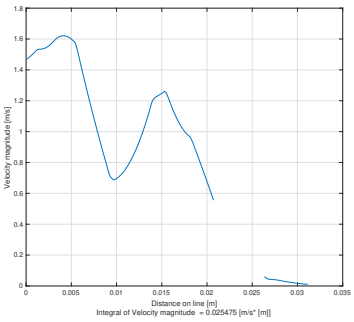

Figure C.130: Local Velocity line plot perpendicular on the leading front of the impeller. See figure 3.12 for clarification.

C.2.23. Glass beads 1.5mm, Cvd = 0.20, Speed 1128 RPM

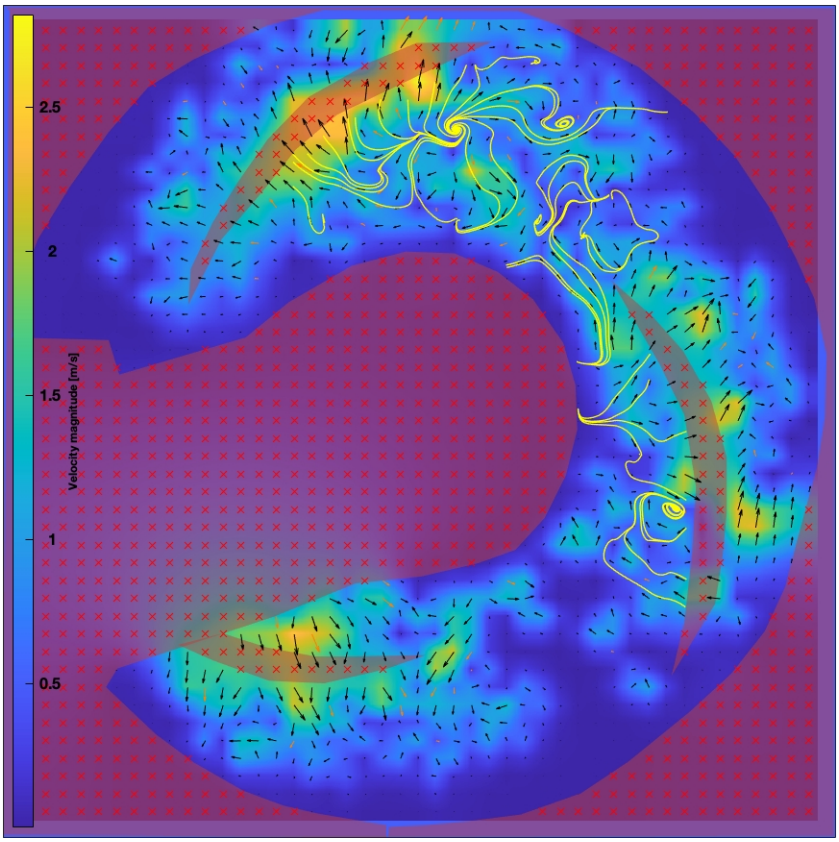

Figure C.131: PIVlab analysis of the streamlines and trajectories.

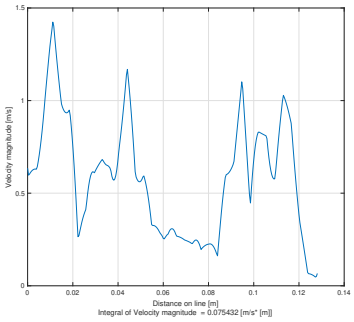

Figure C.132: Local Velocity line plot of the eddy in longitudinal direction.

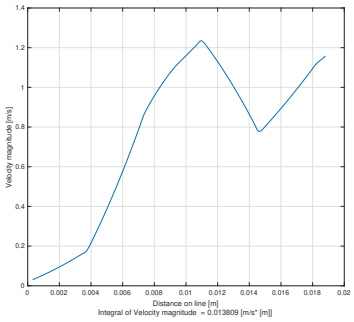

Figure C.133: Local Velocity line plot of the eddy in transverse direction.

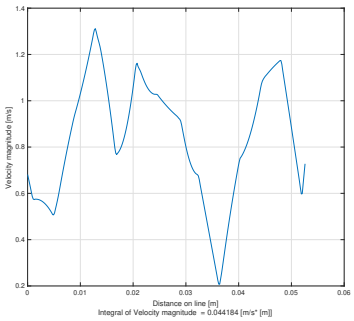

Figure C.134: Local Velocity line plot between the leading front and tail of two impellers.

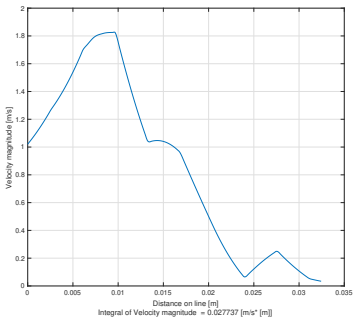

Figure C.135: Local Velocity line plot perpendicular on the leading front of the impeller. See figure 3.12 for clarification.

C.2.24. Glass beads 1.5mm, Cvd = 0.20, Speed 1410 RPM

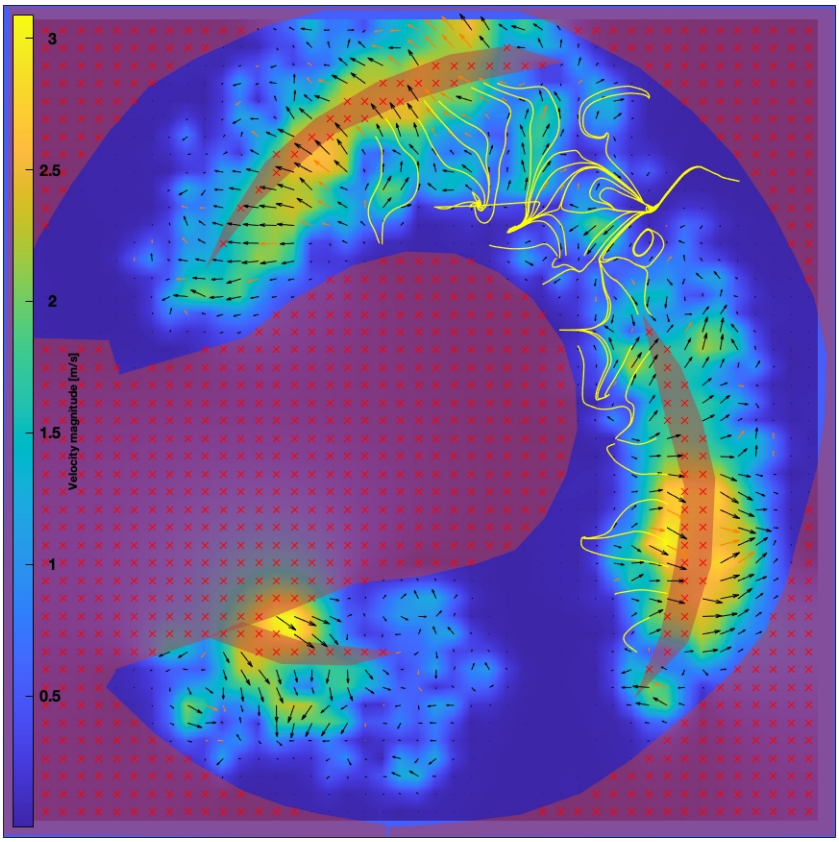

Figure C.136: PIVlab analysis of the streamlines and trajectories.

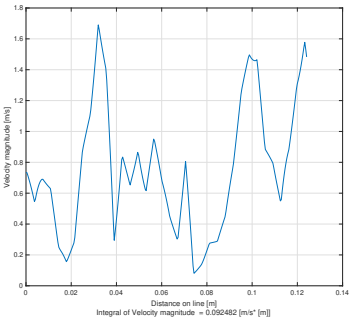

Figure C.137: Local Velocity line plot of the eddy in longitudinal direction.

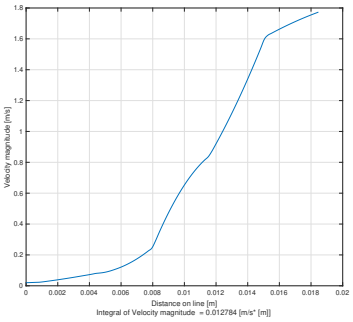

Figure C.138: Local Velocity line plot of the eddy in transverse direction.

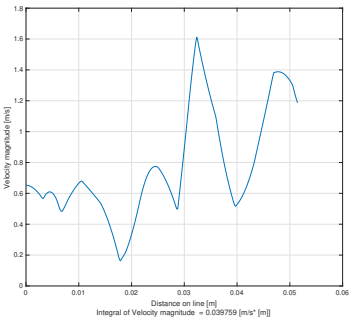

Figure C.139: Local Velocity line plot between the leading front and tail of two impellers.

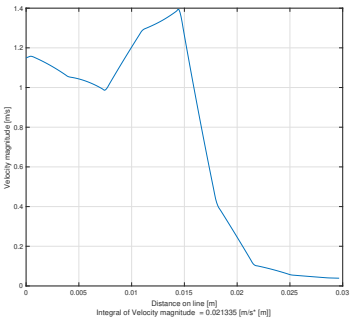

Figure C.140: Local Velocity line plot perpendicular on the leading front of the impeller. See figure 3.12 for clarification.

C.2.25. Glass beads 3.0mm, Cvd = 0.03, Speed 564 RPM

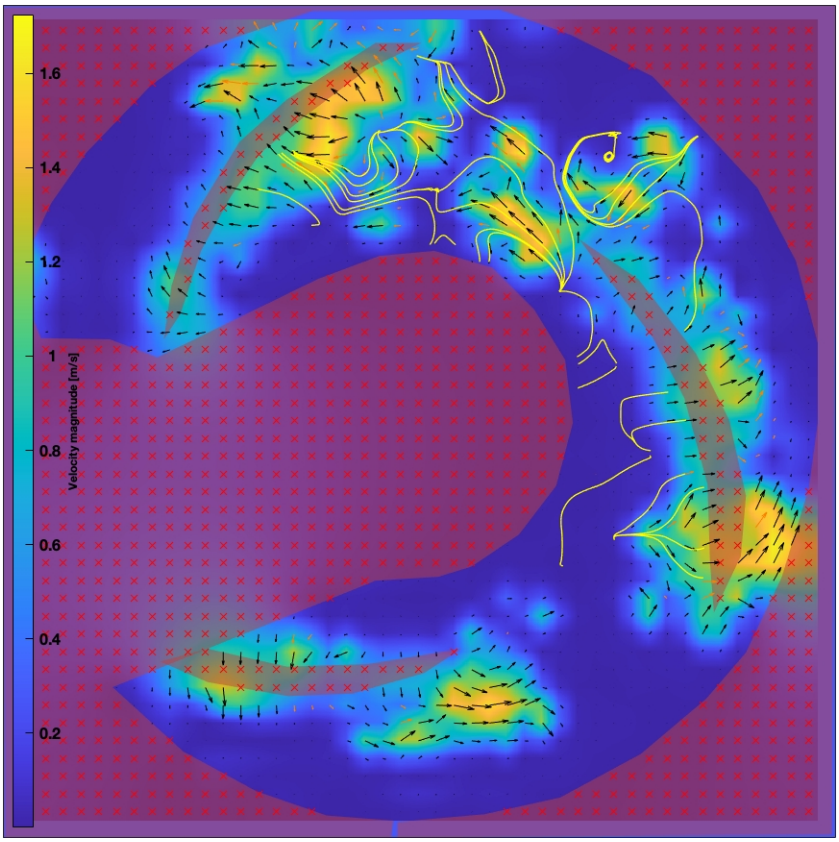

Figure C.141: PIVlab analysis of the streamlines and trajectories.

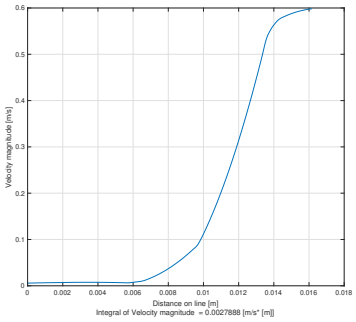

Figure C.142: Local Velocity line plot of the eddy in longitudinal direction.

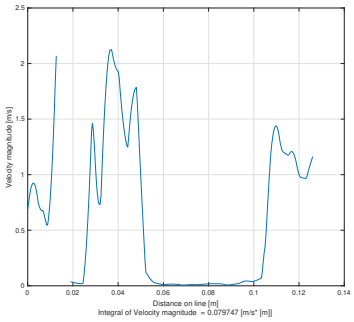

Figure C.143: Local Velocity line plot of the eddy in transverse direction.

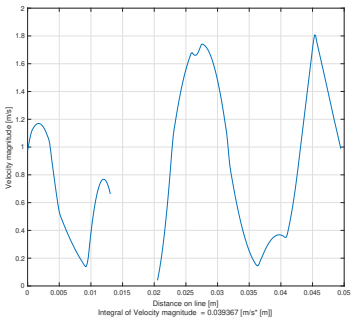

Figure C.144: Local Velocity line plot between the leading front and tail of two impellers.

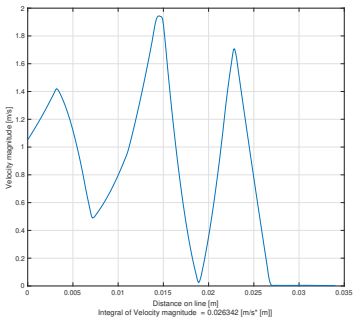

Figure C.145: Local Velocity line plot perpendicular on the leading front of the impeller. See figure 3.12 for clarification.

C.2.26. Glass beads 3.0mm, Cvd = 0.03, Speed 846 RPM

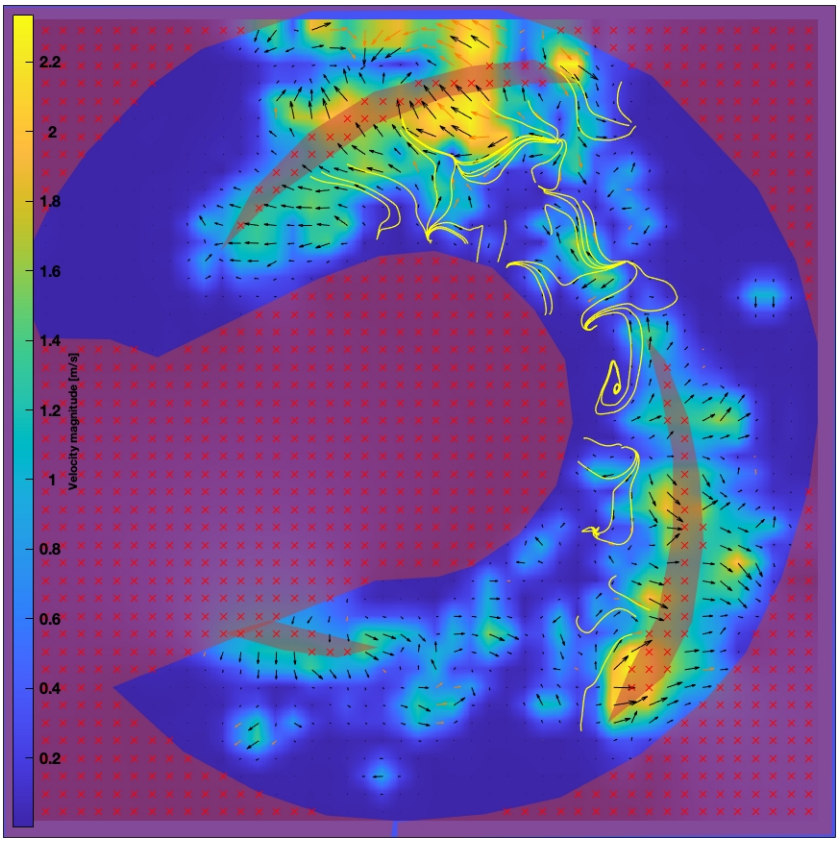

Figure C.146: PIVlab analysis of the streamlines and trajectories.

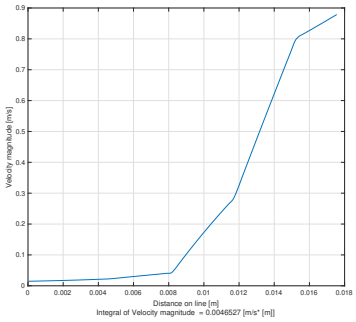

Figure C.147: Local Velocity line plot of the eddy in longitudinal direction.

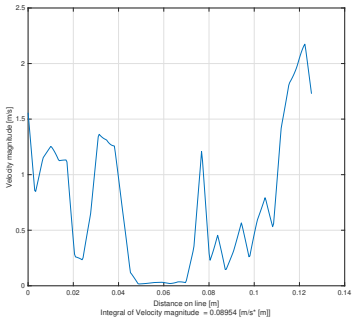

Figure C.148: Local Velocity line plot of the eddy in transverse direction.

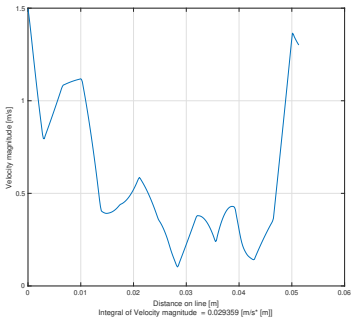

Figure C.149: Local Velocity line plot between the leading front and tail of two impellers.

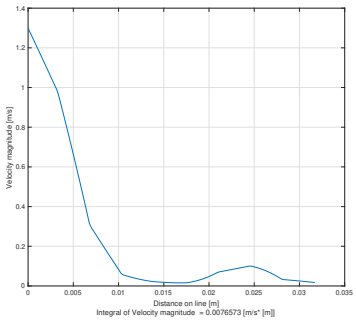

Figure C.150: Local Velocity line plot perpendicular on the leading front of the impeller. See figure 3.12 for clarification.

C.2.27. Glass beads 3.0mm, Cvd = 0.03, Speed 1128 RPM

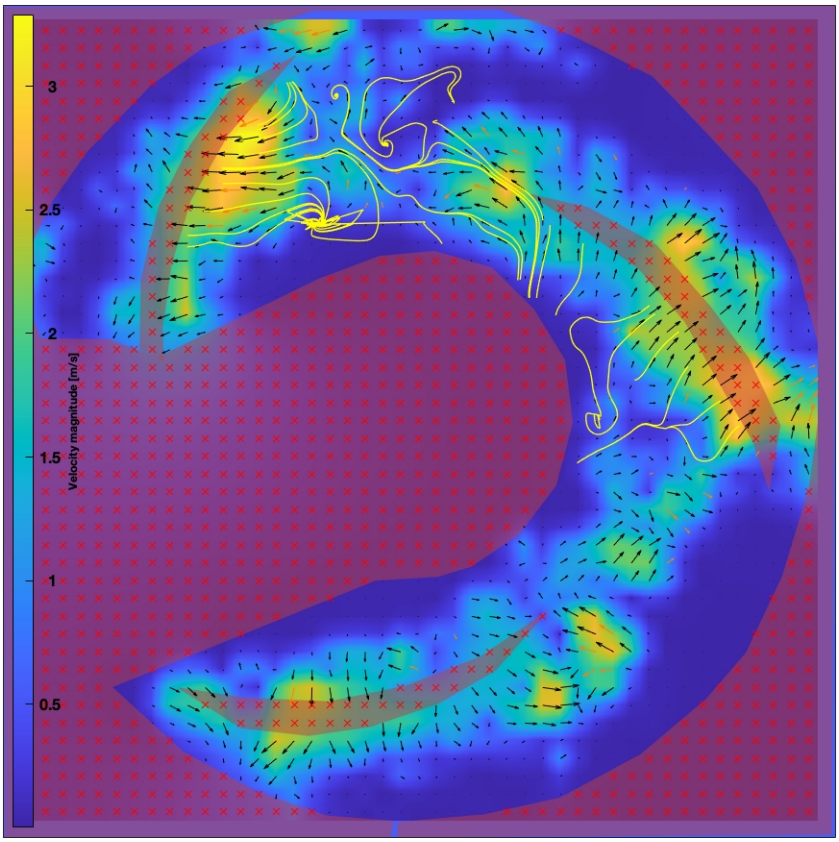

Figure C.151: PIVlab analysis of the streamlines and trajectories.

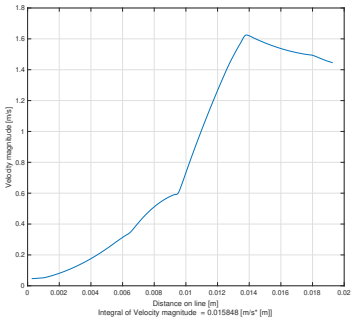

Figure C.152: Local Velocity line plot of the eddy in longitudinal direction.

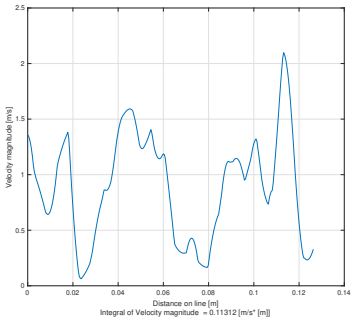

Figure C.153: Local Velocity line plot of the eddy in transverse direction.

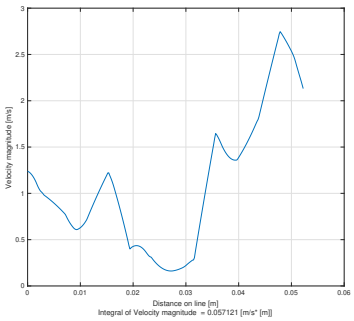

Figure C.154: Local Velocity line plot between the leading front and tail of two impellers.

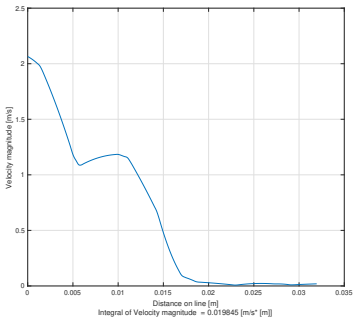

Figure C.155: Local Velocity line plot perpendicular on the leading front of the impeller. See figure 3.12 for clarification.

C.2.28. Glass beads 3.0mm, Cvd = 0.03, Speed 1410 RPM

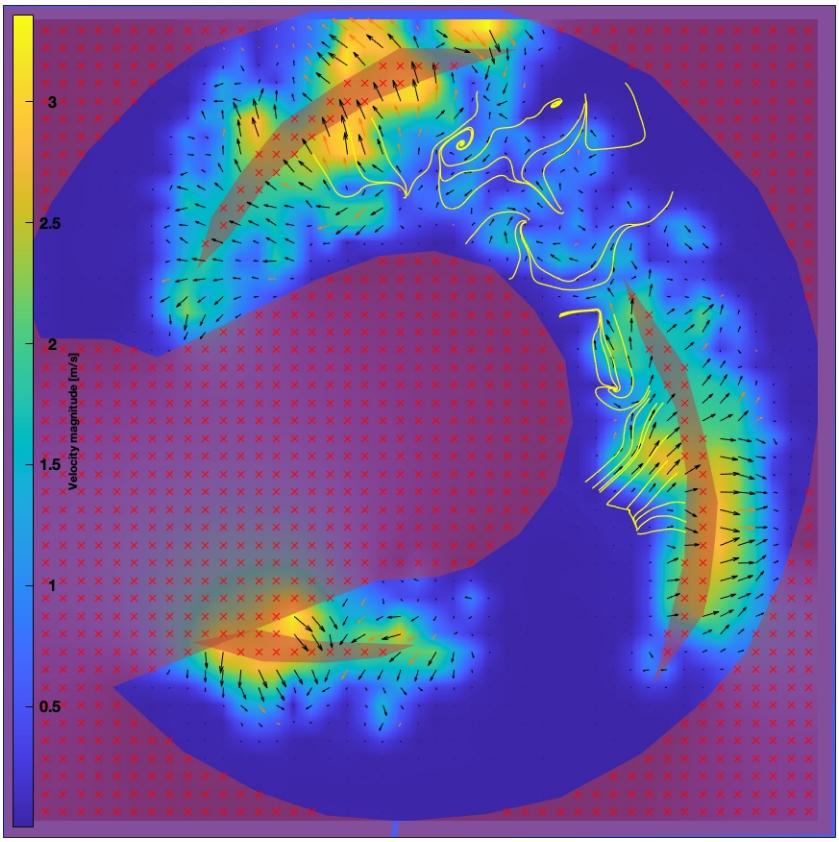

Figure C.156: PIVlab analysis of the streamlines and trajectories.

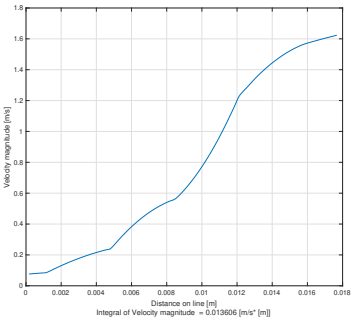

Figure C.157: Local Velocity line plot of the eddy in longitudinal direction.

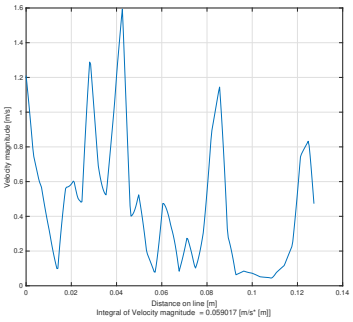

Figure C.158: Local Velocity line plot of the eddy in transverse direction.

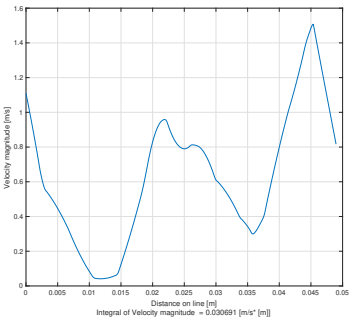

Figure C.159: Local Velocity line plot between the leading front and tail of two impellers.

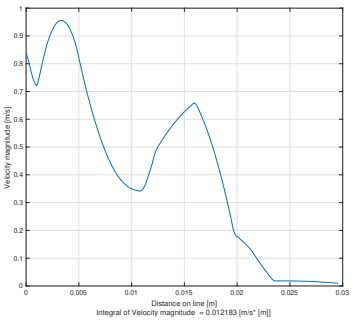

Figure C.160: Local Velocity line plot perpendicular on the leading front of the impeller. See figure 3.12 for clarification.

C.2.29. Glass beads 3.0mm, Cvd = 0.05, Speed 564 RPM

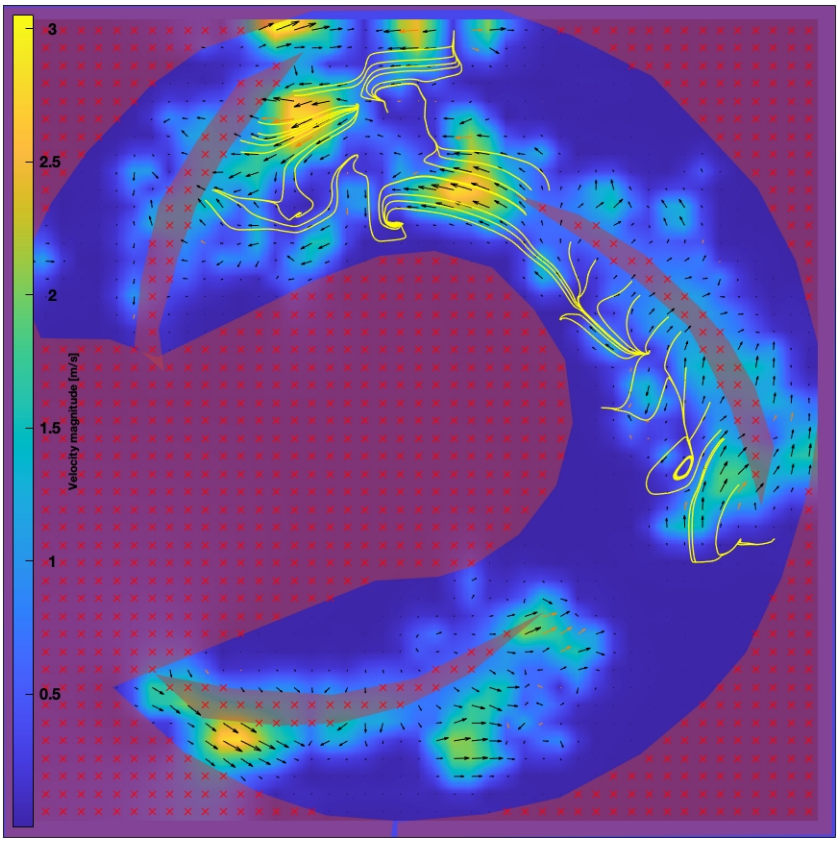

Figure C.161: PIVlab analysis of the streamlines and trajectories.

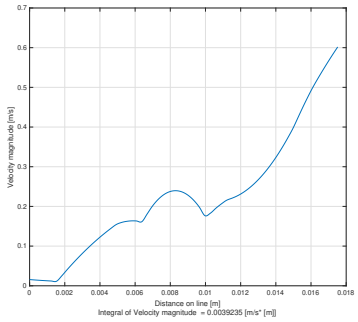

Figure C.162: Local Velocity line plot of the eddy in longitudinal direction.

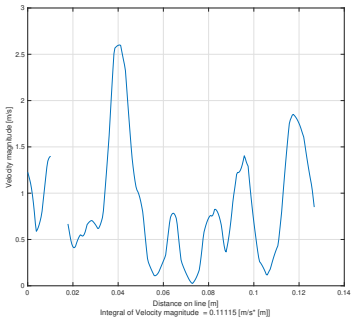

Figure C.163: Local Velocity line plot of the eddy in transverse direction.

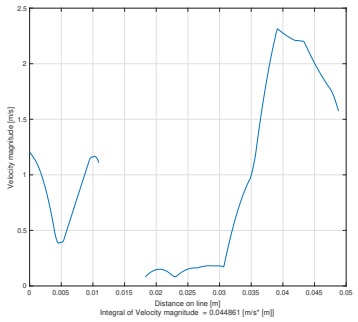

Figure C.164: Local Velocity line plot between the leading front and tail of two impellers.

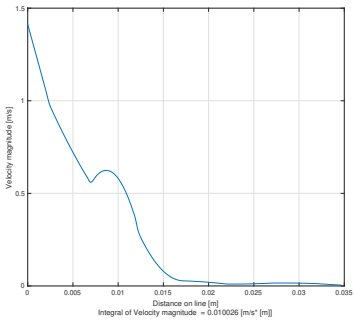

Figure C.165: Local Velocity line plot perpendicular on the leading front of the impeller. See figure 3.12 for clarification.

C.2.30. Glass beads 3.0mm, Cvd = 0.05, Speed 846 RPM

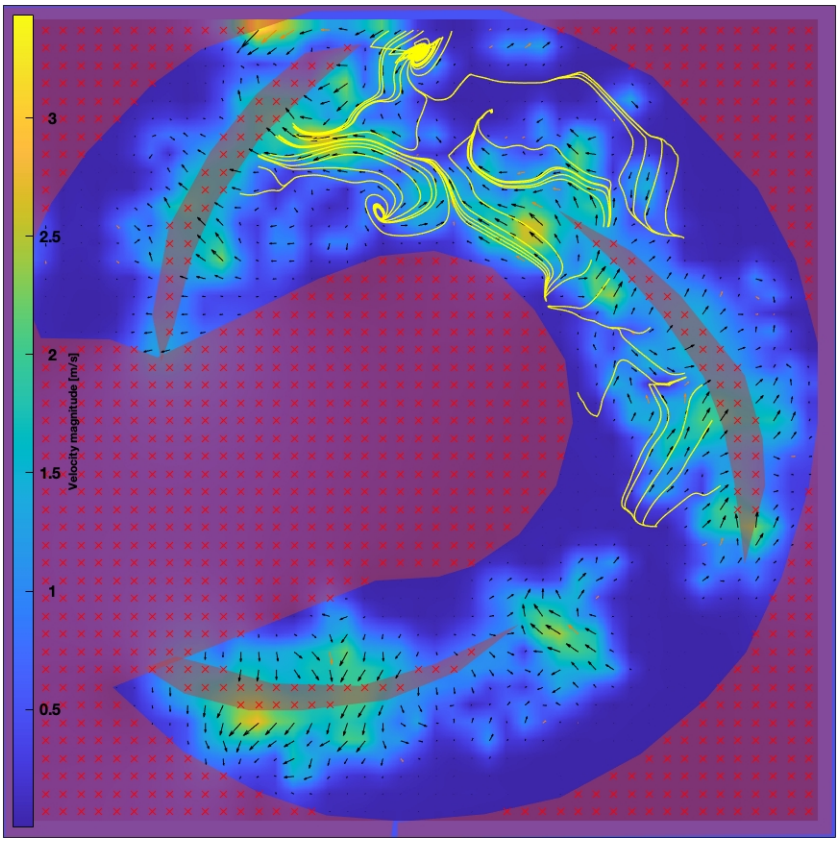

Figure C.166: PIVlab analysis of the streamlines and trajectories.

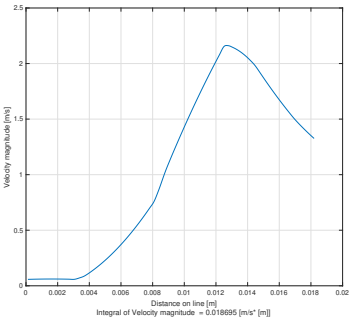

Figure C.167: Local Velocity line plot of the eddy in longitudinal direction.

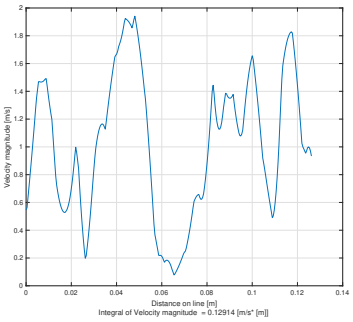

Figure C.168: Local Velocity line plot of the eddy in transverse direction.

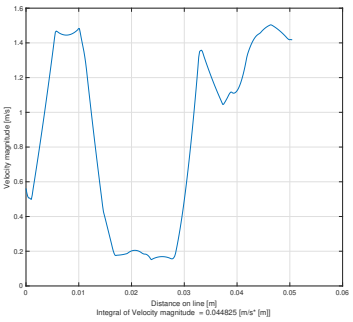

Figure C.169: Local Velocity line plot between the leading front and tail of two impellers.

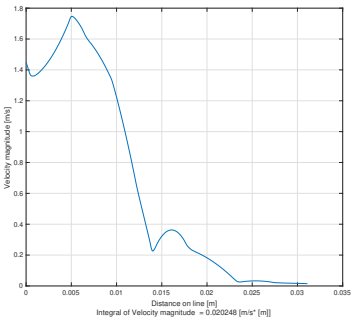

Figure C.170: Local Velocity line plot perpendicular on the leading front of the impeller. See figure 3.12 for clarification.

C.2.31. Glass beads 3.0mm, Cvd = 0.05, Speed 1128 RPM

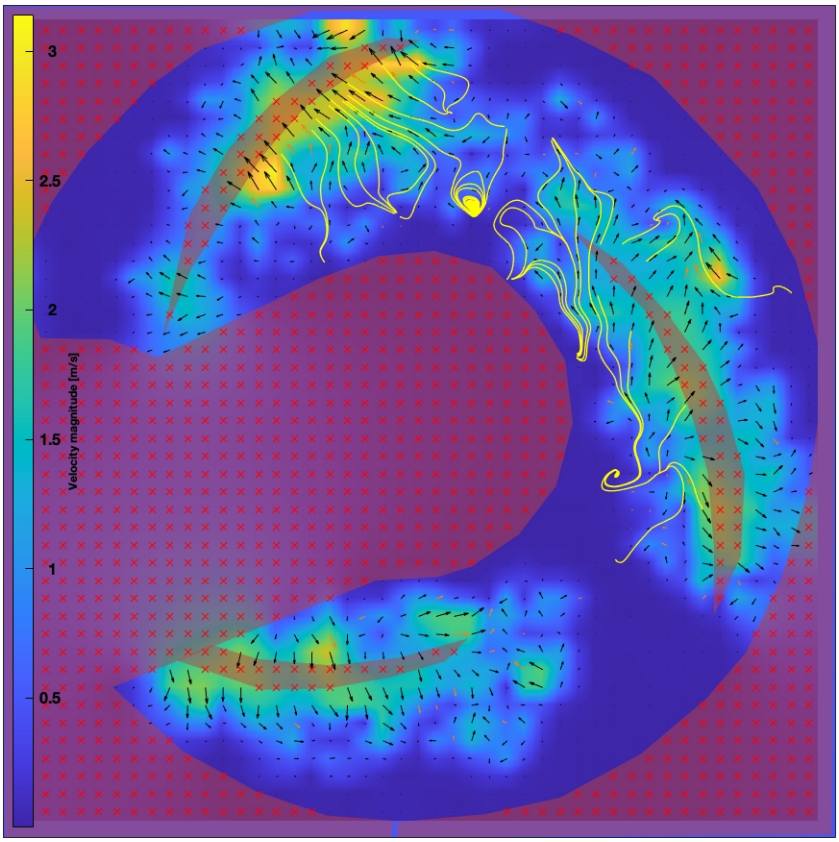

Figure C.171: PIVlab analysis of the streamlines and trajectories.

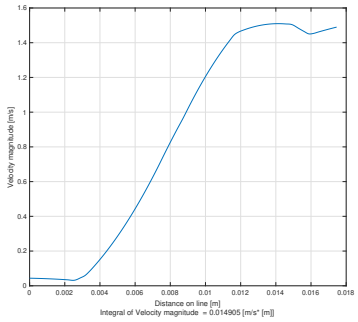

Figure C.172: Local Velocity line plot of the eddy in longitudinal direction.

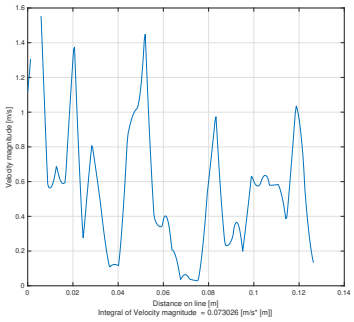

Figure C.173: Local Velocity line plot of the eddy in transverse direction.

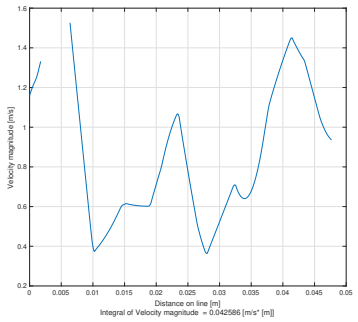

Figure C.174: Local Velocity line plot between the leading front and tail of two impellers.

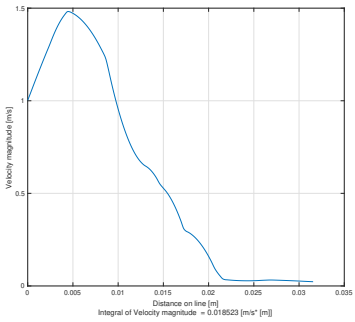

Figure C.175: Local Velocity line plot perpendicular on the leading front of the impeller. See figure 3.12 for clarification.

C.2.32. Glass beads 3.0mm, Cvd = 0.05, Speed 1410 RPM

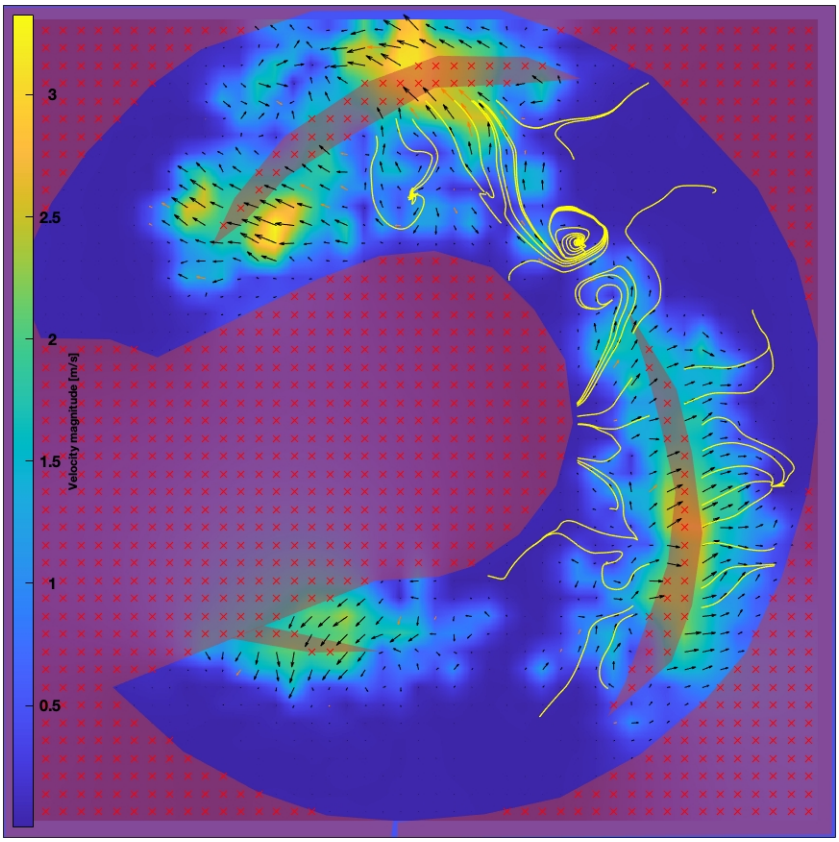

Figure C.176: PIVlab analysis of the streamlines and trajectories.

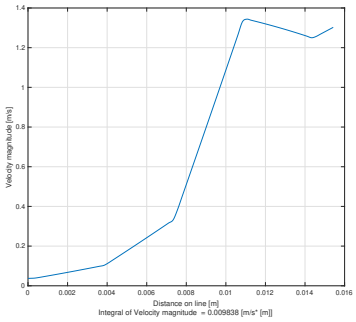

Figure C.177: Local Velocity line plot of the eddy in longitudinal direction.

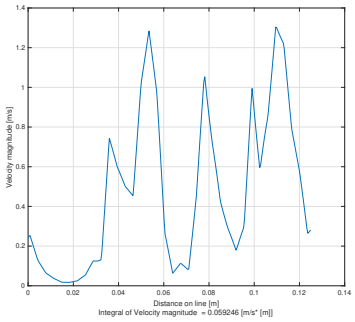

Figure C.178: Local Velocity line plot of the eddy in transverse direction.

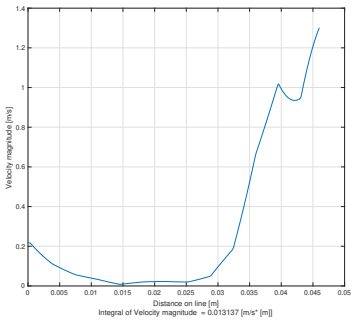

Figure C.179: Local Velocity line plot between the leading front and tail of two impellers.

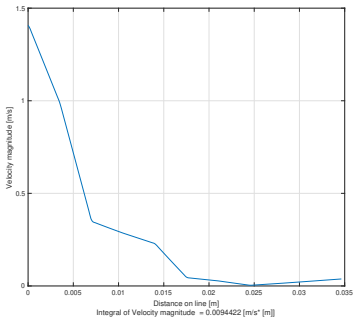

Figure C.180: Local Velocity line plot perpendicular on the leading front of the impeller. See figure 3.12 for clarification.

C.2.33. Glass beads 3.0mm, Cvd = 0.08, Speed 564 RPM

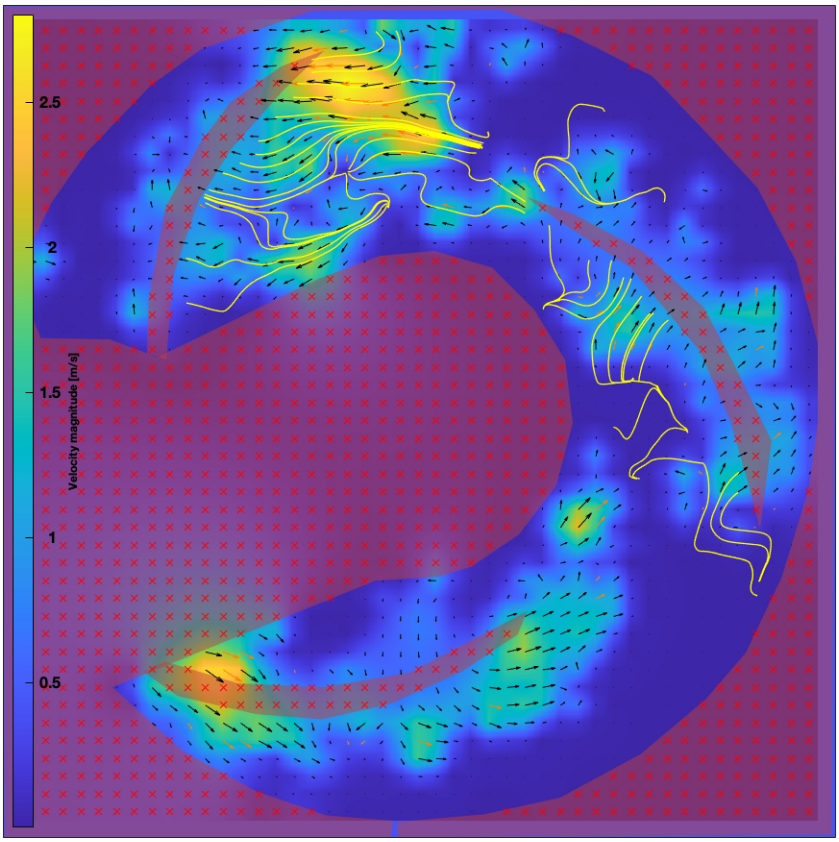

Figure C.181: PIVlab analysis of the streamlines and trajectories.

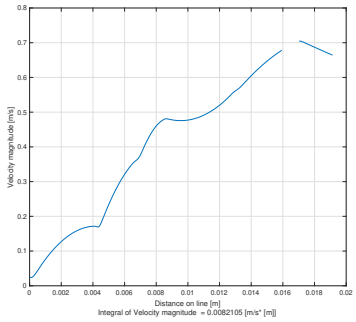

Figure C.182: Local Velocity line plot of the eddy in longitudinal direction.

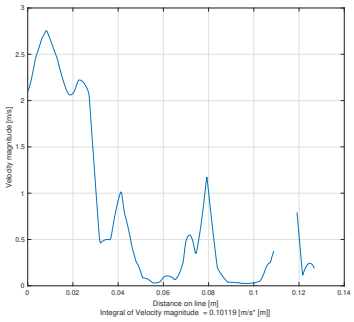

Figure C.183: Local Velocity line plot of the eddy in transverse direction.

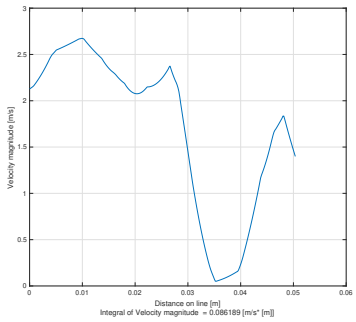

Figure C.184: Local Velocity line plot between the leading front and tail of two impellers.

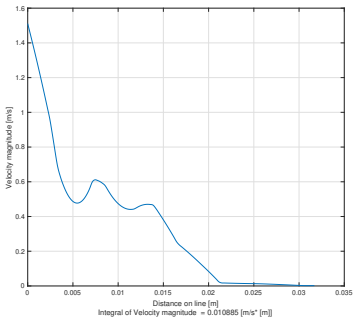

Figure C.185: Local Velocity line plot perpendicular on the leading front of the impeller. See figure 3.12 for clarification.

C.2.34. Glass beads 3.0mm, Cvd = 0.08, Speed 846 RPM

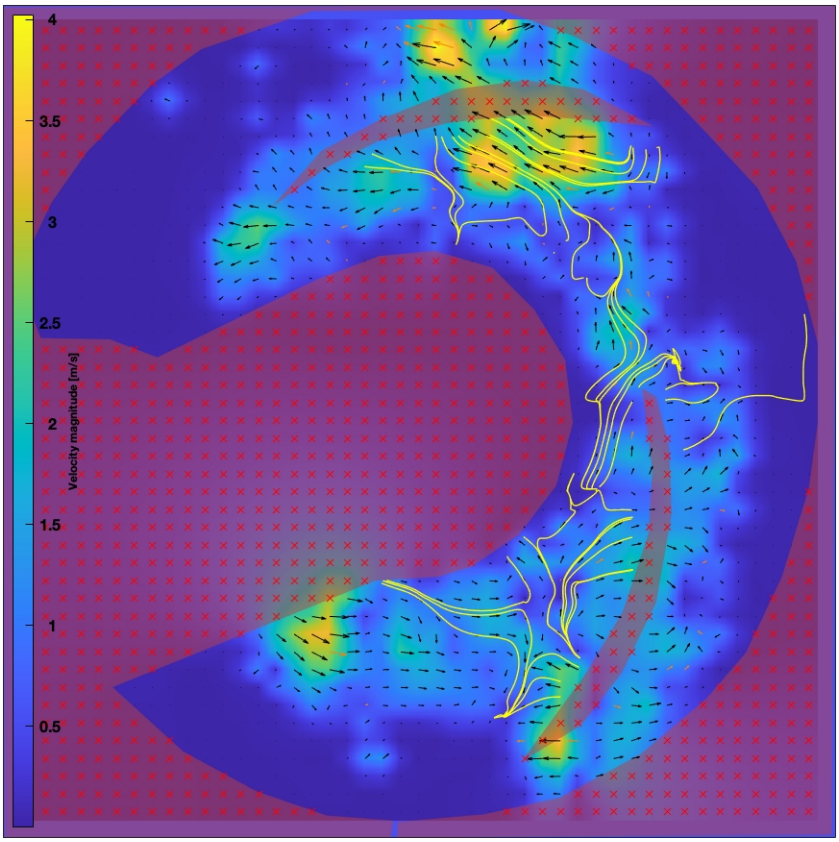

Figure C.186: PIVlab analysis of the streamlines and trajectories.

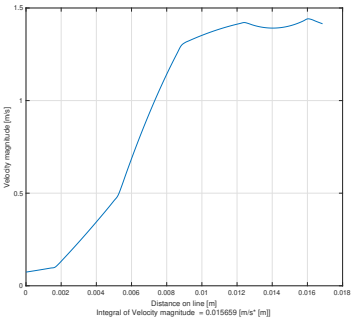

Figure C.187: Local Velocity line plot of the eddy in longitudinal direction.

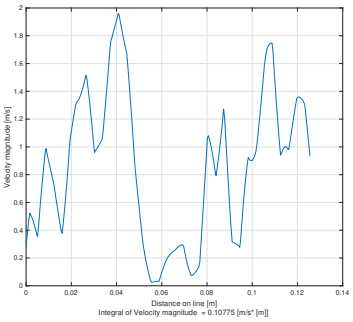

Figure C.188: Local Velocity line plot of the eddy in transverse direction.

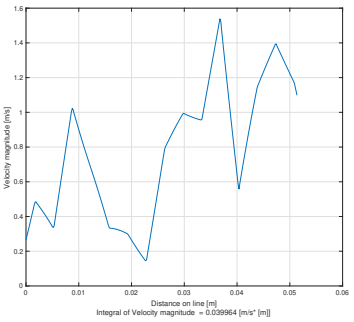

Figure C.189: Local Velocity line plot between the leading front and tail of two impellers.

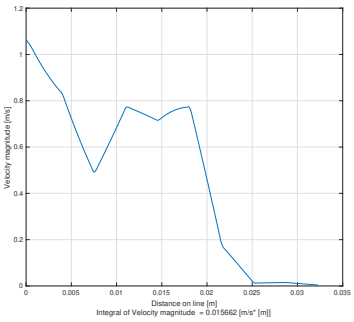

Figure C.190: Local Velocity line plot perpendicular on the leading front of the impeller. See figure 3.12 for clarification.

C.2.35. Glass beads 3.0mm, Cvd = 0.08, Speed 1128 RPM

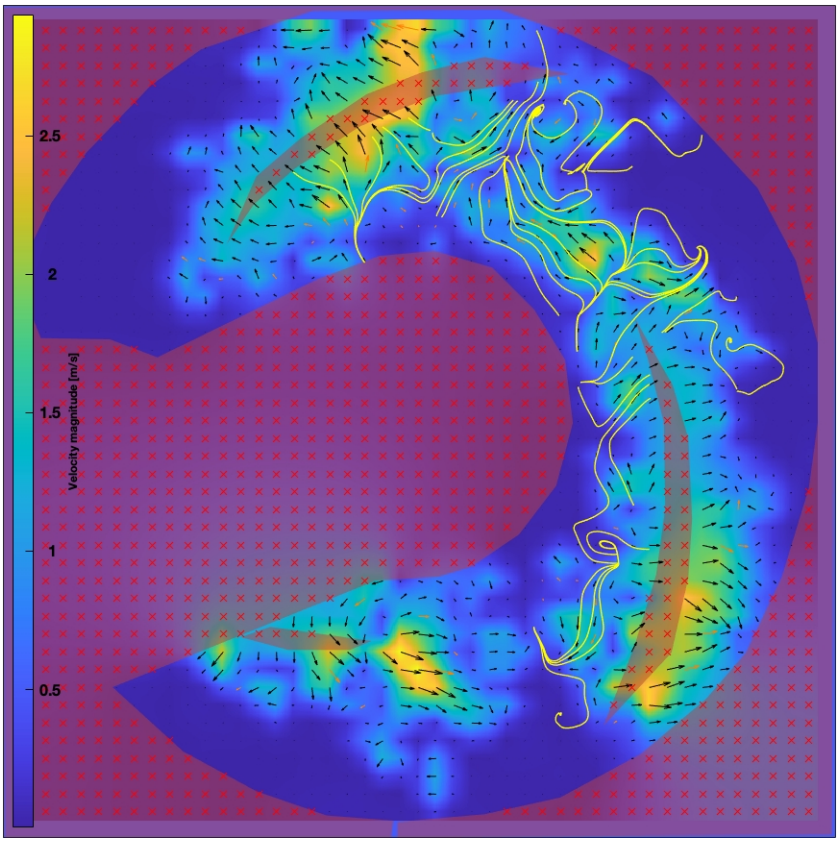

Figure C.191: PIVlab analysis of the streamlines and trajectories.

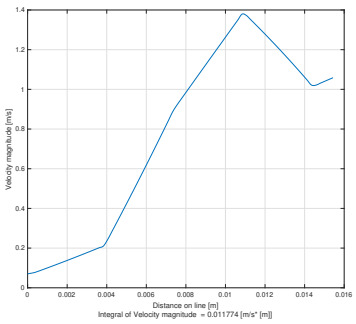

Figure C.192: Local Velocity line plot of the eddy in longitudinal direction.

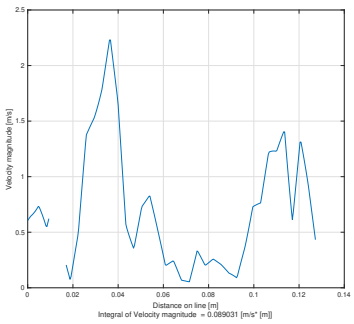

Figure C.193: Local Velocity line plot of the eddy in transverse direction.

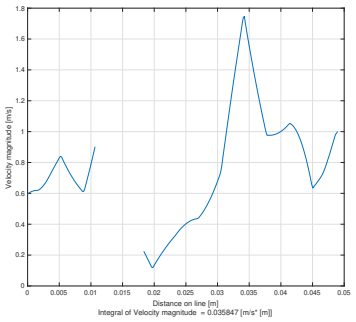

Figure C.194: Local Velocity line plot between the leading front and tail of two impellers.

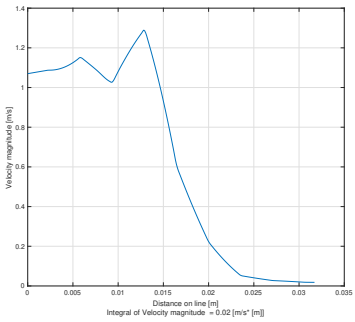

Figure C.195: Local Velocity line plot perpendicular on the leading front of the impeller. See figure 3.12 for clarification.

C.2.36. Glass beads 3.0mm, Cvd = 0.08, Speed 1410 RPM

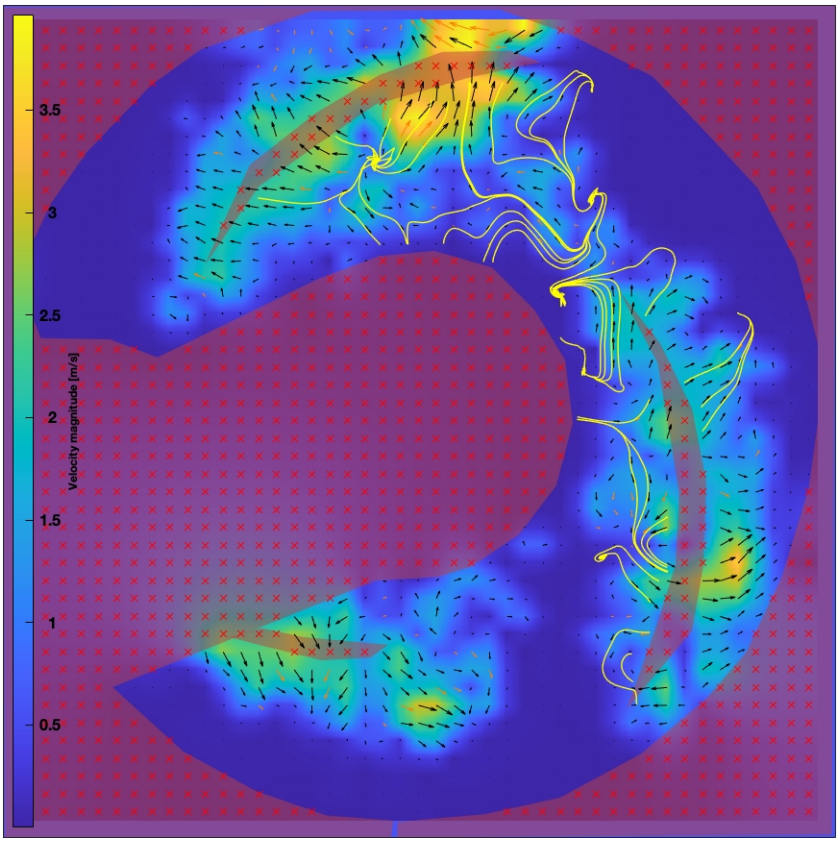

Figure C.196: PIVlab analysis of the streamlines and trajectories.

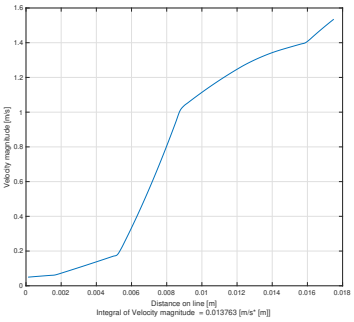

Figure C.197: Local Velocity line plot of the eddy in longitudinal direction.

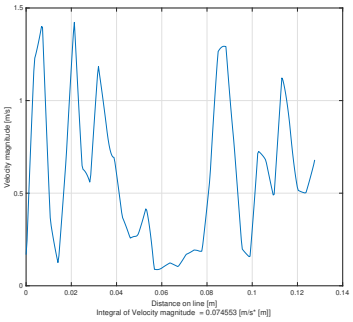

Figure C.198: Local Velocity line plot of the eddy in transverse direction.

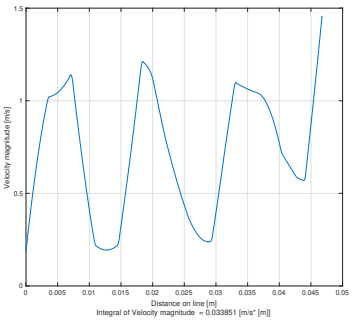

Figure C.199: Local Velocity line plot between the leading front and tail of two impellers.

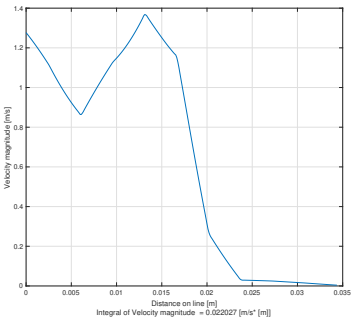

Figure C.200: Local Velocity line plot perpendicular on the leading front of the impeller. See figure 3.12 for clarification.

C.2.37. Glass beads 3.0mm, Cvd = 0.12, Speed 564 RPM

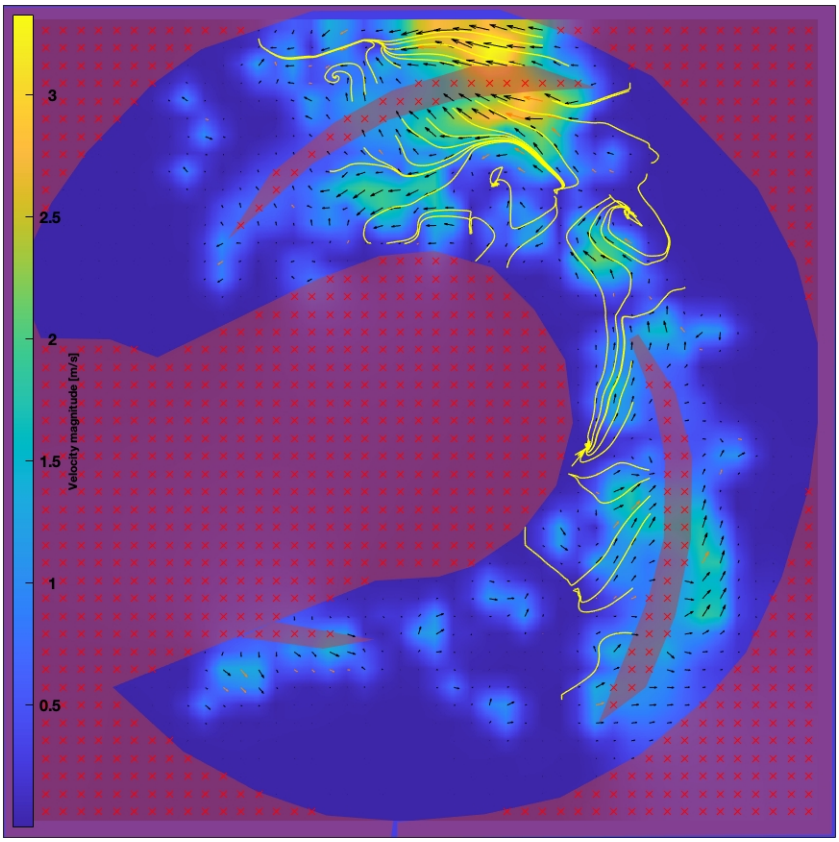

Figure C.201: PIVlab analysis of the streamlines and trajectories.

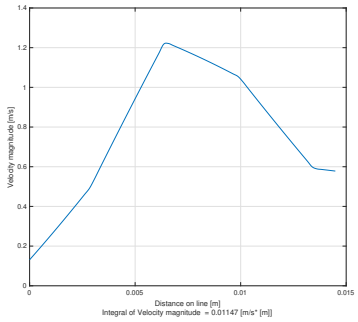

Figure C.202: Local Velocity line plot of the eddy in longitudinal direction.

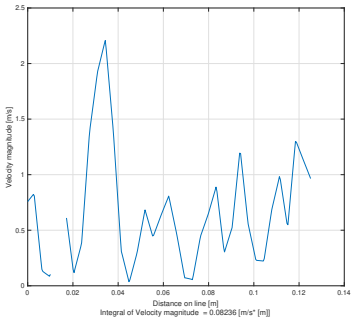

Figure C.203: Local Velocity line plot of the eddy in transverse direction.

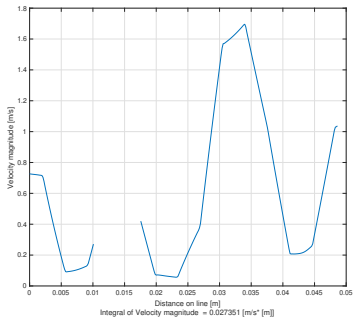

Figure C.204: Local Velocity line plot between the leading front and tail of two impellers.

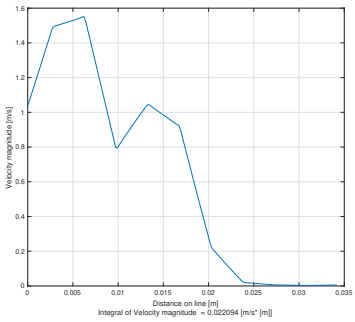

Figure C.205: Local Velocity line plot perpendicular on the leading front of the impeller. See figure 3.12 for clarification.

C.2.38. Glass beads 3.0mm, Cvd = 0.12, Speed 846 RPM

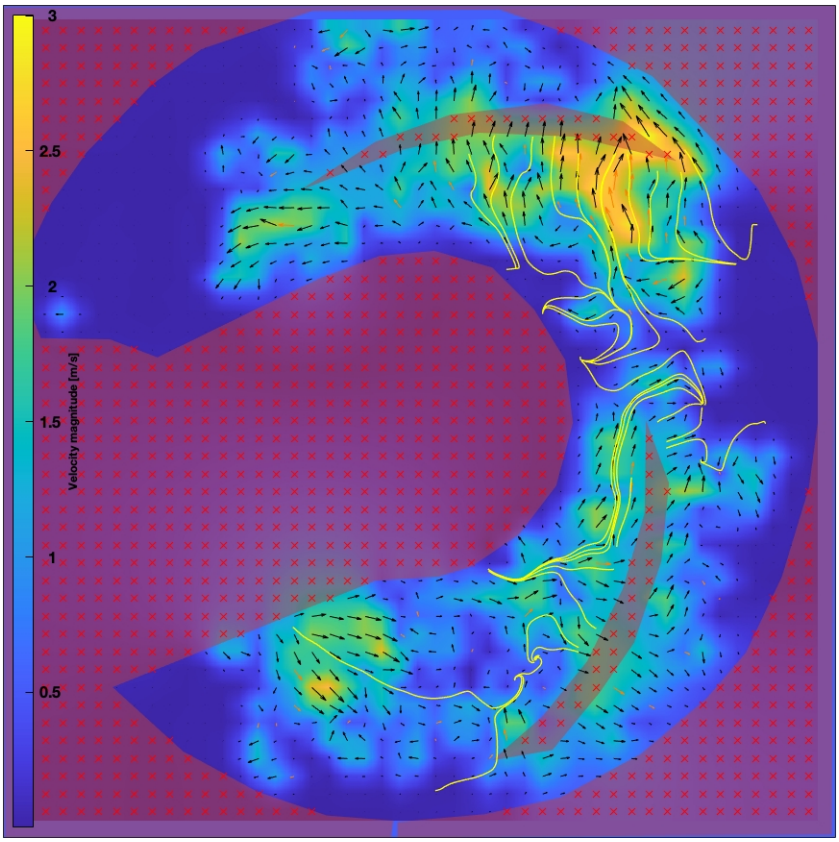

Figure C.206: PIVlab analysis of the streamlines and trajectories.

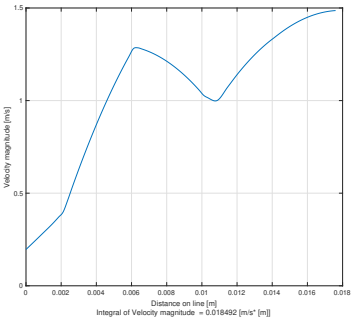

Figure C.207: Local Velocity line plot of the eddy in longitudinal direction.

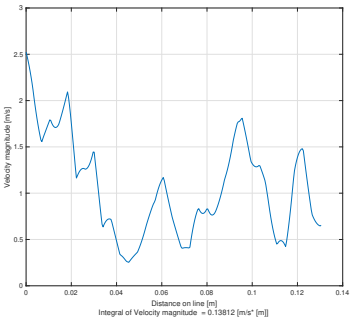

Figure C.208: Local Velocity line plot of the eddy in transverse direction.

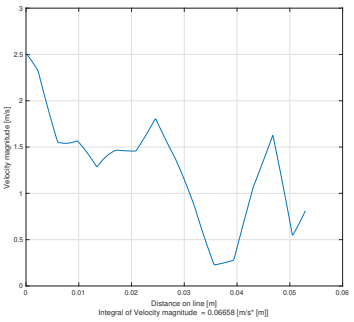

Figure C.209: Local Velocity line plot between the leading front and tail of two impellers.

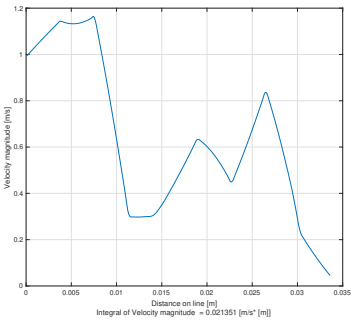

Figure C.210: Local Velocity line plot perpendicular on the leading front of the impeller. See figure 3.12 for clarification.

C.2.39. Glass beads 3.0mm, Cvd = 0.12, Speed 1128 RPM

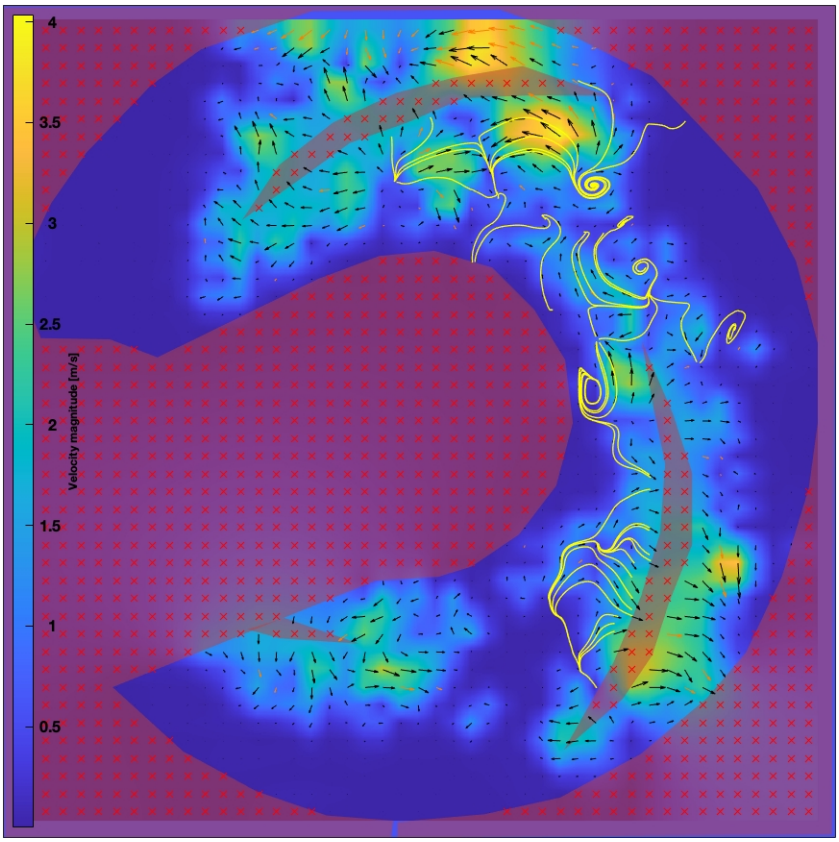

Figure C.211: PIVlab analysis of the streamlines and trajectories.

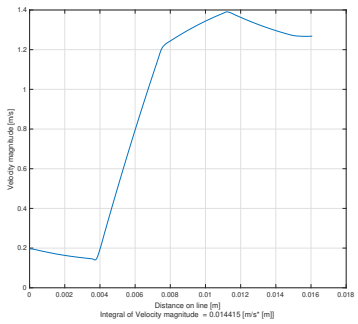

Figure C.212: Local Velocity line plot of the eddy in longitudinal direction.

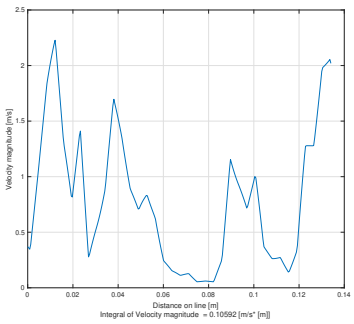

Figure C.213: Local Velocity line plot of the eddy in transverse direction.

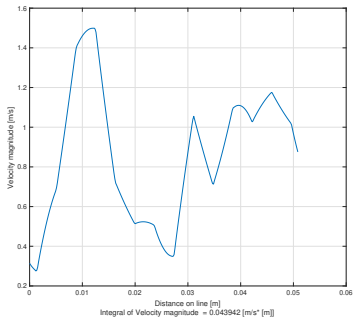

Figure C.214: Local Velocity line plot between the leading front and tail of two impellers.

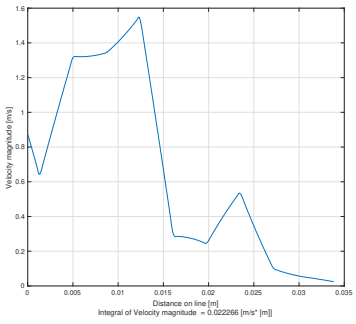

Figure C.215: Local Velocity line plot perpendicular on the leading front of the impeller. See figure 3.12 for clarification.

C.2.40. Glass beads 3.0mm, Cvd = 0.12, Speed 1410 RPM

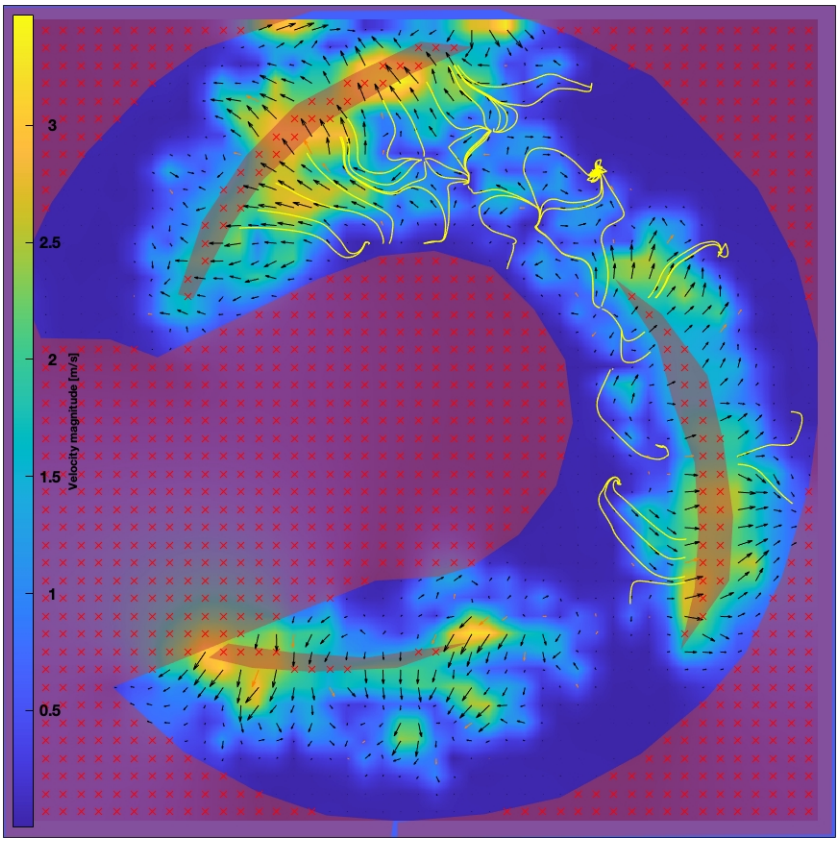

Figure C.216: PIVlab analysis of the streamlines and trajectories.

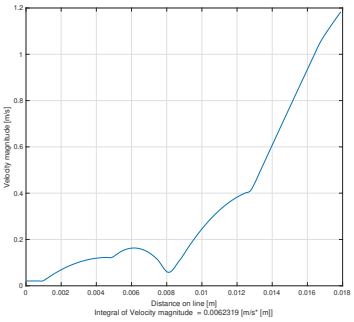

Figure C.217: Local Velocity line plot of the eddy in longitudinal direction.

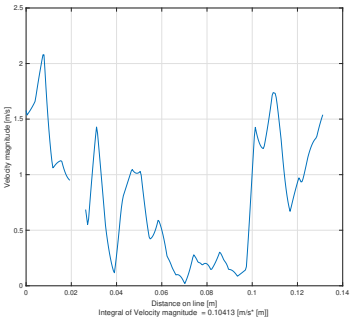

Figure C.218: Local Velocity line plot of the eddy in transverse direction.

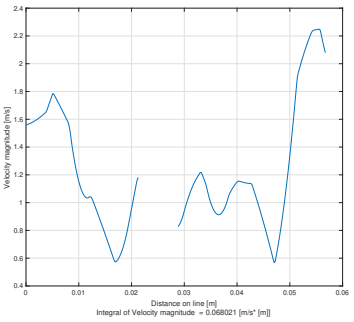

Figure C.219: Local Velocity line plot between the leading front and tail of two impellers.

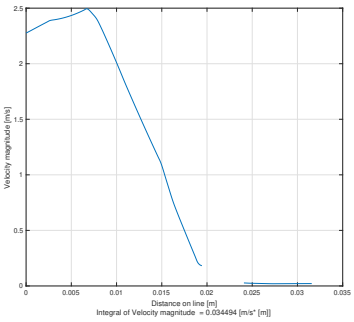

Figure C.220: Local Velocity line plot perpendicular on the leading front of the impeller. See figure 3.12 for clarification.

C.2.41. Glass beads 3.0mm, Cvd = 0.15, Speed 564 RPM

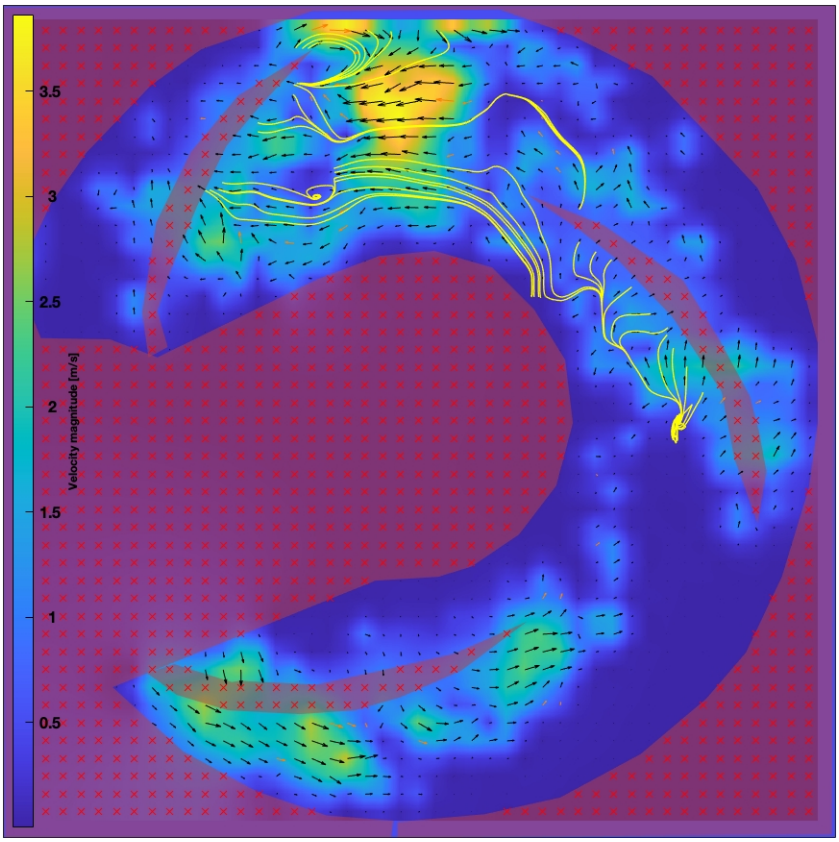

Figure C.221: PIVlab analysis of the streamlines and trajectories.

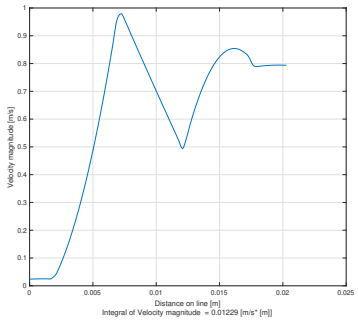

Figure C.222: Local Velocity line plot of the eddy in longitudinal direction.

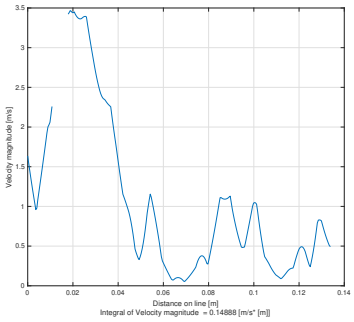

Figure C.223: Local Velocity line plot of the eddy in transverse direction.

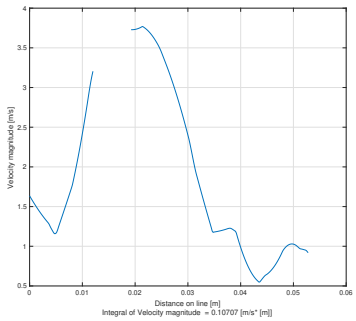

Figure C.224: Local Velocity line plot between the leading front and tail of two impellers.

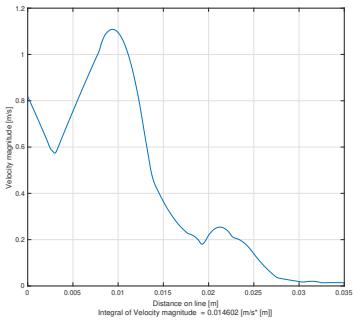

Figure C.225: Local Velocity line plot perpendicular on the leading front of the impeller. See figure 3.12 for clarification.

C.2.42. Glass beads 3.0mm, Cvd = 0.15, Speed 846 RPM

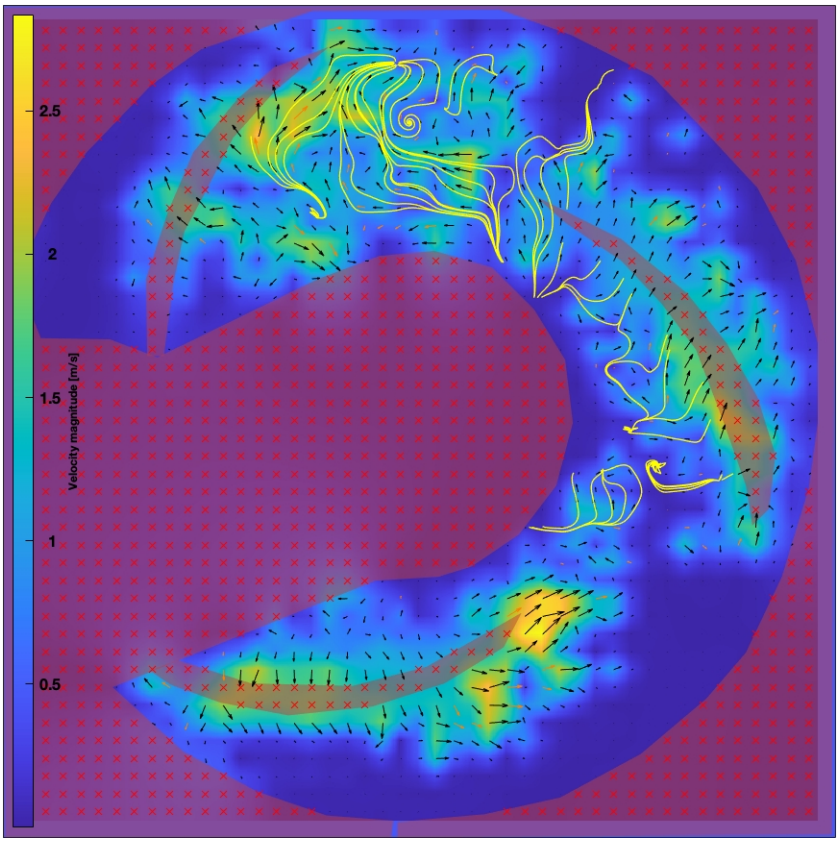

Figure C.226: PIVlab analysis of the streamlines and trajectories.

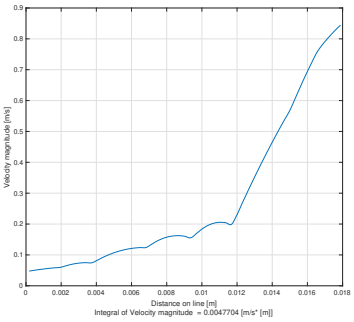

Figure C.227: Local Velocity line plot of the eddy in longitudinal direction.

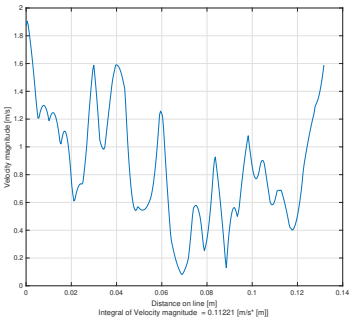

Figure C.228: Local Velocity line plot of the eddy in transverse direction.

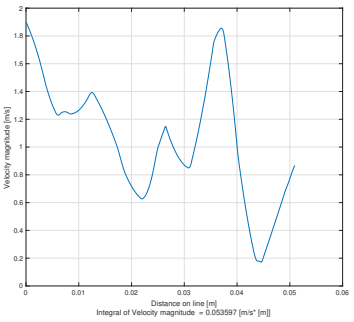

Figure C.229: Local Velocity line plot between the leading front and tail of two impellers.

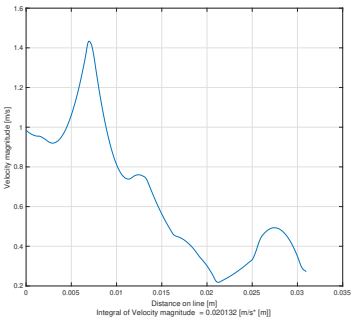

Figure C.230: Local Velocity line plot perpendicular on the leading front of the impeller. See figure 3.12 for clarification.

C.2.43. Glass beads 3.0mm, Cvd = 0.15, Speed 1128 RPM

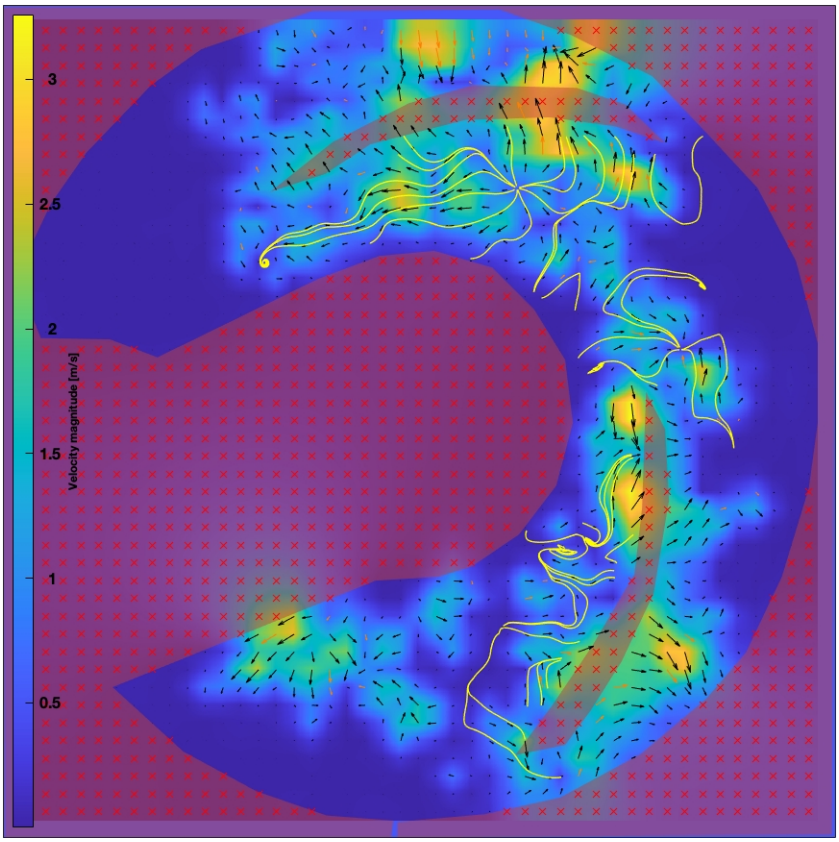

Figure C.231: PIVlab analysis of the streamlines and trajectories.

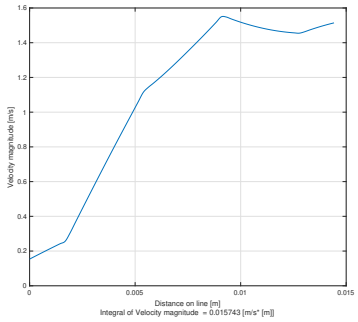

Figure C.232: Local Velocity line plot of the eddy in longitudinal direction.

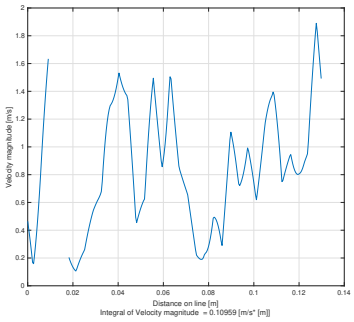

Figure C.233: Local Velocity line plot of the eddy in transverse direction.

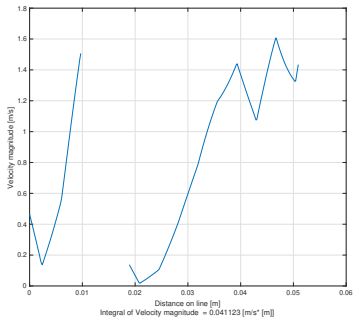

Figure C.234: Local Velocity line plot between the leading front and tail of two impellers.

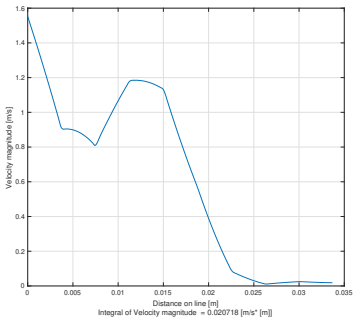

Figure C.235: Local Velocity line plot perpendicular on the leading front of the impeller. See figure 3.12 for clarification.

C.2.44. Glass beads 3.0mm, Cvd = 0.15, Speed 1410 RPM

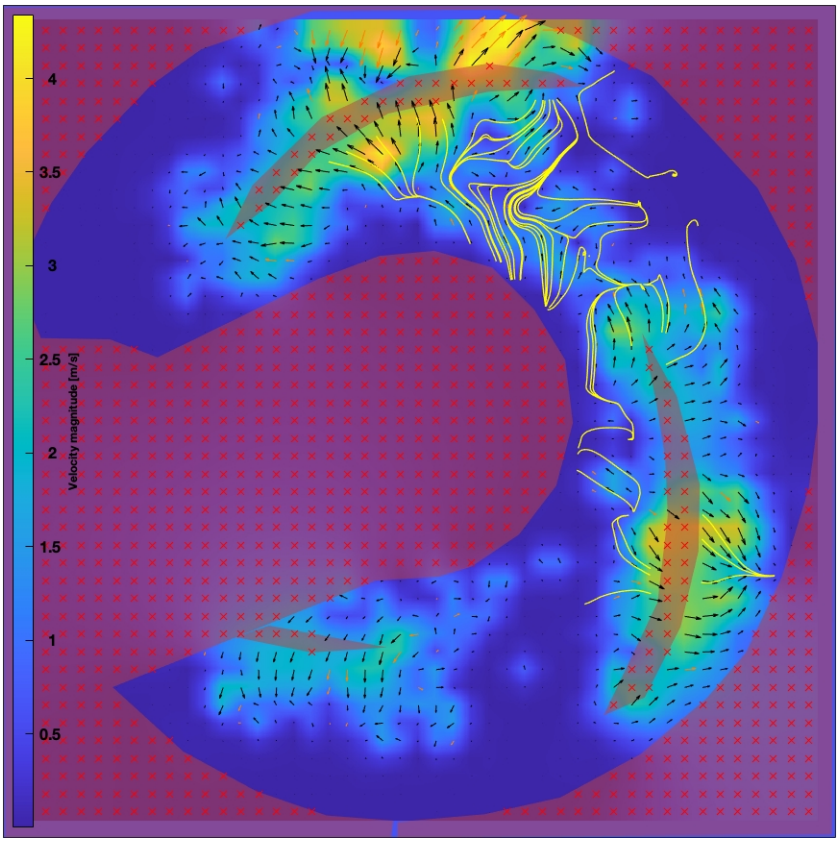

Figure C.236: PIVlab analysis of the streamlines and trajectories.

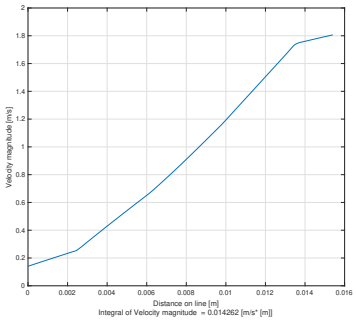

Figure C.237: Local Velocity line plot of the eddy in longitudinal direction.

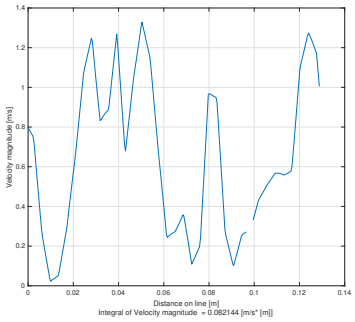

Figure C.238: Local Velocity line plot of the eddy in transverse direction.

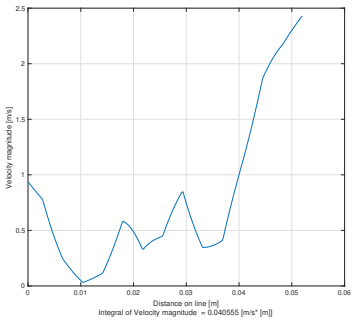

Figure C.239: Local Velocity line plot between the leading front and tail of two impellers.

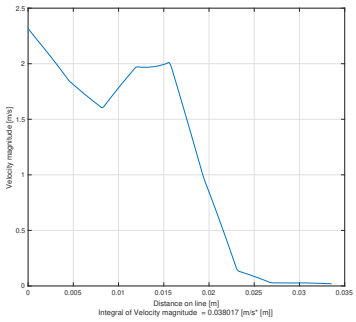

Figure C.240: Local Velocity line plot perpendicular on the leading front of the impeller. See figure 3.12 for clarification.

C.2.45. Glass beads 1.5mm, Cvd = 0.20, Speed 564 RPM

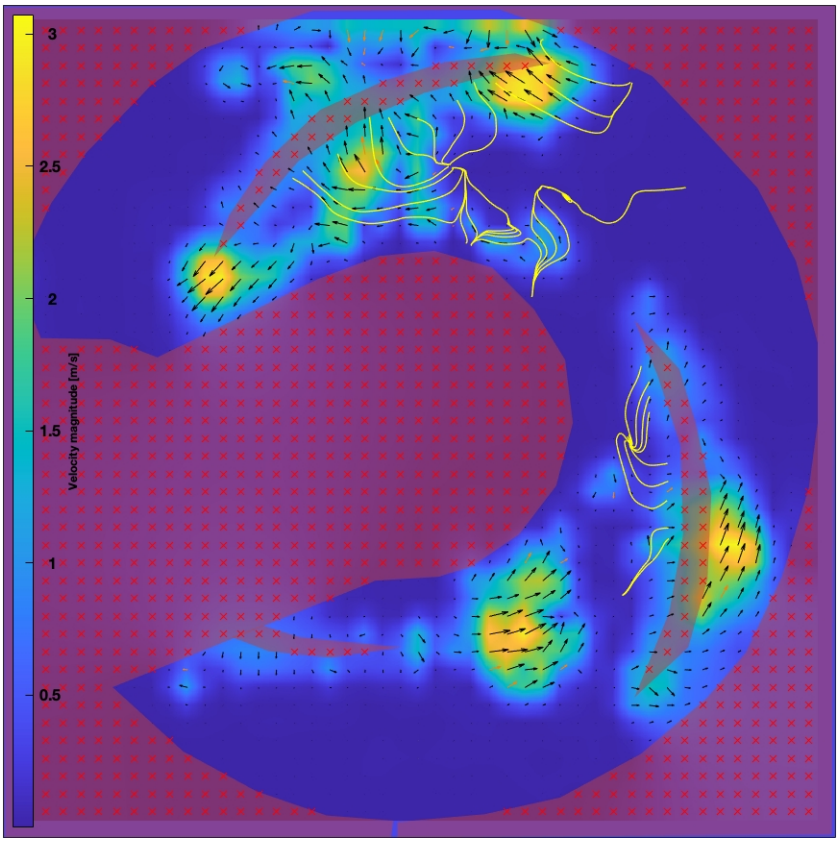

Figure C.241: PIVlab analysis of the streamlines and trajectories.

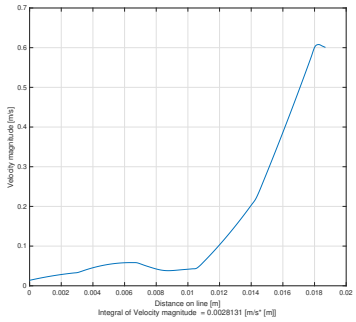

Figure C.242: Local Velocity line plot of the eddy in longitudinal direction.

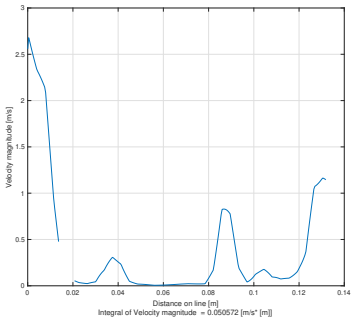

Figure C.243: Local Velocity line plot of the eddy in transverse direction.

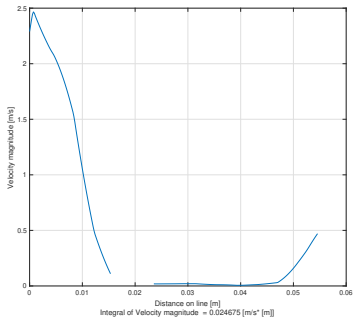

Figure C.244: Local Velocity line plot between the leading front and tail of two impellers.

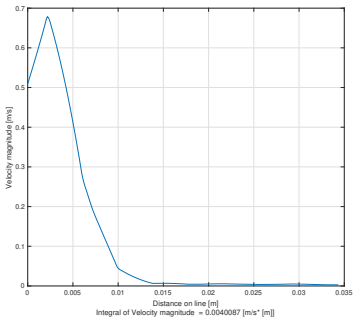

Figure C.245: Local Velocity line plot perpendicular on the leading front of the impeller. See figure 3.12 for clarification.

C.2.46. Glass beads 1.5mm, Cvd = 0.20, Speed 846 RPM

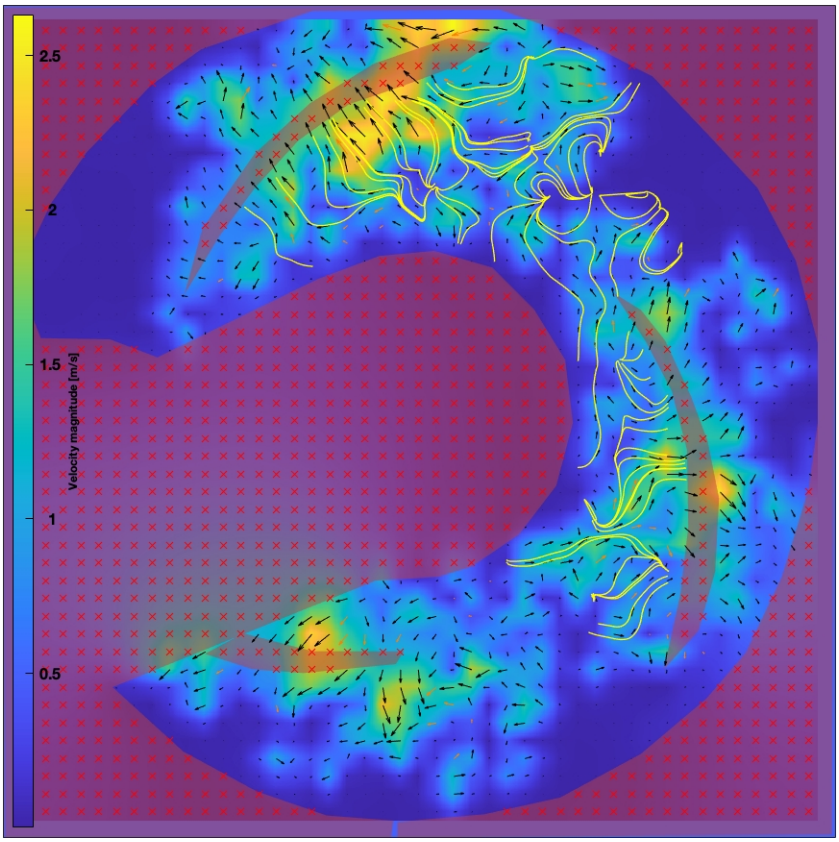

Figure C.246: PIVlab analysis of the streamlines and trajectories.

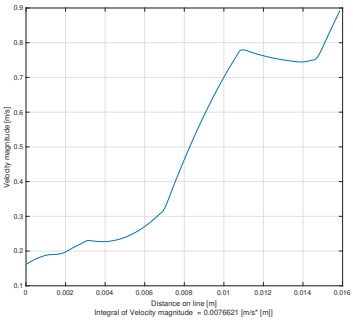

Figure C.247: Local Velocity line plot of the eddy in longitudinal direction.

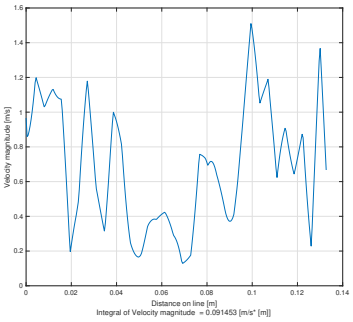

Figure C.248: Local Velocity line plot of the eddy in transverse direction.

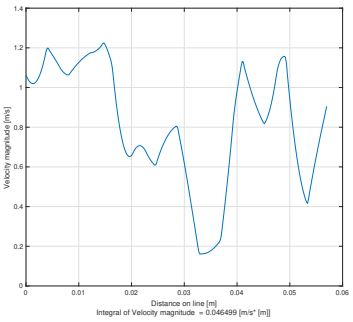

Figure C.249: Local Velocity line plot between the leading front and tail of two impellers.

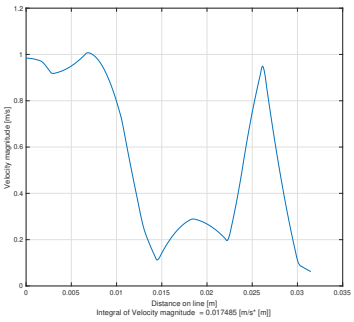

Figure C.250: Local Velocity line plot perpendicular on the leading front of the impeller. See figure 3.12 for clarification.

C.2.47. Glass beads 1.5mm, Cvd = 0.20, Speed 1128 RPM

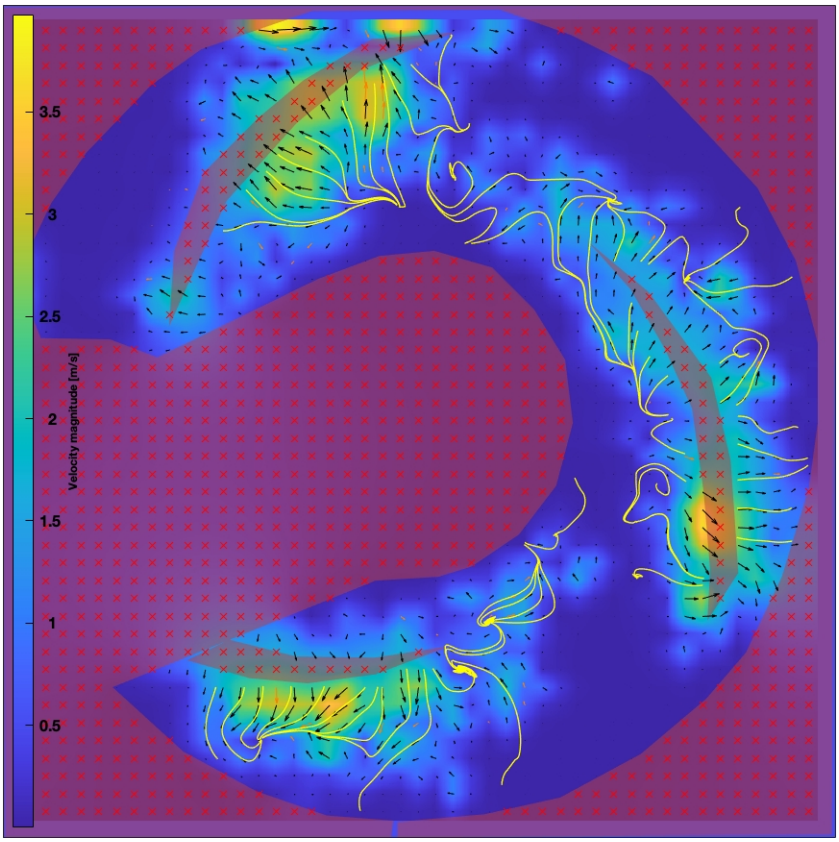

Figure C.251: PIVlab analysis of the streamlines and trajectories.

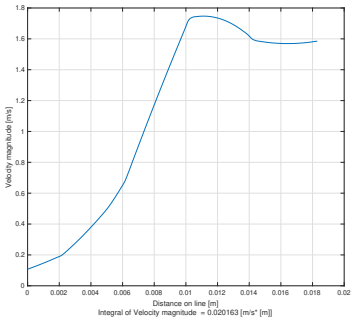

Figure C.252: Local Velocity line plot of the eddy in longitudinal direction.

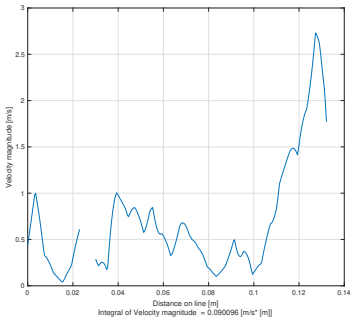

Figure C.253: Local Velocity line plot of the eddy in transverse direction.

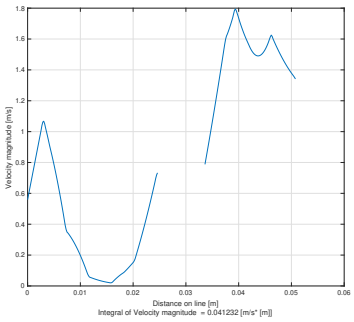

Figure C.254: Local Velocity line plot between the leading front and tail of two impellers.

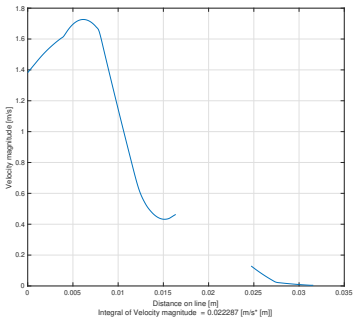

Figure C.255: Local Velocity line plot perpendicular on the leading front of the impeller. See figure 3.12 for clarification.

C.2.48. Glass beads 1.5mm, Cvd = 0.20, Speed 1410 RPM

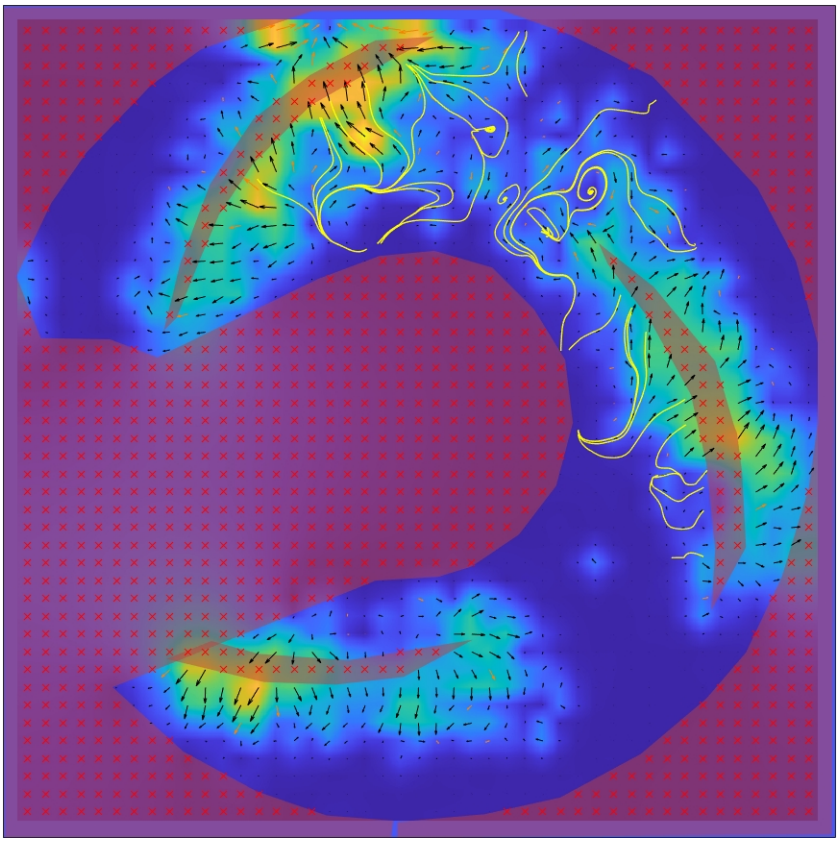

Figure C.256: PIVlab analysis of the streamlines and trajectories.

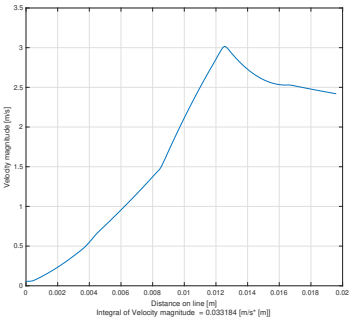

Figure C.257: Local Velocity line plot of the eddy in longitudinal direction.

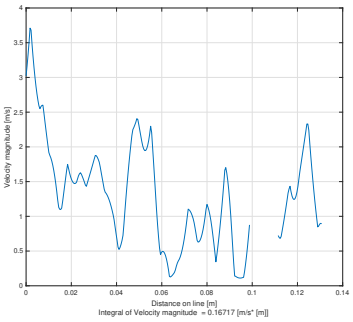

Figure C.258: Local Velocity line plot of the eddy in transverse direction.

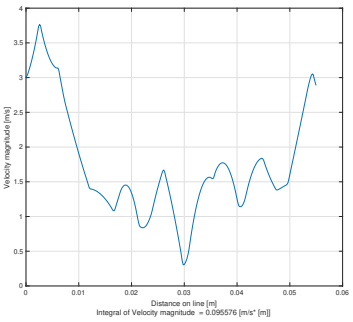

Figure C.259: Local Velocity line plot between the leading front and tail of two impellers.

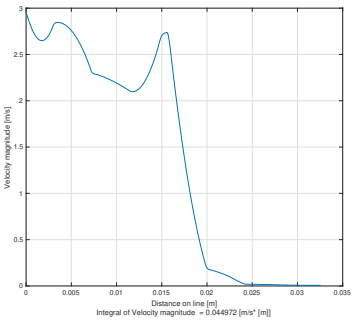

Figure C.260: Local Velocity line plot perpendicular on the leading front of the impeller. See figure 3.12 for clarification.

D

Scripts and data conversions

In this appendix, an Arduino base code and multiple Matlab scripts can be found. These codes and scripts are used for data collection, conversion and analyzing of the experiments. This way any possible conversion error in data that is (maybe) found latter can be traced back.

D.1. Arduino base code

Below is the Arduino base code displayed that regulated the analogue signal input data into digital readable information.

```
1
2 // Just a code to write the 6 analogue input values from the system ...
      into a CVS file for Matlab conversion and storage
3
4 int diffsensor1 = A0; // select input pin for differential sensor 1
5 int diffsensor2 = A1; // select input pin for differential sensor 2
6 int abssensor1 = A2; // select input pin for absolute sensor 1
7 int abssensor2 = A3; // select input pin for absolute sensor 2
8 int tempsensor = A4; // select input pin for temperature sensor 1
9 int flowsensor = A5; // select input pin for flow sensor 1
10
11 int diffsensor1_value = 0;
12 int diffsensor2_value = 0;
13 int abssensor1_value = 0;
14 int abssensor2_value = 0;
15 int tempsensor_value = 0;
16 int flowsensor_value = 0;
17
18 int t_sample = 8; // Or 2,4,6,8. 2 and 4 only working when 1 sensor ...
      is pushed through serial
19
20 void setup() {
21   Serial.begin(230400); //normal 9600 or 115200
22 }
23
24 void loop() {
25
26   diffsensor1_value = analogRead(diffsensor1);
27   diffsensor2_value = analogRead(diffsensor2);
28   abssensor1_value = analogRead(abssensor1);
```

```
29    abssensor2_value = analogRead(abssensor2);
30    tempsensor_value = analogRead(tempsensor);
31    flowsensor_value = analogRead(flowsensor);
32
33    Serial.print(diffsensor1_value);
34    Serial.print(",");
35
36    Serial.print(diffsensor2_value);
37    Serial.print(",");
38
39    Serial.print(abssensor1_value);
40    Serial.print(",");
41
42    Serial.print(abssensor2_value);
43    Serial.print(",");
44
45    Serial.print(tempsensor_value);
46    Serial.print(",");
47
48    Serial.print(flowsensor_value);
49
50    delay(t_sample); //Sampling frequency in milliseconds
51    Serial.println();
52
53 }
```

D.2. Matlab data conversion

For data storage and conversion, originating from the Arduino serial output, four different script are used. These scripts are displayed in the following four subsections and their specific tasks are explained.

D.2.1. Data store file

A basic file to store incoming serial data from the Arduino into a matrix. Depending on the toggle (true/false) data can be converted afterwards for data processing and analysing.

```
1  % A matlab script for datalogging of a study on particle trajectories near
2  % impeller blades of a centrifugal dredge pump.
3
4  % Written by Tim van den Boogaard, Student number: 4617762
5  close all
6  clear all
7  clc
8
9  %% Change only these values on specific tests.
10
11 test_number = 1; %manually improve while doing tests
12 Hertz_setting = 20; %adjustable on frequency regulator pump.
13 total_record = 10; % time in seconds
14
15 collect_data = false; %only store RAW data
16 convert_data = true; % convert data
17
18 day = "04";
19 month = "Sep";
20
21 desired_Cvd = 0.03;
22
23 test_material = 2; % 0. Water only 1. Polystyreen beads, 2. Glass beads.
24
25 test_kind = 2; %1. Pump_Curve, 2. Flow_Verification
```

```
26
27
28  %% Basic settings
29  rho_fluid = 998; %kg/m^3
30  g = 9.81; %m/s^2
31
32  weight_internal_water = 16.63; %kg internal volume setup from measurements see excel ...
        sheet
33  volume_internal = weight_internal_water/rho_fluid; %m^3
34
35  if test_material == 1
36      rho_particles = 1025; %kg/m^3 sources from Thijs.
37  elseif test_material == 2
38      rho_particles = 2500; %kg/m^3 for 1.5 & 3 mm balls. Double verify from data sheet.
39  else
40      rho_particles = rho_fluid;
41  end
42
43  S_s = rho_particles/1000;
44  particle_dia_glass = 1.5; %mm for glass.
45  particle_dia_glass_1 = 3; %mm for glass.
46  particle_dia_poly = 2; %mm for polystyreen.
47
48  weighted_particles_kg = volume_internal * desired_Cvd * rho_particles;
49  weighted_particles_gram = weighted_particles_kg * 1000
50  Cvd = desired_Cvd;
51
52  sample_time = 50; %in milliseconds from arduino file
53  M = (total_record*1000)/sample_time; %number of loop steps for conversions sheet.
54
55  %% Fixed parameters
56  internal_dia_pipe = 45.3/1000; % in mm to m converted
57  area_internal_pipe = 0.25*pi*internal_dia_pipe^2;
58  impeller_diameter = 0.3;
59
60  arduino_v = 5; %Volts analoge max.
61  arduino_mv_steps = 1024; %actaully 1024 including zero.
62  arduino_mv = arduino_v/arduino_mv_steps; %arduino measures 0-5volt in 1024 steps ...
        (zero is also a step)
63  arduino_mv_1v = 1024/arduino_v;
64
65  z = 1.155; % m, Height between pressure sensors Rosemount ΔP
66
67  h_v = 0.3; %Vapour head of water at 25 degrees.
68  h_a = 1;
69
70  %% Pump specs
71  Hertz_max = 50;
72  RPM_max = 1410; %RPM with slip included
73  Electro_power = 1100; %watt
74  Synchroon_RPM_50HZ = 1500; %Synchroon RPM
75
76  poles = 4;
77  Synchroon_RPM = (240 * Hertz_setting)/(2*poles);
78  Slip_motor = ((Synchroon_RPM_50HZ - RPM_max)/Synchroon_RPM_50HZ);
79  RPM = Synchroon_RPM*(1-Slip_motor); %sample value
80  T = (60*Electro_power)/(2*pi*RPM_max); %sample value T constant due to frequency ...
        regulator
81
82  %% Sensor specs
83
84  rosemount = 7*10^3; %max Δ pressure range.
85  absolute_pressure = 10*10^5; %max Δ pressure range.
86  flow_max = (250/1000)/60; %dm^3/m = m3/s
87
88
89  zero_rosemount_1 = 216.3967; %204.8 is 1 volt in arduino
90  zero_rosemount_2 = 211.91;
91  zero_absolute_1 = 107.5117;
92  zero_absolute_2 = 113.7083;
93  zero_flow = 200.1058;
```

```
94  temp_correction = 488.7667; %unspecified yet
95
96
97  %% Specify file name for test
98
99  if collect_data == true
100     if test_kind == 1
101         sFile = "Pump_curve_" + Hertz_setting + "HZ_TEST"+ test_number +"_RAW_"+ date ...
                +".csv";
102     else
103         sFile = "Flow_Verification_" + Hertz_setting + "HZ_C" + Cvd + "_TEST"+ ...
                test_number +"_RAW_" + date + ".csv";
104     end
105
106 % Read arduino serial port data and save RAW data
107
108  if exist(sFile) == 0  % if the file does not exists, read instrumentation
109
110     delete(instrfindall);   %pre-emptively close all ports
111     s1 = serial('/dev/cu.usbmodem14201');    %define serial port to read the Arduino
112     s1.BaudRate=9600;     %define baud rate
113     fopen(s1);
114     s1.ReadAsyncMode = 'continuous';
115     readasync(s1);
116     while(s1.BytesAvailable ≤ 0)  %wait until Arduino outputs data
117         %
118     end
119     mData = [];
120     for i=1:M %while if constant acquisition is needed.
121             sSerialData = fscanf(s1); %read sensor
122             flushinput(s1);
123             t = strsplit(sSerialData);
124             mData(i,1) = str2double(t(1));
125             mData(i,2) = str2double(t(2));
126             mData(i,3) = str2double(t(3));
127             mData(i,4) = str2double(t(4));
128             mData(i,5) = str2double(t(5));
129             mData(i,6) = str2double(t(6));
130
131
132     end
133     delete(instrfindall);    % close the serial port
134     csvwrite(sFile,mData); %Save raw data without being converted
135
136 else  % if the file exists, load it
137     f = msgbox('File RAW already exist', 'Error', 'error');
138
139  end
140 else % if data collection is turned of pop up
141     f = msgbox('DATA collection is off', 'Error', 'error');
142 end
143
144 %%  Convert data from RAW to usefull data.
145
146 if convert_data == true
147
148 if test_kind == 1
149     sFile_RAW = "Pump_curve_" + Hertz_setting + "HZ_TEST" + test_number + "_RAW_"+ ...
            day+"-"+month+"-2020.csv";
150     m_Data = csvread(sFile_RAW);
151     sFile_CONV = "Pump_curve_" + Hertz_setting + "HZ_TEST" + test_number + "_CONV_"+ ...
            day+"-"+month+"-2020.xlsx";
152 else
153     sFile_RAW = "Flow_Verification_"+ Hertz_setting +"HZ_C"+ Cvd +"_TEST" + ...
            test_number + "_RAW_"+day+"-"+month+"-2020.csv";
154     m_Data = csvread(sFile_RAW);
155     sFile_CONV = "Flow_Verification_"+ Hertz_setting +"HZ_Cvd"+ Cvd +"_TEST" + ...
            test_number + "_CONV_"+day+"-"+month+"-2020.xlsx";
156 end
157
158 if exist(sFile_CONV) == 0
```

```
159     m_converted_Data = [];
160
161     for i=1:M
162     %Put in formulas to calcute real sensor value
163     m_converted_Data(i,1) = (1.7563*(m_Data(i,1)/arduino_mv_1v)-2.7778)*1000; %down ...
            voltage range 1-5v
164     m_converted_Data(i,2) = (1.7511*(m_Data(i,2)/arduino_mv_1v)-1.7201)*1000;
165     m_converted_Data(i,3) = (2.0060*(m_Data(i,3)/arduino_mv_1v)-0.0863)*10^5; % Pa, ...
            Absolute pressure transmitter, Range 0-5 V pout
166     m_converted_Data(i,4) = (2.0182*(m_Data(i,4)/arduino_mv_1v)-0.0807)*10^5; % Pa, ...
            Absolute pressure transmitter, Range 0-5 V pin
167     m_converted_Data(i,5) = ((62.034*(m_Data(i,5)/arduino_mv_1v)-60.1736)/60000); % ...
            m^3/s, Flow meter, Range 1-5 V
168     m_converted_Data(i,6) = 30*(arduino_mv*m_Data(i,6))-50; % Celcius, Temperature, 0-5V
169
170     m_converted_Data(i,7) = 0;
171
172     m_converted_Data(i,8) =     ...
            ((abs(m_converted_Data(i,1))+abs(m_converted_Data(i,2)))/(g*z*2))+rho_fluid; ...
            % Rho_mixture
173     m_converted_Data(i,9) =     ...
            (m_converted_Data(i,8)-rho_fluid)/(rho_particles-rho_fluid); % Delivered ...
            concentration value
174     m_converted_Data(i,10) =    ...
            (m_converted_Data(i,3)-m_converted_Data(i,4))/(rho_fluid*g); %Head watercolom
175
176     %m_converted_Data(i,10) =    (m_converted_Data(i,3)/(rho_fluid*g));  %Head watercolom
177     m_converted_Data(i,11) =    (2*pi*RPM*T)/60; % Power in
178     m_converted_Data(i,12) =    ...
            (rho_fluid*g*(m_converted_Data(i,5))*m_converted_Data(i,10)); % Power out
179     m_converted_Data(i,13) =    (m_converted_Data(i,12)/m_converted_Data(1,11))*100; ...
            % Efficiency
180     m_converted_Data(i,14) =    (h_a - h_v + ...
            ((m_converted_Data(i,5)/(area_internal_pipe))^2/(2*g))); % NPSH
181
182     m_converted_Data(i,15) = 0;
183
184     m_converted_Data(i,16) = (m_converted_Data(i,5))/(RPM*6*impeller_diameter^3); ...
            %Dimensionless discharge
185     m_converted_Data(i,17) = ...
            (g*m_converted_Data(i,10))/((RPM*6)^2*impeller_diameter^2); %Dimensionless head
186     m_converted_Data(i,18) = ...
            (m_converted_Data(i,11)/(rho_fluid*(RPM*6)^3*impeller_diameter^5)); % ...
            Dimensionless power
187     end
188
189     writematrix(m_converted_Data,sFile_CONV);
190     %cvswrite(sFile_CONV,m_converted_Data);   % save the data to a CSV file
191 else
192     f = msgbox('File CONV already exist', 'Error', 'error');
193     m_converted_Data = csvread(sFile_CONV);
194 end
195
196 else
197     f = msgbox('CONV is turned off', 'Error', 'error');
198     end
```

D.2.2. Basic plot Pump Curve

Script for plotting the basic pump curves at water and mixture condition from the converted data origination of "Data_store_file.m"

```
1 %% Plot converted data from xlsx file into usefull graphs and figures
2
3 clc
4 clear all
5 close all
6
7 %% TO DO IN CODE
```

```
8
9
10
11  %% Define
12
13  day = "28";
14  month = "May";
15  test = 1;
16  Hertz_setting = 20;
17
18
19  water_pump_multiple = false; % 3 test runs in water conditions test must be set on 1
20  multiple_hz = true; %hertz_setting above on 20
21
22  %% Define load sFiles from data_store_file
23
24  sFile_1 = "Pump_curve_"+Hertz_setting+"HZ_TEST"+test+"_CONV_"+day+"-"+month+"-2020.xlsx";
25  m_converted_Data_1 = sortrows(xlsread(sFile_1),5);
26
27  if water_pump_multiple == true
28      sFile_2 = ...
            "Pump_curve_"+Hertz_setting+"HZ_TEST"+2+"_CONV_"+day+"-"+month+"-2020.xlsx";
29      m_converted_Data_2 = sortrows(xlsread(sFile_2),5);
30      sFile_3 = ...
            "Pump_curve_"+Hertz_setting+"HZ_TEST"+3+"_CONV_"+day+"-"+month+"-2020.xlsx";
31      m_converted_Data_3 = sortrows(xlsread(sFile_3),5);
32  end
33
34  if multiple_hz == true
35      sFile_30 = "Pump_curve_30HZ_TEST"+test+"_CONV_"+day+"-"+month+"-2020.xlsx";
36      m_converted_Data_30 = sortrows(xlsread(sFile_30),5);
37      sFile_40 = "Pump_curve_40HZ_TEST"+test+"_CONV_"+day+"-"+month+"-2020.xlsx";
38      m_converted_Data_40 = sortrows(xlsread(sFile_40),5);
39      sFile_50 = "Pump_curve_50HZ_TEST"+test+"_CONV_"+day+"-"+month+"-2020.xlsx";
40      m_converted_Data_50 = sortrows(xlsread(sFile_50),5);
41  end
42
43  [M,N] = size(m_converted_Data_1);
44
45  sample_time = 50; %milliseconds from arduino
46  total_record = (M*sample_time)/1000; %total recording time with sensors
47  time_step = total_record/M;
48
49
50  %% Data filtering and smoothing
51
52      x1 = max(m_converted_Data_1(1:M,5),0);
53      y1 = max(m_converted_Data_1(1:M,10),0);
54      C1 = smoothdata(y1,'gaussian',200);
55
56      y_Power = smoothdata(max(m_converted_Data_1(1:M,12),0),'gaussian',50);
57      y_Efficiency = smoothdata(max(m_converted_Data_1(1:M,13),0),'gaussian',50);
58      y_NPSH = m_converted_Data_1(1:M,14);
59
60  if water_pump_multiple == true
61      x2 = max(m_converted_Data_2(1:M,5),0);
62      y2 = max(m_converted_Data_2(1:M,10),0);
63      C2 = smoothdata(y2,'gaussian',200);
64      y_Power_2 = smoothdata(max(m_converted_Data_2(1:M,12),0),'gaussian',50);
65      y_Efficiency_2 = smoothdata(max(m_converted_Data_2(1:M,13),0),'gaussian',50);
66      y_NPSH_2 = m_converted_Data_2(1:M,14);
67
68      x3 = max(m_converted_Data_3(1:M,5),0);
69      y3 = max(m_converted_Data_3(1:M,10),0);
70      C3 = smoothdata(y3,'gaussian',200);
71      y_Power_3 = smoothdata(max(m_converted_Data_3(1:M,12),0),'gaussian',50);
72      y_Efficiency_3 = smoothdata(max(m_converted_Data_3(1:M,13),0),'gaussian',50);
73      y_NPSH_3 = m_converted_Data_3(1:M,14);
74  end
75
76  if multiple_hz == true
```

```
    x30_filtered = max(m_converted_Data_30(1:M,5),0);
    y30_filtered = max(m_converted_Data_30(1:M,10),0);
    x30 = x30_filtered;
    y30 = y30_filtered;
    C30 = smoothdata(y30_filtered,'gaussian',200);
    y_Power_30 = smoothdata(max(m_converted_Data_30(1:M,12),0),'gaussian',50);
    y_Efficiency_30 = smoothdata(max(m_converted_Data_30(1:M,13),0),'gaussian',50);
    y_NPSH_30 = m_converted_Data_30(1:M,14);

    x40_filtered = max(m_converted_Data_40(1:M,5),0);
    y40_filtered = max(m_converted_Data_40(1:M,10),0);
    x40 = x40_filtered;
    y40 = y40_filtered;
    C40 = smoothdata(y40_filtered,'gaussian',200);
    y_Power_40 = smoothdata(max(m_converted_Data_40(1:M,12),0),'gaussian',50);
    y_Efficiency_40 = smoothdata(max(m_converted_Data_40(1:M,13),0),'gaussian',50);
    y_NPSH_40 = m_converted_Data_40(1:M,14);

    x50_filtered = max(m_converted_Data_50(1:M,5),0);
    y50_filtered = max(m_converted_Data_50(1:M,10),0);
    x50 = x50_filtered;
    y50 = y50_filtered;
    C50 = smoothdata(y50_filtered,'gaussian',200);
    y_Power_50 = smoothdata(max(m_converted_Data_50(1:M,12),0),'gaussian',50);
    y_Efficiency_50 = smoothdata(max(m_converted_Data_50(1:M,13),0),'gaussian',50);
    y_NPSH_50 = m_converted_Data_50(1:M,14);
end


%% Plot figures single test and speed

if multiple_hz == false
    if water_pump_multiple == false

figure(1)
title({'Pump characteristics'},'fontsize',18)
movegui(figure(1),'west')
hold on
grid on

% Top two plots
tiledlayout(2,2)
nexttile
plot(x1,C1,'r');
xlabel('Discharge [m^3/s]','fontsize',10)
ylabel('Head [m]','fontsize',10)
nexttile
plot(x1,y_NPSH);
xlabel('Discharge [m^3/s]','fontsize',10)
ylabel('NPSH [m]','fontsize',10)

% Botom two plots
nexttile
plot(x1,y_Efficiency)
xlabel('Discharge [m^3/s]','fontsize',10)
ylabel('Efficiency [-]','fontsize',10)
nexttile
plot(x1,y_Power)
xlabel('Discharge [m^3/s]','fontsize',10)
ylabel('Power [w]','fontsize',10)

    end
end

%% Plot one speed and multiple test
if water_pump_multiple == true
    figure(1)
    title({'Pump characteristics'},'fontsize',18)
    movegui(figure(1),'west')
    hold on
    grid on
```

```
148
149     % Top two plots
150     tiledlayout(2,2)
151     nexttile
152     plot(x1,C1,'r',x2,C2,'g',x3,C3,'b');
153     xlabel('Discharge [m^3/s]','fontsize',10)
154     ylabel('Head [m]','fontsize',10)
155     legend('Test 1','Test 2','Test 3')
156     nexttile
157     plot(x1,y_NPSH,'r',x2,y_NPSH_2,'g',x3,y_NPSH_3,'b');
158     xlabel('Discharge [m^3/s]','fontsize',10)
159     ylabel('NPSH [m]','fontsize',10)
160
161     % Botom two plots
162     nexttile
163     plot(x1,y_Efficiency,'r',x2,y_Efficiency_2,'g',x3,y_Efficiency_3,'b')
164     xlabel('Discharge [m^3/s]','fontsize',10)
165     ylabel('Efficiency [-]','fontsize',10)
166     nexttile
167     plot(x1,y_Power,'r',x2,y_Power_2,'g',x3,y_Power_3,'b')
168     xlabel('Discharge [m^3/s]','fontsize',10)
169     ylabel('Power [w]','fontsize',10)
170 end
171
172
173 %% Plot multiple speeds and one test
174 if multiple_hz == true
175     figure(1)
176     title({'Pump characteristics'},'fontsize',18)
177     movegui(figure(1),'west')
178     hold on
179     grid on
180
181     % Top two plots
182     tiledlayout(2,2)
183     nexttile
184     plot(x1,C1,'r',x30,C30,'g',x40,C40,'b', x50, C50,'k');
185     xlabel('Discharge [m^3/s]','fontsize',10)
186     ylabel('Head [m]','fontsize',10)
187     legend('20Hz','30Hz','40Hz','50Hz')
188     nexttile
189     plot(x1,y_NPSH,'r',x30,y_NPSH_30,'g',x40,y_NPSH_40,'b', x50, y_NPSH_50,'k');
190     xlabel('Discharge [m^3/s]','fontsize',10)
191     ylabel('NPSH [m]','fontsize',10)
192
193     % Botom two plots
194     nexttile
195     plot(x1,y_Efficiency,'r',x30,y_Efficiency_30,'g',x40,y_Efficiency_40,'b', x50, ...
            y_Efficiency_50, 'k')
196     xlabel('Discharge [m^3/s]','fontsize',10)
197     ylabel('Efficiency [-]','fontsize',10)
198     nexttile
199     plot(x1,y_Power,'r',x30,y_Power_30,'g',x40,y_Power_40,'b', x50, y_Power_50,'k')
200     xlabel('Discharge [m^3/s]','fontsize',10)
201     ylabel('Power [w]','fontsize',10)
202 end
```

D.2.3. Basic plot Flow Verification

Script for plotting head, discharge, temperature and concentration along time with a time step of 50 ms. This script is not used for FFT analyzes on the unsteady head due to serial vs Matlab problem. The Matlab student license is limited on clock speeds of max 50 HZ. For FFT analyzes, frequencies up to 250 Hz are needed.

```
1 %% Plot converted data from xlsx file into usefull graphs and figures
2 % Written by; T van den Boogaard
3 % Student number; 4617762
4
5 clc
```

```
clear all
close all

%% Define

day = "25";
month = "Aug";
test = 1;
Hertz_setting = 20;
Cvd = 0.03;

multiple_hz = true; %hertz_setting above on 20

%% Define load sFiles from data_store_file

sFile_1 = "Flow_Verification_"+ Hertz_setting +"HZ_Cvd"+ Cvd +"_TEST" + test + ...
    "_CONV_"+day+"-"+month+"-2020.xlsx";
m_converted_Data_1 = xlsread(sFile_1);

if multiple_hz == true
    sFile_30 = "Flow_Verification_30HZ_Cvd"+ Cvd +"_TEST" + test + ...
        "_CONV_"+day+"-"+month+"-2020.xlsx";
    m_converted_Data_30 = xlsread(sFile_30);
    sFile_40 = "Flow_Verification_40HZ_Cvd"+ Cvd +"_TEST" + test + ...
        "_CONV_"+day+"-"+month+"-2020.xlsx";
    m_converted_Data_40 = xlsread(sFile_40);
    sFile_50 = "Flow_Verification_50HZ_Cvd"+ Cvd +"_TEST" + test + ...
        "_CONV_"+day+"-"+month+"-2020.xlsx";
    m_converted_Data_50 = xlsread(sFile_50);
end

[M,N] = size(m_converted_Data_1);

sample_time = 50; %milliseconds from arduino
total_record = (M*sample_time)/1000; %total recording time with sensors
time_step = total_record/M;

%% Data grouping for plotting

x = [time_step:time_step:total_record];
%y_head = smoothdata(m_converted_Data_1(1:M,10),'gaussian',5);
y_head = m_converted_Data_1(1:M,10);
y_discharge = m_converted_Data_1(1:M,5);
y_temp = smoothdata(m_converted_Data_1(1:M,6),'gaussian',50);
y_Cvd = m_converted_Data_1(1:M,9);

if multiple_hz == true
    %y_head_30 = smoothdata(m_converted_Data_30(1:M,10),'gaussian',5);
    y_head_30 = m_converted_Data_30(1:M,10);
    y_discharge_30 = m_converted_Data_30(1:M,5);
    y_temp_30 = smoothdata(m_converted_Data_30(1:M,6),'gaussian',50);
    y_Cvd_30 = m_converted_Data_30(1:M,9);

    %y_head_40 = smoothdata(m_converted_Data_40(1:M,10),'gaussian',5);
    y_head_40 = m_converted_Data_40(1:M,10);
    y_discharge_40 = m_converted_Data_40(1:M,5);
    y_temp_40 = smoothdata(m_converted_Data_40(1:M,6),'gaussian',50);
    y_Cvd_40 = m_converted_Data_40(1:M,9);

    %y_head_50 = smoothdata(m_converted_Data_50(1:M,10),'gaussian',5);
    y_head_50 = m_converted_Data_50(1:M,10);
    y_discharge_50 = m_converted_Data_50(1:M,5);
    y_temp_50 = smoothdata(m_converted_Data_50(1:M,6),'gaussian',50);
    y_Cvd_50 = m_converted_Data_50(1:M,9);
end

%% Plot figures single test and speed

if multiple_hz == false

    figure(1)
```

```
    movegui(figure(1),'west')
    hold on
    grid on

    % Top two plots
    tiledlayout(2,2)
    nexttile
    plot(x,y_head);
    xlabel('Time [s]','fontsize',10)
    ylabel('Head [m]','fontsize',10)
    nexttile
    plot(x,y_discharge);
    xlabel('Time [s]','fontsize',10)
    ylabel('Discharge [m^3/s]','fontsize',10)

    % Botom two plots
    nexttile
    plot(x,y_temp)
    xlabel('Time [s]','fontsize',10)
    ylabel('Temperature [-]','fontsize',10)
    nexttile
    plot(x,y_Cvd)
    xlabel('Time [s]','fontsize',10)
    ylabel('Delivered volumetric concentration [-]','fontsize',10)

end


%% Plot multiple speeds and one test
if multiple_hz == true

    figure(1)
    movegui(figure(1),'west')
    hold on
    grid on

    % Top two plots
    tiledlayout(2,2)
    nexttile
    plot(x,y_head,x,y_head_30,x,y_head_40,x,y_head_50);
    xlabel('Time [s]','fontsize',10)
    ylabel('Head [m]','fontsize',10)
    nexttile
    plot(x,y_discharge,x,y_discharge_30,x,y_discharge_40,x,y_discharge_50);
    xlabel('Time [s]','fontsize',10)
    ylabel('Discharge [m^3/s]','fontsize',10)

    % Botom two plots
    nexttile
    plot(x,y_temp,x,y_temp_30,x,y_temp_40,x,y_temp_50)
    xlabel('Time [s]','fontsize',10)
    ylabel('Temperature [-]','fontsize',10)
    nexttile
    plot(x,y_Cvd,x,y_Cvd_30,x,y_Cvd_40,x,y_Cvd_50)
    xlabel('Time [s]','fontsize',10)
    ylabel('Delivered volumetric concentration [-]','fontsize',10)

end

%% Plot FFT spectra for impeller interaction analyzation

y_norm_head = normalize(y_head);
Y   = fft(y_norm_head);
Y5  = fft(normalize(y_discharge));

if multiple_hz == true
    Y30 = fft(normalize(y_head_30));
    Y40 = fft(normalize(y_head_40));
    Y50 = fft(normalize(y_head_50));

    Y35 = fft(normalize(y_discharge_30));
```

```
    Y45 = fft(normalize(y_discharge_40));
    Y55 = fft(normalize(y_discharge_50));

end
    Fs = M/total_record;
    T = 1/Fs;
    L = M;
    t = x;

    figure(2)
    tiledlayout(4,2)
    nexttile
    plot(x,y_norm_head)
    P2 = abs(Y/L);
    P1 = P2(1:L/2+1);
    P1(2:end-1) = 2*P1(2:end-1);
    f = Fs*(0:(L/2))/L;
    nexttile
    plot(f,P1)
    title('Single-Sided Amplitude Spectrum of X(t)')
    xlabel('f (Hz)')
    ylabel('|P1(f)|')

    nexttile
    plot(x,normalize(y_head_30))
    P32 = abs(Y30/L);
    P31 = P32(1:L/2+1);
    P31(2:end-1) = 2*P31(2:end-1);
    nexttile
    plot(f,P31)
    title('Single-Sided Amplitude Spectrum of X(t)')
    xlabel('f (Hz)')
    ylabel('|P1(f)|')

    nexttile
    plot(x,normalize(y_head_40))
    P42 = abs(Y40/L);
    P41 = P42(1:L/2+1);
    P41(2:end-1) = 2*P41(2:end-1);
    nexttile
    plot(f,P41)
    title('Single-Sided Amplitude Spectrum of X(t)')
    xlabel('f (Hz)')
    ylabel('|P1(f)|')

    nexttile
    plot(x,normalize(y_head_50))
    P52 = abs(Y50/L);
    P51 = P52(1:L/2+1);
    P51(2:end-1) = 2*P51(2:end-1);
    nexttile
    plot(f,P51)
    title('Single-Sided Amplitude Spectrum of X(t)')
    xlabel('f (Hz)')
    ylabel('|P1(f)|')

    %% Discharge figure plot to FFT

    figure(3)
    tiledlayout(4,2)
    nexttile
    plot(x,normalize(y_discharge))
    P2D = abs(Y5/L);
    P1D = P2D(1:L/2+1);
    P1D(2:end-1) = 2*P1D(2:end-1);
    f = Fs*(0:(L/2))/L;
    nexttile
    plot(f,P1D)
    title('Single-Sided Amplitude Spectrum of X(t)')
    xlabel('f (Hz)')
    ylabel('|P1(f)|')
```

```
215
216     nexttile
217     plot(x,normalize(y_discharge_30))
218     P32D = abs(Y35/L);
219     P31D = P32D(1:L/2+1);
220     P31D(2:end-1) = 2*P31D(2:end-1);
221     nexttile
222     plot(f,P31D)
223     title('Single-Sided Amplitude Spectrum of X(t)')
224     xlabel('f (Hz)')
225     ylabel('|P1(f)|')
226
227     nexttile
228     plot(x,normalize(y_discharge_40))
229     P42D = abs(Y45/L);
230     P41D = P42D(1:L/2+1);
231     P41D(2:end-1) = 2*P41D(2:end-1);
232     nexttile
233     plot(f,P41D)
234     title('Single-Sided Amplitude Spectrum of X(t)')
235     xlabel('f (Hz)')
236     ylabel('|P1(f)|')
237
238     nexttile
239     plot(x,normalize(y_discharge_50))
240     P52D = abs(Y55/L);
241     P51D = P52D(1:L/2+1);
242     P51D(2:end-1) = 2*P51D(2:end-1);
243     nexttile
244     plot(f,P51D)
245     title('Single-Sided Amplitude Spectrum of X(t)')
246     xlabel('f (Hz)')
247     ylabel('|P1(f)|')
```

D.2.4. Unsteady head FFT analyze script

This script supplied the possibility to analyze the impeller interaction on the head. It should be noted that serial data was collected through some simple terminal commands to bypass the clock speed limitations in Matlab.

Use terminal commands in mac osx interface;

```
1     cd /Users/"NamePc"/.... your local folder location
2     script -a -t0 test_50HZ_8sec_halve.csv
3     screen /dev/cu.usbmodem14201 230400
```

```
1  %% Plot converted data from xlsx file into usefull graphs and figures
2  % Written by; T van den Boogaard
3  % Student number; 4617762
4
5  clc
6  clear all
7  %close all
8
9  %% Define
10 HZ = 20;
11 test = 1;
12 Cvd = 0.00;
13
14 gaussian_head = 20;
15 sample_time = 8; %milliseconds from arduino OLD 50
16
17 multiple_hz = true;
18
19 %% Define load sFiles from data_store_file
```

```
20
21 if multiple_hz == true
22     sFile_20 = "test_20HZ_8sec_halve.csv";
23     m_Data_20= csvread(sFile_20);
24     sFile_30 = "test_30HZ_8sec_halve.csv";
25     m_Data_30= csvread(sFile_30);
26     sFile_40 = "test_40HZ_6sec_halve.csv";
27     m_Data_40= csvread(sFile_40);
28     sFile_50 = "test_50HZ_4sec_halve.csv";
29     m_Data_50= csvread(sFile_50);
30
31 %       [M2,N2] = size(m_Data_20);
32 %       [M3,N3] = size(m_Data_30);
33 %       [M4,N4] = size(m_Data_40);
34 %       [M5,N5] = size(m_Data_50);
35      M2 = 3400;
36      M3 = 3400;
37      M4 = 4500;
38      M5 = 6500;
39
40     time_step2 = 0.008;
41     time_step3 = 0.008;
42     time_step4 = 0.006;
43     time_step5 = 0.004;
44
45     sample_time2 = 8;
46     sample_time3 = 8;
47     sample_time4 = 6;
48     sample_time5 = 4;
49
50     total_record2 = (M2*sample_time2)/1000;
51     total_record3 = (M3*sample_time3)/1000;
52     total_record4 = (M4*sample_time4)/1000;
53     total_record5 = (M5*sample_time5)/1000;
54
55     y_head_20 = normalize(m_Data_20(1:M2,1));
56     y_head_30 = normalize(m_Data_30(1:M3,1));
57     y_head_40 = normalize(m_Data_40(1:M4,1));
58     y_head_50 = normalize(m_Data_50(1:M5,1));
59
60     Y2 = fft(y_head_20);
61     Y3 = fft(y_head_30);
62     Y4 = fft(y_head_40);
63     Y5 = fft(y_head_50);
64
65     L2 = M2; L3 = M3; L4 = M4; L5 = M5;
66     Fs2 = 1/time_step2; Fs3 = 1/time_step3;
67     Fs4 = 1/time_step4; Fs5 = 1/time_step5;
68     T2 = time_step2; T3 = time_step3;
69     T4 = time_step4; T5 = time_step5;
70     t2 = (0:L2-1)*T2; t3 = (0:L3-1)*T3;
71     t4 = (0:L4-1)*T4; t5 = (0:L5-1)*T5;
72
73     sample_base2 = (M2+1)-L2:M2; sample_base4 = (M4+1)-L4:M4;
74     sample_base3 = (M3+1)-L3:M3; sample_base5 = (M5+1)-L5:M5;
75
76 else
77     sFile = "test_" + HZ + "HZ_" +sample_time + "sec_halve.csv";
78     m_Data= csvread(sFile);
79     [M,N] = size(m_Data);
80     total_record = (M*sample_time)/1000; %total recording time with sensors
81     time_step = total_record/M;
82 end
83 %% Multiple frequency plots per concentration.
84
85 if multiple_hz == true
86     figure(1)
87     tiledlayout(2,2)
88     P22 = abs(Y2(sample_base2)/L2);
89     P12 = P22(1:L2/2+1);
90     P12(2:end-1) = 2*P12(2:end-1);
```

```
    f2 = Fs2*(0:(L2/2))/L2;
    nexttile
    plot(f2,P12)
    xlim([0 60])
    %ylim([0 0.2])
    title('Single-Sided Amplitude Spectrum of X(t)')
    xlabel('f (Hz)')
    ylabel('|P1(f)|')
    legend("20Hz")

    P23 = abs(Y3(sample_base3)/L3);
    P13 = P23(1:L3/2+1);
    P13(2:end-1) = 2*P13(2:end-1);
    f3 = Fs3*(0:(L3/2))/L3;
    nexttile
    plot(f3,P13)
    xlim([0 60])
    %ylim([0 0.2])
    title('Single-Sided Amplitude Spectrum of X(t)')
    xlabel('f (Hz)')
    ylabel('|P1(f)|')
    legend("30Hz")

    P24 = abs(Y4(sample_base4)/L4);
    P14 = P24(1:L4/2+1);
    P14(2:end-1) = 2*P14(2:end-1);
    f4 = Fs4*(0:(L4/2))/L4;
    nexttile
    plot(f4,P14)
    xlim([0 80])
    %ylim([0 0.2])
    title('Single-Sided Amplitude Spectrum of X(t)')
    xlabel('f (Hz)')
    ylabel('|P1(f)|')
    legend("40Hz")

    P25 = abs(Y5(sample_base5)/L5);
    P15 = P25(1:L5/2+1);
    P15(2:end-1) = 2*P15(2:end-1);
    f5 = Fs5*(0:(L5/2))/L5;
    nexttile
    plot(f5,P15)
    xlim([0 80])
    %ylim([0 0.2])
    title('Single-Sided Amplitude Spectrum of X(t)')
    xlabel('f (Hz)')
    ylabel('|P1(f)|')
    legend("50Hz")

     Data_20 = [f2.' P12];
     Data_30 = [f3.' P13];
     Data_40 = [f4.' P14];
     Data_50 = [f5.' P15];

     cvd = 0.15;
     particle = 30;
     sFile_FTT_20 = "test_FFT_20_" + particle +"mix_" + cvd +".xlsx";
     writematrix(Data_20,sFile_FTT_20);
     sFile_FTT_30 = "test_FFT_30_" + particle +"mix_" + cvd +".xlsx";
     writematrix(Data_30,sFile_FTT_30);
     sFile_FTT_40 = "test_FFT_40_" + particle +"mix_" + cvd +".xlsx";
     writematrix(Data_40,sFile_FTT_40);
     sFile_FTT_50 = "test_FFT_50_" + particle +"mix_" + cvd +".xlsx";
     writematrix(Data_50,sFile_FTT_50);
end


%% Data grouping for plotting

if multiple_hz == false
    Fs = 1/time_step;
```

```
162     T = time_step;
163     L = M;
164     t = (0:L-1)*T;
165 
166     x = (M+1-L)*time_step:time_step:total_record;
167     sample_base = (M+1)-L:M;
168     y_head = normalize(m_Data(1:M,1));
169     Y = fft(y_head);
170 
171     figure(2)
172     tiledlayout(2,1)
173     nexttile
174     plot(x,smoothdata(y_head(sample_base),'gaussian',gaussian_head))
175     xlim([0 150*time_step])
176     title('Zero mean head noise')
177     xlabel('Time [S]')
178     ylabel('Head noise [bits]')
179     P2 = abs(Y(sample_base)/L);
180     P1 = P2(1:L/2+1);
181     P1(2:end-1) = 2*P1(2:end-1);
182     f = Fs*(0:(L/2))/L;
183     nexttile
184     plot(f,P1)
185     xlim([0 80])
186     title('Single-Sided Amplitude Spectrum of X(t)')
187     xlabel('f (Hz)')
188     ylabel('|P1(f)|')
189 end
```